SHOT NOISE, REFRACTIVE INDEX TOMOGRAPHY AND ABERRATIONS ESTIMATION IN DIGITAL HOLOGRAPHIC MICROSCOPY

THÈSE N^{O} 3913 (2007)

PRÉSENTÉE LE 4 OCTOBRE 2007

À LA FACULTÉ DES SCIENCES ET TECHNIQUES DE L'INGÉNIEUR

LABORATOIRE D'OPTIQUE APPLIQUÉE

PROGRAMME DOCTORAL EN PHOTONIQUE

ÉCOLE POLYTECHNIQUE FÉDÉRALE DE LAUSANNE

POUR L'OBTENTION DU GRADE DE DOCTEUR ÈS SCIENCES

PAR

Florian CHARRIÈRE

ingénieur physicien diplômé EPF

de nationalité suisse et originaire de Cerniat (FR)

acceptée sur proposition du jury:

Prof. Ph. Renaud, président du jury

Prof. C. Depeursinge, directeur de thèse

Dr M. Egli, rapporteur

Prof. M. Gu, rapporteur

Prof. O. Martin, rapporteur

ÉCOLE POLYTECHNIQUE
FÉDÉRALE DE LAUSANNE

Suisse

2007

Abstract

The present thesis develops some specific aspects of digital holographic microscopy (DHM), namely the effect of shot noise on the phase image accuracy, the use of DHM in micro-tomography and in aberrations evaluation of a microscope objective (MO).

DHM is an imaging technique, allowing to measure quantitatively the wavefront transmitted through or reflected by a specimen seen through a MO. A hologram, composed by the interference of the wave coming from the object with a reference wave, is recorded with a camera and then numerically processed to extract both amplitude and phase information. Thanks to its interferometric nature, DHM provides phase images, corresponding to a nanometric accuracy along the optical axis of the microscope, revealing extremely detailed information about the specimen surface in reflection configuration or its internal structure in transmission configuration. DHM has proven its efficiency on numerous applications fields going from cells biology to MEMS-MOEMS devices.

In a first part, the use of DHM as metrological tools in the field of micro-optics testing is demonstrated. DHM measurement principle is compared with techniques employed in Twyman-Green, Mach-Zehnder, and white-light interferometers. Refractive microlenses are characterized with reflection DHM and the data are confronted with data obtained with standard interferometers. Specific features of DHM such as digital focussing, measurement of shape differences with respect to a perfect model, surface roughness measurements, and evaluation of a lens optical performance are discussed. The capability to image non-spherical lenses without modification of the optical setup, a key advantage of DHM against conventional interferometers, is demonstrated on a cylindrical mircrolens and a square lenses array.

A second part treats the effect of shot noise in DHM. DHM is a single shot imaging technique, and its short hologram acquisition time (down to microseconds) offers a reduced sensitivity to vibrations. Real time observation is achievable, thanks to present performances of personal computers and digital camera. Fast dynamic imaging at low-light level involves few photons, requiring proper settings of the system (integration time and gain of the camera; power of the light source) to minimize the influence of shot noise on the hologram when the highest phase accuracy is aimed. With simulated and experimental data, a systematic analysis of the fundamental shot noise influence on phase accuracy in DHM is presented. Different configurations of the reference wave and the object wave intensities are also discussed, illustrating the detection limit and the coherent amplification of the object wave.

In a third part, DHM has for the first time been applied to perform optical diffraction tomography of biological specimens: a pollen grain and living amoebas. Quantitative 2D phase images are acquired for regularly-spaced angular positions of the specimen covering a total angle of π, allowing to build 3D quantitative refractive index distributions by an inverse Radon transform. A precision of 0.01 for the refractive index estimation and a spatial resolution in the micron range are shown. For the amoebas, morphometric measurements are extracted from the tomographic reconstructions.

The fourth part presents a DHM technique to determine the integral refractive index and morphology of cells. As the refractive index is a function of the cell dry mass, depending on the intra-cellular concentration and the organelles arrangement, the optical phase shift induced by the specimen on the transmitted wave can be regarded as a powerful endogenous contrast agent. The dual-wavelengths technique proposed in this thesis exploits the dispersion of the perfusion medium to obtain a set of equations, allowing decoupling the contributions of the refractive index and the cellular thickness to the total phase signal. The two wavelengths are chosen in the vicinity of the absorption peak of a dye added to the perfusion medium, where the absorption is accompanied by a strong variation of the refractive index as a function of the wavelength. The technique is demonstrated on yeasts.

The last part exposes two methods capable of measuring the complex 3D amplitude point spread function (APSF) of an optical imaging system. The first approach consists in evaluating in amplitude and phase the image of a single emitting point, a 60 nm diameter tip of a Scanning Near Field Optical

Microscopy (SNOM) fiber, with an original digital holographic setup. A single hologram giving access to the transverse APSF, the 3D APSF is obtained by performing an axial scan of the SNOM fiber. The method is demonstrated on an 20x 0.4 NA MO. For a 100x 1.3 NA MO, measurements performed with the new setup are compared with the prediction of an analytical aberrations model. The second method allows measuring the APSF of a MO with a single holographic acquisition of its pupil wavefront. The aberration function is extracted from this pupil measurements and then inserted in a scalar model of diffraction allowing to calculate the distribution of the complex wavefront propagated around the focal point. The results are compared with a direct measurement of the APSF achieved with the first proposed approach.

Keywords: digital holography, microscopy, phase imaging, shot noise, tomography, refractive index, cellular morphology, optical aberrations characterization, amplitude point spread function, pupil function

Résumé

Dans la présente thèse sont développés certains aspects de microscopie par holographie digitale (DHM) : l'effet du bruit de grenaille (shot noise) sur la précision des images de phase, l'utilisation de la DHM en micro-tomographie et l'évaluation des aberrations d'un objectif de microscope.

La DHM est une technique d'imagerie, permettant de mesurer quantitativement le front d'onde transmis ou réfléchi par un échantillon vu au travers d'un objectif de microscope. Un hologramme, formé par l'interférence entre l'onde provenant de l'objet et une onde de référence, est enregistré au moyen d'une caméra avant d'être traité numériquement pour en extraire l'information d'amplitude et de phase. De par sa nature interférométrique, la DHM fournit des images de phase de précision nanométrique le long de l'axe optique du microscope, contenant des informations détaillées de la surface de l'échantillon dans une configuration en réflexion ou de la structure interne de celui-ci dans une configuration en transmission. La DHM a notamment prouvé son efficacité dans de nombreux champs d'applications allant de la biologie cellulaire aux systèmes MEMS-MOEMS.

Dans une première partie, l'utilisation de la DHM en tant qu'instrument de métrologie pour le test d'éléments de micro-optique est démontrée. Son principe de mesure est comparé à ceux des interféromètres de Twyman-Green, Mach-Zehnder et en lumière blanche. Des micro-lentilles réfractives sont caractérisées au moyen d'un DHM en réflexion, et les résultats obtenus sont confrontés avec ceux provenant d'interféromètres standards. Certaines modalités spécifiques de la DHM, comme la focalisation digitale, la mesure de forme relativement à un modèle idéal, la mesure de rugosité de surface et l'évaluation de performance optique d'une lentille sont discutées. La capacité de mesurer des lentilles non sphériques sans aucune modification du système optique, un avantage clef de la DHM par rapport aux interféromètres conventionnels, est démontrée sur une lentille cylindrique et un réseau de lentilles carrées.

Une deuxième partie traite de l'effet du bruit de grenaille en DHM. La DHM est une technique d'imagerie requérant une image unique acquise dans un temps très court (quelques microsecondes au minimum), offrant par là une sensibilité réduite aux vibrations. Des observations en temps réelles sont possibles grâce aux performances actuelles des caméras numériques et des ordinateurs personnels. L'imagerie dynamique à haute vitesse implique peu de photons, nécessitant un réglage approprié du système (temps d'intégration et gain de la caméra ; puissance de la source) afin de minimiser l'influence du bruit de grenaille sur l'hologramme et garantir une excellente précision sur la phase. Au moyen de simulations et de données expérimentales, une analyse systématique de l'influence fondamentale du bruit de grenaille sur la précision des images de phase en DHM est présentée. Différentes configurations d'intensités relatives entre l'onde de référence et l'onde objet sont aussi discutées, illustrant la limite de détection et l'amplification cohérente de l'onde objet.

Dans une troisième partie, la DHM est utilisée de façon innovante pour réaliser une tomographie optique de diffraction d'échantillons biologiques : un grain de pollen et des amibes vivantes. Des images (2D) quantitatives de la phase sont enregistrées, pour des orientations de l'échantillon régulièrement espacées angulairement et couvrant un angle total de π, permettent de reconstruire, par transformée de Radon inverse, la distribution 3D de l'indice de réfraction de l'échantillon. L'indice de réfraction est obtenu avec une précision de 0.01 pour une résolution spatiale de l'ordre du micron. Pour les amibes, des mesures morphologiques sont extraites des reconstructions tomographiques.

La quatrième partie présente une technique basée sur la DHM pour déterminer l'indice de réfraction intégré et la morphologie de cellules. L'indice de réfraction étant fonction de la masse sèche des cellules, dépendant elle-même de la concentration intracellulaire et de la distribution des organelles, le déphasage induit par l'échantillon sur l'onde transmise peut se révéler un agent de contraste puissant. La technique à deux longueurs d'onde proposée dans cette thèse exploite la dispersion du milieu de perfusion pour obtenir un système de deux équations, permettant de découpler, dans le signal de phase total, les contributions de l'indice de réfraction et de l'épaisseur cellulaire. Les deux longueurs d'onde sont choisies à proximité

du pic d'absorption d'un colorant ajouté au milieu de perfusion, là où le pic d'absorption est accompagné d'une forte variation de l'indice de réfraction en fonction de la longueur d'onde. La technique est appliquée pour démonstration sur des levures.

La dernière partie expose deux méthodes permettant la mesure de la réponse impulsionnelle complexe (APSF) tridimentionnelle d'un système optique d'imagerie. La première approche consiste à mesurer, avec un système holographique original, l'amplitude et la phase l'image d'un point source unique, soit une fibre de microscope optique de champ proche (SNOM) d'un diamètre de 60 nm. Un unique hologramme donnant accès à l'APSF transverse, l'APSF 3D est obtenue en réalisant un déplacement axial de la fibre SNOM. La méthode est démontrée sur un objective de microscope 20x 0.4 NA. Pour objectif 100x 1.3 NA, les mesures obtenues avec le nouveau système sont comparées avec les prédictions d'un modèle analytique des aberrations. La seconde méthode permet de mesurer l'APSF d'un objectif de microscope avec une unique acquisition holographique de son front d'onde pupillaire. La fonction d'aberrations est extraite de cette mesure et insérée dans un modèle scalaire de diffraction, permettant de calculer la distribution complexe du champ autour du point focal. Les résultats sont comparés avec une mesure directe de l'APSF via la première approche.

Mots clefs: holographie digitale, microscopie, image de phase, bruit de grenaille (shot noise), tomographie, indice de réfraction, morphologie cellulaire, caractérisation des aberrations optiques, réponse impulsionnelle complexe, fonction pupillaire

Acknowledgements

Firstly I would like to express my gratitude to Prof. Christian Depeursinge, who offered me the opportunity to join his group for my current thesis. His limitless scientific curiosity and inventiveness made him an inexhaustible source of ideas. The freedom and trust he accorded to his group members contributed to building a positive research atmosphere.
Thanks to Prof. Min Gu, Dr. Marcel Egli, Ass. Prof. Olivier Martin and Prof. Philippe Renaud for participating in the present work as jury members, and for their wise comments on the manuscript.
Thanks to Dr. Tristan Colomb, for his help in disentangling vicious LabView wires, and for the good times spent writing papers together, especially those which weren't ours! To Jonas Kühn, Nicolas Pavillon and Etienne Shaffer, I wish you all good luck with the capricious OPAs system: concentrating your efforts, you should tame the beast! Good luck in the future to Dr. Stéphane Chamot in generating photons, being simulated or the Oblo's projection room. Yves Delacretaz, I hope you will one day see your endoscope in someone's throat for real!
Many thanks to Anca Marian, for bringing some femininity to the group for a few years: I truly appreciated our discussions on life far more than on the diffraction theory and weird phase behaviors. I hope you will guide me through Brasov one day!
My best wishes to all the Lyncée Tec crew: Etienne Cuche, Yves Emery, Nicolas Aspert, Frédéric Montfort, Sébastien Bourquin, François Marquet, Claude Joris, Eduardo Salanas. Considering the work accomplished from the first DHM prototype I saw to the actual monsters regularly going out from the foundry, I am quite confident about your future. I would like to thank particularly Etienne for his advices at the beginning of my thesis: I greatly appreciated our discussions, being scientific or not. Many thanks also to Yves for his unbridled (uncontrollable?) enthusiasm and his delicious méchouis: I am sure one day an ostrich won't be enough!
Thanks to Benjamin Rappaz and MDPhD Pierre Marquet for the stimulating atmosphere during those famous challenging multiwavelengths DHM measuring sessions, and for the wise analysis of the multicolored Valencia wines.
Thanks to Thierry Jean Heger de la Coudre and Edward Mitchell, as collaborating with you was sincerely a pleasure: not only did I enter the fascinating world of testate amoebas, finding myself smuggling stolen moss through Japanese customs to help the scientific research, but I discovered the textile businessman hidden inside me. Pseudopod your life forever.
Thanks to both our secretaries Yvette Bernhard and Manuelle Borruat, Alejo Salamanca for taking care of informatics, Claude Amendola and Michel St-Ghislain for the mechanics and Ronald Gianotti for the electronics. Thanks to all my colleagues in the Applied Optics Institute, specially Daniel Salzmann, Pascal Jourdain, François Aguet, Cédric Vonesch, Adrian Bachmann, Johann Rohner, Gérard Harbach, Alexandre Perentes and Patrick Hoffmann, for their advice, help, discussions, friendship, shared beers... Also thanks to the trainees, Michel Speiser, Rafael Frey and Jérôme Parent, for the work accomplished during their stay.
Thanks to Jamasp Jhabvala for having spiced up many of my EPFL lunches with racy anecdotes on the Lausanne's music scene and keeping me posted about the most unexpected experimental musical acts performed in the area... Qqlkjqw!
I would also like to thank my sister Céline, my quasi-sisters Laure and Claire, Françoise, and all my friends, especially those who will never read the present thesis, for all the great moments shared with no connection with the narrow scientific microcosm.
Merci à mes parents Antoinette et Lucien, la curiosité et l'ouverture d'esprit qu'ils m'ont inculquées me seront sûrement plus utiles que bien des formules contenues dans cette thèse.

All my love to Anne, for sure we will make many more winters together... (p.)

List of Notations

Roman Letters

C	Curvature compensation parameter
d	Reconstruction distance
$I_H(x, y)$	Intensity distribution in the hologram
$I_{\boldsymbol{R}}$	Intensity of the reference wave
$I_{\boldsymbol{O}}$	Intensity of the object wave
i	$\sqrt{-1}$
k	Wavenumber
k_x, k_y or k_{Dx}, k_{Dy}	Tilt compensation parameters
N	Number of pixels
n	Refractive index
$\boldsymbol{O}$	Object wave
$P_\alpha, P_{\alpha\beta}$	Aberration compensation parameters
$\boldsymbol{R}$	Reference wave
$\boldsymbol{R}_D$	Digital reference wave
t	Temporal variable

Greek Letters

$\Delta\varphi$	Phase difference
Δn	Refractive index difference
$\Delta x, \Delta y$ or $\bar{x}, \bar{y}$	Pixel size of CCD camera
$\Delta\xi, \Delta\eta$	Pixel size in the reconstruction plane
Γ_M^P	Numerical parametric lens in plane P developed with polynomial model M ($P = H$, hologram plane; $P = I$, image plane) ($M = S$, standard polynomials; $M = Z$, Zernike polynomials)
λ	Wavelength
φ	Phase
Φ	Curvature compensating digital phase mask
π	3.141592...
Ψ	Reconstructed wave front
σ	Standard deviation
θ	Angle between reference and object wave
oxy	Hologram plane
$o\xi\eta$	Image plane

Acronyms

2D	2-Dimentionnal
3D	3-Dimentionnal
APSF	Amplitude Point Spread Function
CCD	Charged Coupled Device
CMOS	Complementary Metal Oxide Semiconductor
CF	Convolution Formulation
FFT	Fast Fourier Transform
FFT^{-1}	Inverse Fast Fourier Transform
DHM	Digital Holographic Microscopy
FT	Fourier Transform
FT^{-1}	Inverse Fourier Transform
IPSF	Intensity Point Spread Function
KK	Kramers Kronig
MEMS	Micro Electro Mechanical Systems
MOEMS	Micro Opto Electro Mechanical Systems
MO	Microscope Objective
NA	Numerical Aperture
NPL	Numerical Parametric Lens
ODT	Optical Diffraction Tomography
OPL	Optical Path Length
PF	Pupil Function
PPSF	Phase Point Spread Function
PSI	Phase Shifting Interferometry
RI	Refractive Index
ROI	Region Of Interest
SFTF	Single Fourier Transform Formulation
SNR	Signal to Noise Ratio
STD	Standard Deviation

Contents

Chapter 1

Preamble

Context and goal of the thesis

Digital holographic microscopy (DHM) is an imaging technique, which allows to measure quantitatively in amplitude and phase the wavefront transmitted through or reflected by a specimen seen through a microscope objective. A hologram, composed by the interference of the wave coming from the object with a reference wave, is recorded with a camera and then numerically processed to extract both amplitude and phase information. Thanks to its interferometric nature, DHM can provides phase images with a corresponding accuracy in the nanometer range along the optical axis of the microscope, revealing extremely detailed information about the specimen surface in reflection configuration or internal structure in transmission configuration. The principle of DHM, from hologram acquisition to numerical reconstruction, is schematized in Fig. 1.1. Dynamic imaging in real time is easily achieved thanks to the actual performance of digital cameras and personal computers. Since the mid 1990s, when the digital camera became available at reasonable cost and the computers powerful enough to successively achieve holograms reconstruction, DHM has been developed considerably in terms of optical arrangements or reconstruction algorithms. DHM has proven its efficiency on numerous applications fields going from cells biology to MEMS-MOEMS devices.

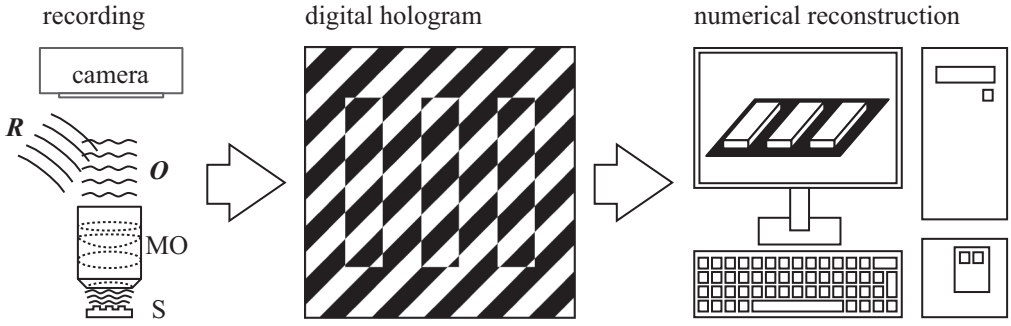

Figure 1.1: Principle of DHM; S specimen, MO microscope objective, O object wave, R reference wave.

In spite of the broad development and large popularity of DHM, really few works have studied the accuracy of the technique. As DHM counts among the interferometry techniques, its performances are naturally often compared to white-light, Mach-Zehnder or Michelson classical interferometers. So came the idea of the first paper presented in this thesis, discussing some advantages and drawbacks of digital holography vs classical interferometry, through an application of DHM dedicated to microlenses characterization (chapter 3). Questioning about the best achievable performances and the limitation of the technique lead to the problematic of shot noise in DHM. The shot noise is a manifestation of the quantic nature of photons, and can therefore not be avoided in any image acquisition procedure, in our case the hologram recording. If the statistical behavior of shot noise on the hologram is well known, its effect on the phase image digitally reconstructed from the hologram is for the first time the object of a complete study (chapter 4). The quality of the reconstructed phase image as a function of the intensity repartition between the reference and object wave in presence of shot noise is treated in a first paper (section 4.1),

while a second paper deals with the absolute phase accuracy achievable as a function of the hologram light intensity (section 4.2).

The word holography literally means that all the information is recorded, alluding to the fact that both the amplitude and phase are collected, describing a wavefront completely. If this assumption is true when the wavefront is considered, it is only partially true when it refers about the object that produces this wavefront. In reflection configuration, the amplitude provides information on the reflectivity of the specimen, while the phase depicts its topography, so the term holography is obviously not abusive. In transmission configuration, the phase depends on simultaneously two parameters: the thickness and the refractive index (i.e. optical density) of the specimen. Therefore, except in the case of a sparse distribution of highly diffracting particles, a single reconstructed wavefront does not reveal the 3-dimensional inner content of the specimen, but more a sort of projection of the 3-dimensional structure. The formalism to build a volumetric map of a specimen from optical data, called optical diffraction tomography, was developed in the late 1960s. By collecting diffracted wavefronts for different orientation of the specimen, the ambiguity between thickness and density can be solved. Optical diffraction tomography based on DHM measurements has been investigated (chapter 5), leading to two papers: one demonstrating the principle of the technique on a pollen grain (section 5.1), the second making use of the technique on living cells (testate amoebas) to determine morphologic data (section 5.2). In some cases, the 3-dimensional imaging is not an absolute requirement, an integrated value of the thickness and refractive index being sufficient, and different strategies has been developed to decouple those values. A novel method is presented here for cell imaging (chapter 6), based on dual-wavelength measurement: taking advantage of the known dispersion function of the perfusion medium, one can obtain a set of two equations, one for each wavelength, allowing to calculate separately the thickness and refractive index.

In DHM as in any other microscopy technique the setup may suffer from optical aberrations, causing losses in resolution and accuracy, or even image distortion. Achieving a proper wavefront reconstruction in amplitude and phase from a single hologram may actually be a complicated task in the presence of aberrations. During the late 1990s, Dr. Etienne Cuche from the group of Prof. Christian Depeursinge in Lausanne proposed a novel way of reconstructing digital holograms, which has been further developed, generalized and automatized by Dr. Tristan Colomb in the same group few years later. They are two main concepts behind the use in DHM of the so-called numerical optics and numerical parametric lenses. The first is that a recorded hologram can be accurately reconstructed with no *a priori* information about the exact optical configuration of the microscope, by taking advantage of known constant phase areas in the field of view. The second makes a parallel between aberrations correction in an actual setup and during hologram reconstruction, where numerical lenses are used instead of actual lenses. This technique has proved its efficiency and versatility in numerous applications, and has been used extensively in all the works gathered together in this thesis. A more conventional manner would be inspired by the conventional bright field microscopy: the aberrations are carefully estimated by measuring the point spread function of the microscope with a sub-resolution object, after what the images are digitally processed (deconvolution) to get rid of the aberrations. The first difficulty with this approach applied to DHM concerns the acquisition of the point spread function of the objective, which needs to be acquired not only in intensity, as in bright field microscopy, but also in phase. Two papers proposing an original setup for complex amplitude point spread function (APSF) measurement of microscope objectives with DHM are presented at the end of the current thesis (chapter 7): in the first, the APSF is recorded directly in the image plane (section 7.1), while in the second, the APSF is derived from an evaluation of the aberrations in the pupil plane of the microscope objective (section 7.2).

Structure of the dissertation

The core of the thesis is constituted by eight papers (7 published, 1 in preparation), covering the chapters 3 to 7. The present first chapter is followed by an introductive chapter on digital holographic microscopy, containing a brief history of the technique with a panorama of actual developments and a summary of the hologram reconstruction procedure. As each paper already includes an introduction motivating individual works, with contextual bibliography, there is no additional introduction besides this preamble for each specific subject treated in the thesis.

For chapter 5 presenting results obtained with DHM-based optical diffraction tomography, a complementary discussion has been added after the papers. A general conclusion summarizes the main results of the thesis at the end, while more specific conclusions and comments on each study are given in the related papers.

Chapter 2

Introduction

2.1 From classical holography to digital holography

Digital Holography finding its origin in the late 1960s, the present chapter does not pretend to give a complete review of this rich technique, which embraces numerous research fields such as microscopy, metrology, optical diffraction tomography, data storage or even cryptography. Some milestones regarding the pioneer works on the technique will be reminded, while some details will be given on specific aspects and recent developments to motivate and inscribe the work achieved during this thesis in a more precise context.

2.1.1 Classical holography

After the first publication on the technique by Denis Gabor in 1948 [Gab48], numerous seminal studies were realized in the field of holography, today referred as classical holography. The works initiated by D. Gabor [Gab48, Gab49, Gab51, Gab66, Gab71], E.N. Leith [Lei63, Lei64, Lei82], A. Lohmann [Loh65], R.J. Collier [Col71], J. Upatnieks [Upa66], G. Stroke [Str69], Y.N. Denisyuk [Den74, Den80], R.F. Vanligte [Van66], J.W. Goodman [Goo68], R. Dändliker [Dän70] or H. Tiziani [Tiz72, Tiz81], still find echoes in the present research. A historic review on holography can be found in a paper by Leith [Lei97], and most of the developments and results have been summarized in different books [Goo68, Str69, Smi69, Col71, Han79, Fra87, Har96].

2.1.2 Classical recording and reconstruction of a hologram

A hologram is the result of the interference between two coherent waves, an object wave $\boldsymbol{O}$ emanating by the object and a reference wave $\boldsymbol{R}$. In the hologram plane *0xy*, these two waves produce an interference pattern with a two-dimensional (2D) intensity distribution $I_H(x, y)$:

$$I_H(x,y) = (\boldsymbol{R}+\boldsymbol{O})(\boldsymbol{R}+\boldsymbol{O})^* = |\boldsymbol{R}|^2 + |\boldsymbol{O}|^2 + \boldsymbol{R}^*\boldsymbol{O} + \boldsymbol{R}\boldsymbol{O}^*, \tag{2.1}$$

where $|\boldsymbol{R}|^2 = I_{\boldsymbol{R}}$ is the intensity of the reference wave and $|\boldsymbol{O}|^2 = I_{\boldsymbol{O}}(x, y)$ the intensity of the object wave. $\boldsymbol{R}^*\boldsymbol{O}$ and $\boldsymbol{R}\boldsymbol{O}^*$ are the interference terms with $\boldsymbol{R}^*$ and $\boldsymbol{O}^*$ denoting the complex conjugates of the two waves. In classical holography, this interference pattern is principally recorded on photographic plates, photorefractive material, or photopolymers.

To recover the initial object wavefront, the developped hologram must be illuminated again by a wave. Assuming a plane reference wave with a uniform intensity $I_{\boldsymbol{R}}$ and a hologram transmittance proportional to the exposure, the so-called reconstructed wavefront Ψ is obtained by multiplying Eq. 2.1 with a wave $\boldsymbol{U}$:

$$\Psi(x,y) = \boldsymbol{U}I_H(x,y) = \boldsymbol{U}I_{\boldsymbol{R}} + \boldsymbol{U}I_{\boldsymbol{O}} + \boldsymbol{U}\boldsymbol{R}^*\boldsymbol{O} + \boldsymbol{U}\boldsymbol{R}\boldsymbol{O}^*. \tag{2.2}$$

The two first terms of Eq. 2.2 form the zero order of diffraction, which are be sometimes called zero order (ZO). The third and the fourth terms are produced by the interference terms and generate two conjugate or twin images of the object. $\boldsymbol{U}\boldsymbol{R}^*\boldsymbol{O}$ produces a virtual image located at the initial position of the object and $\boldsymbol{U}\boldsymbol{R}\boldsymbol{O}^*$ produces a real image located on the other side of the hologram. If the

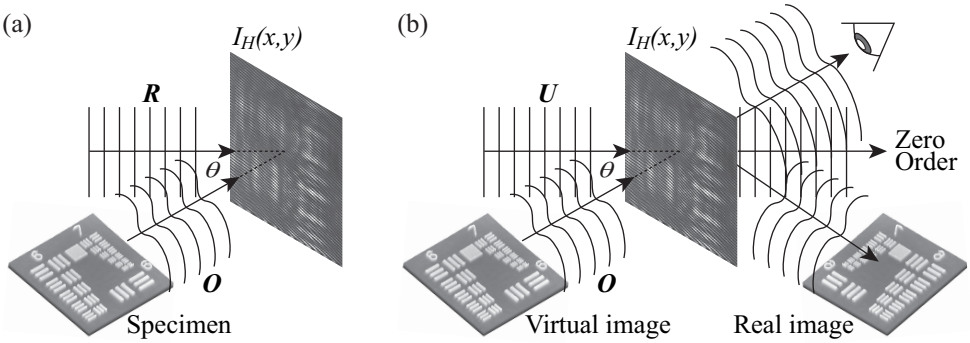

Figure 2.1: Recording (a) and reconstruction (b) of an off-axis hologram.

reconstruction is performed by illuminating the hologram with a replica of the reference wave ($\boldsymbol{U} = \boldsymbol{R}$) the virtual image is a replica of the object wave multiplied by the reference intensity ($I_{\boldsymbol{R}}\boldsymbol{O}$). Reciprocally if $\boldsymbol{U} = \boldsymbol{R}^*$, the real image is a replica of the conjugate object wave multiplied by the reference intensity ($I_{\boldsymbol{R}}\boldsymbol{O}^*$).

In classical holography, the condition $\boldsymbol{U} = \boldsymbol{R}$ or $\boldsymbol{U} = \boldsymbol{R}^*$ is generally required, especially for so-called thick or volume holograms, for which the recording of the interference in the thickness of the photographic emulsion defines a Bragg condition for the illuminating wave (see. e.g. the book by Goodman, chap. 8 [Goo68]). This Bragg condition also acts on the wavelength of the illuminating wave and if light with a broad spectrum (white light) is used for the reconstruction process, only the wavelength used for recording will be selected and participate to the image formation. For thin holograms, the condition $\boldsymbol{U} = \boldsymbol{R}$ or $\boldsymbol{U} = \boldsymbol{R}^*$ cannot be strictly satisfied with a repercussion on the quality of the reconstructed images, in particular their resolution [Cha69]. Following the original idea of Cuche *et al.* [Cuc99a], the phase reconstruction in DHM is performed by replacing the illuminating wave $\boldsymbol{U}$ by a digital reference $\boldsymbol{R}_D$, which must be an exact replica of the optical reference wave. This principle is developed in the section 2.2 of the present chapter.

2.1.3 Off-axis holography

In Gabor's original work, the hologram was recorded in an inline geometry with an object wave and a reference wave having parallel directions of propagation. In this case, the four components of Eq. 2.2 propagate along the same direction and cannot be observed separately. The idea with off-axis holography is to introduce an angle θ between the directions of propagation of the object and reference waves. Therefore, the different terms of the interference propagate along separated directions during the reconstruction. The recording and reconstruction procedures are schematized in Fig. 2.1. Indeed, if we assume a plane reference wave with intensity I_R

$$\boldsymbol{R}(x,y) = \sqrt{I_{\boldsymbol{R}}}\exp\left(ikx\sin\theta\right), \tag{2.3}$$

where $k = 2\pi/\lambda$ is the wavenumber, the intensity on the hologram plane becomes

$$I_H = I_{\boldsymbol{R}} + I_{\boldsymbol{O}} + \sqrt{I_{\boldsymbol{R}}}\exp\left(-ikx\sin\theta\right)\boldsymbol{O} + \sqrt{I_{\boldsymbol{R}}}\exp\left(ikx\sin\theta\right)\boldsymbol{O}^*. \tag{2.4}$$

The phase factor $\exp\left(-ikx\sin\theta\right)$ in the third term, which produces the virtual image, indicates that the wave is deflected with an angle $-\theta$ with respect to the direction of the illuminating wave $\boldsymbol{U}$. The opposite phase factor appears in the fourth term, meaning that the wave producing the real image is deflected with an angle θ. The zero order of diffraction propagates in the same direction as $\boldsymbol{U}$. In other words, the off-axis geometry separates spatially the different orders of diffraction, allowing an individual observation of each term.

2.1.4 Digital holography

In digital holography, the idea is to replace the recording of the hologram on a photosensitive substrate by an electronic camera, such as charge couple device (CCD) cameras or complementary metal oxide semiconductor (CMOS) cameras. Therefore, the cumbersome task of hologram developing is suppressed,

and high acquisition rates become available. The reconstruction is then done completely numerically. A comprehensive review on digital holography has been written by Schnars and Jüptner [Sch02], and a detailed review on digital holography applied to microscopy written by Depeursinge can be found in a book by Poon [Poo06]. For sake of clarity, the major contributions are summarized here.

The idea of digital holography appeared much before the technical medium (CCD and personal computer) were commercially available to effectively implement the technique in the lab, as J.W. Goodman and R.W. Laurence [Goo67] proposed it for the first time in 1967. M.A. Kronrod and L.P. Yaroslavsky [Kro72b, Kro72a] started numerical hologram reconstruction in the early 1970s: in-line Fourier holograms were recorded on photographic plates, before being sampled to be reconstructed numerically.

The technique really started with the arrival of the first CCD cameras in the beginning of the 1990s. In 1993, Coquoz *et al.* implemented a CCD in their endoscopic holographic setup and achieved a fully numerical reconstruction of the wavefront intensity from a single hologram [Coq93]. The same year, a complete digital holographic setup with digital recording and reconstruction was achieved by Schnars and Jüptner [Sch93], demonstrating the possibility to measure specimen deformations by evaluating the phase difference between two states of the specimen; the same setup has then also be used for amplitude reconstruction from single holograms [Sch94].

An important step was the reconstruction not only of the amplitude of the wavefont as in most of the papers quoted above, but also of the phase, containing much more detailed information about the object morphology and composition. Different techniques exist to reconstruct the absolute phase. In-line techniques require phase-shifting procedures done with several holograms acquired successively [Yam97, Zha98, Lai00b, Guo02, Yam03, Awa04, Mil05] or simultaneously [Kol92, Kem99, Mil01, Dun03, Wya03].

A key solution for absolute phase measurements was proposed by Cuche *et al.* in 1999 [Cuc99a] and then by Liebling [Lie03, Lie04b]: they showed that the reconstruction of the phase can be done from a single hologram as in classical holography by the adjustment of several reconstruction parameters. However, the procedure proposed initially for this parameters adjustment is not automated and requires a manual adjustment of the parameters values, making the method a bit hermetic for a non perfectly-trained user. To avoid this adjustment, Ferraro *et al.* [Fer03b] used a reference hologram taken on a flat part of the specimen, and a subtraction procedure for aberrations compensation. This simple technique performs efficiently if the experimental presence of parasitic conditions (vibrations, drifts,...) are well controlled, but fails in providing precise measurements in most of the actual situations, and is therefore not adapted for most practical applications. In his thesis, Colomb generalized and automatized recently the original ideas of Cuche [Col06a]. Introducing the so-called numerical optics and numerical parametric lenses in the reconstruction process, Colomb *et al.* greatly improved the robustness and versatility of DHM thanks to two main features: firstly, a recorded hologram can be accurately reconstructed with no *a priori* information about the exact optical configuration of the microscope, by taking advantage of known constant phase areas in the field of view [Col06d]; secondly, aberrations can be compensated thanks to a parallel made between aberrations correction in an actual setup and during hologram reconstruction, where numerical lenses are used instead of actual lenses [Col06b, Col06c].

The introduction of a microscope objective in the holographic setup gave birth to digital holographic microscopy (DHM), opening new fields of applications [Zha98, Cuc99b, Tis01, Xu01, Dub02, Car04, Cop04]. Because DHM allows for truly noninvasive examination of biological specimen, the interest of digital holography techniques for biomedical applications has considerably increased then [Tyc01, Jav05b, Ahn05, Sos05, Sun05, Son06, Li06, Lue06, Lue07, Man06, Mar07, Moo07, Mic07, Par06a, Cha07, Ell07, Für07, FY07]. Numerous studies on red blood cells (erythrocytes) have noticeably been carried out [Ike05, Tis01, Tis03, Tis04, Tis05, Pop04], some specifically addressing the problematic of the membrane fluctuations [Bra06, Rap06, Rap07, Pop05, Pop06a, Pop06b, Pop06c]. In cell biology, we can also mention studies on neurones [Mar03, Mar05, Mar06b, Mar06a, Rap05], tumorous cells [Car04, Jeo05, Kem06, Dub06] or pollen grains [vH04, Cha05].

Developments in DHM for real 3-dimensional imaging, also called tomographic imaging, have been proposed. They exploit different physical principles to finally discriminate between different sections of the observed specimen: short coherence sources [Ind99, Ped01a, Ped02, Mas05, The05, ML05, Jeo06, Jeo07], multiple wavelengths [Kim99, Kim00, Dak03, Yu05b, Yu05a, Mon06b, Mon05, Yu07] or multiple illumination directions [Vis98, Vis99, Lau02, Józ05, Józ06, Cha06b, Cha06c, Gór04, Gór06, Gór07]. Among the numerous application of DHM, just to give an impression of their diversity without going into detailed description of each specific work, we can mention color digital holography [Kat02, Yam02, Alm04, Jav05a, Yu04], synthetic-wavelength digital holography [Ono98, Wag00, Gas03, Par06b, Küh07], aberrations compensa-

tion techniques [Cuc99b, Sta00, Ind01, Ped01b, DN02, Fer03a, ML05, Yon05, dN05, Col06b, Col06c, Mon06a, Mic07], deformation analysis and shape measurement [Ped97, Nil98, Kem99, Nil00, Yam01, Ma04], particle tracking [Mur00, Coe02, Hin02, Soo02, Fer03a, Leb03, Pan03, Xu03, Mül04, Lew06], refractometry [Keb99, Dub99, Bac05, Seb05, Apo04], information encrypting [Jav00, Taj00, Lai00a, Yu03, Nis04, Nom04, He05, Sit05], electrochemistry [Wan04, Yan04], vibration measurement [Zha04, Bor05, Iem06], micro-optic testing [Keb00, Keb01b, Keb01a, Mül05, Cha06a], ferroelectric material studies [dA04, dN04, Gri04, Pat05], endoscopic devices [Coq95, Sch99, Sch01, Kol03, Ped03], or polarization imaging [Beg99, Col02, Col04, Col05, Yok06, Yok07, Nom07].

2.1.5 Experimental Configurations

Two main configurations exist for the implementation of DHM: a first one for reflection imaging and a second one for transmission imaging. In both cases the basic architecture is derived from a modified Mach-Zehnder interferometer, as illustrated on Fig. 2.2. The light source depends on the applications: HeNe lasers [Cuc99a, Cuc99b], low coherence sources [Mas05, Küh07] or even tunable sources [Kim99, Mon06b]. The combination of a neutral density filter, a half-wave plate and a polarizing beam splitter are used for the adjustment of the intensities in the reference and object arms.

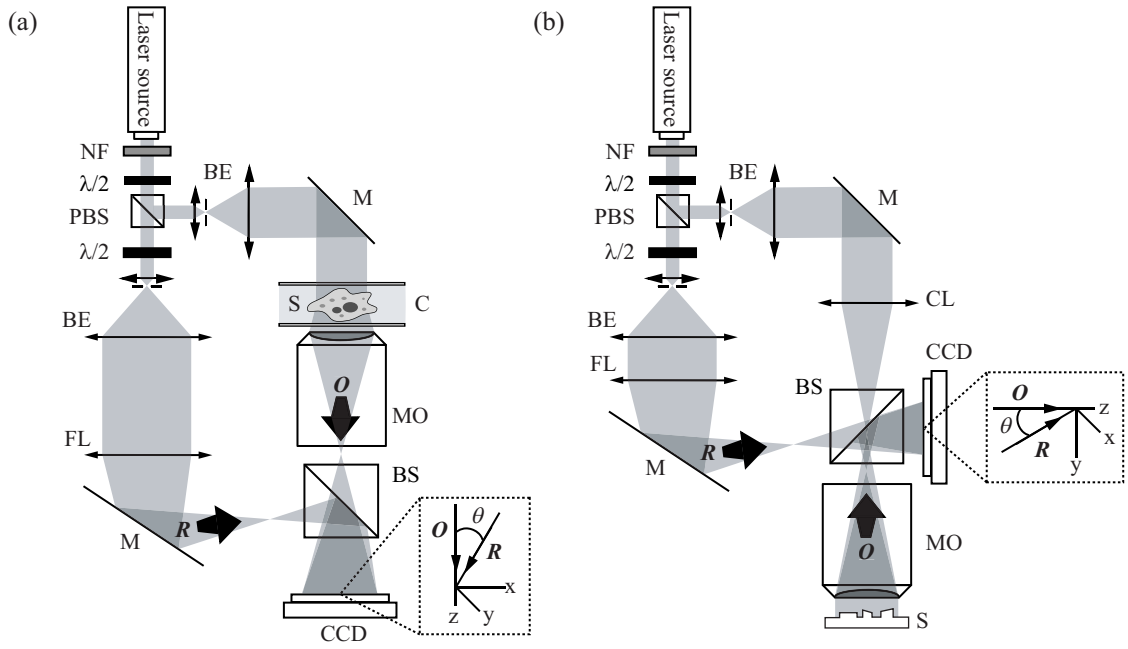

Figure 2.2: Holographic microscope schemes in transmission (a) and reflection (b); NF neutral filter; λ/2 half-wave plate; MO microscope objective; FL field lens; M mirror; PBS polarizing beam splitter; BS beam splitter; O object wave; R reference wave; C specimen chamber; S specimen. Insets: details showing the off-axis geometry at the incidence on the CCDs.

In both transmission and reflections configurations, a MO collects the object wave $\boldsymbol{O}$ resp. transmitted or reflected by the specimen, and produces a magnified image of the specimen behind the CCD camera at a distance d (Fig. 2.3). As explained in details by Cuche *et al.* [Cuc00c], this situation can be considered to be equivalent to a holographic configuration without MO with an object wave $\boldsymbol{O}$ emerging directly from the magnified image of the specimen and not from the specimen itself. High resolution can thus be obtained with a MO with high numerical aperture (NA). Indeed, the high NA MO provides a simple way to adapt the sampling capacity of the camera to the information content of the hologram [Mar03]. As illustrated in Fig. 2.3, a lens or a MO achieve a reduction of the k_x, k_y components of the $\boldsymbol{k}$ vector components in the specimen plane perpendicular to the optical axis. The reduction factor is given by the magnification of the MO. The new components k'_x, k'_y of the $\boldsymbol{k'}$ wavevector of the beam after having crossed the MO can be made as small as required by the Shannon theorem applied to the sampling capacity dictated by the pixel size of the camera. Using a high magnification objective, the match can be optimized. At the same time, by maximizing the NA, the transverse resolution can be pushed to the limit of diffraction and sub-micron resolution can be easily achieved (ordinarily better than 600nm).

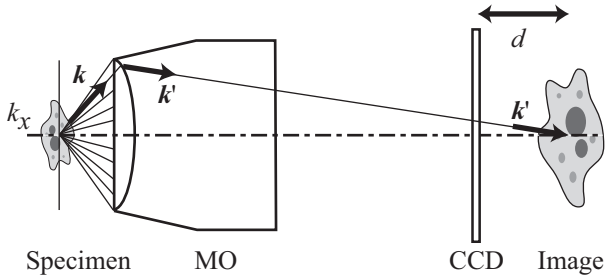

Figure 2.3: Use of a lens or microscope objective to adapt the sampling capacity of a CCD in the hologram plane with the spatial spectrum of the object.

At the exit of the interferometer the interference between the object wave $\boldsymbol{O}$ and the reference wave $\boldsymbol{R}$ creates the hologram intensity of Eq. 2.1. A lens RL can be introduced in the reference arm, see Fig. 2.2 to produce a spherical reference wave with a curvature in the CCD plane very similar to the curvature induced by the MO. This permits to have a hologram composed with equally-spaced straight fringes. This hologram is digitalized and recorded by a black and white CCD camera and then transmitted to a computer. The digital hologram $I_H(k,l)$ is an array of N x N (usually 512 x 512 or 1024 x 1024) 8-bit-encoded numbers resulting from the two dimensional sampling of $I_H(x,y)$ by the CCD camera:

$$I_H(k,l) = \int_{k\Delta x-\Delta x/2}^{k\Delta x+\Delta x/2} \int_{l\Delta y-\Delta y/2}^{l\Delta y+\Delta y/2} I_H(x,y)dxdy. \tag{2.5}$$

where k,l are integers and Δx, Δy define the sampling intervals in the hologram plane (pixel size). A hologram of an USAF test target recorded with a reflection setup is presented in Fig. 2.4.

2.2 Numerical reconstruction of holograms

In the present thesis, the algorithm used for holograms numerical reconstruction comes from the original idea from Cuche *et al.* [Cuc99a, Cuc00a], which was generalized, completed and automatized recently by Colomb *et al.* [Col06a, Col06b, Col06c]. As the complete theory is extensively and comprehensively developed in the later references, only a short summary on the reconstruction techniques will be presented here, trying to emphasize the main concepts without going in too much details regarding the mathematical formalism.

2.2.1 Former reconstruction algorithm

In Cuche's works [Cuc99a, Cuc99b], the algorithm for hologram reconstruction, was formulated as follows:

$$\begin{aligned}\Psi(\xi,\eta) = \Phi(\xi,\eta)\frac{\exp(i2\pi d/\lambda)}{i\lambda d}\exp\left[\frac{i\pi}{\lambda d}(\xi^2+\eta^2)\right] \\ \cdot \iint \boldsymbol{R}_D(x,y)I_H(x,y)\exp\left[\frac{i\pi}{\lambda d}\left((x-\xi)^2+(y-\eta)^2\right)\right]dxdy.\end{aligned} \tag{2.6}$$

This expression describes the Fresnel propagation of the reconstructed wavefront Ψ over a distance d, from the hologram plane *0xy* to the observation plane (or reconstruction plane) $0\xi\eta$. As in Eq. 2.1, $I_H(x,y)$ is the hologram intensity distribution; a typical example of digital hologram can be seen on Fig. 2.4. As proposed by Cuche *et al.*, the removal of the zero order and twin image can be preliminarily performed by applying a user-defined mask to the Fourier spectrum of the off-axis hologram [Cuc00c]. $\boldsymbol{R}_D$ is defined as a computed replica of the experimental reference wave $\boldsymbol{R}$. Assuming an hologram recorded in the off-axis geometry with a plane reference wave, $\boldsymbol{R}_D$ can be expressed as

$$\boldsymbol{R}_D(x,y) = \exp\left[i\frac{2\pi}{\lambda}(k_x x + k_y y) + i\varphi(t)\right], \tag{2.7}$$

where the parameters k_x, k_y define the propagation direction, and $\varphi(t)$ the phase delay between the object and reference waves, which varies during time due to external perturbations, such as mechanical

Figure 2.4: Typical 1024x1024 off-axis hologram of a USAF test target acquired in reflection configuration. Inset: a zoom showing clearly the interference fringes

vibrations or air fluctuations. As explained by Cuche *et al.* [Cuc99a], the k_x and k_y values must be adjusted for proper phase reconstruction, so that the propagation direction of the computed wave-front $\boldsymbol{R}_D$ fits the propagation direction of the experimental wave $\boldsymbol{R}$, while as explained in Ref. [Cuc99b], the role of Φ is to compensate for the wave-front curvature appearing when a microscope objective (MO) is used to improve the transverse resolution. In Ref. [Cuc99b], a simple quadratic model is used for computation, in first approximation of the actual paraboloidal phase curvature induced by an ideal MO:

$$\Phi(\xi,\eta) = \exp\left[\frac{-i\pi}{\lambda C}(\xi^2+\eta^2)\right], \tag{2.8}$$

where C is the parameter that has to be adjusted to compensate for this curvature. Examples illustrating the tilt aberration and the phase curvature induced by the MO are presented in Fig. 2.5.

Using the modulation property of the two dimensional Fresnel Transform [Lie04a], Colomb demonstrated that the digital reference wave $\boldsymbol{R}_D$ in Eq. 2.6 can be replaced by a pseudo-reference wave $\boldsymbol{R}'$ outside the integral [Col06a]:

$$\begin{aligned}\Psi(\xi,\eta) = \Phi(\xi,\eta)\boldsymbol{R}'(\xi,\eta)\frac{\exp(i2\pi d/\lambda)}{i\lambda d}\exp\left[\frac{i\pi}{\lambda d}(\xi^2+\eta^2)\right] \\ \cdot\iint I_H(x,y)\exp\left[\frac{i\pi}{\lambda d}\left((x-\xi)^2+(y-\eta)^2\right)\right]dxdy.\end{aligned} \tag{2.9}$$

where $\boldsymbol{R}'$ is the pseudo-reference wave

$$\boldsymbol{R}'(\xi,\eta) = \exp\left[i\frac{2\pi}{\lambda}(k_x\xi+k_y\eta)+i\varphi'(k_x,k_y,t)\right]. \tag{2.10}$$

This means that passing the digital reference wave outside the Fresnel integral is a straightforward operation that conserves the plane wave nature of the wavefront. Furthermore, for phase reconstruction with DHM, it means that the effects of the off-axis geometry simply has the appearance of a tilt aberration in the observation plane. This tilt can be compensated by multiplying the reconstructed wavefront with a correcting term calculated with the mathematical model of a plane wave. Compared to the former method [Eq. 2.6], the great advantage is that the adjustment of this pseudo-reference wave does not shift the image in the reconstruction plane and the propagation integral does not need to be recomputed if the parameters k_x and k_y change.

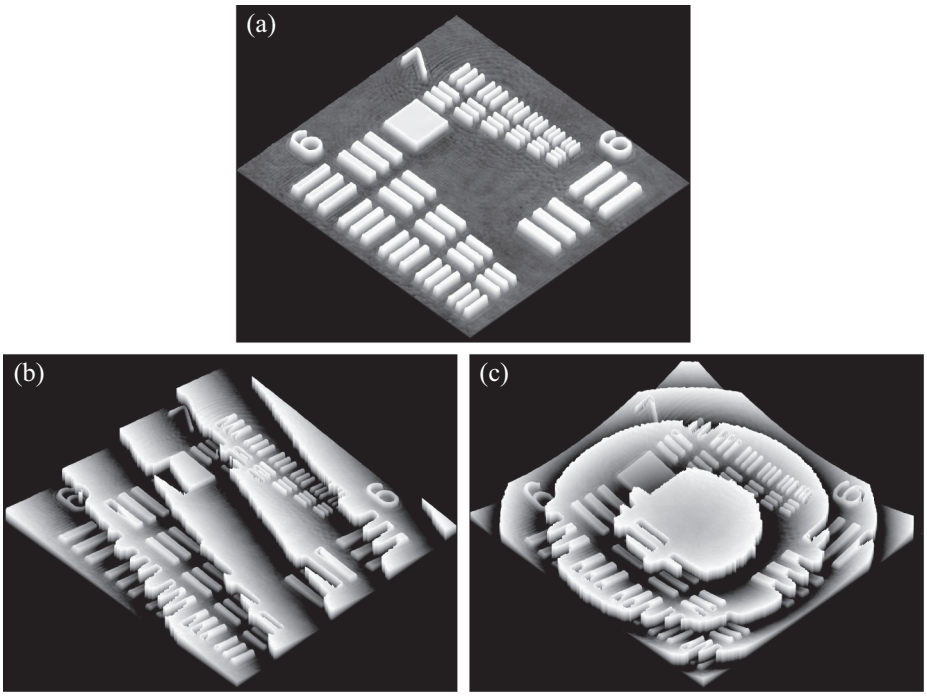

Figure 2.5: Phase images of a USAF test target presented in 3D perspective: (a) with proper adjustment of the reconstruction parameters, (b) with a non-corrected residual tilt aberration coming from the off-axis geometry, (c) with a non-corrected phase curvature induced by the microscope objective. The phase images are coded in 8 bits between $-\pi$ (black) and π (white).

2.2.2 Numerical parametric lens

Equation 2.9 describes the reconstruction algorithm as the Fresnel transform of the hologram intensity I_H multiplied by the product of the digital phase mask Φ with the pseudo digital reference wave $\boldsymbol{R}'$. As $\Phi(\xi,\eta)$ and $\boldsymbol{R}'(\xi,\eta)$ appear now outside the Fresnel integral, they can be merged in a single entity, and the reconstruction algorithm becomes

$$\Psi(\xi,\eta) = \Gamma^I(\xi,\eta)\frac{\exp(i2\pi d/\lambda)}{i\lambda d}\exp\left[\frac{i\pi}{\lambda d}(\xi^2+\eta^2)\right] \cdot \iint I_H(x,y)\exp\left[\frac{i\pi}{\lambda d}\left((x-\xi)^2+(y-\eta)^2\right)\right]dxdy, \tag{2.11}$$

where according to Eqs. 2.8 and 2.10 we have

$$\Gamma^I(\xi,\eta) = \exp\left\{\frac{i\pi}{\lambda}\left[2k_x\xi + 2k_y\eta - \frac{\xi^2+\eta^2}{C}\right] + i\varphi'(k_x,k_y,t)\right\}. \tag{2.12}$$

This new formulation of the digital phase mask involves four reconstruction parameters; k_x and k_y for compensating for the tilt aberration due to the off-axis geometry, the phase offset φ' for compensating for the phase delay between the object and reference waves, and C for compensating for a quadratic wave-front curvature. This expression for the digital phase mask can be seen as a numerical parametric lens (NPL) Γ^I placed in the image plane [Col06d], and can be written as a second order polynomial:

$$\Gamma^I(\xi,\eta) = \exp\left[-i\frac{2\pi}{\lambda}(P_{00}+P_{10}\xi+P_{01}\eta+P_{20}\xi^2+P_{02}\eta^2)\right]. \tag{2.13}$$

where P_{hv} define a new set of phase reconstruction parameters. The physical constants (λ, C and π) are suppressed from the definition of the P_{hv} parameters. But the corresponding physical quantities can be

evaluated if necessary. For example:

$$P_{00} = -\frac{\lambda}{2\pi}\varphi', \tag{2.14}$$

$$P_{10} = -k_x,\ P_{01} = -k_y, \tag{2.15}$$

$$P_{20} = P_{02} = \frac{1}{2C}. \tag{2.16}$$

The four parameter P_{hv} of Eq. 2.13 require a precise adjustment for proper reconstruction of the phase distribution. In the first formulation by Cuche *et al.* [Cuc99a, Cuc99a], the parameter were manually adjusted, and therefore the procedure was quite obscure for a user without appropriate training. The automated procedure proposed by Colomb *et al.* [Col06b] rely on a very intuitive concept: the P_{hv} values are adjusted in order to obtain a constant and homogeneous phase distribution on a flat reference surface located in or at proximity of the specimen. The user simply select some areas in the reconstructed image with a graphic user interface, possibly with help of the amplitude image which does not require such a subtle adjustment of the parameters. On the selected zones, the phase distribution prior any adjustment of the reconstruction parameters is decomposed on a basis of polynomials, up to a certain order, like in a standard fitting procedure: the fitted coefficients of the polynomial basis are precisely the researched P_{hv}. Therefore, the phase can be accurately reconstructed without a prior knowledge of the exact experimental configuration, like the angle between the reference and the object wave or the exact curvature induced by the MO. This is a tremendous advantage, as those parameters may be really difficult to measure properly. The example presented here only considers a second order polynomial fit without any crossed terms ($\xi^\alpha\eta^\beta$, $\alpha, \beta \neq 0$), but the order can be increased at will if higher order aberrations present in the setup require it (spherical, astigmatism, coma, trefoil...); other basis like Zernike polynomial, a polynomial model specifically developed to describe optical aberrations, can of course straightforwardly be used. An illustrated example of the fitting procedure described above is presented on Fig. 2.6.

In the standard polynomial model, the NPL is expressed as:

$$\Gamma_S^I(\xi,\eta) = \exp\left[-i\frac{2\pi}{\lambda}\sum_{\alpha=0}^{x}\sum_{\beta=0}^{y} P_{\alpha\beta}\cdot\xi^\alpha\eta^\beta\right], \tag{2.17}$$

where the index S defined the standard polynomial model, $P_{\alpha\beta}$ define a set of reconstruction parameters, x and y define the polynomial orders in the horizontal and vertical directions respectively. In the Zernike model, the NPL is expressed as:

$$\Gamma_Z^I(\xi,\eta) = \exp\left[-i\frac{2\pi}{\lambda}\sum_{\alpha=0}^{o} P_\alpha\cdot Z_\alpha\right], \tag{2.18}$$

where the index Z defines the Zernike polynomial model, P_α is the α^{th} coefficient of the Zernike term Z_α and o the Zernike polynomial order. The terms Z_α form an orthonormal basis in a continuous way over the interior of a unit circle that defines the extremum values of ξ and η and the increment in the discrete case. The classification of the Zernike polynomials (see Table 2.1) is arbitrary but in this thesis we choose the same classification used in the Zemax program [Zem01].

Since the number of points selected in the image is potentially much larger than the evaluated P_{hv}, the linear system used during the fitting procedure is always overdetermined, making the procedure robust against noise. The extracted zones can be composed by 1-dimensional profiles or 2-dimensional zones, and the procedure may be applied in several steps: a first rough adjustment of just the tilt and curvature fitted on 1-dimensional profiles completed by a more precise aberrations compensation based on 2-dimensional zones.

The main objection that may arise regarding this fitting procedure, is that it requires a known surface with a constant phase in the image and its use seems therefore restricted to specific specimen. Firstly, this condition is fulfilled without difficulty for a large number of applications in which DHM has proved its efficiency: silicon-based micro-engineered systems [Eme05, Eme06, Mon07], micro-optics [Küh06, Cha06a], cell imaging [Mar05, Rap05]. Secondly, if a zone with constant phase is obviously not visible in the image, or is too small for the fit to perform efficiently, the user may calibrate the system on another zone of the specimen before going back to the region of interest, or even on a well-calibrated target, such as a mirror in reflection configuration, or simply through air in transmission configuration. After

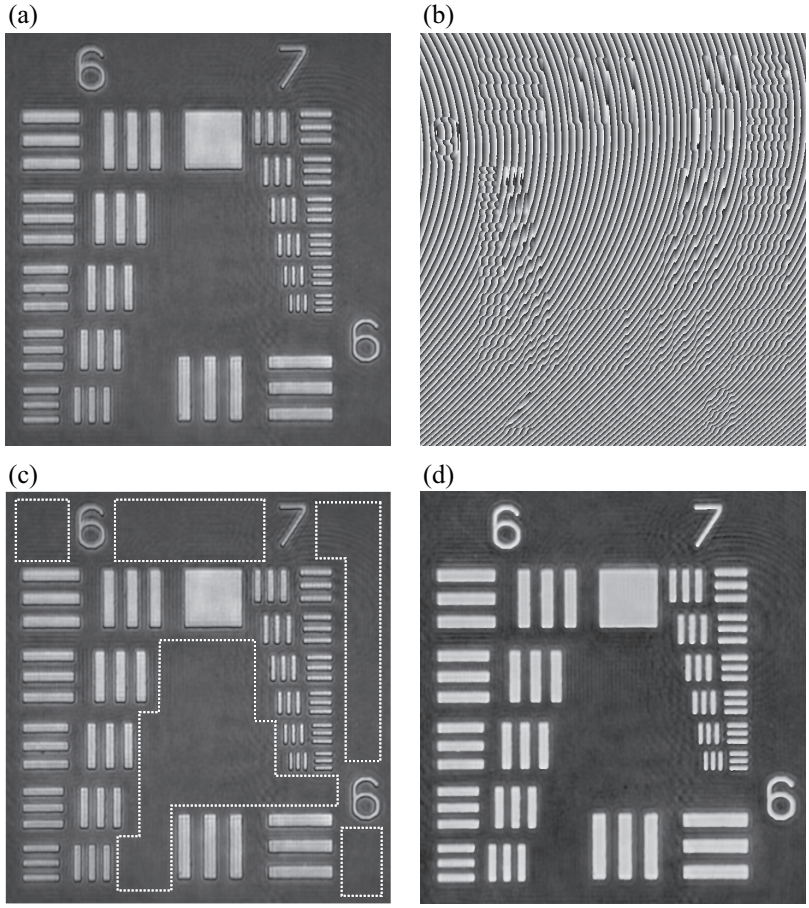

Figure 2.6: Principle of the adjustment of the reconstruction parameters demonstrated on a USAF test target. On the raw amplitude (a) and phase (b) images, the operator selects areas with constant phase, represented here by dashed lines on the amplitude image (c). After the fitting procedure is achieved, the correct reconstruction parameters are found and the phase image is properly reconstructed (d). The phase images are coded in 8 bits between $-\pi$ (black) and π (white).

such a calibration, a simple tilt adjustment is usually performed when introducing the specimen. This calibration procedure may be used when few information about the specimen topography is available, like in roughness measurements [Mon06c].

The concept of numerical optics can be applied one step further to the reconstruction technique: it as been seen that a NPL Γ^I must be inserted in the algorithm for a proper phase reconstruction in the image plane, but a similar lens Γ^H can also be inserted in the hologram plane, multiplying I_H before its propagation through the Fresnel integral:

$$\Psi(\xi,\eta) = \Gamma^I(\xi,\eta)\,\frac{\exp(i2\pi d/\lambda)}{i\lambda d}\,\exp\left[\frac{i\pi}{\lambda d}(\xi^2+\eta^2)\right] \cdot \iint \Gamma^H(x,y)\,I_H(x,y)\exp\left[\frac{i\pi}{\lambda d}\left((x-\xi)^2+(y-\eta)^2\right)\right]dxdy. \tag{2.19}$$

The introduction of a secondary NPL Γ^H with independent parameters has proved to be efficient not only in phase aberration compensation, but also on images distortion correction [Col06d]. Of course Γ^H can be as previously be expressed in term of standard or Zernike polynomial.

More details about this reconstruction parameters adjustment and its numerical implementation can be found in Colomb *et al.* papers [Col06b, Col06d, Col06c] or Colomb's thesis [Col06a], while some interesting considerations about the impact in the reconstructed image of the compensation of the aberrations performed in the hologram plane or in the image plane are discussed in a paper by Montfort *et al.* [Mon06a]. For all the works included in this thesis, this reconstruction technique has been used extensively, thanks to its flexibility, efficiency and rapidity.

	Cartesian form	**Description**
Z_0	1	Piston
Z_1	$\sqrt{4}x$	Tilt x
Z_2	$\sqrt{4}y$	Tilt y
Z_3	$\sqrt{3}(2x^2+2y^2-1)$	Power
Z_4	$\sqrt{6}(2xy)$	Astigmatism y
Z_5	$\sqrt{6}(x^2-y^2)$	Astigmatism x
Z_6	$\sqrt{8}(3x^2y+3y^3-2y)$	Coma y
Z_7	$\sqrt{8}(3x^3+3xy^2-2x)$	Coma x
Z_8	$\sqrt{8}(3x^2y-y^3)$	Trefoil y
Z_9	$\sqrt{8}(x^3-3xy^2)$	Trefoil x
Z_{10}	$\sqrt{5}(6x^4+12x^2y^2+6y^4-6x^2-6y^2+1)$	Primary Spherical
Z_{11}	$\sqrt{10}(4x^4-3x^2+3y^2-4y^4)$	2^{ary} Astig x
Z_{12}	$\sqrt{10}(8x^3y+8xy^3-6xy)$	2^{ary} Astig y
Z_{13}	$\sqrt{10}(x^4-6x^2y^2+y^4)$	Tetrafoil x
Z_{14}	$\sqrt{10}(4x^3y-4xy^3)$	Tetrafoil y
Z_{15}	$\sqrt{12}(10x^5+20x^3y^2+10xy^4-12x^3-12xy^2)+3x)$	2^{ary} Coma x
Z_{16}	$\sqrt{12}(10x^4y+20x^2y^3+10y^5-12x^2y-12y^3)+3y)$	2^{ary} Coma y
Z_{17}	$\sqrt{12}(5x^5-10x^3y^2-15xy^4-4x^3+12xy^2)$	2^{ary} Trefoil x
Z_{18}	$\sqrt{12}(15x^4y+10x^2y^3-5y^5-12x^2y+4y^3)$	2^{ary} Trefoil y
Z_{19}	$\sqrt{12}(x^5-10x^3y^2+5xy^4)$	Pentafoil x
Z_{20}	$\sqrt{12}(5x^4y-10x^2y^3+y^5)$	Pentafoil y
Z_{21}	$\sqrt{7}(20x^6+60x^4y^2+60x^2y^4+20y^6-30x^4$ $-60x^2y^2-30y^4+12x^2+12y^2-1)$	2^{ary} Spherical
Z_{22}	$\sqrt{14}(30x^5y+60x^3y^3+30xy^5-40x^3y-40xy^3+12xy)$	3^{ary} Astig y
Z_{23}	$\sqrt{14}(15x^6+15x^4y^2-20x^4+6x^2-15x^2y^4-15y^6+20y^4-6y^2)$	3^{ary} Astig x
Z_{24}	$\sqrt{14}(24x^5y-20x^3y-24xy^5+20xy^3)$	2^{ary} Tetrafoil y
Z_{25}	$\sqrt{14}(6x^6-5x^4-30x^4y^2-30x^2y^4+30x^2y^2$	
Z_{26}	$\sqrt{14}(6x^5y-20x^3y^3+6xy^5)$	
Z_{27}	$\sqrt{14}(x^6-15x^4y^2+15x^2y^4-y^6)$	

Table 2.1: Cartesian form and description of Zernike standard coefficients in Zemax classification

2.2.3 Discrete formulation

The numerical implementation of Eq. 2.19 can be performed efficiently following two different discrete formulations [Sch02]: the first one consists in developing the propagation with a Single Fourier Transform Formulation (SFTF). The second one writes the propagation with a Convolution Formulation (CF). As suggested by Cuche *et al.*, an apodization function is applied to the hologram prior FFT calculation to prevent the apparition of numerical noise [Cuc00b].

Single Fourier Transform Formulation

As explained by Cuche *et al.* [Cuc99a], a discrete formulation of the hologram illumination and propagation involving a Fast Fourier transform (FFT) can be derived directly from Eq. 2.19:

$$\begin{aligned}\Psi(m,n) = A\,\Gamma^I(m,n)\exp\left[\frac{i\pi}{\lambda d}\left(m^2\Delta\xi^2+n^2\Delta\eta^2\right)\right]\\ \cdot\,\mathrm{FFT}\left\{\Gamma^H(k,l)\;I_H(k,l)\exp\left[\frac{i\pi}{\lambda d}\left(k^2\Delta x^2+l^2\Delta y^2\right)\right]\right\}_{m,n}\end{aligned} \tag{2.20}$$

where m and n are integers ($-N/2 \leqslant m,n \leqslant N/2$), $A = \exp(i2\pi d/\lambda)/(i\lambda d)$, $\Delta\xi$ and $\Delta\eta$, the sampling intervals in the reconstruction plane are defined as follows:

$$\Delta\xi = \frac{\lambda d}{N\Delta x} \text{ and } \Delta\eta = \frac{\lambda d}{N\Delta y}. \tag{2.21}$$

For computational purposes, the samplings $\Delta\xi$ and $\Delta\eta$ which are related to physical scales are suppressed in the NPLs. The discrete formulation of Γ_S therefore is

$$\Gamma_S(m,n) = \exp\left[-i\frac{2\pi}{\lambda}\sum_{\alpha=0}^{H}\sum_{\beta=0}^{V} P_{\alpha\beta}\cdot m^{\alpha}n^{\beta}\right], \tag{2.22}$$

and Γ_H becomes

$$\Gamma_Z(\gamma,\zeta) = \exp\left[-i\frac{2\pi}{\lambda}\sum_{\alpha=0}^{o} P_{\alpha}\cdot Z_{\alpha}\right]. \tag{2.23}$$

Convolution Formulation

Equation 2.11 can be written as a convolution:

$$\Psi(\xi,\eta) = A\,\Gamma^I(\xi,\eta)\left\{\Gamma^H(x,y)\,I_H(x,y)\otimes\exp\left[\frac{i\pi}{\lambda d}(x^2+y^2)\right]\right\}, \tag{2.24}$$

where $\otimes$ is the symbol of convolution. The property of the equivalence between the convolution in the space domain and the multiplication in the frequency domain allows writting:

$$\begin{aligned}\Psi(\xi,\eta) &= A\,\Gamma^I(\xi,\eta)\,\mathrm{FT}^{-1}\left\{\mathrm{FT}\left[\Gamma^H(x,y)\,I_H(x,y)\right]FT\left[\exp\left[\frac{i\pi}{\lambda d}(x^2+y^2)\right]\right]\right\}\\ &= A\,\Gamma^I(\xi,\eta)\,\mathrm{FT}^{-1}\left\{\mathrm{FT}\left[\Gamma^H(x,y)\,I_H(x,y)\right]\exp\left[-i\pi\lambda d(\nu_x^2+\nu_y^2)\right]\right\},\end{aligned} \tag{2.25}$$

where ν_x and ν_y are the coordinates in the spatial frequencies domain and FT the Fourier transform. The discrete formulation of the Eq. 2.25 is

$$\Psi(m,n) = A\,\Gamma^I(m,n)\,\mathrm{FFT}^{-1}\left\{\mathrm{FFT}\left[\Gamma^H(x,y)\,I_H(x,y)\right]\exp\left[-i\pi\lambda d(\nu_k^2+\nu_l^2)\right]\right\}, \tag{2.26}$$

where $\nu_k = k/(N\Delta x)$, $\nu_l = l/(N\Delta y)$, and Γ^H and Γ^I have the same formulation as in Eqs. 2.22 and2.23.

2.2.4 Single fourier transform vs convolution formulation

The two discrete formulations (Eqs. 2.20 and 2.26) have proper advantages and disadvantages. In term of calculation speed, CF is a little more time consuming [Dem74, Sch02], essentially due to one more FFT to compute, but still allows a reconstruction rate of 15Hz for 512x512 holograms with a standard 3GHz computer. On the other hand, CF has the advantage that the size of the propagated image is at the same scale as the one in the hologram plane [Sch02], what is not the case for SFTF. Considering a N x N points hologram with sampling steps Δx and Δy, a reconstruction distance d and a wavelength λ, the sampling steps $\Delta\xi$ and $\Delta\eta$ are given by Eq. 2.21 [Sch02, Cuc99a].

Thus, the image scaling factors α_ξ and α_η are simply

$$\alpha_\xi = \frac{N\Delta x^2}{\lambda d} \text{ and } \alpha_\eta = \frac{N\Delta y^2}{\lambda d}. \tag{2.27}$$

At first sight one seems to loose (or gain) resolution by applying SFTF. On closer examination, it can be seen that $\lambda d/(N\Delta x)$ corresponds to the resolution limit given by the diffraction theory of optical system: the hologram is the aperture of the optical system with side length $N\cdot\Delta x$. According to the theory of diffraction at a distance d behind the hologram, $\Delta\xi = \lambda d/(N\Delta x)$ is therefore the diameter of the Airy disk (or speckle diameter) in the plane of the reconstructed image, which limits the resolution. This can be regarded as an automatic scaling algorithm, setting the resolution of the reconstructed image in the Fresnel approximation always to the physical limit [Sch02].

Equation 2.27 shows that the scaling depends on the wavelength λ and on the reconstruction distance d. Therefore CF is often preferred when it is necessary to compare reconstruction images performed with different wavelengths (color holography [Kat02], multiple-wavelengths tomography [Mon05] or synthetical wavelength [Gas03, Küh07]). Recently, Ferraro *et al.* presented a zero-padding method permitting to control the image size in SFTF [Fer04]. The drawback of this technique is that the pixel number of the resulting padded holograms are not of the form $N = 2^n$ which is an optimal condition for FFT in terms of time consumption. It has also been demonstrated that scaling is also possible in CF by keeping constant the number of pixels [Col06d].

Introduction bibliography

[Ahn05] A. Ahn, C. Yang, A. Wax, G. Popescu, C. Fang-Yen, K. Badizadegan, R. R. Dasari and M. S. Feld. "Harmonic phase-dispersion microscope with a Mach-Zehnder interferometer". Appl. Opt. **44**(7): 1188–1190 (2005).

[Alm04] P. Almoro, M. Cadatal, W. Garcia and C. Saloma. "Pulsed full-color digital holography with a hydrogen Raman shifter". Appl. Opt. **43**(11): 2267–2271 (2004).

[Apo04] V. Apostolopoulos, L. Laversenne, T. Colomb, C. Depeursinge, R. P. Salathé and M. Pollnau. "Femtosecond-irradiation-induced refractive-index changes and channel waveguiding in bulk Ti3+:Sapphire". Appl. Phys. Lett. **85**(7): 1122–1124 (2004).

[Awa04] Y. Awatsuji, M. Sasada and T. Kubota. "Parallel quasi-phase-shifting digital holography". Appl. Phys. Lett. **85**(6): 1069–1071 (2004).

[Bac05] B. L. Bachim and T. K. Gaylord. "Microinterferometric optical phase tomography for measuring small, asymmetric refractive-index differences in the profiles of optical fibers and fiber devices". Appl. Opt. **44**(3): 316–327 (2005).

[Beg99] D. Beghuin, E. Cuche, P. Dahlgren, C. Depeursinge, G. Delacretaz and R. P. Salathe. "Single acquisition polarisation imaging with digital holography". Electron. Lett. **35**(23): 2053–2055 (1999).

[Bor05] D. N. Borza. "Mechanical vibration measurement by high-resolution time-averaged digital holography". Measurement Science and Technology **16**(9): 1853–1864 (2005).

[Bra06] N. Brazhe, A. Brazhe, A. Pavlov, L. Erokhova, A. Yusipovich, G. Maksimov, E. Mosekilde and O. Sosnovtseva. "Unraveling Cell Processes: Interference Imaging Interwoven with Data Analysis". Journal of Biological Physics **32**: 191–208 (2006).

[Car04] D. Carl, B. Kemper, G. Wernicke and G. v. Bally. "Parameter-optimized digital holographic microscope for high-resolution living-cell analysis". Appl. Opt. **43**(36): 6536–6544 (2004).

[Cha69] E. B. Champagne and N. G. Massey. "Resolution in holography". Appl. Opt. **8**(9): 1879–1885 (1969).

[Cha05] F. Charrière, P. Marquet, M. Von Ehr, E. Cuche and C. Depeursinge. "Digital holographic microscopy applied to pollen cells analysis and recognition". In C. D. Depeursinge, ed., "Progress in Biomedical Optics and Imaging - Proceedings of SPIE", (Munich, 2005), *Novel Optical Instrumentation for Biomedical Applications II*, vol. 5864, pp. 1–4.

[Cha06a] F. Charrière, J. Kühn, T. Colomb, F. Montfort, E. Cuche, Y. Emery, K. Weible, P. Marquet and C. Depeursinge. "Characterization of microlenses by digital holographic microscopy". Appl. Opt. **45**(5): 829–835 (2006).

[Cha06b] F. Charrière, A. Marian, F. Montfort, J. Kühn, T. Colomb, E. Cuche, P. Marquet and C. Depeursinge. "Cell refractive index tomography by digital holographic microscopy". Opt. Lett. **31**(2): 178–180 (2006).

[Cha06c] F. Charrière, N. Pavillon, T. Colomb, T. Heger, E. Mitchell, P. Marquet, B. Rappaz and C. Depeursinge. "Living specimen tomography by digital holographic microscopy: morphometry of testate amoeba". Opt. Express **14**(16): 7005–7013 (2006).

[Cha07] K. J. Chalut, W. J. Brown and A. Wax. "Quantitative phase microscopy with asynchronous digital holography". Opt. Express **15**(6): 3047–3052 (2007).

[Coe02] S. Coetmellec, D. Lebrun and C. Ozkul. "Application of the two-dimensional fractional-order Fourier transformation to particle field digital holography". J. Opt. Soc. Am. A **19**(8): 1537–1546 (2002).

[Col71] R. J. Collier, D. B. Burckhardt and L. H. Lin. *Optical holography* (New York, 1971).

[Col02] T. Colomb, P. Dahlgren, D. Beghuin, E. Cuche, P. Marquet and C. Depeursinge. "Polarization imaging by use of digital holography". Appl. Opt. **41**(1): 27–37 (2002).

[Col04] T. Colomb, E. Cuche, F. Montfort, P. Marquet and C. Depeursinge. "Jones vector imaging by use of digital holography: simulation and experimentation". Opt. Commun. **231**(1-6): 137–147 (2004).

[Col05] T. Colomb, F. Dürr, E. Cuche, P. Marquet, H. Limberger, R.-P. Salathé and C. Depeursinge. "Polarization microscopy by use of digital holography: application to optical fiber birefringence measurements". Appl. Opt. **44**(21): 4461–4469 (2005).

[Col06a] T. Colomb. *Numerical aberrations compensation and polarization imaging in digital holographic microscopy*. Thesis 3455, Ecole Polytechnique Fédérale de Lausanne (2006).

[Col06b] T. Colomb, E. Cuche, F. Charrière, J. Kühn, N. Aspert, F. Montfort, P. Marquet and C. Depeursinge. "Automatic procedure for aberration compensation in digital holographic microscopy and applications to specimen shape compensation". Appl. Opt. **45**(5): 851–863 (2006).

[Col06c] T. Colomb, J. Kühn, F. Charrière, C. Depeursinge, P. Marquet and N. Aspert. "Total aberrations compensation in digital holographic microscopy with a reference conjugated hologram". Opt. Express **14**(10): 4300–4306 (2006).

[Col06d] T. Colomb, F. Montfort, J. Kühn, N. Aspert, E. Cuche, A. Marian, F. Charrière, S. Bourquin, P. Marquet and C. Depeursinge. "Numerical parametric lens for shifting, magnification and complete aberration compensation in digital holographic microscopy". J. Opt. Soc. Am. A **23**(12): 3177–3190 (2006).

[Cop04] G. Coppola, P. Ferraro, M. Iodice, S. De Nicola, A. Finizio and S. Grilli. "A digital holographic microscope for complete characterization of microelectromechanical systems". Measurement Science and Technology **15**(3): 529–539 (2004).

[Coq93] O. Coquoz, C. Depeursinge, R. Conde and E. d. Haller. "Microendoscopic holography with flexible fiber bundle: experimental approach". In "the Progress in Biomedical Optics", (SPIE, Budapest, 1993), vol. 2083, pp. 314–318.

[Coq95] O. Coquoz, R. Conde, F. Taleblou and C. Depeursinge. "Performances of endoscopic holography with a multicore optical fiber". Appl. Opt. **34**(31): 7186–7193 (1995).

[Cuc99a] E. Cuche, F. Bevilacqua and C. Depeursinge. "Digital holography for quantitative phase-contrast imaging". Opt. Lett. **24**(5): 291–293 (1999).

[Cuc99b] E. Cuche, P. Marquet and C. Depeursinge. "Simultaneous amplitude-contrast and quantitative phase-contrast microscopy by numerical reconstruction of Fresnel off-axis holograms". Appl. Opt. **38**(34): 6994–7001 (1999).

[Cuc00a] E. Cuche. *Numerical reconstruction of digital holograms: application to phase-contrast imaging and microscopy*. Thesis 2182, Ecole Polytechnique Fédérale de Lausanne (2000).

[Cuc00b] E. Cuche, P. Marquet and C. Depeursinge. "Aperture apodization using cubic spline interpolation: application in digital holographic microscopy". Opt. Commun. **182**(1-3): 59–69 (2000).

[Cuc00c] E. Cuche, P. Marquet and C. Depeursinge. "Spatial filtering for zero-order and twin-image elimination in digital off-axis holography". Appl. Opt. **39**(23): 4070–4075 (2000).

[Dän70] R. Dändliker and D. Weiss. "Reconstruction of three-dimensional refractive index from scattered waves". Opt. Commun. **1**(7): 323–328 (1970).

[dA04] M. de Angelis, S. De Nicola, A. Finizio, G. Pierattini, P. Ferraro, S. Grilli and M. Paturzo. "Evaluation of the internal field in lithium niobate ferroelectric domains by an interferometric method". Appl. Phys. Lett. **85**(14): 2785–2787 (2004).

[Dak03] A. Dakoff, J. Gass and M. K. Kim. "Microscopic three-dimensional imaging by digital interference holography". Journal of Electronic Imaging **12**(4): 643–647 (2003).

[Dem74] T. H. Demetrakopoulos and R. Mittra. "Digital and optical reconstruction of images from suboptical diffraction patterns". Appl. Opt. **13**(3): 665–670 (1974).

[Den74] Y. N. Denisyuk. "Holograph motion pictures". Sov Phys Tech Phys **18**(12): 1549–1551 (1974).

[Den80] Y. N. Denisyuk. "Holography and its prospects (review)". Journal of applied spectroscopy **33**(3): 901–915 (1980).

[DN02] S. De Nicola, P. Ferraro, A. Finizio and G. Pierattini. "Wave front reconstruction of Fresnel off-axis holograms with compensation of aberrations by means of phase-shifting digital holography". Optics and Lasers in Engineering **37**(4): 331–340 (2002).

[dN04] S. de Nicola, P. Ferraro, A. Finizio, S. Grilli, G. Coppola, M. Iodice, P. De Natale and M. Chiarini. "Surface topography of microstructures in lithium niobate by digital holographic microscopy". Measurement Science and Technology **15**(5): 961–968 (2004).

[dN05] S. de Nicola, A. Finizio, G. Pierattini, P. Ferraro and D. Alfieri. "Angular spectrum method with correction of anamorphism for numerical reconstruction of digital holograms on tilted planes". Opt. Express **13**(24): 9935–9940 (2005).

[Dub99] F. Dubois, L. Joannes, O. Dupont, J. L. Dewandel and J. C. Legros. "An integrated optical set-up for fluid-physics experiments under microgravity conditions". Measurement Science and Technology **10**(10): 934–945 (1999).

[Dub02] F. Dubois, C. Minetti, O. Monnom, C. Yourassowsky, J. C. Legros and P. Kischel. "Pattern recognition with a digital holographic microscope working in partially coherent illumination". Appl. Opt. **41**(20): 4108–4119 (2002).

[Dub06] F. Dubois, C. Yourassowsky, O. Monnom, J. C. Legros, O. Debeir, P. Van Ham, R. Kiss and C. Decaestecker. "Digital holographic microscopy for the three-dimensional dynamic analysis of in vitro cancer cell migration". Journal of Biomedical Optics **11**(5): 054032 (5 pages) (2006).

[Dun03] C. Dunsby, Y. Gu and P. M. W. French. "Single-shot phase-stepped wide-field coherence-gated imaging". Opt. Express **11**(2): 105–115 (2003).

[Ell07] A. K. Ellerbee, T. L. Creazzo and J. A. Izatt. "Investigating nanoscale cellular dynamics with cross-sectional spectral domain phase microscopy". Opt. Express **15**(13): 8115–8124 (2007).

[Eme05] Y. Emery, E. Cuche, F. Marquet, N. Aspert, P. Marquet, J. Kühn, M. Botkine, T. Colomb, F. Montfort, F. Charrière and C. Depeursinge. "Digital Holography Microscopy (DHM): Fast and robust systems for industrial inspection with interferometer resolution". In W. Osten, C. Gorecki and E. Novak, eds., "Optical Measurement Systems for Industrial Inspection Iv, Pts 1 and 2", (Spie-Int Society Optical Engineering, Bellingham, 2005), *Proceedings of the Society of Photo-Optical Instrumentation Engineers (Spie)*, vol. 5856, pp. 930–937.

[Eme06] Y. Emery, E. Cuche, F. Marquet, N. Aspert, P. Marquet, J. Kühn, M. Botkine, T. Colomb, F. Montfort, F. Charrière, C. Depeursinge, P. Debergh and R. Conde. "Digital Holographic Microscopy (DHM) for metrology and dynamic characterization of MEMS and MOEMS - art. no. 61860N". In H. Urey and A. ElFatatry, eds., "Mems, Moems, and Micromachining Ii", (Spie-Int Society Optical Engineering, Bellingham, 2006), *Proceedings of the Society of Photo-Optical Instrumentation Engineers (Spie)*, vol. 6186, pp. N1860–N1860.

[Für07] S. Fürhapter, A. Jesacher, C. Maurer, S. Bernet and M. Ritsch-Marte. "Spiral Phase Microscopy". In "Advances in Imaging and Electron Physics", (2007), vol. 146, pp. 1–56.

[Fer03a] P. Ferraro, G. Coppola, S. De Nicola, A. Finizio and G. Pierattini. "Digital holographic microscope with automatic focus tracking by detection sample displacement in real time". Opt. Lett. **28**(14): 1257–1259 (2003).

[Fer03b] P. Ferraro, S. De Nicola, A. Finizio, G. Coppola, S. Grilli, C. Magro and G. Pierattini. "Compensation of the inherent wave front curvature in digital holographic coherent microscopy for quantitative phase-contrast imaging". Appl. Opt. **42**(11): 1938–1946 (2003).

[Fer04] P. Ferraro, S. D. Nicola, G. Coppola, A. Finizio, D. Alfieri and G. Pierattini. "Controlling image size as a function of distance and wavelength in Fresnel-transform reconstruction of digital holograms". Opt. Lett. **29**(8): 854–856 (2004).

[Fra87] M. Françon. *Holographie* (Paris, 1987).

[FY07] C. Fang-Yen, S. Oh, Y. Park, W. Choi, S. Song, H. S. Seung, R. R. Dasari and M. S. Feld. "Imaging voltage-dependent cell motions with heterodyne Mach-Zehnder phase microscopy". Opt. Lett. **32**(11) (2007).

[Gór04] W. Górski. "The influence of diffraction in microinterferometry and microtomography of optical fibers". Optics and Lasers in Engineering **41**(3): 565–583 (2004).

[Gór06] W. Górski. "Tomographic microinterferometry of optical fibers". Optical Engineering **45**(12): 125002 (2006).

[Gór07] W. Górski and W. Osten. "Tomographic imaging of photonic crystal fibers". Opt. Lett. **32**(14): 1977–1979 (2007).

[Gab48] D. Gabor. "A New Microscopic Principle". Nature **161**(4098): 777–778 (1948).

[Gab49] D. Gabor. "Microscopy by Reconstructed Wave-Fronts". Proceedings of the Royal Society of London. Serie A, Mathematical and Physical Sciences **197**(1051): 454–487 (1949).

[Gab51] D. Gabor. "Microscopy by Reconstructed Wave Fronts: II". The Proceedings of the Physical Society **64**(6): 449–470 (1951).

[Gab66] D. Gabor and W. P. Goss. "Interference Microscope with Total Wavefront Reconstruction". J. Opt. Soc. Am. **56**(7): 849–858 (1966).

[Gab71] D. Gabor. *Holography, 1948-1971.* Nobel Lecture, Imperial Colleges of Science and Technology (1971).

[Gas03] J. Gass, A. Dakoff and M. K. Kim. "Phase imaging without 2 pi ambiguity by multiwavelength digital holography". Opt. Lett. **28**(13): 1141–1143 (2003).

[Goo67] J. W. Goodman and R. W. Lawrence. "Digital image formation from electronically detected holograms". Appl. Phys. Lett. **11**(3): 77–79 (1967).

[Goo68] J. W. Goodman. *Introduction to Fourier Optics* (San Francisco, Calif., 1968).

[Gri04] S. Grilli, P. Ferraro, M. Paturzo, D. Alfieri and P. De Natale. "In-situ visualization, monitoring and analysis of electric field domain reversal process in ferroelectric crystals by digital holography". Opt. Express **12**(9): 1832–1842 (2004).

[Guo02] C. S. Guo, L. Zhang, H. T. Wang, J. Liao and Y. Y. Zhu. "Phase-shifting error and its elimination in phase-shifting digital holography". Opt. Lett. **27**(19): 1687–1689 (2002).

[Han79] *Handbook of optical holography* (H.J. Caulfield Ed., New York, 1979).

[Har96] P. Hariharan. *Optical holography:principles, techniques, and applications* (1996).

[He05] M.-Z. He, L.-Z. Cai, Q. Liu and X.-L. Yang. "Phase-only encryption and watermarking based on phase-shifting interferometry". Appl. Opt. **44**(13): 2600–2606 (2005).

[Hin02] K. D. Hinsch. "Holographic particle image velocimetry". Measurement Science and Technology **13**(7): R61–R72 (2002).

[Iem06] U. Iemma, L. Morino and M. Diez. "Digital holography and Karhunen-LoÃ¨ve decomposition for the modal analysis of two-dimensional vibrating structures". Journal of Sound and Vibration **291**(1-2): 107–131 (2006).

[Ike05] T. Ikeda, G. Popescu, R. R. Dasari and M. S. Feld. "Hilbert phase microscopy for investigating fast dynamics in transparent systems". Opt. Lett. **30**(10): 1165–1167 (2005).

[Ind99] G. Indebetouw and P. Klysubun. "Optical sectioning with low coherence spatio-temporal holography". Opt. Commun. **172**: 25–29 (1999).

[Ind01] G. Indebetouw and P. Klysubun. "Spatiotemporal digital microholography". J. Opt. Soc. Am. A **18**(2): 319–325 (2001).

[Józ05] A. Jóźwicka and M. Kujawińska. "Digital holographic tomograph for amplitude-phase microelements testing". In "Proc. SPIE-Int. Soc. Opt. Eng.", (2005), vol. 5958, pp. 1–9.

[Józ06] A. Jóźwicka and M. Kujawińska. "Experimental proof-of-principle 3D measurements of microobjects by digital holographic tomography". In "Proc. SPIE-Int. Soc. Opt. Eng.", (2006), vol. 6188.

[Jav00] B. Javidi and T. Nomura. "Securing information by use of digital holography". Opt. Lett. **25**(1): 28–30 (2000).

[Jav05a] B. Javidi, P. Ferraro, S.-H. Hong, S. D. Nicola, A. Finizio, D. Alfieri and G. Pierattini. "Three-dimensional image fusion by use of multiwavelength digital holography". Opt. Lett. **30**(2): 144–146 (2005).

[Jav05b] B. Javidi, I. Moon, S. Yeom and E. Carapezza. "Three-dimensional imaging and recognition of microorganism using single-exposure on-line (SEOL) digital holography". Opt. Express **13**(12): 4492 – 4506 (2005).

[Jeo05] K. Jeong, L. Peng, J. J. Turek, M. R. Melloch and D. D. Nolte. "Fourier-domain holographic optical coherence imaging of tumor spheroids and mouse eye". Appl. Opt. **44**(10): 1798–1805 (2005).

[Jeo06] K. Jeong, D. D. Nolte and J. J. Turek. "Digital Holographic Optical Coherence Imaging of Mouse Eye". In "Conference on Lasers and Electro-Optics/Quantum Electronics and Laser Science Conference and Photonic Applications Systems Technologies", (Optical Society of America, Long Beach, California, 2006), vol. Technical Digest (CD), p. paper CTuG4.

[Jeo07] K. Jeong, J. Turek and D. Nolte. "Fourier-domain digital holographic optical coherence imaging of living tissue". Appl. Opt. **46**(22): 4999–5008 (2007).

[Küh06] J. Kühn, E. Cuche, Y. Emery, T. Colomb, F. Charrière, F. Montfort, M. Botkine, N. Aspert and C. Depeursinge. "Measurements of corner cubes microstructures by high-magnification Digital Holographic Microscopy - art. no. 618804". In C. Gorecki, A. K. Asundi and W. Osten, eds., "Optical Micro- and Nanometrology in Microsystems Technology", (Spie-Int Society Optical Engineering, Bellingham, 2006), *Proceedings of the Society of Photo-Optical Instrumentation Engineers (Spie)*, vol. 6188, pp. 18804–18804.

[Küh07] J. Kühn, T. Colomb, F. Montfort, F. Charrière, Y. Emery, E. Cuche, P. Marquet and C. Depeursinge. "Real-time dual-wavelength digital holographic microscopy with a single hologram acquisition". Opt. Express **15**(12): 7231–7242 (2007).

[Kat02] J. Kato, I. Yamaguchi and T. Matsumura. "Multicolor digital holography with an achromatic phase shifter". Opt. Lett. **27**(16): 1403–1405 (2002).

[Keb99] V. Kebbel, M. Adams, H. J. Hartmann and W. Juptner. "Digital holography as a versatile optical diagnostic method for microgravity experiments". Measurement Science and Technology **10**(10): 893–899 (1999).

[Keb00] V. Kebbel, H.-J. Hartmann and W. P. O. Jüptner. "Characterization of micro-optics using digital holography". In "Proc. SPIE-Int. Soc. Opt. Eng.", (2000), vol. 4101, p. B/.

[Keb01a] V. Kebbel, H. J. Hartmann and W. P. O. Jüptner. "Application of digital holographic microscopy for inspection of micro-optical components". In "Proc. SPIE-Int. Soc. Opt. Eng.", (2001), vol. 4398, pp. 189–198.

[Keb01b] V. Kebbel, H. J. Hartmann and W. P. O. Jüptner. "A new approach for testing of aspherical micro-optics with high numerical aperture". In "Proc. SPIE-Int. Soc. Opt. Eng.", (2001), vol. 4451, pp. 345–355.

[Kem99] Q. Kemao, M. Hong and W. Xiaoping. "Real-time polarization phase shifting technique for dynamic deformation measurement". Optics and Lasers in Engineering **31**(4): 289–295 (1999).

[Kem06] B. Kemper, D. Carl, J. Schnekenburger, I. Bredebusch, M. Schafer, W. Domschke and G. von Bally. "Investigation of living pancreas tumor cells by digital holographic microscopy". Journal of Biomedical Optics **11**(3): 034005 (2006).

[Kim99] M. K. Kim. "Wavelength-scanning digital interference holography for optical section imaging". Opt. Lett. **24**(23): 1693–1695 (1999).

[Kim00] M. K. Kim. "Tomographic three-dimensional imaging of a biological specimen using wavelength-scanning digital interference holography". Opt. Express **7**(9): 305–310 (2000).

[Kol92] C. L. Koliopoulos. "Simultaneous phase-shift interferometer". In V. J. Doherty, ed., "Advanced Optical Manufacturing and Testing II", (SPIE, 1992), vol. 1531, pp. 119–127.

[Kol03] E. Kolenovic, W. Osten, R. Klattenhoff, S. C. Lai, C. von Kopylow and W. Juptner. "Miniaturized digital holography sensor for distal three-dimensional endoscopy". Appl. Opt. **42**(25): 5167–5172 (2003).

[Kro72a] M. A. Kronrod, N. S. Merzlyakov and L. P. Yaroslavsky. "Reconstruction of holograms with a computer". Sov Phys-Tech Phys **17**: 333–334 (1972).

[Kro72b] M. A. Kronrod, L. P. Yaroslavsky and N. S. Merzlyakov. "Computer synthesis of transparency holograms". Sov Phys-Tech Phys **17**: 329–332 (1972).

[Lai00a] S. Lai and M. A. Neifeld. "Digital wavefront reconstruction and its application to image encryption". Opt. Commun. **178**(4-6): 283–289 (2000).

[Lai00b] S. C. Lai, B. King and M. A. Neifeld. "Wave front reconstruction by means of phase-shifting digital in-line holography". Opt. Commun. **173**(1-6): 155–160 (2000).

[Lau02] V. Lauer. "New approach to optical diffraction tomography yielding a vector equation of diffraction tomography and a novel tomographic microscope". J. Microsc. **205**: 165–176 (2002).

[Leb03] D. Lebrun, A. M. Benkouider, S. Coetmellec and M. Malek. "Particle field digital holographic reconstruction in arbitrary tilted planes". Opt. Express **11**(3): 224–229 (2003).

[Lei63] E. N. Leith and J. Upatnieks. "Wavefront Reconstruction with Continuous-Tone Objects". J. Opt. Soc. Am. **53**(12): 1377–1381 (1963).

[Lei64] E. N. Leith and J. Upatnieks. "Wavefront Reconstruction with Diffused Illumination and Three-Dimensional Objects". J. Opt. Soc. Am. **54**(11): 1295–1301 (1964).

[Lei82] E. N. Leith and G. J. Swanson. "Holographic aberration compensation with partially coherent light". Opt. Lett. **7**(12): 596–598 (1982).

[Lei97] E. N. Leith. "Overview of the developments of holography". Journal of imaging science and technology **41**(3): 201–204 (1997).

[Lew06] N. I. Lewis, W. Xu, S. K. Jericho, H. J. Kreuzer, M. H. Jericho and A. D. Cembella. "Swimming speed of three species of Alexandrium (Dinophyceae) as determined by digital in-line holography". Phycologia **45**(1): 61–70 (2006).

[Li06] X. Li, T. Yamauchi, H. Iwai, Y. Yamashita, H. Zhang and T. Hiruma. "Full-field quantitative phase imaging by white-light interferometry with active phase stabilization and its application to biological samples". Opt. Lett. **31**(12): 1830–1832 (2006).

[Lie03] M. Liebling, T. Blu and M. Unser. "Fresnelets: New multiresolution wavelet bases for digital holography". Ieee Transactions on Image Processing **12**(1): 29–43 (2003).

[Lie04a] M. Liebling. *On Fresnelets, Interference fringes, and digital holography.* No. 2977, EPFL (2004).

[Lie04b] M. Liebling, T. Blu and M. Unser. "Complex-wave retrieval from a single off-axis hologram". J. Opt. Soc. Am. A **21**(3): 367–377 (2004).

[Loh65] A. W. Lohmann. "Reconstruction of vectorial wavefronts". Appl. Opt. **4**(12): 1667–1668 (1965).

[Lue06] N. Lue, G. Popescu, T. Ikeda, R. R. Dasari, K. Badizadegan and M. S. Feld. "Live cell refractometry using microfluidic devices". Opt. Lett. **31**(18): 2759–2761 (2006).

[Lue07] N. Lue, W. Choi, G. Popescu, T. Ikeda, R. R. Dasari, K. Badizadegan and M. S. Feld. "Quantitative phase imaging of live cells using fast Fourier phase microscopy". Appl. Opt. **46**(10): 1836–1842 (2007).

[Mül04] J. Müller, V. Kebbel and W. Jüptner. "Characterization of spatial particle distributions in a spray-forming process using digital holography". Measurement Science and Technology **15**(4): 706–710 (2004).

[Mül05] J. Müller, V. Kebbel and W. Jüptner. "Digital holography as a tool for testing high-aperture micro-optics". Optics and Lasers in Engineering **43**(7): 739–751 (2005).

[Ma04] L. H. Ma, H. Wang, Y. Li and H. Z. Jin. "Numerical reconstruction of digital holograms for three-dimensional shape measurement". J. Opt. A-Pure Appl. Opt. **6**(4): 396–400 (2004).

[Man06] C. J. Mann, L. Yu and M. K. Kim. "Movies of cellular and sub-cellular motion by digital holographic microscopy". Biomed. Eng. Online **5**(21) (2006).

[Mar03] P. Marquet. *Développement d'une nouvelle technique de microscopie optique tridimensionnelle, la microscopie holographique digitale. Perspectives pour l'étude de la plasticite neuronale.* Ph.D. thesis, Université de Lausanne (2003).

[Mar05] P. Marquet, B. Rappaz, P. J. Magistretti, E. Cuche, Y. Emery, T. Colomb and C. Depeursinge. "Digital holographic microscopy: a noninvasive contrast imaging technique allowing quantitative visualization of living cells with subwavelength axial accuracy". Opt. Lett. **30**(5): 468–470 (2005).

[Mar06a] P. Marquet, P. Magistretti, B. Rappaz, T. Colomb, J. Kühn and C. Depeursinge. "Quantitative Measurements of Dynamic Cell Morphometry and Intracellular Integral Refractive Index with Digital Holographic Microscopy". In O. S. o. America, ed., "Biomedical Optics", (Fort Lauderdale, Florida, 2006), p. paper ME24.

[Mar06b] P. Marquet, B. Rappaz, T. Colomb, F. Charrière, J. Kühn, Y. Emery, E. Cuche, C. Depeursinge and P. Magistretti. "Digital holographic microscopy, a new optical imaging technique to investigate cellular dynamics - art. no. 61910U". In R. Grzymala and O. Haeberle, eds., "Biophotonics and New Therapy Frontiers", (Spie-Int Society Optical Engineering, Bellingham, 2006), *Proceedings of the Society of Photo-Optical Instrumentation Engineers (Spie)*, vol. 6191, pp. U1910–U1910.

[Mar07] P. Marquet, Y. Emery, T. Colomb, F. Charrière, J. Kühn, C. Depeursinge, B. Rappaz, P. Jourdain and P. Magistretti. "Digital holographic microscopy for the study of cellular structure and dynamics". In "Focus on Microscopy FOM07", (Valencia, 2007).

[Mas05] P. Massatsch, F. Charrière, E. Cuche, P. Marquet and C. Depeursinge. "Time-domain optical coherence tomography with digital holographic microscopy". Appl. Opt. **44**(10): 1806–1812 (2005).

[Mic07] L. Miccio, D. Alfieri, S. Grilli, P. Ferraro, A. Finizio, L. De Petrocellis and S. D. Nicola. "Direct full compensation of the aberrations in quantitative phase microscopy of thin objects by a single digital hologram". Appl. Phys. Lett. **90**: 041104 (3 pages) (2007).

[Mil01] J. E. Millerd and N. J. Brock. "Methods and apparatus for splitting, imaging, and measuring wavefronts in interferometry" (2001).

[Mil05] G. A. Mills and I. Yamaguchi. "Effects of quantization in phase-shifting digital holography". Appl. Opt. **44**(7): 1216–1225 (2005).

[ML05] L. Martínez-León, G. Pedrini and W. Osten. "Applications of short-coherence digital holography in microscopy". Appl. Opt. **44**(19): 3977–3984 (2005).

[Mon05] F. Montfort. *Tomography using multiple wavelengths in digital holographic microscopy*. Thesis 3345, Ecole Polytechnique Fédérale de Lausanne (2005).

[Mon06a] F. Montfort, F. Charrière, T. Colomb, E. Cuche, P. Marquet and C. Depeursinge. "Purely numerical compensation for microscope objective phase curvature in digital holographic microscopy: influence of digital phase mask position". J. Opt. Soc. Am. A **23**(11): 2944–2953 (2006).

[Mon06b] F. Montfort, T. Colomb, F. Charrière, J. Kühn, P. Marquet, E. Cuche, S. Herminjard and C. Depeursinge. "Submicrometer optical tomography by multiple-wavelength digital holographic microscopy". Appl. Opt. **45**(32): 8209–8217 (2006).

[Mon06c] F. Montfort, Y. Emery, E. Solanas, E. Cuche, N. Aspert, P. Marquet, C. Joris, J. Kühn and C. Depeursing. "Surface roughness parameters measurements by Digital Holographic Mcroscopy (DHM)". In "Proc. SPIE-Int. Soc. Opt. Eng.", (Xinjiang, 2006), *Third International Symposium on Precision Mechanical Measurements*, vol. 6280 I.

[Mon07] F. Montfort, Y. Emery, F. Marquet, E. Cuche, N. Aspert, E. Solanas, A. Mehdaoui, A. Ionescu and C. Depeursinge. "Process engineering and failure analysis of MEMS and MOEMS by Digital Holography Microscopy (DHM)". In "Proc. SPIE-Int. Soc. Opt. Eng.", (San Jose, CA, 2007), *Reliability, Packaging, Testing, and Characterization of MEMS/MOEMS VI*, vol. 6463.

[Moo07] I. Moon and B. Javidi. "Three-dimensional identification of stem cells by computational holographic imaging". Journal of the Royal Society Interface **4**(13): 305–313 (2007).

[Mur00] S. Murata and N. Yasuda. "Potential of digital holography in particle measurement". Optics and Laser Technology **32**(7-8): 567–574 (2000).

[Nil98] B. Nilsson and T. E. Carlsson. "Direct three-dimensional shape measurement by digital light-in-flight holography". Appl. Opt. **37**(34): 7954–7959 (1998).

[Nil00] B. Nilsson and T. E. Carlsson. "Simultaneous measurement of shape and deformation using digital light-in-flight recording by holography". Optical Engineering **39**(1): 244–253 (2000).

[Nis04] N. K. Nishchal, J. Joseph and K. Singh. "Fully phase encryption using digital holography". Optical Engineering **43**(12): 2959–2966 (2004).

[Nom04] T. Nomura, K. Uota and Y. Morimoto. "Hybrid optical encryption of a 3-D object using a digital holographic technique". Optical Engineering **43**(10): 2228–2232 (2004).

[Nom07] T. Nomura, B. Javidi, S. Murata, E. Nitanai and T. Numata. "Polarization imaging of a 3D object by use of on-axis phase-shifting digital holography". Opt. Lett. **32**(5): 481–483 (2007).

[Ono98] R. Onodera and Y. Ishii. "Two-wavelength interferometry that uses a Fourier-transform method". Appl. Opt. **37**(34): 7988–7994 (1998).

[Pan03] G. Pan and H. Meng. "Digital holography of particle fields: reconstruction by use of complex amplitude". Appl. Opt. **42**(5): 827–833 (2003).

[Par06a] Y. Park, G. Popescu, K. Badizadegan, R. R. Dasari and M. S. Feld. "Diffraction phase and fluorescence microscopy". Opt. Express **14**(18): 8263–8268 (2006).

[Par06b] D. Parshall and M. Kim. "Digital holographic microscopy with dual wavelength phase unwrapping". Appl. Opt. **45**(3): 451–459 (2006).

[Pat05] M. Paturzo, P. Ferraro, S. Grilli, D. Alfieri, P. D. Natale, M. d. Angelis, A. Finizio, S. D. Nicola, G. Pierattini, F. Caccavale, D. Callejo and A. Morbiato. "On the origin of internal field in Lithium Niobate crystals directly observed by digital holography". Opt. Express **13**(14): 5416–5423 (2005).

[Ped97] G. Pedrini and H. J. Tiziani. "Quantitative evaluation of two-dimensional dynamic deformations using digital holography". Optics and Laser Technology **29**(5): 249–256 (1997).

[Ped01a] G. Pedrini and S. Schedin. "Short coherence digital holography for 3D microscopy". Optik **112**(9): 427–432 (2001).

[Ped01b] G. Pedrini, S. Schedin and H. J. Tiziani. "Aberration compensation in digital holographic reconstruction of microscopic objects". J. Mod. Opt. **48**(6): 1035–1041 (2001).

[Ped02] G. Pedrini and H. J. Tiziani. "Short-coherence digital microscopy by use of a lensless holographic imaging system". Appl. Opt. **41**(22): 4489–4496 (2002).

[Ped03] G. Pedrini, I. Alexeenko, W. Osten and H. J. Tiziani. "Temporal phase unwrapping of digital hologram sequences". Appl. Opt. **42**(29): 5846–5854 (2003).

[Poo06] T.-C. Poon. *Digital Holography and Three-Dimensional Display* (New York, 2006).

[Pop04] G. Popescu, L. P. Deflores, J. C. Vaughan, K. Badizadegan, H. Iwai, R. R. Dasari and M. S. Feld. "Fourier phase microscopy for investigation of biological structures and dynamics". Opt. Lett. **29**(21): 2503–2505 (2004).

[Pop05] G. Popescu, T. Ikeda, C. Best, K. Badizadegan, R. Dasari and M. Feld. "Erythrocyte structure and dynamics quantified by Hilbert phase microscopy". Journal of Biomedical Optics **10**(6): 060503 (2005).

[Pop06a] G. Popescu, K. Badizadegan, R. R. Dasari and M. S. Feld. "Observation of dynamic subdomains in red blood cells". Journal of Biomedical Optics **11**(4): 040503–3 (2006).

[Pop06b] G. Popescu, T. Ikeda, R. Dasari and M. Feld. "Diffraction phase microscopy for quantifying cell structure and dynamics". Opt. Lett. **31**(6): 775–777 (2006).

[Pop06c] G. Popescu, T. Ikeda, K. Goda, C. A. Best-Popescu, M. Laposata, S. Manley, R. R. Dasari, K. Badizadegan and M. S. Feld. "Optical measurement of cell membrane tension". Phys. Rev. Lett. **97**: 218101 (4 pages) (2006).

[Rap05] B. Rappaz, P. Marquet, E. Cuche, Y. Emery, C. Depeursinge and P. J. Magistretti. "Measurement of the integral refractive index and dynamic cell morphometry of living cells with digital holographic microscopy". Opt. Express **13**(23): 9361 – 9373 (2005).

[Rap06] B. Rappaz, F. Charrière, J. Kühn, P. Marquet, C. Depeursinge and P. Magistretti. "Measurement of the integral refractive index of erythrocytes with a Digital Holographic Microscope". In "EOS European Optical Society Annual Meeting", (Paris, 2006).

[Rap07] B. Rappaz, A. Barbul, F. Charrière, J. Kühn, P. Marquet, R. Korenstein, C. Depeursinge and P. Magistretti. "Erythrocytes volume and refractive index measurement with a digital holographic microscope". In "Progress in Biomedical Optics and Imaging - Proceedings of SPIE", (San Jose, CA, 2007), *Optical Diagnostics and Sensing VII*, vol. 6445.

[Sch93] U. Schnars and J. W. PO. "Principles of direct holography for interferometry". In W. J. Osten and W., eds., "FRINGE 93: Proc. 2nd Int. Workshop on Automated Processing of Fringe Patterns", (Berlin: Akademie, 1993), pp. 115–120.

[Sch94] U. Schnars and W. Jüptner. "Direct Recording of Holograms by a Ccd Target and Numerical Reconstruction". Appl. Opt. **33**(2): 179–181 (1994).

[Sch99] S. Schedin, G. Pedrini, H. J. Tiziani and F. M. Santoyo. "All-fibre pulsed digital holography". Opt. Commun. **165**(4-6): 183–188 (1999).

[Sch01] S. Schedin, G. Pedrini, H. J. Tiziani and A. K. Aggarwal. "Comparative study of various endoscopes for pulsed digital holographic interferometry". Appl. Opt. **40**(16): 2692–2697 (2001).

[Sch02] U. Schnars and W. P. O. Juptner. "Digital recording and numerical reconstruction of holograms". Measurement Science and Technology **13**(9): R85–R101 (2002).

[Seb05] M. Sebesta and M. Gustafsson. "Object characterization with refractometric digital Fourier holography". Opt. Lett. **30**(5): 471–473 (2005).

[Sin05] P. Singh, M. S. Faridi, C. Shakher and R. S. Sirohi. "Measurement of focal length with phase-shifting Talbot interferometry". Appl. Opt. **44**(9): 1572–1576 (2005).

[Sit05] G. Situ and J. Zhang. "Multiple-image encryption by wavelength multiplexing". Opt. Lett. **30**(1306-1308) (2005).

[Smi69] H. Smith. *Principles of holography* (New York, 1969).

[Son06] W. Z. Song, X. M. Zhang, A. Q. Liu, C. S. Lim, P. H. Yap and H. M. M. Hosseini. "Refractive index measurement of single living cells using on-chip Fabry-Pérot cavity". Appl. Phys. Lett. **89**: 203901 (3 pages) (2006).

[Soo02] S. Soontaranon, J. Widjaja and T. Asakura. "Direct analysis of in-line particle holograms by using wavelet transform and envelope reconstruction method". Optik **113**(11): 489–494 (2002).

[Sos05] O. Sosnovtseva, A. N. Pavlov, N. A. Brazhe, A. R. Brazhe, L. A. Erokhova, G. Maksimov and E. Mosekilde. "Interference Microscopy under Double-Wavelet Analysis: A New Approach to Studying Cell Dynamics". Phys. Rev. Lett. **94**: 218103 (4 pages) (2005).

[Sta00] A. Stadelmaier and J. H. Massig. "Compensation of lens aberrations in digital holography". Opt. Lett. **25**(22): 1630–1632 (2000).

[Str69] G. Stroke. *An introduction to coherent optics and holography* (Academic press, New York, 1969).

[Sun05] H. Sun, M. A. Player, J. Watson, D. C. Hendry, R. G. Perkins, G. Gust and D. M. Paterson. "The use of digital/electronic holography for biological applications". J. Opt. A-Pure Appl. Opt. **7**(6): S399–S407 (2005).

[Taj00] E. Tajahuerce and B. Javidi. "Encrypting three-dimensional information with digital holography". Appl. Opt. **39**(35): 6595–6601 (2000).

[The05] A. Thelen, J. Bongartz, D. Giel, S. Frey and P. Hering. "Iterative focus detection in hologram tomography". J. Opt. Soc. Am. A **22**(6): 1176–1180 (2005).

[Tis01] T. V. Tishko and V. P. Titar. "Holographic microscopy. Methods, devices, applications". Lfnm'2001: Proceedings of the 3rd International Workshop on Laser and Fiber-Optical Networks Modeling pp. 162–167 (2001).

[Tis03] T. V. Tishko, V. P. Titar, T. M. Barchotkina and D. N. Tishko. "Application of the holographic interference microscope for investigation of ozone therapy influence on blood erythrocytes of patients In vivo". Advanced Optoelectronics and Lasers **5582**: 119–126 (2003).

[Tis04] T. V. Tishko, V. P. Titar and D. N. Tishko. "Application of the holographic phase contrast method for 3-D imaging of phase microobjects". Lfnm 2004: Proceedings of the 6th International Conference on Laser and Fiber-Optical Networks Modeling pp. 254–256 (2004).

[Tis05] T. V. Tishko, V. P. Titar and D. N. Tishko. "Holographic methods of three-dimensional visualization of microscopic phase objects". Journal of Optical Technology **72**(2): 203–209 (2005).

[Tiz72] H. J. Tiziani. "Optical Methods for the Vibration Analysis of a Tuning Fork of an Electric Watch". Optik **34**(4): 442–455 (1972).

[Tiz81] H. J. Tiziani, J. Klenk and K. Leonhardt. "Holography and speckle techniques for real-time displacement deformation and vibration analysis". In "Proceedings of the Society of Photo-Optical Instrumentation Engineers", (1981), vol. 236, pp. 62–67.

[Tyc01] V. P. Tychinski. "Coherent phase microscopy of intracellular processes". Physics-Uspekhi **44**(6): 617–629 (2001).

[Upa66] J. Upatnieks, A. V. Lugt and E. Leith. "Correction of lens aberrations by means of holograms". Appl. Opt. **5**(4): 589–593 (1966).

[Van66] R. F. Vanligte and H. Osterberg. "Holographic microscopy". Nature **211**: 282–283 (1966).

[vH04] R. van Hout and J. Katz. "A method for measuring the density of irregularly shaped biological aerosols such as pollen". J. Aerosol Sci. **35**: 1369–1384 (2004).

[Vis98] G. N. Vishnyakov and G. G. Levin. "Optical Microtomography of Phase Objects". Optics and Spectroscopy **85**(1): 73–77 (1998).

[Vis99] G. N. Vishnyakov, G. G. Levin, A. V. Likhachev and V. V. Pikalov. "Phase Tomography of 3D Biological Microobjects: Numerical Simulation and Experimental Results". Optics and Spectroscopy **87**(3): 413–419 (1999).

[Wag00] C. Wagner, W. Osten and S. Seebacher. "Direct shape measurement by digital wavefront reconstruction and multiwavelength contouring". Optical Engineering **39**(1): 79–85 (2000).

[Wan04] C. Wang, S. H. Chen, X. G. Yang and L. Li. "Investigation of chloride-induced pitting processes of iron in the H2SO4 solution by the digital holography". Electrochemistry Communications **6**(10): 1009–1015 (2004).

[Wya03] J. C. Wyant. "Dynamic interferometry". Optics and Photonics News **14**(4): 36–41 (2003).

[Xu01] L. Xu, X. Y. Peng, J. M. Miao and A. K. Asundi. "Studies of digital microscopic holography with applications to microstructure testing". Appl. Opt. **40**(28): 5046–5051 (2001).

[Xu03] W. Xu, M. H. Jericho, H. J. Kreuzer and I. A. Meinertzhagen. "Tracking particles in four dimensions with in-line holographic microscopy". Opt. Lett. **28**(3): 164–166 (2003).

[Yam97] I. Yamaguchi and T. Zhang. "Phase-shifting digital holography". Opt. Lett. **22**(16): 1268–1270 (1997).

[Yam01] I. Yamaguchi, J. Kato and S. Ohta. "Surface shape measurement by phase-shifting digital holography". Optical Review **8**(2): 85–89 (2001).

[Yam02] I. Yamaguchi, T. Matsumura and J. Kato. "Phase-shifting color digital holography". Opt. Lett. **27**(13): 1108–1110 (2002).

[Yam03] I. Yamaguchi, J. Kato and H. Matsuzaki. "Measurement of surface shape and deformation by phase-shifting image digital holography". Optical Engineering **42**(5): 1267–1271 (2003).

[Yan04] X. G. Yang, S. H. Chen, C. Wang and L. Li. "In-line digital holography for the study of dynamic processes of electrochemical reaction". Electrochemistry Communications **6**(7): 643–647 (2004).

[Yok06] M. Yokota, Y. Terui and I. Yamaguchi. "Analysis of polarization state by digital holography with polarization modulation". Optical Review **13**(6): 405–409 (2006).

[Yok07] M. Yokota, Y. Terui and I. Yamaguchi. "Polarization analysis with digital holography by use of polarization modulation for single reference beam". Optical Engineering **46**(5): 055801 (7 pages) (2007).

[Yon05] L. Yongqian, Z. Zhenyu and L. Xiaoying. "Elimination of reference phase errors in phase-shifting interferometry". Measurement Science and Technology **16**(6): 1335–1340 (2005).

[Yu03] L. F. Yu and L. L. Cai. "Multidimensional data encryption with digital holography". Opt. Commun. **215**(4-6): 271–284 (2003).

[Yu04] L. Yu and M. Kim. "Full-color three-dimensional microscopy by wide-field optical coherence tomography". Opt. Express **12**(26): 6632–6641 (2004).

[Yu05a] L. Yu and M. K. Kim. "Wavelength-scanning digital interference holography for tomographic three-dimensional imaging by use of the angular spectrum method". Opt. Lett. **30**(16): 092–2094 (2005).

[Yu05b] L. Yu and M. K. Kim. "Wavelength scanning digital interference holography for variable tomographic scanning". Opt. Express **13**(15): 5621 – 5627 (2005).

[Yu07] L. Yu and Z. Chen. "Improved tomographic imaging of wavelength scanning digital holographic microscopy by use of digital spectral shaping". Opt. Express **15**(3): 878–886 (2007).

[Zem01] "ZEMAX: Optical Design Program, User's Guide, Version 10.0" (Focus Software, Tucson, 2001), pp. 126–127.

[Zha98] T. Zhang and I. Yamaguchi. "Three-dimensional microscopy with phase-shifting digital holography". Opt. Lett. **23**(15): 1221–1223 (1998).

[Zha04] F. Zhang, J. D. R. Valera, I. Yamaguchi, M. Yokota and G. Mills. "Vibration Analysis by Phase Shifting Digital Holography". Optical Review **11**(5): 297–299 (2004).

Chapter 3

Characterization of microlenses by digital holographic microscopy

Paper published in Applied Optics **45**, 829-835 (2006).

Characterization of microlenses by digital holographic microscopy

Florian Charrière, Jonas Kühn, Tristan Colomb, Frédéric Montfort, Etienne Cuche, Yves Emery, Kenneth Weible, Pierre Marquet, and Christian Depeursinge

We demonstrate the use of digital holographic microscopy (DHM) as a metrological tool in micro-optics testing. Measurement principles are compared with those performed with Twyman–Green, Mach–Zehnder, and white-light interferometers. Measurements performed on refractive microlenses with reflection DHM are compared with measurements performed with standard interferometers. Key features of DHM such as digital focusing, measurement of shape differences with respect to a perfect model, surface roughness measurements, and optical performance evaluation are discussed. The capability of imaging nonspherical lenses without any modification of the optomechanical setup is a key advantage of DHM compared with conventional measurement tools and is demonstrated on a cylindrical microlens and a square lens array.

OCIS codes: 090.0090, 090.1760, 120.3620.

1. Introduction

Since its principle was proposed by Goodman and Lawrence[1] and by Kronrod *et al.*[2] more than 30 years ago, digital holographic microscopy (DHM) has been developed for a wide range of applications. In particular, off-axis DHM allows the extraction of both amplitude and phase information for a wave diffracted by a specimen from a single hologram.[3,4] The phase information provides 3D quantitative mapping of the phase shift induced by microscopic specimens with a resolution along the optical axis (axial resolution) better than 1°. Thanks to the performance of personal computers and progress in digital image acquisition, DHM currently provides cost-effective and easy-to-use instruments with high acquisition rates (camera limited) for real-time measurements and quality control in production facilities.

F. Charrière (florian.charriere@a3.epfl.ch), J. Kühn, T. Colomb, F. Monfort, and C. Depeursinge are with the Ecole Polytechnique Fédérale de Lausanne, Imaging and Applied Optics Institute, CH-1015 Lausanne, Switzerland. E. Cuche and Y. Emery are with Lyncée Tec SA, PSE-A, CH-1015 Lausanne, Switzerland. K. Weible is with SUSS MicroOptics SA, Jacquet-Droz 7, CH-2007 Neuchâtel, Switzerland. P. Marquet is with the Centre de Neurosciences Psychiatriques, Département de Psychiatrie, DP-CHUV, Site de Cery, CH-1008 Prilly-Lausanne, Switzerland.

Received 13 May 2005; revised 8 August 2005; accepted 8 August 2005.

0003-6935/06/050829-07$15.00/0

In a general context, DHM technology has been successfully applied for numerous operating modes, for instance, tomography on a biological sample performed with wavelength scanning,[5] investigation of the polarization state of an object by use of two orthogonally polarized wavefronts,[6] and multiple-wavelength interferometry of dynamic systems.[7]

This paper investigates some of the possibilities offered by DHM for micro-optics quality control, a domain with high performance demands in terms of speed, precision, automation, and productivity. The results are compared with those performed with Twyman–Green, Mach–Zehnder, and white-light interferometers (WLIs). Kebbel *et al.*[8] demonstrated measurement on a cylindrical lens with a dual-wavelength lensless DHM configuration, requiring averaging of 15 frames. This system achieved an axial resolution of 283 nm. We demonstrate off-axis DHM measurements requiring a single hologram acquisition and yielding an axial precision of 3.7 nm ($\lambda/175$) for measurement of silicon lenses in reflection configuration and 15.8 nm ($\lambda/40$) for quartz lenses in transmission configuration, i.e., at least as good as other conventional interferometers.

2. Metrology of Microlens Arrays—State of the Art

The constraints imposed on microlens arrays can be extremely demanding. Precise control of the shape, surface quality, and optical performance of the microlenses are required, as well as uniformity of these parameters across the array. Many different metrol-

ogy approaches exist, and noncontact techniques are preferred.[9,10] The Twyman–Green interferometer is probably the most precise tool for shape characterization, and direct analysis of optical performance is often performed with Mach–Zehnder interferometers. To achieve high precision, these types of interferometer require complex manipulations and optimization procedures that are often difficult to implement as an automated process of quality control, especially for entire wafers. WLIs with fully automated measurement capabilities are commercially available. However, these instruments are often not suited for characterization of the entire lens profile, yielding accurate information for only the vertex of refractive microlenses.

To be able to precisely control and optimize the performance of refractive microlens arrays, all the standard metrology tools mentioned above can be exploited with each giving a partial view of the total picture. It is only by combining the information from all these measurements that the tight constraints imposed on microlens arrays can be controlled and maintained. The specificities of the various types of interferometers are described hereafter.

Twyman–Green interferometers seem to be the most accurate tools for characterizing the shape of spherical or weakly aspherical lenses. Measurements in reflection provide the deviation of the surface shape from an ideal sphere, with an axial resolution in the range of $\lambda/20$. A piezoelectric transducer is used to shift the reference mirror to introduce a phase shift of $\pi/2$ between individual measurements. A phase-shifting algorithm is then used to calculate the reflected wavefront.[11] The measured unwrapped phase is used to make a direct comparison of the measured and the desired lens profiles and also permits the measurement of the radius of curvature (ROC) of the lens. Strong aspherical and nonspherical (e.g., cylindrical) lenses cannot be characterized in this way. The instrument used for this paper has been described in Ref. 12. One has to note that, in practice, ROC measurement with a Twyman–Green interferometer is performed by fringe analysis with the lens in a cat's eye configuration, i.e., when the focal point of the microscope objective coincides with the vertex of the microlens. In this position, the fringes of the hologram are perfectly straight lines. The lens is then mechanically moved until the fringes disappear, i.e., when the ROC of the lens matches the ROC of the illuminating wavefront; the vertical displacement of the microlens from the cat's eye position to the standard measurement position corresponds to the ROC of the microlens. ROC measured this way depends on the mechanical stage precision and remains in the micrometer precision range.

Mach–Zehnder interferometers allow for direct analysis of the optical performance of the microlenses. Transmission Mach–Zehnder measurements allow the aberrations of microlenses to be determined. The interferometer model used for this paper has been described in Ref. 12. An illumination microscope objective of high quality is used to generate a spherical wavefront, which is then collimated by the microlens under test. The interference of this wavefront with a plane reference wavefront allows for the determination of the optical quality of the microlens and yields an accuracy in the range of $\lambda/20$. Adapting the optomechanical setup allows Mach–Zehnder interferometers to also be used for the characterization nonspherical microlenses. For cylindrical lenses for instance, the microscope objective that is used to produce the spherical beam is removed. Consequently, a collimated beam impinges on the microlens and the interference pattern describes the phase delay introduced by the microlens. The phase is recovered by a standard phase-shifting technique and unwrapping algorithm. This phase delay can be used to calculate the lens profile that must have produced it. In this way, cylindrical lens profiles can be compared to the theoretically desired lens shape.

The WLI used for comparison in this paper is a WYKO NT3300. It is built in a reflection configuration and is capable of scanning over a complete 200 mm $\times$ 200 mm field. High-precision measurements with subnanometer resolution can be obtained when using the phase-shifting interferometric (PSI) mode, which requires a narrowband filter to produce a nearly monochromatic illumination light source. However, when using the PSI mode, the total depth that can be measured is limited. The entire lens surface may be measured for only small-NA lenses, but in general only the vertex area of the lens may be measured with the PSI mode. This is useful for obtaining the ROC of the best-fit sphere at that vertex of the lens but does not provide substantial information about the full lens shape.

The measurement time is mostly determined by the autofocus routine based on the fringe visibility detection and varies from 2 to 6 s depending on the amount of light reflected. The autofocus also allows for positioning correction along the optical axis during transverse measurement scanning of microcomponents. Therefore it is important that the sample is correctly disposed, so that the height error due to an incorrect tilt adjustment remains in the autofocus range along the entire sample.

Another application of the WLI is to use the vertical scanning interferometry (VSI) mode to perform a noncontact measurement of the lens height. Information is normally lost at the edge of the lenses due to the steep profile, but the height information at the vertex and at the surrounding substrate can be used to determine the lens height without any contact of the lens surface. VSI measurements are performed with the white-light source without the narrowband filter. Phase shifting is not performed. Instead, the optical head is scanned vertically while digital signal processing is performed to determine the peak of the visibility of the white-light fringes for each pixel in the detector array. The result is a mapping of the height of the imaged surface with a nanometer resolution. This mode is not used in standard micro-optic control.

In summary, reflection Twymann–Green mea-

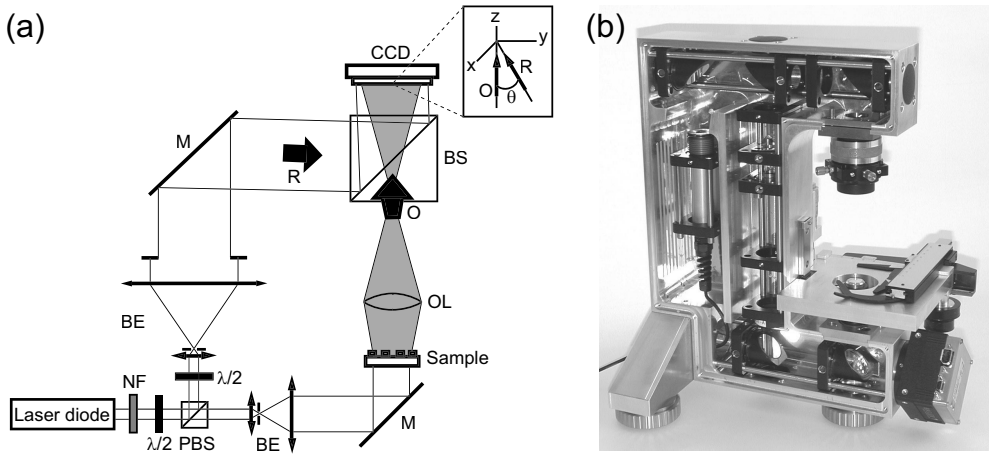

Fig. 1. Holographic microscope for transmission imaging: (a) experimental setup and (b) integrated instrument. NF, neutral-density filter; PBS, polarizing beam splitter; BE, beam expander with spatial filter; λ/2, half-wave plate; OL, objective lens; M, mirror; BS, beam splitter; O, object wave; R, reference wave. Inset, detail showing the off-axis geometry at incidence on the CCD.

surements allow precise characterization of the full lens shape, Mach–Zender measurements provide lens aberrations, WLI measurements in the PSI mode provide the ROC and deviation from the best-fit sphere for the vertex of the lens within less than 1% resolution, and WLI measurements in the VSI mode provide the lens height. A common drawback of all these techniques is the use of PSI phase measurement procedures that are highly sensitive to external perturbations and that require the use of piezoelectric-transducer-controlled moving parts to modulate the phase between successive acquisitions. This results in a relatively low measurement rate between 2 and 6 s per lens, mainly due to the autofocus procedure, and implementation costs owing to the need of vibration-insulating devices. Moreover, all these techniques require accurate control of the specimen position and orientation, which make them difficult to implement for automated quality control applications.

3. Digital Holographic Microscopy

A. Experimental Setup

The transmission (Fig. 1) and reflection (Fig. 2) DHM used for the present study are described in detail in Ref. 4. The results presented here were obtained with an objective lens of 8.00 mm focal length with a NA of 0.50 defining ×20 magnification. As a light source, we used a circular laser diode module with a wavelength of 635 nm. The camera is a standard 512 × 512 pixel, 8 bit, black-and-white CCD with a pixel size of 6.7 μm × 6.7 μm and a maximum frame rate of 25 Hz. Both instruments used for this paper have a transverse resolution around 1 μm. The field of view is 250 μm × 250 μm for the transmission setup and 300 μm × 300 μm for the reflection setup. The transverse resolution, as well as the transverse scale calibration, is determined with the help of a USAF 1951 resolution test target. Note that the transverse resolution, as well as the field of view (FOV) of DHM, can be easily adapted to different specimen sizes, as long as the lateral resolution remains sufficient to properly unwrap the modulo-2π reconstructed phase distribution.

Measurements presented here have been conducted without any system for insulating against vibrations of the building. This is possible thanks to the remarkably high measurement stability and robustness of DHM, which results from the fact that the off-axis configuration allows all the necessary information to be recorded with a single image acquisition of very short duration. The camera used here comprises an electronic shutter, which allows the exposure time to be reduced to 20 μs. With a 2.8 Ghz Pentium 4 processor the 3D phase reconstruction rate, described in the next chapter, is 15 frames/s, which is what makes DHM ideal for systematic investigations on large volumes of full wafers of microoptic samples.

B. Hologram Reconstruction

The procedure for hologram processing, in particular for phase reconstruction, is described in detail in Refs. 4, 13, and 14. For the sake of completeness, a short summary is given here. Holograms acquired by the CCD are first submitted to a procedure of apodization[14] and filtered in the Fourier plane to remove the zeroth-order and the twin image.[13] Then, the resulting hologram I_H, is multiplied by a digital reference wave R_D that simulates an illumination wave,[4] and a propagation calculation in the Fresnel approximation is applied to reconstruct a focused image of the specimen in a plane of coordinates $0\xi\eta$, where a digital phase mask $\Phi(m, n)$ is applied to compensate for the wavefront curvature induced by the objective lens (see Ref. 4). In summary, the reconstructed wavefront $\Psi(m\Delta\xi, n\Delta\eta)$ is computed according to the

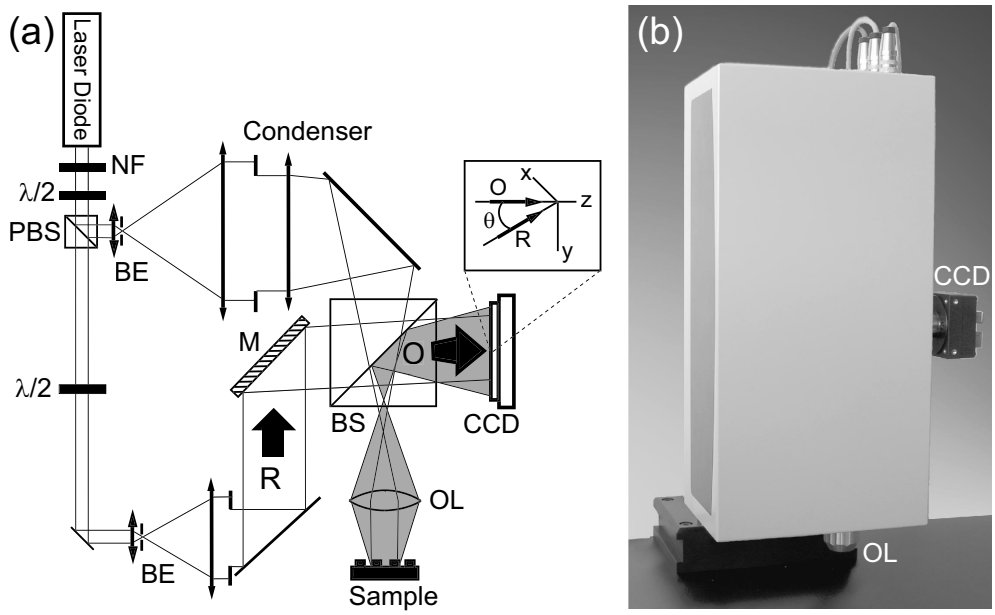

Fig. 2. Holographic microscope for reflection imaging: (a) experimental setup and (b) integrated instrument. Inset, detail showing the off-axis geometry at incidence on the CCD.

following expression:

$$\Psi(m\Delta\xi,\ n\Delta\eta) = A\Phi(m,\ n)\exp\left[\frac{i\pi}{\lambda d}(m^2\Delta\xi^2 + n^2\Delta\eta^2)\right] \times \mathrm{FFT}\left\{\mathbf{R}_D(k,\ l)I_H(k,\ l) \times \exp\left[\frac{i\pi}{\lambda d}(k^2\bar{x}^2 + l^2\bar{y}^2)\right]\right\}_{m,n}, \quad (1)$$

where m and n are integers ($-N/2 \le m, n < N/2$), FFT is the fast Fourier transform operator, $A = \exp(i2\pi d/\lambda)/(i\lambda d)$, $\Delta\xi$ and $\Delta\eta$ are the sampling intervals in the observation plane, $\bar{x}$ and $\bar{y}$ are the pixel size of the CCD, and k and l are integer variables. The digital reference wave is computed using the expression of a plane wave

$$\mathbf{R}_D(k,\ l) = \exp[i(k_{Dx}\cdot k\bar{x} + k_{Dy}\cdot l\bar{y})], \quad (2)$$

where k_{Dx} and k_{Dy} are the two components of the wave vector. The digital phase mask is computed according to the expression of a parabolic wavefront

$$\Phi(m,\ n) = \exp\left[-i\pi/(\lambda d_1)m^2\Delta\xi^2 - i\pi/(\lambda d_2)n^2\Delta\eta^2\right], \quad (3)$$

where parameters d_1 and d_2 define the field curvature along 0ξ and 0η, respectively, digitally adjusted to correct the defocusing aberration due to the objective lens. $\Delta\xi$ and $\Delta\eta$ are the sampling intervals in the observation plane.

C. Parameter Adjustment

Equation (1) requires the adjustment of four parameters for proper reconstruction of the phase distribution. k_{Dx} and k_{Dy} compensate for the tilt aberration resulting from the off-axis geometry or resulting from an imperfect orientation of the specimen surface, which should be accurately oriented perpendicular to the optical axis. d_1 and d_2 correct the wavefront curvature according to a parabolic model; in principle, these two parameters have similar values, but in the presence of astigmatism it may be that better results can be achieved with slightly different values. As explained in Ref. 4, the parameter values are adjusted to obtain a constant and homogeneous phase distribution on a flat reference surface located in or near the specimen. With microlenses the substrate is ideal to serve as a reference surface. The manual procedure described in Ref. 4 was implemented here as a semiautomated procedure. First, the program extracts two lines—a horizontal line along 0ξ and a vertical line along 0η—whose locations are defined by the operator in the reference surface. Then, 1D phase data extracted along the two lines are unwrapped[15] to remove 2π phase jumps, and a curve-fitting procedure is applied to evaluate the unwrapped phase data with a 1D polynomial function of the second order. k_{Dx} and d_1 are iteratively adjusted to minimize the deviation between the fitted curve and the ideal horizontal constant profile. In the same way, k_{Dy} and d_2 are adjusted until the vertical profile is as close as possible to the ideal vertical constant profile. In general, fewer than five iterations are necessary to reach optimal parameter values. If a reference area is not available on the specimen, the parameters are first

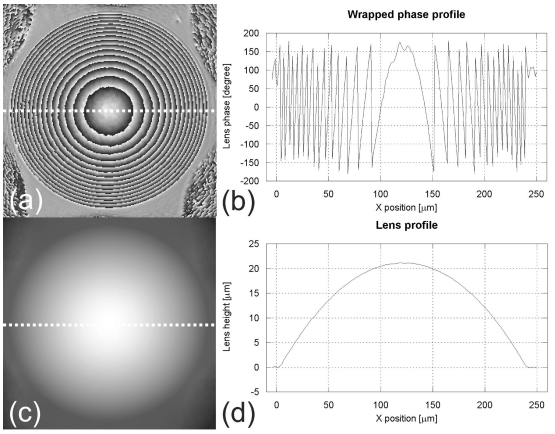

Fig. 3. Phase images of a quartz refractive transmission lens (diameter of 240 μm, maximal measured height of 21.15 μm, measured ROC of 351 μm) obtained with transmission DHM: (a) wrapped and (c) unwrapped 2D representations with corresponding (b) phase and (d) height profiles taken along the two dashed lines in (a) and (c).

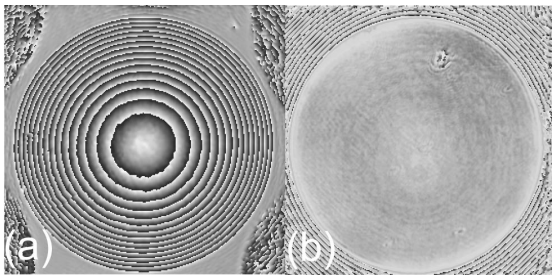

Fig. 4. Comparison between the real and the ideal profile is possible with DHM. By adjusting the reconstruction parameters involved in the reconstruction process, either the wavefront deformations of the objective lens are compensated [standard mode, (a)] or the spherical surface of the lens (here a quartz transmission lens) is compensated (compensation mode). The residue is obtained as the difference between the real and the ideal profile, presented in (b).

calculated on another reference surface (air in transmission, a mirror in reflection); then a simple digital tilt adjustment of the phase, corresponding to an adjustment of k_{Dx} and k_{Dy}, is performed with the same procedure described above when the specimen is observed.

The digital processing of holograms presented in this study is a novel approach in the sense that it performs a numerical reshaping of complex wavefronts and of their propagation, thereby replacing the need for complex optical adjustment procedures. For instance, orienting a mirror or a beam splitter with translation or rotation tables—a task that has to be performed very accurately in classical interferometry—is simply replaced here by the digital adjustment of the wave vector components k_{Dx} and k_{Dy}. Even more relevant is the digital correction of the wavefront deformation induced by the microscope objective. In comparison, in Linnik interference microscopy, the experimental counterpart of adjusting d is achieved by introducing in the reference arm a second identical microscope objective that must be once again aligned with high precision.

D. Performance for Phase Measurements

DHM provides quantitative phase mapping. In reflection, the phase information provides the surface topography and permits direct measurement of the lens shape and associated parameters such as the ROC. As for white-light interferometry, reflection measurements are restricted to the vertex of the lens, except if the lens curvature is small enough to ensure proper phase unwrapping up to the lens border. In transmission, the phase information gives the distribution of the optical path length, which describes the phase function of the lens. The geometrical thickness of the lens can then be deduced from the knowledge of its refractive index, as well as the lens shape, height, and ROC if the lens has a flat face (e.g., a plano–convex lens).

The precision for phase measurements, which define the axial resolution of DHM, was evaluated with two definitions. The first is measurement of the spatial standard deviation or spatial root-mean-square error (RMSE) over the whole FOV with a flat reference sample. In transmission, with simply ambient air as a reference specimen, the spatial RMSE is 4.1°, which corresponds to a thickness of 15.8 nm for quartz ($\lambda/40$) and to an equivalent height of 3.7 nm ($\lambda/175$) in reflection, where a mirror is used as a reference. The second definition is measurement of the temporal standard deviation, or rms repeatability, for each pixel over 4500 successive measurements during 5 min and averaged over the whole FOV. Measurements yield 0.46°, corresponding to 1.8 nm for quartz ($\lambda/355$) in transmission and 0.4 nm ($\lambda/1565$) in reflection.

4. Results: Measurement on Microlenses with Digital Holographic Microscopy

Three different types of microlenses are analyzed: a quartz refractive transmission lens, a silicon refractive reflective lens, and a cylindrical quartz transmission lens.

Figure 3 presents the measurements of a 240 μm diameter quartz spherical lens observed in transmission. Figure 3(a) presents the modulo-2π phase image in 3D perspective, and Fig. 3(c) presents the unwrapped phase image. Two profiles extracted from the center of the lens are presented in Figs. 3(b) and 3(d). Phase unwrapping is performed numerically using a noniterative least-squares algorithm.[15] In Fig. 3(a), one can observe four disturbed zones at the corners of the image. This corresponds to the four nearest lenses on the array, which are not resolved here because in these regions light deviations occur over large angles that cannot be collected by the objective lens. This also causes the depletion in the

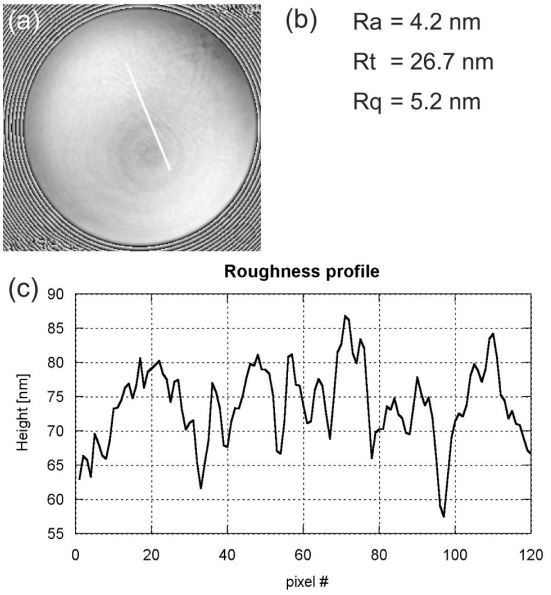

Fig. 5. Roughness measurement on the surface of a silicon refractive reflective lens (diameter of 241 μm, height of 4.38 μm). A comparison between the real and the ideal profile is possible with DHM. After adjustment of the reconstruction parameters, the residue is obtained as the difference between the real and the ideal profile, presented in (a). Some standard roughness values calculated over a profile are presented in (b), and the extracted profile, corresponding to the white line in (a), is presented in (c).

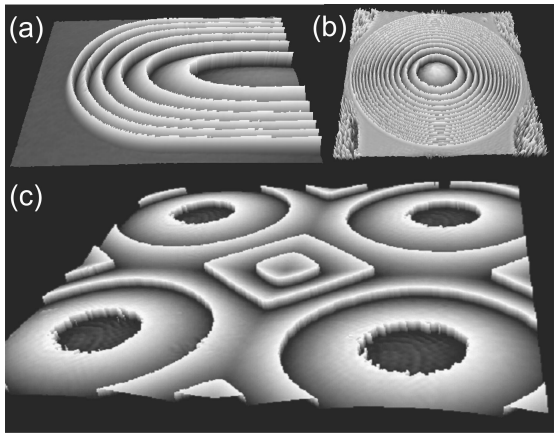

Fig. 6. Perspective phase images of three different lens types measured with the same transmission DHM: (a) cylindrical quartz refractive transmission lens (diameter of 160 μm, maximal measured height of 7.73 μm, measured ROC of 417.8 μm), (b) quartz refractive transmission lens (diameter of 240 μm, maximal measured height of 21.15 μm, measured ROC of 351 μm), and (c) square quartz lens array (pitch of 500 μm, maximal height of 5.5 μm, ROC of 5600 μm).

corners of the unwrapped image in Fig. 3(c) because the unwrapping procedure fails in these zones. The results presented in Fig. 3 allow direct estimation of the lens shape, in particular the ROC and the height.

An interesting feature of DHM is that the digital phase mask [Eq. (3)] involved in the reconstruction process can be defined flexibly by changing the reconstruction parameters k_{Dx}, k_{Dy}, d_1, and d_2. This offers original and efficient possibilities in micro-optics testing since it permits a theoretical model to be fitted to the observed sample and a direct representation of the deviation from this perfect shape to be obtained. The usual parameter adjustment is performed on the phase data extracted from the micro-optical component surface itself instead of calculating it on a flat reference.

Figure 4 illustrates this original feature of DHM with the same quartz lens previously presented. Figure 4(a) shows the phase image obtained by the standard adjustment procedure, and Fig. 4(b) shows the reconstruction of the same hologram when the parameters are adjusted by fitting the phase data on two profiles (one vertical and one horizontal) extracted from the center of the lens. A first advantage of this representation of the lens is that small defects, scratches or material inhomogeneities, become more apparent. The surface quality, roughness, for example, can also be evaluated independently of the lens shape. For example, Fig. 5(a) presents the deviation from a parabolic surface of a silicon lens (diameter of 241 μm, height of 4.38 μm) observed in reflection; Fig. 5(b) presents a profile extracted from Fig. 5(a), showing an average roughness of Ra = 4.2 nm and a peak-to-valley roughness of Rt = 26.7 nm. The representation in Fig. 4(b) is equivalent to the result provided by a Twyman–Green or a Mach–Zehnder interferometer working with an objective illumination lens producing a spherical wave and positioned in a confocal arrangement with the test lens. With DHM, passing from one imaging mode to the other is a straightforward and purely software operation that can be performed on a single hologram without any change in the experimental arrangement. The deviation from the ideal sphere is given in the paraxial or thin lens approximation as a result of the parabolic model used to calculate the digital phase mask [Eq.(3)]. If desired, other mathematical models can be used to compute the digital phase mask, such as higher-order polynomial functions or Zernike polynomials.

To verify the accuracy of DHM, measurements on a silicon microlens array obtained with DHM are compared with a reference measurement performed on the same sample by SUSS MicroOptics SA with a WLI. The lens diameter is 241 μm and the lens height is 4.38 μm. The ROC obtained with both techniques on the same ten lenses is compared. The measurements are in good agreement: The average ROC measurement is 1643 ± 5 μm for DHM and 1632 ± 2 μm for the WLI. The difference between the measurements is therefore less than 1% (0.71%).

To point out the versatility of DHM, three microoptical components of different shapes were investigated with the same transmission microscope without

any modification of the system except an adaptation of the FOV performed by simply changing the microscope objective. The phase perspective images of these lenses are presented in Fig. 6. The lenses under investigation were a cylindrical quartz refractive transmission lens [Fig. 6(a); diameter of 160 μm, maximal measured height of 7.73 μm, measured ROC of 417.8 μm], a quartz refractive transmission lens [Fig. 6(b); diameter of 240 μm, maximal measured height of 21.15 μm, measured ROC of 351 μm], and a square quartz lens array [Fig. 6(c); pitch of 500 μm, maximal height of 5.5 μm, ROC of 5600 μm). This illustrates that DHM is definitely not limited only to spherical lenses and that no important modification of the setup or careful adjustment of the sample is required.

5. Conclusion

This paper has illustrated some of the possibilities offered by DHM technology in micro-optics testing. The digital reconstruction process involved in DHM makes it a versatile tool for obtaining rapidly from a single hologram a wide range of information on microlenses such as surface topography, diffracted wavefront, phase function, aberrations, ROC, lens height, and surface roughness.

Compared to classical PSI, DHM offers similar performance in terms of resolution, precision, repeatability, and FOV but can be considered as an attractive solution as a result of five main features:

- The acquisition rate is higher because a complete description of the complex wavefront is obtained from a single hologram.
- The sensitivity to external perturbations (vibration and ambient light) is reduced since the capture time can be reduced to a few tens of microseconds.
- The accuracy is not intrinsically limited by the precision of the control of moving parts, such as piezoelectric transducers.
- A DHM instrument can be used without adaptations to investigate a wide variety of micro-optical component shapes, including cylindrical, square, and strongly aspheric lenses.
- It is easy to use and flexible for implementations in automated processes for quality control because of the robustness of the technique regarding positioning tolerances.

This research was supported by Swiss National Science Foundation grant 205320-103885 and by CTI grants 6606.2 and 7152.1. Applications to the shape control of micro-optics were carried out with the help of the projet DISCO (Distance Shape Control) directed by the Bremer Institut für Angewandte Strahltechnik.

References

1. J. W. Goodman and R. W. Lawrence, "Digital image formation from electronically detected holograms," Appl. Phys. Lett. **11,** 77–79 (1967).
2. M. A. Kronrod, N. S. Merzlyakov, and L. P. Yaroslavskii, "Reconstruction of a hologram with a computer," Sov. Phys. Tech. Phys. **17,** 333–334 (1972).
3. U. Schnars and W. Jüptner, "Direct recording of holograms by a CCD target and numerical reconstruction," Appl. Opt. **33,** 179–181 (1994).
4. E. Cuche, P. Marquet, and C. Depeursinge, "Simultaneous amplitude and quantitative phase-contrast microscopy by numerical reconstruction of Fresnel off-axis holograms," Appl. Opt. **38,** 6994–7001 (1999).
5. M. K. Kim, "Tomographic three-dimensional imaging of a biological specimen using wavelength-scanning digital interference holography," Opt. Express **7,** 305–310 (2000).
6. T. Colomb, E. Cuche, F. Montfort, P. Marquet, and C. Depeursinge, "Jones vector imaging by use of digital holography: simulation and experimentation," Opt. Commun. **231,** 137–147 (2004).
7. N. Demoli, D. Vukicevic, and M. Torzynski, "Dynamic digital holographic interferometry with three wavelengths," Opt. Express **11,** 767–774 (2003).
8. V. Kebbel, J. Muller, and W. P. O. Juptner, "Characterization of aspherical micro-optics using digital holography: improvement of accuracy," in *Interferometry XI: Applications,* Proc. SPIE **4778,** 188–197 (2002).
9. K. O. Mersereau, C. R. Nijander, A. Y. Feldblum, and W. P. Towsend, "Testing and measurement of microlenses," in *Miniature and Micro-optics and Micromechanics,* Proc. SPIE **1992,** 210–215 (1993).
10. J. Schwider, S. Haselbeck, H. Schreiber, H. Sickinger, O. Falkenstorrer, N. Lindlein, T. Keinonen, S. Sheridan, and N. Strwubl, "Production and control of refractive and diffractive microlenses," in *Miniature and Micro-Optics and Micromechanics,* Proc. SPIE **1992,** 102–113 (1993).
11. P. Hariharan, B. F. Oreb, and T. Eiju, "Digital phase-shifting interferometry: a simple error-compensating phase calculation algorithm," Appl. Opt. **26,** 2504–2506 (1987).
12. K. J. Weible, R. Volkel, M. Eisner, S. Hoffmann, T. Scharf, and H. P. Herzig, "Metrology of refractive microlens arrays," in *Optical Micro- and Nanometrology in Manufacturing Technology,* Proc. SPIE **5458,** 43–51 (2004).
13. E. Cuche, P. Marquet, and C. Depeursinge, "Spatial filtering for zero-order and twin-image elimination in digital off-axis holography," Appl. Opt. **39,** 4070–4075 (2000).
14. E. Cuche, P. Marquet, and C. Depeursinge, "Aperture apodization using cubic spline interpolation: application in digital holographic microscopy," Opt. Commun. **182,** 59–69 (2000).
15. H. Takajo and T. Takahashi, "Noniterative method for obtaining the exact solution for the normal equation in least-squares phase estimation from the phase difference," J. Opt. Soc. Am. A **5,** 1818–1827 (1988).

Chapter 4

The role of shot noise in DHM

4.1 Shot-noise influence on the reconstructed phase image signal-to-noise ratio in digital holographic microscopy

Paper published in Applied Optics **45**, 7667-7673 (2006).

Shot-noise influence on the reconstructed phase image signal-to-noise ratio in digital holographic microscopy

Florian Charrière, Tristan Colomb, Frédéric Montfort, Etienne Cuche, Pierre Marquet, and Christian Depeursinge

In digital holographic microscopy, shot noise is an intrinsic part of the recording process with the digital camera. We present a study based on simulations and real measurements describing the shot-noise influence in the quality of the reconstructed phase images. Different configurations of the reference wave and the object wave intensities will be discussed, illustrating the detection limit and the coherent amplification of the object wave. The signal-to-noise ratio (SNR) calculation of the reconstructed phase images based on the decision statistical theory is derived from a model for image quality estimation proposed by Wagner and Brown [Phys. Med. Biol. **30**, 489 (1985)]. It will be shown that a phase image with a SNR above 10 can be obtained with a mean intensity lower than 10 photons per pixel and per hologram coming from the observed object. Experimental measurements on a glass–chrome probe will be presented to illustrate the main results of the simulations.

OCIS codes: 090.0090, 030.4280, 030.5290, 110.3000.

1. Introduction

Digital holographic microscopy (DHM) is currently undergoing important developments, causing its popularity to increase continually. Its success is due to its capacity to extract both the amplitude and the phase signal of the wavefront diffracted by an object from a hologram recorded through a digital camera and to provide three-dimensional (3D) quantitative phase images. The principle of digital holography (DH) was first proposed by Goodman and Lawrence[1] and by Kronrod *et al*. 30 years ago.[2] At the beginning, holograms were registered on photographic plates, but the digital camera quickly became a more convenient tool. In DH, the intensity distribution of the hologram is processed by a digitally computed replica of the reference wave, after which the amplitude and phase distributions of the complex object wavefront are extracted simultaneously. Quantitative phase information on the nanometer scale is easily achievable with DH and can be extracted from a single hologram.[3,4] The transverse resolution is diffraction limited, as with classical microscopes, but axial resolutions of half a degree have already been reached in a reflection geometry with the phase information DH provides. This corresponds to an axial resolution of approximately 1 nm with a wavelength of 633 nm. Numerous applications and developments based on DH are now being developed. Among others, we can mention DH applications in metrology,[5,6] live cell imaging,[7,8] tomography of biological specimens,[9,10] polarization and birefringence imaging,[11,12] and aberration compensation.[13–15]

Despite the large number of applications and reconstruction methods, to the best of our knowledge, no systematic theory has been developed to quantify the quality of the reconstructed phase images. The most general statistical approach was conducted by Goodman,[16] but most developments were derived in the field of speckle interferometry and are not immediately applicable to the case of specimens with minimum roughness that are mostly investigated in DHM (polished surfaces, clean biological preparations, and optical devices). Some studies on the noise reduction were proposed for specific applications: Monnom *et al*.[17] have demonstrated improved visibility of the reconstructed intensity images by reducing the noise due to out-of-focus objects, but the amelio-

F. Charrière (florian.charriere@a3.epfl.ch), T. Colomb, and C. Depeursinge are with the Imaging and Applied Optics Institute, Ecole Polytechnique Fédérale de Lausanne, CH-1015 Lausanne, Switzerland. F. Montfort and E. Cuche are with the Lyncée Tec SA, PSE-A, CH-1015 Lausanne, Switzerland. P. Marquet is with the Département de Psychiatrie DP-CHUV, Centre de Neurosciences Psychiatriques, Site de Cery, CH-1008 Prilly-Lausanne, Switzerland.

Received 30 March 2006; revised 23 May 2006; accepted 26 May 2006; posted 30 May 2006 (Doc. ID 69529).

0003-6935/06/297667-07$15.00/0

ration is not clearly quantified and the phase behavior is not considered; Paganin *et al.*[18] investigated the effect of uniformly distributed noise during the acquisition of the out-of-focus images required for their amplitude-based phase-retrieving algorithm, the results being applicable only in their phase-sensitive technique; De Ruijter and Weiss[19] have discussed extensively the detection limit in quantitative off-axis electron holography, but their estimation of the phase variance relies principally on the fringe visibility over the hologram zone from which the phase is deduced, and this estimation therefore only holds with smooth phase variation. We propose here a general model for image quality estimation based on the decision statistical theory proposed by Wagner and Brown.[20] This model is then applied in a study of the influence of shot noise on the reconstructed phase images based on simulations. We will establish the influence of the repartition of the total intensity between the reference and the object beams and the influence of the reference beam intensity for a given object beam intensity. Experimental confirmation of the first simulation will be given.

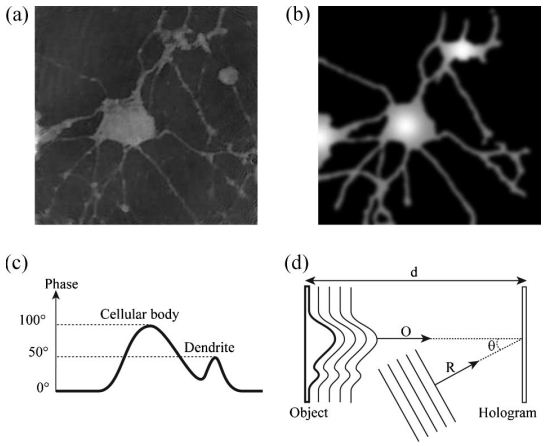

Fig. 1. (a) Real neuron phase image registered with DHM, (b) virtual neuron phase image, (c) virtual neuron characteristics summary, and (c) schematic of the off-axis hologram simulation (propagation of the wavefront on a distance d via the Fresnel integral): O, object wave; R, reference wave.

2. Theory

A. Simulations

Simulated holograms have been used to investigate the behavior of the reconstructed phase images' signal-to-noise ratios (SNRs). The main test object used for simulations is a virtual object representing a mouse neuronal cell, the shape of which has been derived from an actual neuron imaged with DHM presented in Fig. 1(a) (more details on DHM applied to cell imaging can be found in Ref. 8). This test object has been chosen to ensure a broad distribution of spatial frequencies representative of a common imaged object. It is considered a pure phase object (i.e., no absorption) imaged in transmission, for which the measured signal represents the phase shift induced by the specimen, which is proportional to the optical path length resulting from the integration of the refractive index of the specimen along the optical axis. The characteristics of this virtual object imaged in transmission with a 63× microscope objective at a wavelength of $\lambda = 633$ nm are presented in Figs. 1(b) and 1(c). The shape was schematized in order to suppress the noise due to the preparation containing the neuron, but the broad distribution of spatial frequencies was preserved.

The holograms are computed following the off-axis geometry presented in Fig. 1(d). The complex wavefront, resulting from the interaction of the illumination plane wave with our pure phase object, is propagated along a distance $d = 20$ cm according to the Fresnel approximation, to figure the acquisition of a nonfocused complex field on the CCD camera. The number of pixels considered for the object wavefront and for the hologram is $N = 512 \times 512$. The size of the hologram and of the virtual object is 5.12 mm × 5.12 mm, corresponding to the size of the real image of a mouse neuron cell seen through a microscope objective (63× magnification).[8] The off-axis hologram is obtained by computing the interference between the propagated object wave and a plane reference wave, whose propagation direction defines an angle $\theta = 0.7°$ with respect to the object wave propagation direction. Then shot noise is introduced on the image to simulate a real recorded intensity. The shot noise follows a Poisson's statistic[6]; i.e., the variance of the number of photons hitting a single pixel of the detector equals the mean number of photons hitting this pixel. The image is stored in an 8-bit image format, considering an ideal detector, which can set the lower intensity value to 0 and the maximum value to 255.

B. Processing the Hologram by the Convolution Approach

The method used to process the simulated holograms is based on the convolution approach described by Schnars and Jüptner in Ref. 4. The main advantage of this method is that the pixel sizes of the image and of the hologram are equal. It is therefore convenient to compute the SNR with the formula of Eq. (1) because the correspondence between a reconstructed image point and the initial object point is straightforward. With the other classical Fresnel–Kirchhoff integral reconstruction, described in Refs. 3 and 4, a rescaling of the reconstructed image is necessary for a pixel-to-pixel comparison, which can introduce some additional numerical noise. As described in Ref. 21, the removal of the zero order and of the twin image as well as the spatial filtering is performed by applying a user-defined mask to the Fourier spectrum of the off-axis hologram.

The intensity distribution in the hologram plane can be described by the following expression:

$$I_H(x, y) = \underbrace{OO^* + RR^*}_{\text{zero order}} + \underbrace{OR^*}_{\text{real image}} + \underbrace{R^*O}_{\text{virtual image}}, \quad (1)$$

where O and R are, respectively, the interfering object and reference. In classical holography, the reconstruction of the wavefront is achieved by illuminating the hologram with a replica of the reference wave. The wavefront $\Psi(x, y) = \mathbf{R}(x, y)I_H(x, y)$ propagates toward an observer, where the 3D image of the object is reconstructed. In digital holography, the reconstruction of the wavefront $\Psi(k\bar{x}, l\bar{y})$, where $\bar{x}$ and $\bar{y}$ are the pixel size of the CCD and k and l are integer values, is obtained the same way by multiplying the hologram intensity distribution $I_H(k, l)$ with a digitally computed reference wave $\mathbf{R}_D(k, l)$, called the digital reference wave. Assuming a plane reference wave, $\mathbf{R}_D$ can be described as follows:

$$\mathbf{R}_D(k,\ l) = A_R \exp[i(k_{Dx}k\bar{x} + k_{Dy}l\bar{y})], \tag{2}$$

where k_{Dx} and k_{Dy} are the two components of the wave vector in the hologram plane and A_R is an amplitude constant. The digitally reconstructed wavefront $\Psi(k\bar{x}, l\bar{y})$ is first computed in the hologram plane x_0y_0 and can afterward be evaluated at any distance from the hologram plane by the calculation of the scalar diffraction of the wavefront in the Fresnel approximation. $\Psi(m\Delta\xi, n\Delta\eta)$ is computed at a distance d from the hologram plane, in an observation plane $O\xi\eta$, by use of the following Fresnel propagation formula:

$$\Psi(m\Delta\xi,\ n\Delta\eta) = A\Phi(m,\ n)\mathrm{FFT}^{-1}\{\mathrm{FFT}[\mathbf{R}_D(k,\ l) \times I_H(k,\ l)]_{p,q} \exp[-i\pi\lambda d(p^2 + q^2)]\}_{m,n}, \tag{3}$$

where p, q and m, n are integers ($-N/2 \le m, n < N/2$), FFT is the fast Fourier transform operator, FFT^{-1} is the inverse fast Fourier transform operator, $A = \exp(i2\pi d/\lambda)/(i\lambda d)$ is a propagation constant, and $\Phi(m, n) = \exp[-i\pi/(\lambda d_1)m^2\Delta\xi^2 - i\pi/(\lambda d_2)n\Delta\eta^2]$ is the so-called digital phase mask with parameters d_1 and d_2 digitally adjusted to correct the phase aberration due to the microscope objective. $\Delta\xi = \bar{x}$ and $\Delta\eta = \bar{y}$ are the sampling intervals in the observation plane.

Considering only the virtual images of Eq. (1), the propagated wavefront corresponding to the computed digital reference wave is

$$\Psi = \mathbf{R}_D\mathbf{R} * \mathbf{O}, \text{ with } \mathbf{R}_D = \exp[i(k_{Dx}k\bar{x} + k_{Dy}l\bar{y})], \tag{4}$$

where k_{Dx} and k_{Dy} are two parameters adjusted to achieve identical propagation directions for $\mathbf{R}$ and $\mathbf{R}_D$.

Equation (3) requires the adjustment of four parameters for the proper reconstruction of the phase distribution. k_{Dx} and k_{Dy} compensate for the tilt aberration resulting from the off-axis geometry or resulting from an imperfect orientation of the specimen surface, which should be accurately oriented perpendicular to the optical axis. d_1 and d_2 correct the wavefront curvature induced by the microscope objective according to a parabolic model. Note that in the present study, these last two parameters only need to be adjusted during the processing of real acquired holograms because in the simulation no curvature induced by the microscope objective was considered. As explained in Ref. 3, the parameter values are adjusted in order to obtain a constant and homogeneous phase distribution on a flat reference surface located in or in the proximity of the specimen. The manual procedure described in Ref. 3 has been implemented here as a semiautomated procedure. First, the program extracts two lines—a horizontal line along 0ξ and a vertical line along 0η—whose location is defined by the operator in the reference surface. Then 1D phase data extracted along the two lines are unwrapped[22] to remove 2π phase jumps, and a curve-fitting procedure is applied to evaluate the unwrapped phase data with a 1D polynomial function of the second order. k_{Dx} and d_1 are iteratively adjusted to minimize the deviation between the fitted curve and the ideal horizontal constant profile. Similarly, k_{Dy} and d_2 are adjusted until the vertical profile is as close as possible to the ideal vertical constant profile. In general, less than five iterations are necessary to reach optimal parameter values. If a reference area is not available on the specimen, the parameters are first calculated on another reference surface (air in transmission, a mirror in reflection); then a simple digital tilt adjustment of the phase, corresponding to an adjustment of k_{Dx} and k_{Dy}, is performed with the same procedure described above when the specimen is observed.

Note that this digital adjustment method has been generalized to a multiprofile automatic procedure with a correction of the optical aberrations of the higher order. An extensive description of the technique and its applications to specimen shape compensation is presented in Ref. 15.

C. Signal-to-Noise Ratio of Phase Images

The SNR evaluation of an arbitrary image based on the statistical decision theory, proposed by Wagner and Brown,[20] is calculated according to the following expression:

$$\mathrm{SNR} = \frac{\iint \mathrm{d}f_x\mathrm{d}f_y|F[S(x,\ y)]|^2}{\sqrt{\iint \mathrm{d}f_x\mathrm{d}f_y|F[S(x,\ y)]|^2\ W(f_x,\ f_y)}}, \tag{5}$$

where $S(x, y)$ is the signal describing our image, F is the Fourier transform, and $W(f_x, f_y)$ is the Wiener spectrum of the noise, expressed by

$$W(f_x,\ f_y) = \lim_{L_x,L_y\to\infty} \frac{1}{4L_xL_y}\left|\int_{-L_x}^{L_x}\mathrm{d}x\int_{-L_y}^{L_y}\mathrm{d}y\Delta S(x,\ y) \times \exp[-2\pi i(xf_x + yf_y)]\right|^2, \tag{6}$$

where $\Delta S(x, y)$ is the absolute variation of $S(x, y)$ caused by the noise. This SNR provides an absolute scale for image system performance assessment and leads to instrumentation design goals and constraints for imaging system optimization since no observer can surpass the performance of the ideal observer. The dependence of the detectable detail size on exposure or imaging time follows immediately from the analysis (see Ref. 20 for details). This expression assumes the case of a quasi-ideal observer needing to determine whether a well-known specific object described by the function $S(x, y)$ is present in the field of view: The higher the SNR, the higher the object presence probability. A white noise is considered, even if the image noise is colored. An extention of this theory to a perfect observer who does not have this limitation is possible, and, in this case, the SNR expression presented here corresponds to the lower bound of the extended SNR, i.e., the most pessimistic SNR value.

Complete *a priori* knowledge of $S(x, y)$ is necessary to measure the SNR with this expression to allow a proper computation of the Wiener spectrum. This can easily be performed with simulations, because the image object is perfectly known, but can become difficult in real measurements.

D. Signal-to-Noise Ratio of the Hologram

To give a more intuitive description of the behavior of the phase image SNR in some particular limit cases described in Section 3, it is useful also to evaluate the SNR of the hologram itself. When two waves interfere, in our case, an object wave with intensity I_{Obj} and a reference wave with intensity I_{Ref}, the intensity of the interference pattern may be expressed as

$$I_{\mathrm{interference}} = I_{\mathrm{Obj}} + I_{\mathrm{Ref}} + \sqrt{I_{\mathrm{Obj}} I_{\mathrm{Ref}}}\cos(\varphi), \tag{7}$$

where φ is the phase difference between the two waves. The maximal variation of the amplitude is $2\sqrt{I_{\mathrm{Obj}}\, I_{\mathrm{Ref}}}$, as $\cos(\varphi)$ can take values between -1 and 1. In our study, the 8-bit detector is assumed to be perfect; i.e., the minimal intensity is set to 0 and the maximal intensity is set to 255. The maximal signal therefore corresponds exactly to the amplitude variation of $2\sqrt{I_{\mathrm{Obj}}\, I_{\mathrm{Ref}}}$. For a given pixel on the hologram, the maximal SNR value on the hologram can be expressed as

$$\mathrm{SNR}_{\mathrm{holo}} = \frac{2\sqrt{I_{\mathrm{Obj}} I_{\mathrm{Ref}}}}{\sqrt{I_{\mathrm{Obj}} + I_{\mathrm{Ref}}}}, \tag{8}$$

where the numerator is the maximal signal collected on a given pixel, and the denominator is the corresponding shot noise.

3. Results and Discussion

In what follows, the so-called total intensity represents the mean intensity diffracted by the object I_{Obj} added to the reference wave intensity I_{Ref}. For the simulations, the ideal function $S(x, y)$ corresponds to the phase function of the virtual neuron [see Fig. 1(c)], while the absolute variation $\Delta S(x, y)$ is calculated as the absolute difference between $S(x, y)$ and the phase of Ψ [Eq. (4)], the actual phase signal reconstructed from the hologram taking the shot noise (Poisson's statistic) into account.

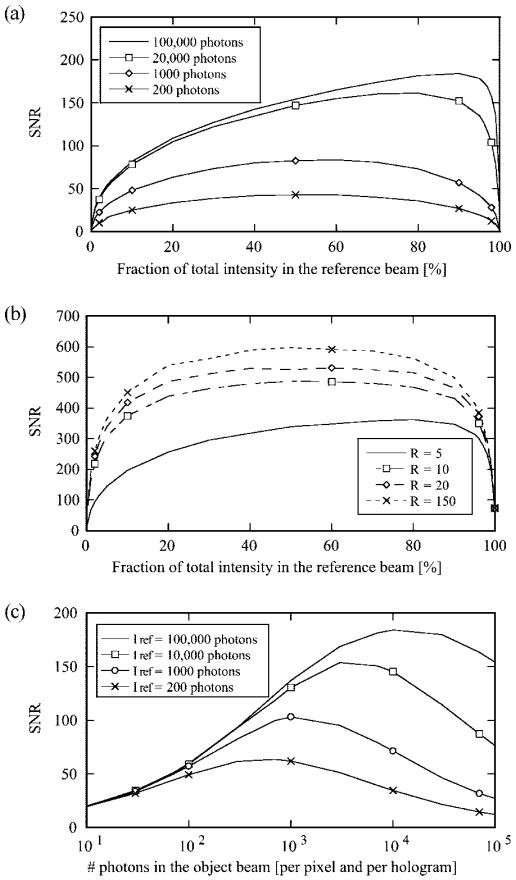

Fig. 2. (a) SNR on the neuron phase image as a function of the repartition of the total intensity between the two beams for different total intensities, (b) SNR on Gaussian objects as a function of the repartition of the total intensity between the two beams for a different object radius, and (c) SNR on the neuron phase image as a function of the object intensity for different reference intensities.

A first simulation shows that, in the case of a constant total intensity, a variation in the repartition of this intensity between the reference and the object beam is followed by a variation of the reconstructed image SNR. Figure 2(a) represents the SNR curves as a function of the percentage of intensity in the plane reference wave; the different curves are obtained for different total intensities expressed in the total number of photons per pixel and per hologram, the values of which are shown on the graphic. It can be observed that the SNR decreases abruptly at both graph extremities, when almost the total intensity is concentrated in either the reference or the object beam, i.e., when one of

the intensities tends to zero. This is easily understood when calculating the limits of Eq. (8):

$$\lim_{I_{\mathrm{Obj}}\to 0} \mathrm{SNR}_{\mathrm{holo}} = \frac{2\sqrt{I_{\mathrm{Obj}} I_{\mathrm{Ref}}}}{\sqrt{I_{\mathrm{Obj}} + I_{\mathrm{Ref}}}} = \frac{0}{\sqrt{I_{\mathrm{Ref}}}} = 0, \tag{9}$$

$$\lim_{I_{\mathrm{Ref}}\to 0} \mathrm{SNR}_{\mathrm{holo}} = \frac{2\sqrt{I_{\mathrm{Obj}} I_{\mathrm{Ref}}}}{\sqrt{I_{\mathrm{Obj}} + I_{\mathrm{Ref}}}} = \frac{0}{\sqrt{I_{\mathrm{Obj}}}} = 0. \tag{10}$$

If the SNR of the hologram tends to be zero, it is obvious that the SNR of the reconstructed phase images also becomes zero. In Fig. 2(a), it can be seen that for a low total intensity, the SNR curve is symmetric with respect to the intensity distribution and the maximal SNR value comes for an equal intensity repartition in each beam: At lower intensities, the SNR on the hologram is quite low and its maximum, i.e., the maximum of the expression $2\sqrt{I_{\mathrm{Obj}} I_{\mathrm{Ref}}}$, appears when both intensities are equal. Figure 2(a) also shows that for an intensity close to the camera saturation (camera saturation intensity is commonly around 100,000 photons per pixel for a camera with a gain of 1), the SNR maximum is clearly not centered and one had better put more intensity in the reference beam to increase the SNR. This dissymmetry discovered thanks to the simulation is more difficult to understand intuitively. One interpretation can be the following: The shot-noise perturbation on the hologram for a given pixel depends on the total intensity impinging on this pixel; if the intensity on each pixel comes mainly from the reference beam that is uniform over the hologram, the shot-noise perturbation on the hologram is much more uniform, and therefore uniformly distributed in the spectrum of the hologram, compared to a nonuniform noise distribution following the object beam intensity, and consequently the object spatial frequencies, in the case of a more intense object beam. One must also note that the maximum SNR value not only depends on the total intensity but also depends on the complexity of the object spectrum. To illustrate this fact, holograms were generated with some Gaussian phase objects characterized by a maximal phase value of π and an adjustable width defined by R, the radius in number of pixels taken at the FWHM value of the Gaussian phase object. The curves, calculated for a total average intensity of 100,000 photons per pixel and per hologram, are shown in Fig. 2(b); the different curves correspond to the different values of R chosen. It is clear that the SNR reaches greater values for broader phase objects with a thinner spectrum. For broader phase objects also, the shape of the curve is more symmetric, due to the simpler form of the object and its correspondent thin spectrum: For great values of R, the broad Gaussian phase objects tend to resemble a plane wave, making the system more and more symmetric. The results of these first two simulations should play a role of primary importance in the design of an experimental DHM setup, as one can usually distribute arbitrarily the intensity of the laser source between the reference and the object beam of the interferometer.

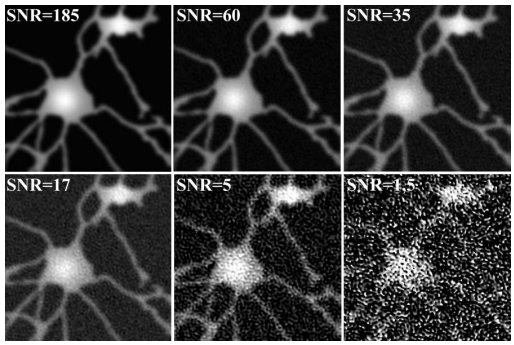

Fig. 3. Degradation of the reconstructed neuron phase image for different SNR values.

A second simulation presented in Fig. 2(c) shows the SNR curves as a function of the intensity in the object beam for a constant reference beam intensity; the different curves are obtained for different reference beam intensities (also in mean number of photons recorded per pixel and per hologram). This graphic illustrates that for a given intensity of the object beam, it is possible to improve the reconstructed image SNR by simply increasing the reference intensity. This gain in SNR is due to the coherent amplification of the object beam by the reference beam during the hologram acquisition. The maximum SNR improvement depends on the intensity coming from the object, and no significant improvement can be observed below a mean number of ten photons per pixel and per hologram. As before, this saturation of the SNR is understood when looking at what happens to the SNR of the hologram:

$$\lim_{I_{\mathrm{Ref}}\to\infty} \mathrm{SNR}_{\mathrm{holo}} = \frac{2\sqrt{I_{\mathrm{Obj}} I_{\mathrm{Ref}}}}{\sqrt{I_{\mathrm{Obj}} + I_{\mathrm{Ref}}}} = \frac{2\sqrt{I_{\mathrm{Ref}}}\sqrt{I_{\mathrm{Obj}}}}{\sqrt{I_{\mathrm{Ref}}}\sqrt{\frac{I_{\mathrm{Obj}}}{I_{\mathrm{Ref}}} + 1}} = 2\sqrt{I_{\mathrm{Obj}}}. \tag{11}$$

This limit calculation illustrates that the upper limit of the hologram SNR is determined by the object beam intensity only. It also shows that thanks to the coherent detection, the SNR on the hologram is twice as high as it would be with standard intensity image detection.

The images presented in Fig. 3 show the evolution of the reconstructed phase images for the neuron with a decreasing SNR to illustrate how the degradation of the image occurs.

To illustrate the results obtained with simulations, some measurements on a glass–chrome probe were made with a reflection DHM setup, schematically shown in Fig. 4. The laser source used is a 635 nm laser diode by Coherent, the camera is an 8-bit, black-and-white, 512 × 512 pixel (9.47 μm size) Hitachi CCD, and the microscope objective has a magnification of 10× and a numerical aperture of 0.30. A

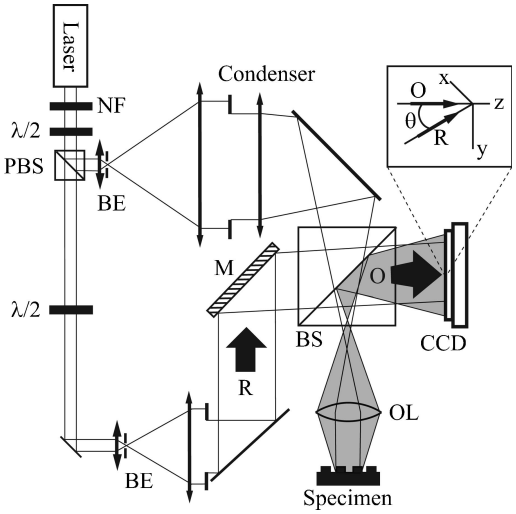

Fig. 4. Schematic of the holographic microscope for reflection imaging. NF, neutral-density filter; PBS, polarizing beam splitter; BE, beam expander with spatial filter; λ/2, half-wave plate; M, mirror; BS, beam splitter; O, object wave; R, reference wave.

quartz–chrome binary grating was used as the test object. Figures 5(a) and 5(b) resume the properties of the specimen. This grating was chosen because its Fourier spectrum is broad enough (high spatial frequencies due to abrupt steps), and its simple precise shape allows us to define an exact mathematical description of the grating to properly calculate the SNR according to Eq. (5), which is much more complicated if not impossible with mouse neurons because their shape is not known *a priori*. Figure 6 resumes the experimental realization of the first simulation, in which the total intensity is constant, here approximately 20,000 photons per pixel and per hologram, but the repartition of the intensity in the two beams varies. Repartition was simply adjusted with the help of the first λ/2 combined with the polarizing beam splitter. The asymmetry in the SNR curve with respect to the intensity repartition observed in the simulation [Fig. 2(a)] is also clearly reproduced in the

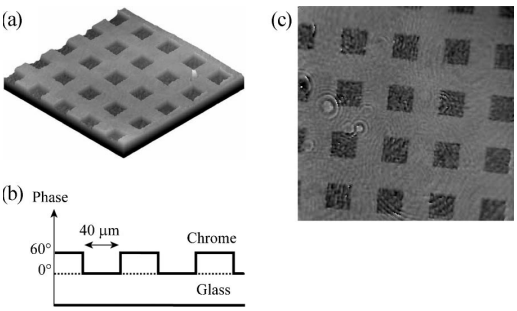

Fig. 5. (a) Glass–chrome specimen reflection DHM phase image perspective, (b) specimen characteristics summary, and (c) specimen phase image for an average illumination intensity of 2.9 nW/cm^2.

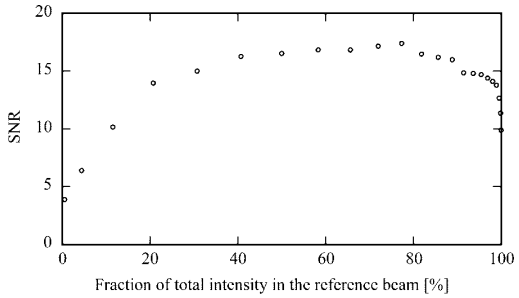

Fig. 6. SNR of the glass–chrome probe phase image as a function of the repartition of the total intensity between the two beams.

experiment, confirming the advantage of putting more intensity in the reference beam as in the object beam to improve the SNR. Just to illustrate that imaging at very low object intensity is possible, as predicted by previous simulations, a phase image of the glass–chrome specimen was taken with a diffracted object intensity of 2.9 nW/cm^2, corresponding approximately to 170 photons per pixel and per hologram for an integration time of 0.02 s. The SNR of this phase image, shown in Fig. 5(c), is 9.9. Concentric circles and parasitic fringes on the image are due to coherent noise (multiple reflections of the beams on the optics of the setup, especially the microscope objective) and are much more limiting for low object intensity imaging than for shot noise in the presented setup. The important readout noise of the CCD used is also a strong limitation, so that imaging with a few photons per pixel and per hologram becomes really difficult in our case.

Even if the real measurements reproduce the simulation qualitatively well, a note needs to be made about the numerical values reached by the SNR. As already mentioned above, an exact numerical description of the object is required to compute the SNR. The superposition of the numerical description of the object and the reconstructed phase image of the object was done with a maximal precision of one pixel. The present DHM setup is subject to coherent noise due to the large coherence length of the laser source: Interference patterns, which were not considered in simulations, appear on the hologram due to multiple reflections on optical components in the system. Finally, our detector is, of course, not ideal: The dynamic range is manually adjusted, and the readout noise is not negligible. This passage from the simulated world to the real world therefore drastically diminishes the highest values reached by the SNR, but the behavior of the curves is preserved.

4. Conclusion

The SNR model, based on the decision statistical theory, applied here to evaluate the behavior of DHM phase images under the influence of the shot noise, is a general tool for image quality estimation. Even if its application on real phase images may be difficult, owing to the required *a priori* description of the

object, it is readily adapted to studies based on simulations. Evaluations of important DHM processes, involving reconstruction algorithms, filtering techniques, and different noise models, can be envisaged this way.

Results obtained during the present work with simulations on total intensity repartition between the reference beam and the object beam are directly applicable to the experimental setup in order to reduce the shot-noise influence in reconstructed phase images. For the first time, to our knowledge, it has been demonstrated that in some cases a reference beam with its intensity equal to the object beam intensity is not the most favorable case regarding the reconstructed phase image quality. The influence on the phase signal SNR thanks to the object beam coherent amplification in digital holography has also been illustrated for the first time.

This work has been supported by the Swiss National Science Foundation (grant 205320-103885/1).

References

1. J. W. Goodman and R. W. Lawrence, "Digital image formation from electronically detected holograms," Appl. Phys. Lett. **11,** 77–79 (1967).
2. M. A. Kronrod, N. S. Merzlyakov, and L. P. Yaroslavskii, "Reconstruction of a hologram with a computer," Sov. Phys. Tech. Phys. **17,** 333–334 (1972).
3. E. Cuche, P. Marquet, and C. Depeursinge, "Simultaneous amplitude and quantitative phase-contrast microscopy by numerical reconstruction of Fresnel off-axis holograms," Appl. Opt. **38,** 6994–7001 (1999).
4. U. Schnars and W. P. O. Jüptner, "Digital recording and numerical reconstruction of holograms," Meas. Sci. Technol. **13,** R85–R101 (2002).
5. V. Kebbel, J. Muller, and W. P. O. Jüptner, "Characterization of aspherical micro-optics using digital holography: improvement of accuracy," in *Interferometry XI: Applications,* Proc. SPIE **4778,** 188–197 (2002).
6. F. Charrière, J. Kühn, T. Colomb, F. Montfort, E. Cuche, Y. Emery, K. Weible, P. Marquet, and C. Depeursinge, "Characterization of microlenses by digital holographic microscopy," Appl. Opt. **45,** 829–835 (2006).
7. G. Popescu, L. P. Deflores, J. C. Vaughan, K. Badizadegan, H. Iwai, R. R. Dasari, and M. S. Feld, "Fourier phase microscopy for investigation of biological structures and dynamics," Opt. Lett. **29,** 2503–2505 (2004).
8. P. Marquet, B. Rappaz, P. J. Magistretti, E. Cuche, Y. Emery, T. Colomb, and C. Depeursinge, "Digital holographic microscopy: A noninvasive contrast imaging technique allowing quantitative visualization of living cells with subwavelength axial accuracy," Opt. Lett. **30,** 468–470 (2005).
9. M. K. Kim, "Tomographic three-dimensional imaging of a biological specimen using wavelength-scanning digital interference holography," Opt. Express **7,** 305–310 (2000).
10. F. Charrière, F. Montfort, J. Kühn, T. Colomb, A. Marian, E. Cuche, P. Marquet, and C. Depeursinge, "Cell refractive index tomography by digital holographic microscopy," Opt. Lett. **31,** 178–180 (2006).
11. S. Grilli, P. Ferraro, M. Paturzo, D. Alfieri, and P. De Natale, "*In situ* visualization, monitoring and analysis of electric field domain reversal process in ferroelectric crystals by digital holography," Opt. Express **12,** 1832–1842 (2004).
12. T. Colomb, E. Cuche, F. Montfort, P. Marquet, and C. Depeursinge, "Jones vector imaging by use of digital holography: simulation and experimentation," Opt. Commun. **231,** 137–147 (2004).
13. P. Ferraro, S. De Nicola, A. Finizio, G. Coppola, S. Grilli, C. Magro, and G. Pierattini, "Compensation of the inherent wave front curvature in digital holographic coherent microscopy for quantitative phase-contrast imaging," Appl. Opt. **42,** 1938–1946 (2003).
14. C. Liu, Z. G. Liu, F. Bo, Y. Wang, and J. Q. Zhu, "Digital holographic aberration compensation in electron holography," Opt. Eng. **42,** 651–655 (2003).
15. T. Colomb, E. Cuche, F. Charrière, J. Kühn, N. Aspert, F. Montfort, P. Marquet, and C. Depeursinge, "Automatic procedure for aberrations compensation in digital holographic microscopy and applications to specimen shape compensation," Appl. Opt. **45,** 851–863 (2006).
16. J. W. Goodman, *Statistical Optics* (Wiley, 1985).
17. O. Monnom, F. Dubois, C. Yourassowsky, and J. C. Legros, "Improvement in visibility of an in-focus reconstructed image in digital holography by reduction of the influence of out-of-focus objects," Appl. Opt. **44,** 3827–3832 (2005).
18. D. Paganin, A. Barty, P. J. McMahon, and K. A. Nugent, "Quantitative phase-amplitude microscopy. III. The effects of noise," J. Microsc. **214,** 51–61 (2004).
19. W. J. De Ruijter and J. K. Weiss, "Detection limits in quantitative off-axis electron holography," Ultramicroscopy **50,** 269–283 (1993).
20. R. F. Wagner and D. G. Brown, "Unified SNR analysis of medical imaging-systems," Phys. Med. Biol. **30,** 489–518 (1985).
21. E. Cuche, P. Marquet, and C. Depeursinge, "Spatial filtering for zero-order and twin-image elimination in digital off-axis holography," Appl. Opt. **39,** 4070–4075 (2000).
22. H. Takajo and T. Takahashi, "Noniterative method for obtaining the exact solution for the normal equation in least-squares phase estimation from the phase difference," J. Opt. Soc. Am. A **5,** 1818–1827 (1988).

4.2 Influence of shot noise on phase measurement accuracy in digital holographic microscopy

Paper published in Optics Express **15**, 8818-8831 (2007).

Influence of shot noise on phase measurement accuracy in digital holographic microscopy

Florian Charrière[1], Benjamin Rappaz[2], Jonas Kühn[1], Tristan Colomb[3], Pierre Marquet[3] and Christian Depeursinge[1]

[1]*Ecole Polytechnique Fédérale de Lausanne (EPFL), Imaging and Applied Optics Institute, CH-1015 Lausanne, Switzerland*
[2]*Ecole Polytechnique Fédérale de Lausanne (EPFL), Brain Mind Institute, CH-1015 Lausanne, Switzerland*
[3]*Centre de Neurosciences Psychiatriques, Département de psychiatrie DP-CHUV, Site de Cery, CH-1008 Prilly-Lausanne, Switzerland*
[2] *http://apl.epfl.ch/page12232.html*
Corresponding author: florian.charriere@a3.epfl.ch

Abstract: Digital Holographic Microscopy (DHM) is a single shot interferometric technique, which provides quantitative phase images with subwavelength axial accuracy. A short hologram acquisition time (down to microseconds), allows DHM to offer a reduced sensitivity to vibrations, and real time observation is achievable thanks to present performances of personal computers and charge coupled devices (CCDs). Fast dynamic imaging at low-light level involves few photons, requiring proper camera settings (integration time and gain of the CCD; power of the light source) to minimize the influence of shot noise on the hologram when the highest phase accuracy is aimed. With simulated and experimental data, a systematic analysis of the fundamental shot noise influence on phase accuracy in DHM is presented.

OCIS codes: (090.1760) Computer holography, (030.4280) Noise in imaging systems, (030.5290) Photon statistics, (120.5050) Phase measurement.

References and links

1. J. W. Goodman and R. W. Lawrence, "Digital image formation from electronically detected holograms," Appl. Phys. Lett. **11,** 77-79 (1967).
2. M.A. Kronrod, N. S. Merzlyakov, and L. P. Yaroslavskii, "Reconstruction of a hologram with a computer," Sov. Phys. Tech. Phys. **17,** 333-334 (1972).
3. E. Cuche, P. Marquet, and C. Depeursinge, "Simultaneous amplitude-contrast and quantitative phase-contrast microscopy by numerical reconstruction of Fresnel off-axis holograms," Appl. Opt. **38**, 6994-7001 (1999).
4. U. Schnars and W. P. O. Jüptner, "Digital recording and numerical reconstruction of holograms," Meas. Sci. Technol. **13,** R85-R101 (2002).
5. P. Ferraro, S. De Nicola, A. Finizio, G. Coppola, S. Grilli, C. Magro, and G. Pierattini, "Compensation of the inherent wave front curvature in digital holographic coherent microscopy for quantitative phase-contrast imaging," Appl. Opt. **42,** 1938-1946 (2003).
6. C. Liu, Z.G. Liu, F. Bo, Y. Wang, and J.Q. Zhu, "Digital holographic aberration compensation in electron holography," Opt. Eng. **42,** 651-655 (2003).
7. T. Colomb, F. Montfort, J. Kühn, N. Aspert, E. Cuche, A. Marian, F. Charrière, S. Bourquin, P. Marquet and C. Depeursinge, "Numerical parametric lens for shifting, magnification and complete aberration compensation in digital holographic microscopy," J. Opt. Soc. Am. A **23**, 3177-3190 (2006).
8. V. Kebbel, J. Muller, and W. P. O. Jüptner, "Characterization of aspherical micro-optics using digital holography: improvement of accuracy," in *Interferometry XI: Applications*, Proc. SPIE **4778**, 188-197 (2002).
9. F. Charrière, J. Kühn, T. Colomb, F. Monfort, E. Cuche, Y. Emery, K. Weible, P. Marquet, and C. Depeursinge, "Characterization of microlenses by digital holographic microscopy," Appl. Opt. **45**, 829-835 (2006).

#82596 - $15.00 USD Received 1 May 2007; revised 22 Jun 2007; accepted 22 Jun 2007; published 28 Jun 2007

10. S. Grilli, P. Ferraro, M. Paturzo, D. Alfieri, and P. De Natale, "In-situ visualization, monitoring and analysis of electric field domain reversal process in ferroelectric crystals by digital holography," Opt. Express **12**, 1832-1842 (2004).
11. G. Popescu, L. P. Deflores, J. C. Vaughan, K. Badizadegan, H. Iwai, R. R. Dasari, and M. S. Feld, "Fourier phase microscopy for investigation of biological structures and dynamics," Opt. Lett. **29**, 2503-2505 (2004).
12. B. Rappaz, P. Marquet, E. Cuche, Y. Emery, C. Depeursinge, and P. Magistretti, "Measurement of the integral refractive index and dynamic cell morphometry of living cells with digital holographic microscopy," Opt. Express **13**, 9361-9373 (2005).
13. G. N. Vishnyakov, G. G. Levin, A. V. Likhachev, V. V. Pikalov, "Phase Tomography of 3D Biological Microobjects: numerical simulation and experimental results," Opt. Spectrosc. **87**, 413-419 (1999).
14. M. K. Kim, "Tomographic three-dimensional imaging of a biological specimen using wavelength-scanning digital interference holography," Opt. Express **7,** 305-310 (2000).
15. V. Lauer, "New approach to optical diffraction tomography yielding a vector equation of diffraction tomography and a novel tomographic microscope," J. Microsc. **205**, 165–176 (2002).
16. F. Charrière, N. Pavillon, T. Colomb, Ch. Depeursinge, T. Heger, E. A.D. Mitchell, P. Marquet and B. Rappaz, "Living specimen tomography by digital holographic microscopy: morphometry of testate amoeba," Opt. Express **14**, 7005-7013 (2006).
17. T. Colomb, F. Dürr, E. Cuche, P. Marquet, H. Limberger, R.-P. Salathé, and Ch. Depeursinge, "Polarization microscopy by use of digital holography: application to optical fiber birefringence measurements," Appl. Opt. **44**, 4461-4469 (2005).
18. J. W. Goodman, *Statistical Optics* (John Wiley & Sons, New York, 1985).
19. O. Monnom, F. Dubois, C. Yourassowsky, and J. C. Legros, "Improvement in visibility of an in-focus reconstructed image in digital holography by reduction of the influence of out-of-focus objects," Appl. Opt. **44**, 3827-3832 (2005).
20. D. Paganin, A. Barty, P. J. McMahon and K. A. Nugent, "Quantitative phase-amplitude microscopy. III. The effects of noise," J. Microsc. **214**, 51-61 (2004).
21. W. J. De Ruijter and J. K. Weiss, "Detection limits in quantitative off-axis electron holography," Ultramicroscopy **50**, 269-283 (1993).
22. G. A. Mills, and I. Yamaguchi, "Effects of quantization in phase-shifting digital holography," Appl. Opt. **44**, 1216-1225 (2005).
23. T. Baumbach, E. Kolenovic, V. Kebbel, and W. Jüptner, "Improvement of accuracy in digital holography by use of multiple holograms," Appl. Opt. **45**, 6077-6085 (2006).
24. R. F. Wagner and D. G. Brown, "Unified SNR Analysis of Medical Imaging-Systems," Phys. Med. Biol. **30,** 489-518 (1985).
25. F. Charrière, T. Colomb, F. Montfort, E. Cuche, P. Marquet and Ch. Depeursinge, "Shot noise influence in reconstructed phase image SNR in digital holographic microscopy," Appl. Opt. **45**, 7667-7673 (2006).
26. G. Popescu, K. Badizadegan, R. R. Dasari, and M. S. Feld, "Observation of dynamic subdomains in red blood cells," J. Biomed. Opt. **11**, 040503-3 (2006).
27. E. Cuche, P. Marquet, and C. Depeursinge, "Aperture apodization using cubic spline interpolation: application in digital holographic microscopy," Opt. Commun. **182**, 59-69 (2000).

1. Introduction

Digital Holographic Microscopy (DHM) is a recent quantitative phase imaging technique, which is developing rapidly, offering both sub-wavelength axial accuracy and real time observation capabilities. Following the pioneer works of Goodman or Kronrod on digital holography [1-2], the method is based on the digital acquisition of a single hologram formed by an object beam passing through a microscope objective and interfering with a reference beam. The object wavefield is recovered when the hologram is re-illuminated by a digitally computed replica of the reference wave, allowing quantitative measurement of both phase and amplitude [3-4]. The transverse resolution is diffraction limited, as with classical microscopes. However, interferometric phase measurements are performed with a high precision, providing nanometric accuracy images of the optical path length through the specimen in transmission DHM, or topographic images in reflection DHM. Compared to phase-shifting interferometers, DHM offers competitive performances in terms of resolution, precision, repeatability and field of view, and has in addition three main advantages. Firstly, measurements are performed in a much shorter interval of time, as a complete measurement of the complex wavefront is obtained from a single hologram capture (down to few microseconds integration time), resulting in a reduced sensitivity to external perturbations such as vibrations. Secondly, as full measurement of the wavefront is obtained and stored digitally, DHM allows digital focusing

#82596 - $15.00 USD Received 1 May 2007; revised 22 Jun 2007; accepted 22 Jun 2007; published 28 Jun 2007

and resulting in an extended depth of focus. Thirdly, wave front curvatures including different kind of aberrations can be numerically corrected, allowing a dramatic simplification of the optical design [5-7]. A variety of applications of this new type of optical microscopy have been described. Among others, we can mention: DHM applications in microlenses metrology [8-9]; material science [10]; live cell imaging [11-12] where DHM quantitative phase distribution contains information concerning both morphology and refractive index of the observed specimen [12]; tomography of biological specimen based on quantitative phase data acquired with DHM [13-16]; polarization and birefringence imaging [17].

In spite of the number of applications and reconstruction methods, few systematic investigations have been performed to quantify the quality and the accuracy of the reconstructed phase images. A general statistical approach was conducted by Goodman [18], but most developments were derived within the framework of speckle interferometry and are not directly applicable to the case of specimens with minimum roughness mostly investigated in DHM (polished surfaces, clean biological preparations, optical devices…). More specifically in the frame of digital holography, some studies concerning the noise reduction were proposed for specific applications: Monnom *et al.* have demonstrated an improved visibility of the reconstructed intensity images by reducing the noise due to out-of-focus objects, but the resulting amelioration is not clearly quantified and the phase behavior is not considered [19]; Paganin *et al.* investigated the effect of a uniformly distributed noise during the acquisition of the out-of-focus images required for their amplitude-based phase-retrieving algorithm; the results are however only applicable to their phase sensitive technique [20]; Ruijter and Weiss have extensively discussed the detection limit in quantitative off-axis electron holography, but their estimation of the phase variance relies principally on the fringe visibility over the hologram zone from which the phase is deduced and consequently this estimation is valid for objects with smooth phase variation only [21]; Mills and Yamaguchi have inspected the effect of the hologram quantization in phase-shifting digital holography, but have restricted their study to amplitude images [22]; Baumbach and *al.* by reducing the speckle noise in digital holography, using a proper averaging of several recorded holograms with different speckle pattern, have improved the accuracy of shape and deformation measurements [23].

In a previous paper, we proposed a general study of the signal-to-noise ratio of DHM phase images, based on the decision statistical theory proposed by Wagner and Brown [24], treating the effect of shot noise jointly with the influence of the intensity ratio between the reference and the object beams [25]. Practically, the SNR calculated within the frame of decision statistical theory helps an observer to decide if a known object is present in the noisy image or not. However despite the effect of shot noise has been discussed quantitatively, the phase accuracy in DHM images has not been addressed. Thanks to the continuous progress of personal computers and CCD, DHM is a fast growing field, particularly in the direction of dynamic measurements for life sciences [12, 26] or industrial applications. As fast dynamic imaging at low-light level involves few photons, the influence of shot noise on the hologram must be thoroughly investigated. Indeed under improper imaging conditions, it may cause a fundamental limitation in the accuracy of the reconstructed phase. Surprisingly, only few works, described in the above-mentioned references, have been reported on the subject of noise in interferometric phase measuring instruments, making difficult the definition of standard conditions for a proper comparison of the different methods performances; even commercial instruments claim performances obtained under not clearly defined measurement conditions. In this paper, for the first time to our knowledge, the influence of shot noise to the phase accuracy in DHM is clearly studied using both simulated and experimental data.

2. Material and method

2.1 Setup: the transmission DHM

The transmission DHM (Fig. 1) used for the present study has been described in details in Refs. [3] or [7]. Results presented here have been obtained with a 20x 0.4 NA microscope

#82596 - $15.00 USD Received 1 May 2007; revised 22 Jun 2007; accepted 22 Jun 2007; published 28 Jun 2007

objective. As light source, a circularized laser diode module with wavelength of 682.5 nm is used. The camera is a standard 1392 x 1040 pixels, 8 bits, black and white CCD, with a pixel size of 6.45 µm x 6.45 µm, and a maximum frame rate of 25Hz. The field of view is around 250 µm x 250 µm for a 512 x 512 pixels hologram.

The transverse resolution as well as the field of view are calibrated with the help of a USAF 1951 resolution test target. The camera comprises an electronic shutter, which enables to reduce the exposure time down to 1 µs, and an electronic gain adjustable from 0 to 25dB. With an INTEL Core 2 Duo 6600 2.4GHz, the phase image reconstruction rate described in the next chapter, reaches the value of 15 frames per second.

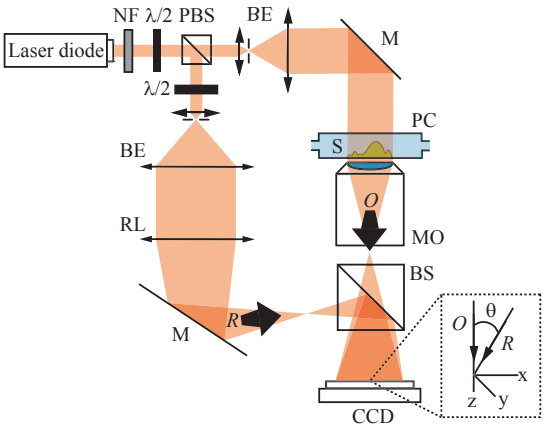

Fig. 1. Holographic microscope for transmission imaging: NF neutral density filter; PBS polarizing beam splitter; BE beam expander with spatial filter; λ/2 half-wave plate; MO microscope objective; RL field lens; M mirror; BS beam splitter; ***O*** object wave; ***R*** reference wave; PC perfusion chamber; S specimen. Inset: a detail showing the off-axis geometry at the incidence on the CCD.

2.2 Reconstruction of the holograms

The method used to process the simulated holograms is based on the convolution approach described by Schnars and Jüptner in Ref. [4] or by Colomb *et al*. in Ref. [7], where the concept of numerical lenses has been introduced to the classical formulation in order to compensate for aberrations in the optical system. As described in Ref. [7], the removal of the zero order and twin image as well as the spatial filtering are performed by applying a user-defined mask to the Fourier spectrum of the off-axis hologram. For sake of clarity, a summary of the reconstruction technique is given hereafter (see Ref. [7] for details).

The intensity distribution in the hologram plane can be described by the following expression:

$$I_H(x,y) = \underbrace{\boldsymbol{OO}^* + \boldsymbol{RR}^*}_{\text{zero order}} + \underbrace{\boldsymbol{OR}^*}_{\text{real image}} + \underbrace{\boldsymbol{R}^*\boldsymbol{O}}_{\text{virtual image}}, \tag{1}$$

where ***O*** and ***R*** are respectively the interfering object and reference complex wavefront. In digital holography, the reconstruction of the wavefront $\Psi(k\Delta x, l\Delta y)$, where Δx and Δy are the pixel size of the CCD and k, l are integer values, is obtained by multiplying the hologram intensity distribution $I_H(k,l)$ with a digitally computed reference wave $\boldsymbol{R_D}(k,l)$, called the digital reference wave. Assuming a plane reference wave, $\boldsymbol{R_D}$ can be described as follows:

#82596 - $15.00 USD Received 1 May 2007; revised 22 Jun 2007; accepted 22 Jun 2007; published 28 Jun 2007

$$\boldsymbol{R_D}(k,l) = A_R \exp\left[\mathrm{i}\left(k_{Dx}\cdot k\Delta x + k_{Dy}\cdot l\Delta y\right)\right], \quad (2)$$

where k_{Dx}, and k_{Dy} are the two components of the wave vector in the hologram plane and A_R is an constant amplitude. The digitally reconstructed wave front $\Psi(k\Delta x,l\Delta y)$ is first computed in the hologram plane x_Oy_O, and can afterward be evaluated at any distance from the hologram plane by the calculation of the scalar diffraction of the wavefront in the Fresnel approximation. $\Psi(m\Delta\xi, n\Delta\eta)$ is computed at a distance d from the hologram plane, in an observation plane $O\xi\eta$, by use of the following Fresnel propagation formula in the convolution formulation:

$$\Psi(m\Delta\xi,n\Delta\eta)=A\Phi(m,n)\cdot \mathrm{FFT}^{-1}\left\{\mathrm{FFT}\left\{\boldsymbol{R_D}(k,l)I_H(k,l)\right\}_{p,q}\cdot\exp\left[-\mathrm{i}\pi\lambda d\left(p^2+q^2\right)\right]\right\}_{m,n}, \quad (3)$$

where p,q and m,n are integers ($-N/2 \le m, n < N/2$), FFT is the Fast Fourier Transform operator, FFT^{-1} is the Inverse Fast Fourier Transform operator, $A=\exp(\mathrm{i}2\pi d/\lambda)/(\mathrm{i}\lambda d)$ is a propagation constant, and $\Phi(m,n)=\exp(-\mathrm{i}\pi m^2\Delta\xi^2/(\lambda d_1)-\mathrm{i}\pi\, n^2\Delta\eta^2/(\lambda d_2))$ is the so-called digital phase mask with parameters d_1 and d_2 digitally adjusted to correct the phase aberration due to the microscope objective. $\Delta\xi=\Delta x$ and $\Delta\eta=\Delta y$ are the sampling intervals in the observation plane.

Considering only the virtual image of Eq. (1), the propagated wave front corresponding to the computed digital reference wave is:

$$\Psi = \boldsymbol{R_D R^* O}, \text{ with } \boldsymbol{R_D} = \exp\left[\mathrm{i}(k_{Dx}\cdot k\Delta x + k_{Dy}\cdot l\Delta y)\right], \quad (4)$$

where k_{Dx} and k_{Dy}, are two parameters adjusted to achieve identical propagation directions for $\boldsymbol{R}$ and $\boldsymbol{R_D}$.

Equation (3) requires the adjustment of four parameters for proper reconstruction of the phase distribution. The adjustment of k_{Dx} and k_{Dy} compensates for the tilt aberration resulting from the off axis geometry, while d_1 and d_2 allows to correct the wave front curvature induced by the microscope objective according to a parabolic model. Note that, in the present study, these last two parameters do not require to be adjusted in the simulated data where the curvature induced by the microscope objective was not considered. As explained in Refs. [3] or [7], the parameter values are adjusted in order to obtain a constant and homogeneous phase distribution on a flat reference surface located in or within close proximity of the specimen. The manual procedure described in Ref. [3] has been recently generalized to an automated procedure enabling the correction of optical aberrations of higher order, as described in Ref. [7].

2.3 Evaluation of the phase accuracy in the reconstructed images

As previously mentioned, there is no precise definition of the phase accuracy in absolute phase-sensitive systems, including standard interferometric systems (white-light, Mach-Zehnder, Michelson, Linnik…) or DHM. Frame averaging as well as or numerical processing of the images are commonly achieved, and basically the claimed accuracy is established for the overall procedure, while its precise characteristics including the number of samples, the total integration time, or the numerical processing methods are not specified. A definition tends nowadays to impose itself as standard: the standard spatial deviation (STD) is calculated on a defined zone of a blank phase image from which the average of 10 blank phase images has been subtracted. This way, the assumed stable phase pattern due to optics imperfections or optics misalignments is removed, allowing taking into account the temporal fluctuating noise only. Within this paper, aiming at evaluating the effect of shot noise, we have considered the STD as a measure of the phase accuracy. The cases of single-shot imaging vs temporal image averaging have been treated separately to avoid any confusion. The same analyzing procedure

#82596 - $15.00 USD Received 1 May 2007; revised 22 Jun 2007; accepted 22 Jun 2007; published 28 Jun 2007

has been applied to both the experimentally recorded and simulated holograms. First, the holograms were reconstructed according to the convolution method described above, considering a reconstruction distance d = 3 cm. The standard deviation of the phase was then calculated in a central zone of 256 x 256 pixels. The reason of evaluating the phase statistics on a restricted central zone of the reconstructed phase image, is to prevent the influence of border effects due to the discontinuity introduced by the windowing of the hologram when it is processed by both the FFT calculation and the apodization function applied to the hologram [27].

3 Holograms simulations

3.1 Principle of the simulations

Simulated holograms presented in this study have been achieved in order to theoretically determine the influence of the shot noise on the phase accuracy in DHM, either as a function of the optical power impinging the CCD or as a function of time for a given optical power. Theoretical holograms without specimen have been calculated, to determine the shot noise influence only. For all the simulations, 512 x 512 pixels holograms have been considered. All the calculations have been done in the Matlab environment. Two plane waves of equal intensities have been considered to interfere in an off-axis configuration. The calculation parameters have been adjusted according to the experimental conditions given above in the setup description: a square pixel size of 6.45 µm, a laser wavelength of 682.5 nm, and a quantification of the simulated hologram on 8 bits. The angle θ between the object and reference wave defining the off-axis configuration has been adjusted to 1.7°, with a fringes orientation of 45° with regard to the CCD vertical axis, corresponding to the experimental arrangement. After a perfect hologram has been simulated with the parameters described above, shot noise has been added, in order to simulate a realistic recorded hologram. The shot noise follows a Poisson's statistics [17], i.e. the variance of the number of photons impinging a specific pixel of the detector is equal to the mean number of photons hitting this pixel. One should remember that the shot noise depends only of the optical power, i.e. the number of photons, on the CCD, and is unavoidable in any light imaging recording process. No consideration of the other characteristics of the CCD including the full well capacity, gain linearity, readout noise or dark noise have been taken into account in the simulations, those noise sources behavior being dependent of each CCD model.

3.2 Role of the quantization of the holograms

A first simulation has been achieved in order to determine the possible role of the hologram quantization, i.e. the number of bits used to store the hologram in a digital form. The primary goal here was to establish whether an encoding on 8 bits per pixel of the simulated holograms could guarantee a sufficient accuracy or not. Consequently, a perfect hologram has been simulated with no additional noise, and stored in various format from 16 bits down to 1 bit. The spatial STD of the phase as a function of the number of bits is shown in Fig. 2(a).

#82596 - $15.00 USD Received 1 May 2007; revised 22 Jun 2007; accepted 22 Jun 2007; published 28 Jun 2007

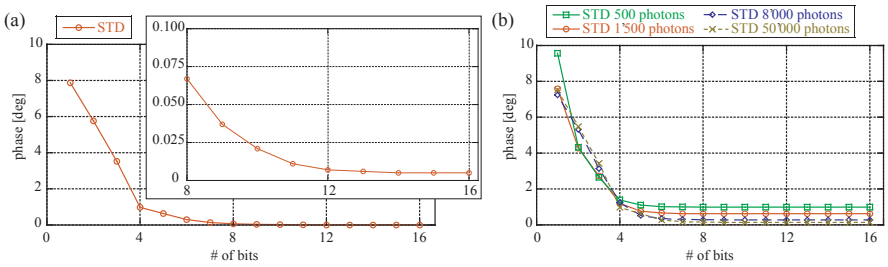

Fig. 2. Effect of hologram quantization on the standard deviation of the reconstructed phase a) for a noise-free hologram, inset exhibits a zoom on the high quantization values, and b) for a hologram with an average number of photons per pixel of 500, 1500, 8'000 and 50'000 with the corresponding shot noise.

It can be seen on Fig. 2(a), that the minimal phase STD achievable is 0.005° (λ/72'000). This minimal value is obtained for the perfect holograms encoded with 14, 15 and 16 bits, showing that the best precision of our simulation/reconstruction procedure is achieved and that accuracy can not be improved by encoding the holograms with a higher number of bits. On the other hand, the 8 bits-hologram produces a phase STD of 0.067° (λ/5'370), which far exceeds the phase STD of 0.5° corresponding to the reconstruction of a blank experimental hologram. An 8 bits storing has therefore proved to be accurate enough for both simulated and experimental data, causing no accuracy limitation during the reconstruction process.

A second simulation has been performed in order to evaluate the quantization effect on holograms with shot noise. The simulated holograms correspond to experimental holograms with an average number of photons per pixel of respectively 500, 1'500, 8'000 and 50'000. The value of 8'000 photons represents the optimal configuration available on the transmission DHM described in paragraph 2.1: with a well depth of 16ke$^-$ for the CCD pixels, an average value of 8'000 photons allows an optimal sampling of the hologram by the CCD. This configuration is achieved with an integration time of 510 µs for an irradiance on the specimen plane of few hundreds of microwatts per square centimetre, and can therefore be considered as our standard imaging conditions in transmission DHM for cells observation [11, 13]. The value of 50'000 photons corresponds to the illumination of a CCD pixel with a 100ke$^-$ full well capacity, which represents the nowadays CCDs largest full well capacity. The values of 500 and 1'500 photons were chosen to represent some non-optimal configurations available with our DHM transmission setup. In contrast, Fig. 2(b) shows that as far as noisy holograms are considered. Consequently, the phase STD as a function the number of bits presents, for values greater than 6 bits, plateaus at values depending on the simulated illumination levels only. This observation comforts us with the decision of using only an 8 bits encoding during our simulations, and demonstrates also that a quantization on 8 bits does not contribute to significantly restrict phase accuracy in our standard experimental conditions.

#82596 - $15.00 USD Received 1 May 2007; revised 22 Jun 2007; accepted 22 Jun 2007; published 28 Jun 2007

3.3 Shot noise-limited phase image accuracy

The central part of this work concerns the fundamental limitation imposed by the shot noise on the accuracy of the reconstructed phase images. The Poisson's statistic describing the photons behavior defines the unbeatable inferior limit of the phase accuracy reconstructed from on a single hologram, when a perfect detector with no additional electronic or thermal noise is considered. Results presented on Fig. 3 depict the STD in the reconstructed images as a function of the optical level, expressed through the average number of photons per pixels for simulated holograms with shot noise.

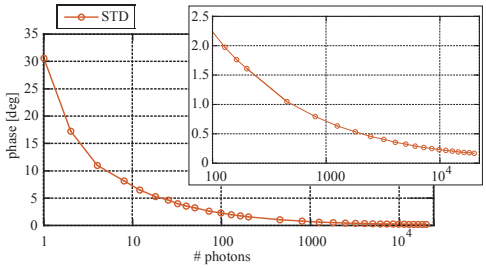

Fig. 3. Standard deviation of the phase value in the reconstructed images as a function of the optical power, expressed by the average number of photons per pixels for simulated holograms with shot noise; inset shows a zoom on the high optical power values.

This graph can be used as a simple look-up table to determine the best achievable accuracy for a given experimental configuration, knowing the integration time, the gain and the full well capacity of the CCD. For example, let us consider the optimal DHM transmission configuration used for cellular imaging in the present work: the CCD is claimed by the manufacturer to have a 16ke$^-$ full well capacity; considering the power of the laser source, a maximal integration time of 510 µs can be set before saturation of the CCD, corresponding to an average number of photons per pixel of 8'000. Under this configuration, the simulated shot noise causes a phase STD of 0.25° (λ/1'440). Note that for the precedent calculations a quantum efficiency of 1 has been considered for the CCD (otherwise a simple proportionality factor exists between the number of photons impinging on a given pixel and the effective number of electrons in the well). This small example illustrates that improper imaging conditions can severely decrease the performance of a DHM setup, emphasizing the importance of the results presented on Fig. 3.

#82596 - $15.00 USD Received 1 May 2007; revised 22 Jun 2007; accepted 22 Jun 2007; published 28 Jun 2007

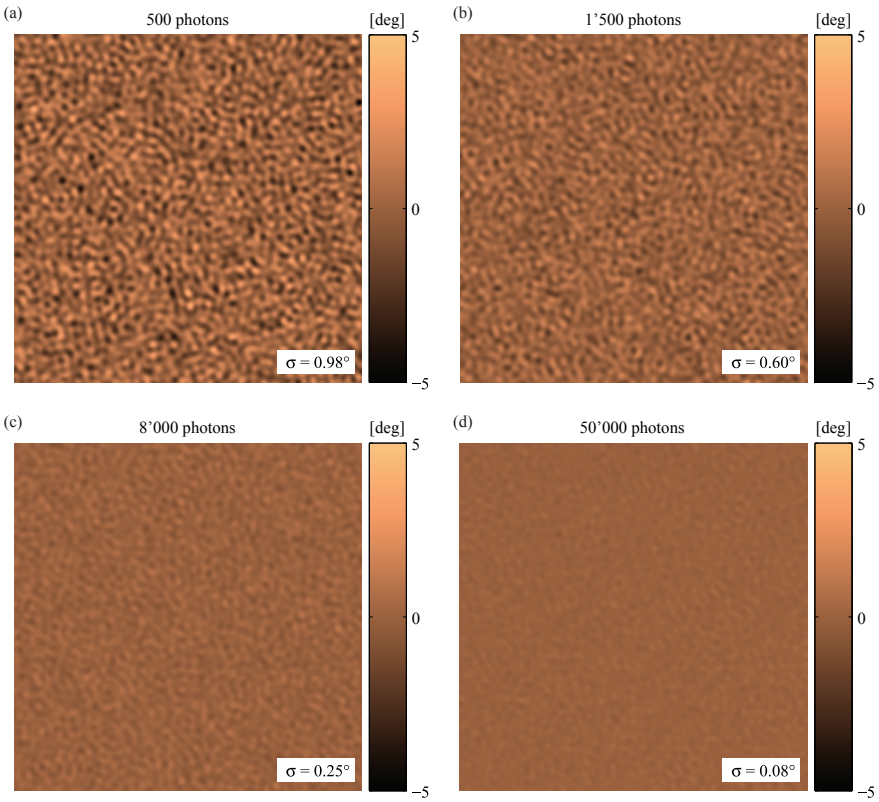

Fig. 4. Phase image (central zone of 256x256 pixels) showing the shot noise structure for simulated holograms with a mean number of photons per pixel of respectively 500 (a), 1'500 (b), 8'000 (c) and 50'000 (d); insets: the phase STD σ calculated on the phase images are indicated. A movie comprising 50 phase images illustrates the noise fluctuation [2.0 Mb].

On Fig. 4 are presented some examples of reconstructed phase images for different illumination levels: 500, 1'500, 8'000 and 50'000 mean photons per pixel. Central zones of 256x256 pixels are presented with the same color-coding scale to properly appreciate the effect of shot noise at the different illumination levels. The movie accessible from Fig. 4 allows one to appreciate the fluctuating noise in the phase images caused by shot noise. Fifty images reconstructed from simulated holograms are displayed in the movie at a rate of 6 frames per second. The observed fluctuating granular pattern has been identified to be the specific signature of shot noise. This pattern is somehow similar to a speckle pattern, with grain size corresponding to the numerical point spread function dictated by the Fresnel propagation of the algorithm used for the holograms reconstruction: the shot noise is not spatially-correlated from a pixel to another in the hologram, therefore the observed grains in the reconstructed phase image result from the addition of the numerical point spread functions multiplied by all the hologram pixels random amplitude perturbations.

In accordance with intuition, it can be seen on the graphs of Fig. 3, that the more photons involved in the hologram formation, the more accurate the reconstructed phase images. Experimentally this augmentation of the number of photons can be done in two ways: increasing the optical power of the laser source or increasing the integration time. As one of the strength of DHM is its interferometric accuracy without any insulating system, one tends to maintain a short integration time for the hologram acquisition to prevent perturbations

#82596 - $15.00 USD Received 1 May 2007; revised 22 Jun 2007; accepted 22 Jun 2007; published 28 Jun 2007

caused by mechanical vibrations. Additionally, the power of the laser source is often fixed and can not be increased at will. Nevertheless, the number of photons can be virtually increased by performing reconstructed phase image averaging. For illustration, four series of hologram with shot noise has been simulated, with respectively an average number of photons per pixel of 500, 1'500, 8'000 (i.e. our standard experimental configuration for cellular imaging) and 50'000. On Fig. 5 are presented the STD of the reconstructed phase image as a function of the number of phase images N used in the averaging procedure. Conjointly, least-square fitted curves are also displayed on Fig. 5 with there analytical expression. It results (see Fig. 5) that, the STD as a function of the number of photons N follows almost a $N^{-1/2}$ law, except for the curve corresponding to the 50'000 mean photons: as it has be seen in the paragraph 3.2, the minimal phase STD achieved with our reconstruction procedure for a single perfect 8-bits hologram is 0.067°, what reduces the effect of averaging when the initial phase STD for a single image is already close to this minimal value, like the 0.13° obtained with 50'000 photons. This minimal noise resulting to the reconstruction algorithm also explains why decay law around $N^{-0.49}$ or $N^{-0.48}$ are observed instead of an exact $N^{-1/2}$ normally expected. This averaging technique allows for reducing the shot noise effect till the required phase accuracy is obtained. It can be seen from the graph that, for the standard case of 8'000 photons, an averaging on 10 images yields a STD of 0.08° (λ/4'500), and an averaging on 100 images allows reaching a phase STD of 0.03° (λ/12'000); at a reconstruction rate of 15 frames per second, such averaging take resp. 0.67 sec and 6.67 sec, what is somehow reasonable considering the potential gain in accuracy obtained thanks to such a procedure.

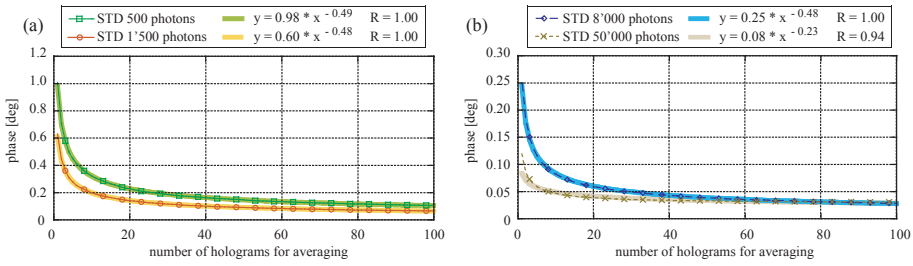

Fig. 5. Effect of averaging demonstrated on a series of simulated holograms for a mean number of photons per pixel of 1500: STD value of the reconstructed phase image as a function of the number of phase images N used in the averaging procedure with a fitted curve, which equation shows clearly the $N^{-1/2}$ tendency; R is the parameter fitter value.

4. Experimental evaluation of the shot noise in a transmission DHM

4.1 Holograms without specimen

The transmission DHM previously described was used to record holograms and confront the simulation with experimental measurements.

In a first step, a series of blank holograms was recorded, i.e. without any specimen in the system, to stress the role played by the shot noise. The maximum integration time possible in our setup before saturation of the signal was determined for no electrical gain set on the CCD. At this time value, the maximum number of photons per pixel reaches the full well capacity of 16ke$^-$. To cover the largest range of intensities, we have started to record holograms with the largest shutter value, and progressively decreased it until no exploitable hologram was recordable for the given illumination level. To maintain a proper sampling of the hologram, the gain was accordingly increased to properly use the 8 bits dynamic range of the CCD. An example of phase image reconstructed from a experimentally recorded hologram with an mean number of 1'500 photons per pixel is presented on Fig. 6(a). The central zone of 256x256 pixels, on which the phase STD has been calculated, is indicated.

#82596 - $15.00 USD Received 1 May 2007; revised 22 Jun 2007; accepted 22 Jun 2007; published 28 Jun 2007

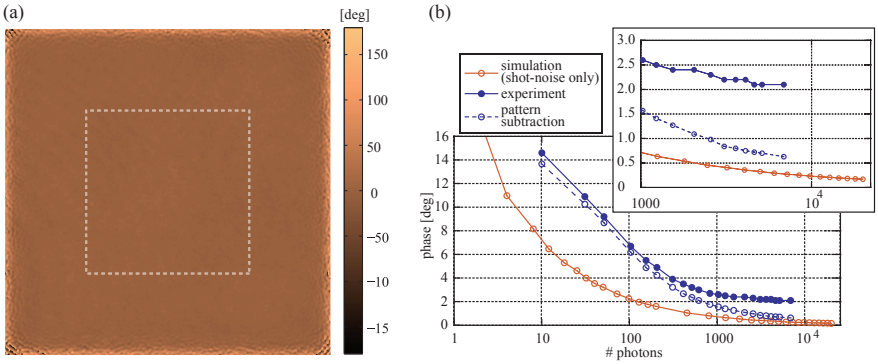

Fig. 6(a). Reconstructed phase image (512x512 pixels, field of view 250 µm x 250 µm) from an experimentally recorded blank hologram with an average photon numbers of 1'500 per pixel; the dashed zone in the image shows the 256x256 pixels square on which the phase STD was calculated. (b) Simulated (shot noise only) and experimental standard deviation of the phase in the reconstructed images as a function of the optical level, expressed as the average number of photons per pixels; the dotted curve corresponds to the experimental dataset after subtraction of the fixed phase pattern from all the reconstructed phase images; inset shows a zoom on the high optical power values.

The measured phase STD as a function of the mean number of photons per pixel is summarized on Fig. 6(b); the lower bound of the phase STD established with simulated data considering shot noise only is also displayed. The experimental values of the phase STD are larger than the shot noise limited values coming from simulation: an offset of about 2° for intensities larger than 1000 photons per pixel is observed for the experimental phase STD data compared to the simulated ones (see inset Fig. 6). This offset is caused by small defects in the setup such as non-perfect alignments of optics, imperfection of the optics surfaces, or optical aberrations. Those optical system imperfections are however stable over time, and produces a constant distortion in the phase images, manifested by a fixed phase pattern. A simple way to extract this pattern consists in averaging several images to reduce the influence of shot noise and readout noise. To verify that this pattern causes the above-mentioned offset, the experimental phase STD is recalculated, after the fixed phase pattern had been subtracted from all the reconstructed phase images. This new curve is also presented on Fig. 6(b). One can observe that this subtraction effectively removes the STD offset at higher mean intensities (above 1000 photons per pixel), showing a simple way to compensate optical imperfections of the system and thus improve its accuracy. In contrast, one observes that this subtraction has not any significant effect at lower intensities (below 100 photons per pixel). This demonstrates that the deviation of the experimental data with respect to the simulations may be explained by the imperfection of the setup for the hologram registered at higher intensities. However, another source of noise is dominating at lower intensities (electronic noise of the CCD). After subtraction of the fixed phase pattern, the averaging procedure described in chapter 3.3 has been applied to the experimental data for the case of 1500 mean photons per pixel on the hologram with a measured STD phase value of 1.34° (λ/270): the STD obtained for 10 phase images averaging is 0.5° (λ/720), going down to 0.37° (λ/830) for 30 holograms. As expected, a reduction of the phase STD is observed, but somehow less efficient as expected for a perfect $N^{-1/2}$ behavior (values resp. 15% and 25% larger than expected), what also confirms the presence of other noise source than shot noise.

Additional measurements realized with a homogeneous white light source have revealed the presence of electronic readout noise in our CCD, especially for the configurations with short integration time and strong gain. The observed readout noise appears to be structured and not uniform over the image, corresponding to the electronic architecture of the CCD itself. The structure of this noise on the CCD chip and its Fourier Transform making its

#82596 - $15.00 USD Received 1 May 2007; revised 22 Jun 2007; accepted 22 Jun 2007; published 28 Jun 2007

periodic structure clearly visible are presented on Fig. 7 for two extreme cases: a high gain with short acquisition time Fig. 7(a) and a no gain with a long acquisition time Fig. 7(b). The situation with large integration time and no gain corresponds to experimental data with high optical power of Fig. 6(b), where the experimental phase STD on reconstructed images, after subtraction of the fixed pattern noise, follows the simulated data; in this case, the readout noise can be considered sufficiently homogenous to affect negligibly the reconstructed phase images. On the other hand, the situation with large gain and short integration time corresponds to the part of the curve of Fig. 6(b), where experimental data does not follow the curve predicted by simulation (below 100 photons per pixel); in this configuration, the readout noise becomes highly structured, and affects consequently the reconstructed phase images. This noise has revealed to be sensitive to both gain and integration time, as well as to light irradiance. Therefore, the proper understanding and modeling of this readout noise is a complex and cumbersome task, which oversteps the subject of the present work focusing on the fundamental physics limitation due to shot noise, and not on the electronic handling of the CCD chip.

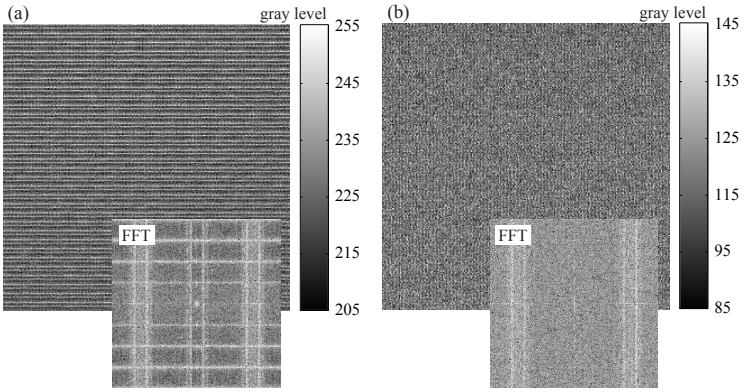

Fig. 7. Acquired frames (256x256 pixels) under homogenous illumination for extremes configurations of the CCD: (a) high gain (25dB) with short acquisition time (5µs) and (b) no gain with a long acquisition time (670 µs). For each frame, its Fourier transform is also displayed in inset.

4.2 Illustration of shot noise on living neurons phase images

In a last step, to illustrate the influence of shot noise on the phase accuracy through a practical example, we have chosen to observe 7-days old living mouse neurons in culture. The optimal case with a mean of 8'000 photons per pixel on the hologram is studied, jointly with the cases of 500 and 1'500 mean photons per pixel. Figure 8 shows the quantitative phase image of neuronal cells with their dendrites network. As depicted on the Fig. 8, the phase contrast on the cellular bodies is around 120° above the surrounding signal. It can be seen on the phase images of Fig. 8, that the signal-to-noise ratio on the cellular bodies is largely sufficient to ensure a good quality image contrast. On the other hand, as can be seen on Fig. 8, the phase signal on the neuronal network is much weaker (10 to 20 degrees). At this signal level, dynamic cell measurements as performed for example in Ref. [14], where cells morphology is investigated, or Ref. 29, where cell membranes fluctuation is studied, may become difficult in the presence of important phase fluctuations due to shot noise and would require spatial and/or temporal averaging to obtain a reliable signal, losing respectively spatial and/or temporal resolution. A comparison between Figs. 8(a), 8(b) and 8(c) allow to appreciate the reduction of the phase fluctuation caused by the shot noise in the case of incorrect versus correct imaging conditions. The cases with 500 and 1'500 mean photons per pixel have been displayed to show how the image degrade, when compared to the standard case of 8'000

#82596 - $15.00 USD Received 1 May 2007; revised 22 Jun 2007; accepted 22 Jun 2007; published 28 Jun 2007

photons, corresponding in our experimental setup to the largest integration time possible before CCD saturation, and therefore to the smallest fluctuations in single-shot phase imaging. The movie accessible from Fig. 8 presents the fluctuating noise during 50 phase images for both correct and incorrect integration time set on the CCD (parts of the phase images have been displayed on a 2x-reduced range to enhance the phase fluctuations). The results established in this work with simulations yield simple look-up tables to set the hologram acquisition parameters properly, or the number of reconstructed phase images used for averaging, to reach the targeted shot noise-limited phase accuracy in DHM required for a particular experiment.

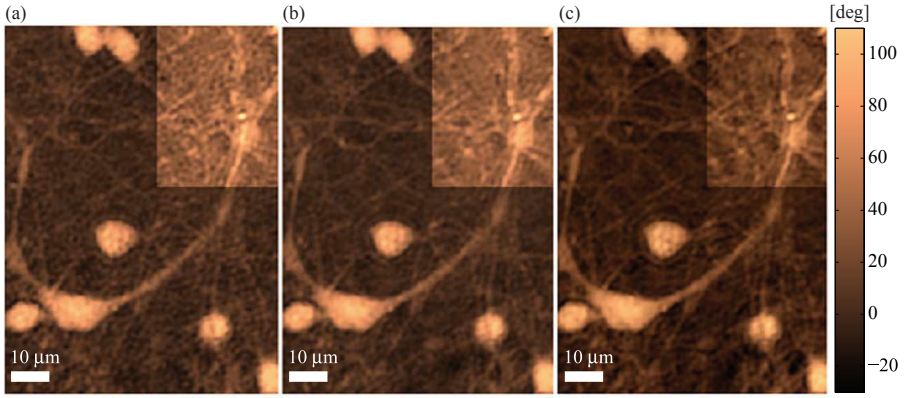

Fig. 8. Phase images (260x340 pixels) of 7-days old mouse neurons in culture, with a mean number of photons of 500 (a), 1'500 (b) and 8'000 (c): insets in images have been displayed on a 2x-reduced phase range to appreciate the reduction of the phase fluctuation caused by the shot noise in the case of non-optimal vs optimal imaging conditions. Movie [2.4Mb] presenting the fluctuating noise in (a), (b) and (c) along 50 phase images.

5. Conclusion

For the first time to our knowledge, a systematic study of the influence of shot noise on phase accuracy in DHM has been conducted. First, simulations have been used to predict the fundamental limitation due to shot noise in the case of an ideal hologram and detector. Standard deviation over the phase images as a function of the mean number of photons per pixel forming the CCD-recorded hologram have been presented, allowing one to directly estimate the phase accuracy for a DHM in an given configuration (irradiance of the source, integration time and gain of the CCD). For example, with an average number of photons of 8'000 (CCD with a 16ke$^-$ full well capacity with optimally sampled hologram), a shot noise-limited accuracy of 0.25° (λ/1'440) in the reconstructed phase images is obtained. An example has been given showing, that diminishing the integration time while keeping the same illumination level and increasing the gain to adapt the signal dynamic, a mean number of photons of 100 already deteriorates the phase accuracy by more than a factor 2, emphasizing the importance of a good comprehension of the shot noise influence on phase image accuracy, and the definition of proper imaging conditions. In a second time, the temporal averaging of a series of holograms has been studied. Practically, the expected $N^{-1/2}$ tendency, where N is the number of holograms, is observed for the STD phase value, allowing to simply reducing the effect of the shot noise as far as the desired phase accuracy is obtained. It has been showed that in the case of 8'000 mean photons per pixel, an averaging on 10 images provides a STD of 0.08° (λ/4'500), and an averaging on 100 images allows reaching a phase STD of 0.03° (λ/12'000) (averaging lasts resp. 0.67 sec and 6.67 sec at a rate of 15 frames per second). Thirdly, experimental validation of the simulations has been done with an actual DHM transmission setup, by presenting noticeably movies of the phase fluctuations

#82596 - $15.00 USD Received 1 May 2007; revised 22 Jun 2007; accepted 22 Jun 2007; published 28 Jun 2007

induced by shot noise on mouse neuronal cells phase images. The experimental data have revealed the presence of two additional noises when compared to the simulations: for intensities lower than 1000 photons per pixel the phase accuracy is limited by the readout noise of the CCD, while for higher intensities the phase accuracy is limited by a stable phase pattern caused by the imperfections in the optical arrangement of the setup. Evidences have been presented that the readout noise of the CCD cannot be simulated easily, because it is not homogenous but spatially structured due to the electronic architecture of the CCD. This could motivate a future study dedicated to this structural noise. After subtraction from the reconstructed phase images of the stable phase pattern, the measured phase accuracy for high intensities is in good agreement with the simulations.

Acknowledgments

This work has been supported by the Swiss National Science Foundation (grant n° 205320-112195/1). The authors also would like to thank the people at Lyncée Tec SA (www.lynceetec.com), PSE-A, CH-1015 Lausanne, for their dynamism and the fructuous discussions during the paper preparation.

#82596 - $15.00 USD Received 1 May 2007; revised 22 Jun 2007; accepted 22 Jun 2007; published 28 Jun 2007

Chapter 5

DHM-based optical diffraction tomography

5.1 Cell refractive index tomography by digital holographic microscopy

Paper published in Optics Letters **31**, 178-180 (2006).

178 OPTICS LETTERS / Vol. 31, No. 2 / January 15, 2006

Cell refractive index tomography by digital holographic microscopy

Florian Charrière, Anca Marian, Frédéric Montfort, Jonas Kuehn, and Tristan Colomb

Ecole Polytechnique Fédérale de Lausanne (EPFL), Imaging and Applied Optics Institute, CH-1015 Lausanne, Switzerland

Etienne Cuche

Lyncée Tec SA, PSE-A, CH-1005 Lausanne, Switzerland

Pierre Marquet

Centre de Neurosciences Psychiatriques, Département de Psychiatrie DP-CHUV, Site de Cery, CH-1008 Prilly-Lausanne, Switzerland

Christian Depeursinge

Ecole Polytechnique Fédérale de Lausanne (EPFL), Imaging and Applied Optics Institute, CH-1015 Lausanne, Switzerland

Received September 12, 2005; accepted October 12, 2005

For what we believe to be the first time, digital holographic microscopy is applied to perform optical diffraction tomography of a pollen grain. Transmission phase images with nanometric axial accuracy are numerically reconstructed from holograms acquired for different orientations of the rotating sample; then the three-dimensional refractive index spatial distribution is computed by inverse radon transform. A precision of 0.01 for the refractive index estimation and a spatial resolution in the micrometer range are demonstrated.

OCIS codes: 090.0090, 090.1760, 110.6880, 110.6960.

Digital holographic microscopy (DHM) provides quantitative measurement of the optical path length (OPL) distribution that allows semitransparent samples, such as living cells, to be described with a diffraction-limited transverse resolution and a subwavelength axial accuracy.[1] However, single images as presented in Ref. 1 reveal not the three-dimensional (3D) internal distribution of cellular components but a phase shift resulting from a mean refractive index (RI) accumulated over the cellular thickness. We show here that standard optical diffraction tomography (ODT) techniques can be efficiently applied to reveal internal structures and to measure 3D RI spatial distributions. Pioneer studies[2,3] have established the theoretical basis of reconstructing the 3D scattering potential of weakly scattering objects by recording the waves scattered from the different directions of parallel illumination. Different techniques have been applied to retrieve the complex waves diffracted by the object, mainly based on phase shifting interferometry[4] (PSI) or on phase retrieval algorithms.[5] The illumination direction can be varied by changing the direction of the beam itself[4] or by changing the orientation of the specimen relative to a fixed illumination beam.[5] The experimental setup used in the present Letter involves a fixed illumination beam and a rotating sample. The main advantages of DHM for complex diffracted wave retrieval is that only a single hologram is needed for each orientation of the specimen instead of at least three images for PSI, reducing the acquisition time and the stability requirements for the system. The biological specimen observed is a yew pollen grain (30 μm diameter), having a 3D-structured nucleus, which makes it an ideal test specimen for the method.

Transmission DHM (Fig. 1) used for the present Letter is described in detail in Ref. 6. Results presented here have been obtained with a 63×0.85 NA

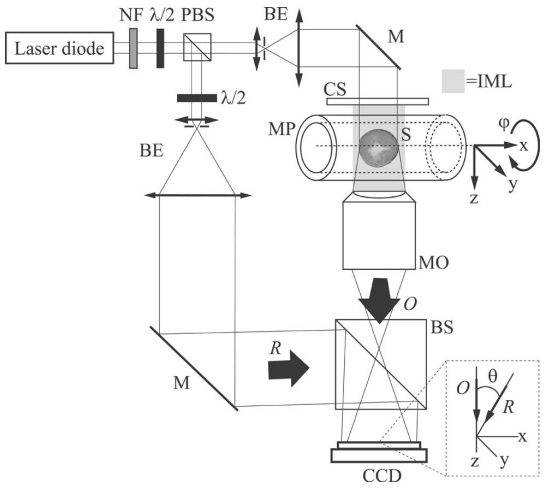

Fig. 1. Holographic microscope for transmission imaging: NF, neutral-density filter; PBS, polarizing beam splitter; BE, beam expander with spatial filter; λ/2, half-wave plate; MO, microscope objective; M, mirror; BS, beam splitter; *O*, object wave; *R*, reference wave; MP, micropipette; S, specimen; IML, index matching liquid. Inset: detail showing the off-axis geometry at the incidence on the CCD.

0146-9592/06/020178-3/$15.00

January 15, 2006 / Vol. 31, No. 2 / OPTICS LETTERS 179

microscope objective (MO). The light source is a laser diode at 635 nm. The camera is a 512×512 pixels, 8 bit, black and white CCD, with square pixels of 6.7 μm, and a maximal frame rate up to 25 Hz. The field of view is 80 μm$\times$80 μm. The transverse resolution (around 1 μm) and the transverse scale calibration are determined with a U.S. Air Force 1951 resolution test target. The pollen cells are in a glass micropipette (MP) filled with a glycerol solution to prevent drying. The MP has an internal diameter of 100 μm, an external diameter of 510 μm, and is fixed on a motorized rotating stage mounted on a micrometric *xyz* stage used to center the pollen cell in the field of view. A second *xy* stage mounted on the rotating stage itself allows for centering the pollen cell under investigation on the rotation axis, to minimize lateral displacements of the specimen in the field of view during the rotation. The rotation of the stage and the acquisition of the holograms are controlled with a personal computer (PC). To minimize strong light refraction by the MP, which acts like a cylindrical lens with regard to the illuminating light, the volume between a glass coverslip and the MO is filled with an index matching fluid suppressing the air–glass interface. The refraction at the MP–glycerol interface is minimal and can be corrected by numerical adjustment of the reconstruction parameters.[6]

Measurements presented here have been achieved without any particular vibration-insulating system; the off-axis configuration enables us to record all necessary information with a single image acquisition of very short exposure time (down to 20 μs with our CCD), leading to a high measurement stability. With a 2.8 GHz Pentium 4, the phase reconstruction rate, described in the next paragraph, is 15 frames/s. The hologram processing, in particular the phase retrieval, is properly described in detail in Ref. 6.

In the case of a weakly diffracting object such as a single biological cell, the OPL of the collimated illuminating photons across the specimen is parallel to the optical axis.[7] The planar phase distribution $\varphi(x,y)$ provided by DHM is directly proportional to this OPL. In our experimental setup, the rotation axis is parallel to the x axis, while the optical axis is the z axis. $\varphi(x,y)$ can then be expressed as $\varphi(x,y)=\int(2\pi/\lambda)\Delta n(x,y,z)\mathrm{d}z$, where λ is the wavelength of the light source and $\Delta n(x,y,z)$ is the 3D RI spatial distribution difference between the pollen cell and its surrounding medium. $\varphi(x,y)$ is thus only proportional to the integration of $\Delta n(x,y,z)$ along the z axis. To proceed to a standard tomographic reconstruction, one must record such two-dimensional (2D) planar phase distribution for different sample orientations covering an angle of 180°. In our study, 90 images were acquired with a 2° step at a rate of 1 Hz. The representation of the data as a function of the angle is known as a sinogram. The 3D signal $\Delta n(x,y,z)$ can be reconstructed from the sinograms by a filtered backprojection algorithm (see, for example, Ref. 8). For this purpose, the standard inverse radon transform *iradon* from the MATLAB programming environment was used in a slice-by-slice implementation. The use of the filtered backprojection algorithm instead of the backpropagation[9] algorithm usually recommended in ODT is consistent with the assumption of a phase proportional to the OPL across the specimen. The maximal spatial resolution of $\Delta n(x,y,z)$ depends on the sampling step used to cover the 180° during the rotation of the specimen and on the spatial resolution of $\varphi(x,y)$. The 2° step used in this study is sufficient for the maximal spatial resolution to be reached.

The reconstruction is summarized in Fig. 2. Figure 2(1) illustrates a cut in the 3D function $\Delta n(x,y,z)$ along the xy plane in the middle of the pollen cell, while Figs. 2(2) and 2(3) show cuts at different positions in the cell along the yz plane and the xz plane, respectively. In this figure, one can appreciate the 3D structure of the nucleus of the pollen grain. Knowing that the RI of the glycerol surrounding the pollen is 1.473, a $\Delta n=0.06\pm0.01$ is measured in the nucleus, leading to a measured value of 1.53. The RI of the pollen wall, around 1 μm thick, is not clearly measurable in the present study. The pollen cells possess a resistant wall layer or exine outside the usual cell wall, which is chemically resistant to minimize damage and prevent drying of the cell. The exine is composed of a group of substances called sporopollenins, which include polymers of monocarboxylic or dicarboxylic fatty acids of high molecular weight organized in a complex structure. The internal cell wall, or intine, is formed by cellulose, pectic substances, callose, and other polysaccharides. The presence of these components involves an important RI value, all of them having a RI above 1.50, and therefore an abrupt phase shift $\Delta\varphi$ between the glycerol and the cell wall. Our hypothesis of a weakly diffracting ob-

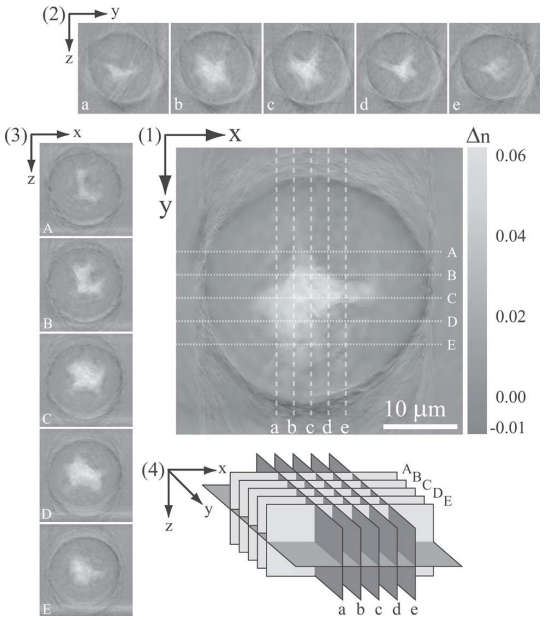

Fig. 2. Tomography of a pollen cell RI: (1) cut along the xy plane in the middle of the pollen cell (2), cuts at different positions in the cell along the yz plane, and (3) the xz plane, and (4) schematic of the presented cuts.

180 OPTICS LETTERS / Vol. 31, No. 2 / January 15, 2006

ject might not be entirely fulfilled with this important RI change in the pollen wall, but as it is very localized (around 1 μm), this assumption remains at least perfectly valid for the rest of the pollen grain. Furthermore, as the wall thickness is comparable to the lateral resolution of the system, difficulties appear during the unwrapping procedure involved in the reconstruction process to avoid 2π jumps in the phase signal, leading to some discrepancies in the phase measurement from one image to another for this critical part of the cell. An increase of the lateral resolution of the system or an adaptation of the embedding medium RI should improve the reliability of the reconstructed phase images. Second, the rotation system induces small movements (in the few micrometers range). Even if a numerical procedure based on the center of mass determination was used to recenter the cell on its rotation axis, the accuracy of this procedure was also limited to about 1 μm, making the tomographic reconstruction of this around 1 μm thick wall difficult. The slowly varying RI of the 12 μm nucleus is not affected by the two artifacts described previously.

Recently a comparative method between height measurement with confocal microscopy and OPL determination with a phase-sensitive technique[10] has shown an accuracy of 0.004 in the measurement of the integrated RI through a muscle cell, but it requires the use of two different setups and therefore specimen manipulation. This kind of approach is not able to separate the RI of the different cell constituents, as it only measures an integrated value. The tomography presented here of course overcomes this drawback and provides 3D RI distributions.

The knowledge of the 3D RI spatial distribution of a cell leads to invaluable information concerning the distribution and the optical properties of the intracellular organelles. In spite of this major issue, ODT applied successfully to cell imaging has, to our knowledge, not provided quantitative results until today.[4,11] Reliable RI values are difficult to obtain from the literature as different measuring techniques were applied to different type of cells. A good review of the available techniques and RIs in the literature can be found in Ref. 12. Most of the presented techniques are designed to evaluate the RI of a specific cell component (membrane, nucleus, cytoplasm, etc.), and in this sense the method we propose is more general, as it furnishes a complete 3D distribution of the RI in the cell. In this review the values of the RI for the different components of the cell are given with 0.01 accuracy, making our setup already competitive with other available methods. Furthermore, ODT of optical fibers based on the same specimen rotation principle presented here has already shown RI measurements with an accuracy of 0.001.[5] In spite of the accurate results obtained with optical fibers, this technique has, to our knowledge, never been applied to biological specimens. With a specifically designed mechanical system avoiding any movement, or an appropriate recentering numerical procedure, ODT based on DHM should aim for the same precision in the RI measurement, thanks to the nanometric sensitivity in the phase determination.

In conclusion, we have shown for the first time, to our knowledge, the 3D distribution of the RI of a semitransparent object, in our case a pollen grain, provided by backprojecting OPL values collected with DHM on a series of projections of the preparation taken at various incidence angles. The accuracy of the RI determination is better than 0.01 and the 3D spatial resolution is better than 1 μm in all three dimensions. This approach could find interesting application as a reference measuring technique in material and life sciences.

This research has been supported by the Swiss National Science Foundation (SNSF) Grant 205320-103885/1. The authors thank Benoît Gerber for his participation in the work. F. Charrière's e-mail address is florian.charriere@epfl.ch.

References

1. P. Marquet, B. Rappaz, P. J. Magistretti, E. Cuche, Y. Emery, T. Colomb, and C. Depeursinge, Opt. Lett. **30**, 468 (2005).
2. E. Wolf, Opt. Commun. **1**, 153 (1969).
3. R. Dändliker and K. Weiss, Opt. Commun. **1**, 323 (1970).
4. V. Lauer, J. Microsc. **205**, 165 (2002).
5. A. Barty, K. A. Nugent, D. Paganin, and A. Roberts, Opt. Commun. **175**, 329 (2000).
6. T. Colomb, E. Cuche, F. Charrière, J. Kühn, N. Aspert, F. Montfort, P. Marquet, and C. Depeursinge, "Automatic procedure for aberrations compensation in digital holographic microscopy and applications to specimen shape compensation," Appl. Opt. (to be published).
7. P. Marquet, M.D./Ph.D. dissertation (UNI-Lausanne, 2003), Chap. 5.
8. A. C. Kak and M. Slaney, *Principles of Computerized Tomographic Imaging* (Society for Industrial and Applied Mathematics, 2001), chap. 3.
9. T. C. Wedberg, J. J. Stamnes, and W. Singer, Appl. Opt. **34**, 6575 (1995).
10. C. L. Curl, C. J. Bellair, T. Harris, B. E. Allman, P. J. Harris, A. G. Stewart, A. Roberts, K. A. Nugent, and L. M. D. Delbridge, Cytometry Part A **65**, 88 (2005).
11. T. Noda, S. Kawata, and S. Minami, Appl. Opt. **31**, 670 (1992).
12. A. Dunn, "Light scattering properties of cells," Ph.D. dissertation (University of Texas, Austin, 1997), chap. 1.

5.2 Living specimen tomography by digital holographic microscopy: morphometry of testate amoeba

Paper published in Optics Express **14**, 7005-7013 (2006).

Living specimen tomography by digital holographic microscopy: morphometry of testate amoeba

Florian Charrière, Nicolas Pavillon, Tristan Colomb and Christian Depeursinge

Ecole Polytechnique Fédérale de Lausanne (EPFL), Imaging and Applied Optics Institute, CH-1015 Lausanne, Switzerland
florian.charriere@a3.epfl.ch

http://apl.epfl.ch/page12232.html

Thierry J. Heger[a,b] and Edward A.D. Mitchell[a,b]

[a]*Swiss Federal Research Institute WSL, CH-1015 Lausanne, Switzerland.*
[b]*Ecole Polytechnique Fédérale de Lausanne (EPFL), Laboratory of Ecological Systems, CH-1015 Lausanne, Switzerland.*

http://ecos.epfl.ch/

Pierre Marquet

Centre de Neurosciences Psychiatriques, Département de psychiatrie DP-CHUV, Site de Cery, CH-1008 Prilly-Lausanne, Switzerland

Benjamin Rappaz

Ecole Polytechnique Fédérale de Lausanne (EPFL), Brain Mind Institute, CH-1015 Lausanne, Switzerland

Abstract: This paper presents an optical diffraction tomography technique based on digital holographic microscopy. Quantitative 2-dimensional phase images are acquired for regularly-spaced angular positions of the specimen covering a total angle of π, allowing to built 3-dimensional quantitative refractive index distributions by an inverse Radon transform. A 20x magnification allows a resolution better than 3 μm in all three dimensions, with accuracy better than 0.01 for the refractive index measurements. This technique is for the first time to our knowledge applied to living specimen (testate amoeba, Protista). Morphometric measurements are extracted from the tomographic reconstructions, showing that the commonly used method for testate amoeba biovolume evaluation leads to systematic under evaluations by about 50%.

OCIS codes: (090.1760) Computer holography; (110.6880) Three-dimensional image acquisition; (110.6960) Tomography; (170.6900) Three-dimensional microscopy.

References and links

1. A. Dunn, Light scattering properties of cells, PhD Diss., Univ. of Texas, Austin, 1997.
2. J. Bereiter-Hahn, Cecil H. Fox and BO Thorell, "Quantitative reflection contrast microscopy of living cells," J. Cell Biol. **82**, 767-779 (1979).
3. C. L. Curl, C. J. Bellair, T. Harris, B. E. Allman, P. J. Harris, A. G. Stewart, A. Roberts, K. A. Nugent and L. M. D. Delbridge, "Refractive index measurement in viable cells using quantitative phase-amplitude microscopy and confocal microscopy," Cyt. A **65**, 88 (2005).
4. B. Rappaz, P. Marquet, E. Cuche, Y. Emery, C. Depeursinge, and P. Magistretti, "Measurement of the integral refractive index and dynamic cell morphometry of living cells with digital holographic microscopy," Opt. Express **13**, 9361-9373 (2005).

#71852 - $15.00 USD Received 9 June 2006; revised 20 July 2006; accepted 24 July 2006

5. E. Wolf, "Three-dimensional structure determination of semi-transparent object from holographic data," Opt. Commun. **1**, 153–156 (1969).
6. R. Dändliker, K. Weiss, "Reconstruction of three-dimensional refractive index from scattered waves," Opt. Commun. **1**, 323–328 (1970).
7. V. Lauer, "New approach to optical diffraction tomography yielding a vector equation of diffraction tomography and a novel tomographic microscope," J. Microsc. **205**, 165–176 (2002).
8. G. N. Vishnyakov, G. G. Levin, "Optical microtomography of phase objects, " Opt. Spectrosc. **85**, 73-77 (1998).
9. G. N. Vishnyakov, G. G. Levin, A. V. Likhachev, V. V. Pikalov, "Phase Tomography of 3D Biological Microobjects: Numerical Simulation and Experimental Results," Opt. Spectrosc. **87**, 413-419 (1999).
10. A. Barty, K.A. Nugent, A. Roberts, D. Paganin, "Quantitative phase tomography," Opt. Commun. **175**, 329-336 (2000).
11. T. Noda, S. Kawata and S. Minami, "Three-dimensional phase-contrast imaging by a computed-tomography microscope", Appl. Opt. **31**, 670-674 (1992).
12. F. Charrière, F. Montfort, J. Kühn, T. Colomb, A. Marian, E. Cuche, P. Marquet, and Ch. Depeursinge, "Cell refractive index tomography by digital holographic microscopy," Opt. Lett. **31**, 178-180 (2006).
13. E. A. D. Mitchell, A. Buttler, B. Warner and J.-M. Gobat, "Ecology of testate amoebae (Protozoa: Rhizopoda) in *Sphagnum*-dominated peatlands in the Jura Mountains, Switzerland and France," Ecoscience **6**, 565-576 (1999).
14. E. A. D. Mitchell, D. J. Charman and B. G. Warner, "Testate amoebae analysis in ecological and paleoecological studies of wetlands: past, present and future," Biodivers. Conserv. (to be published).
15. H. Nguyen-Viet, N. Bernard, E. A. D. Mitchell, J. Cortet, P. M. Badot and D. Gilbert, "Relationship between testate amoebae and atmospheric heavy metals (Pb, Cd, Zn, Ni, Cu, Mn and Fe) accumulated in the moss *Barbula indica* Hanoi, Vietnam," Microbial Ecol. (to be published).
16. R. E. Madrid and C. J. Felice, "Microbial biomass estimation," Crit. Rev. Biotechnol., **25**, 97-112 (2005).
17. D. Gilbert, C. Amblard, G. Bourdier and A.-J. Francez, "The microbial loop at the surface of a peatland: Structure, function, and impact of nutrient input," Microbial Ecol. **35**, 83-93 (1998).
18. E. A. D. Mitchell, D. Gilbert, A. Buttler, P. Grosvernier, C. Amblard and J.-M. Gobat, "Structure of microbial communities in *Sphagnum* peatlands and effect of atmospheric carbon dioxide enrichment," Microbial Ecol. **16**, 187-199 (2003).
19. E. Cuche, P. Marquet, and C. Depeursinge, "Simultaneous amplitude-contrast and quantitative phase-contrast microscopy by numerical reconstruction of Fresnel off-axis holograms," Appl. Opt. **38**, 6994-7001 (1999).
20. T. Colomb, E. Cuche, F. Charrière, J. Kühn, N. Aspert, F. Montfort, P. Marquet, and Ch. Depeursinge, "Automatic procedure for aberration compensation in digital holographic microscopy and applications to specimen shape compensation," Appl. Opt. **45**, 851-863 (2006).
21. F. Charrière, E. Cuche, P. Marquet, C. Depeursinge, "Biological cell (pollen grain) refractive index tomography with digital holographic microscopy." in *Three-Dimensional and Multidimensional Microscopy: Image Acquisition and Processing XIII*, J.-A. Conchello, C.J. Cogswell, T. Wilson, eds., Proc. SPIE **6090**, 22-29 (2006).
22. P. Marquet, B. Rappaz, P. J. Magistretti, E. Cuche, Y. Emery, T. Colomb and C. Depeursinge, "Digital holographic microscopy: a noninvasive contrast imaging technique allowing quantitative visualization of living cells with subwavelength axial accuracy," Opt. Lett. **30**, 468-470 (2005).
23. P. Marquet, "Développement d'une nouvelle technique de microscopie optique tridimensionnelle, la microscopie holographique digitale. Perspective pour l'étude le la plasticité neuronale," MD-PhD Thesis Dissertation (Chapt. 5), UNI-Lausanne, 2003.
24. A. C. Kak and M. Slaney. Principles of Computerized Tomographic Imaging. Soc. of Ind. and Appl. Math. SIAM, 2001.
25. T. C. Wedberg, J. J. Stamnes and W. Singer, "Experimental examination of the quantitative imaging properties of optical diffraction tomography," J. Opt. Soc. Am. A **12**, 493-500 (1995).
26. W. Singer, T. C. Wedberg, and J. J. Stamnes, "Comparison of the filtered backpropagation and the filtered backprojection algorithms for quantitative tomography," Appl. Opt. **34**, 6575-6581 (1995).
27. E. A. Paul and F. E. Clark, Soil microbiology and biochemistry, (Second Edition, Academic Press, San Diego, CA. 1996).
28. M. Bölter, J. Bloem, K. Meiners and R. Möller, "Enumeration and biovolume determination of microbial cells - a methodological review and recommendations for applications in ecological research," Biol. Fert. Soils **36**, 249-259 (2002).
29. Dr. Enrique Lara, Swiss Federal Research Institute WSL and Laboratory of Ecological Systems, Ecole Polytechnique Fédérale de Lausanne (EPFL), CH-1015 Lausanne, Switzerland. (personnal communication, 2006).

#71852 - $15.00 USD Received 9 June 2006; revised 20 July 2006; accepted 24 July 2006

1. Introduction

Optical microscopy techniques nowadays offer non-contact, high-resolution and real-time cell imaging facilities. Though, the knowledge of the optical properties of the intracellular organelles is deemed to bring valuable information about cells morphology, cellular internal processes or organelles spatial distribution. A good review of the available techniques and refractive indices in the literature can be found in Ref. 1. Besides the techniques quoted in Ref. 1, different approaches developed to measure the refractive index (RI) of cells should be mentioned. Bereiter-Hahn *et al.* have studied the refractive index variation at the surface of mammalian cells in culture with quantitative reflection contrast microscopy.[2] More recently, Curl *et al.* have compared height measurement achieved with a confocal microscope and optical path length (OPL) measurements with a phase-sensitive technique to deduce the integrated RI through a muscle cell.[3] *Rappaz et al.* have followed dynamically the integrated RI through neuronal cells during a hypotonic stress, comparing absolute phase measurements obtained with digital holographic microscopy for two different perfusion solutions.[4] However, these last two approaches allow to measure the 2D planar distribution of the RI integrated along the optical axis, making the visualization of individual intracellular organelles difficult.

A well-suited technique to address this particular problematic of measuring the 3-dimentionnal (3D) refractive index distribution of a cell, is the so-called optical diffraction tomography (ODT), which theoretical bases have been developed by Wolf[5] and Dändliker[6] in the early seventies. ODT allows, by recording the complex wavefront diffracted by a transparent or semi-transparent object under varying illumination angles, to reconstruct its 3D scattering potential. Lauer used for example phase-shifting interferometry (PSI) to record the Fourier spectrum of the diffracted wavefront, varying the illumination direction by changing the direction of the beam itself.[7] Vishnyakov and Levin combined PSI with a Linnik interferometer also allowing multiple angles illumination.[8-9] Barty *et al.* developed a phase-retrieval algorithm, based on 3 intensity measurements performed on different focus planes, combined with a rotation of the specimen relatively to a fixed illumination beam.[8] There are really few successful applications of ODT techniques to living specimen imaging, mainly due to the difficulty of measuring accurately the complex diffracted wavefront: Lauer used his tomographic microscope to observe bacteria and yeasts,[7] Noda *et al.* investigated green mold (*Aspergillus oryzae*),[9] and Vishnyakov and Levin observed human red blood cells and lymphocites.[8-9] Note that quantitative RI data are found only in Refs. 8-9.

In a recent paper,[12] we have shown for the first time to our knowledge the quantitative 3D distribution of RI of a semi-transparent object, in our case a pollen grain, provided by backprojecting OPL values collected with digital holographic microscopy (DHM) on a series of projections of the preparation taken at various incidence angles. The accuracy of the RI determination was better than 0.01, and the 3D spatial resolution better than 1 μm in all 3D. Furthermore, DHM reconstructs the complex diffracted wavefront from a single hologram for each orientation of the specimen, while at least 3 images are required for PSI, reducing this way the acquisition time and the stability requirements for the system.

In the present paper, the system described in Ref. 12 has been further developed, to allow the first investigation of living biological specimens, thanks to a specifically designed observation chamber. The reconstructed 3D RI distributions, revealing intracellular structures, have permitted to accurately measure the volume of the specimen. The biological specimen observed, presented in Fig. 1, is a testate (or shelled) amoeba ("protozoa", more specifically a protist belonging to the Amoebozoa), *Hyalosphenia papilio*, with a shell approximately 130 μm long, 70 μm wide and 35 μm deep.

This species is commonly found in nutrient-poor peatlands, and the specimens presented in this work were collected in moss (*Sphagnum*) from Praz-Rodet Bog, Canton Vaud, Switzerland (46°33' N, 06°10' E). It is one of the few protozoa to house endosymbiotic algae, visible as small green spheres in Fig. 1(a), and hence its metabolism is referred to as mixotrophy, i.e. combing auto- and heterotrophy). Because of this interesting metabolism, its commonness in peatlands, and its characteristic morphology making it easily identifiable, it

#71852 - $15.00 USD Received 9 June 2006; revised 20 July 2006; accepted 24 July 2006

may represent a good candidate as a model organism for studies in population ecology or ecotoxicology.[13] Beyond the interest for a specific species, testate amoebae are increasingly used in community ecology with applications in the reconstruction of past climates (paleoecology),[14] the monitoring of pollution[15] or environmental changes. In many of these applications it is important to have precise estimates of cell volume. This allows the calculation of the biomass with the help of an appropriate conversion factor.[16] The biovolume is usually achieved using simple measurements and assuming geometrical shapes, but it is unclear if these correspond very well to the reality.[17-18] A much better approach would be to quantify exactly the volume and to determine how this compares to some easily measurable variable such as the length or width. If a clear correlation can be established in such as way for a number of specimens of each species, or morphological type for closely-related species, this data can then be used to derive allometric relationships that can be used in a standard way forever. Another interesting aspect is the presence of endosymbiotic algae. These may also respond to changes in the environment indirectly through the amoeba itself or directly if some contaminant enters the amoeba cell without affecting it directly. It would therefore be interesting to be able to quantify the number of algal cells and their individual volumes. This is clearly not possible using light microscopy, as in Fig. 1(a), but may be possible using holographic tomography.

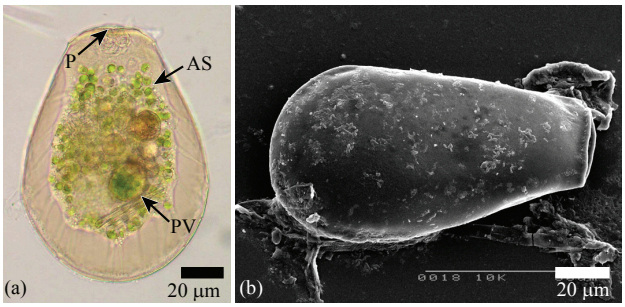

Fig. 1. Images of the testate amoebae *Hyalosphenia papilio*: (a) bright-field microscope image illustrating the amoeba itself and its content, P pseudostome (opening through which the amoeba pseudopods emerge), AS algal symbionts, PV phagocytic vacuoles; (b) SEM image illustrating the shell.

2. Experimental setup

Transmission off-axis DHM (Fig. 2) used for the present study is described in details in Refs. 19 and 20. It is based on a Mach-Zehnder configuration. Half-wave plates and neutral filters are used in conjunction with a polarizing beam splitter to control the light intensity in the two arms of the interferometer. The light source is a polarized laser diode emitting at 635 nm. Results presented here have been obtained with an Olympus 20X 0.4 NA microscope objective (MO). A field lens is inserted in the reference arm in order to obtain a coarse compensation of the phase curvature induced by the MO into the object wave, while the fine tuning compensation is numerically achieved during the hologram reconstruction process, as extensively described in Ref. 14. The camera is a 512 x 512 pixels, 8 bit, black and white CCD, with square pixels of 6.7 µm, and a maximal frame rate up to 25Hz. The field of view is 200 µm x 200 µm. The transverse resolution (around 1.5 µm) as well as the transverse scale calibration have been determined with a USAF 1951 resolution test target. All measurements have been achieved without any particular vibrations-insulating system: since a single hologram is required to reconstruct the complex diffracted wavefront, this is performed in a short time (down to 20 µs with our CCD), leading to high measurement stability. With a Pentium 4 2.8Ghz, the phase reconstruction rate, described in the next paragraph, is 15 frames/second.

#71852 - $15.00 USD Received 9 June 2006; revised 20 July 2006; accepted 24 July 2006

In the present work, the specimen is observed in a specifically designed chamber, principally composed by two microscope coverslips orthogonal to the optical axis. An aluminum frame maintains the two coverslips 4 mm distant, while fixations assure the watetightness of the chamber. One lateral side of the chamber is free to allow the introduction of a micropipette (MP) used to manipulate the specimen, or to change the perfusion medium during observation.[4] The manipulation method is similar to the so-called patch-clamp technique, in which thin MPs are used to maintain contact with a specific part of cells, for example the plasma membrane. These MPs are produced by the elongation of glass tubes during a controlled heating process. Their extremities, with a diameter around 1 micrometer, may then be polished to ensure a good contact with the cell membrane. Here, the specimen may be manipulated (translated or rotated) by one of these MPs, by using a little vacuum to maintain contact between the glass and the testate. To ensure good manipulation and rotation stability, the MP used during the final measurement had extremities about 10 µm, instead of the standard ones. The MP is fixed on a motorized rotating stage, and its position is adjusted with a micrometric xy-stage to place accurately its extremity on the rotation axis, minimizing therefore displacements of the specimen during rotation. A first micrometric xyz-stage allows moving the MP relatively to the chamber, to grab a specific specimen or to drag a selected specimen in a clean area of the preparation for observation, while a second xyz-stage allows moving simultaneously the MP and the chamber for a proper positioning in the field of view. Note that the chamber can be inclined relatively to the optical axis to allow picking up the desired specimen, in case it is laying on the bottom of the chamber due to gravity.

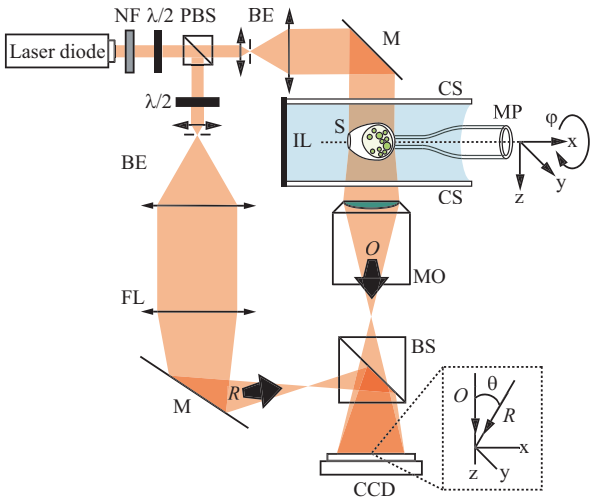

Fig. 2. Holographic microscope for transmission imaging: NF neutral density filter; PBS polarizing beam splitter; BE beam expander with spatial filter; λ/2 half-wave plate; MO microscope objective; FL field lens; M mirror; BS beam splitter; *O* object wave; *R* reference wave; MP micropipette; CS coverslip; S specimen; IL immersion liquid. Inset: a detail showing the off-axis geometry at the incidence on the CCD.

In a previous work,[12] the specimen were embedded in a MP with an internal diameter of 100 µm to allow their rotation in the system. Compared to this first approach, the patch-clamp technique used in this study presents two decisive improvements. Firstly, the MP is now out of the light path going through the specimen: in the previous setup, the MP was acting like a cylindrical lens, introducing astigmatism in the imaging system. Therefore, an index matching liquid was used to minimize this astigmatism, and a numerical procedure was additionally applied to compensate for the residual phase aberrations (see Refs. 20 and 21). Note that the

#71852 - $15.00 USD Received 9 June 2006; revised 20 July 2006; accepted 24 July 2006

index matching liquid used to compensate partially for the astigmatism needed to be carefully chosen and adapted to the used MP, what requested an additional calibration procedure, and also that the requested numerical procedure consisted potentially in an additional noise source when not conducted carefully. This first modification reduces drastically the complexity of the setup and increases therefore its ease of use. Secondly, the previous embedding technique was not applicable on living animal cells, because the perfusion of the cells within the MP was not possible. Furthermore, the current system is more versatile, allowing for facilitated specimen selection and manipulation, compared to the non-displaceable specimen embedded randomly in the MP.

Glycerol (n=1.473) is used here as immersion liquid, to minimize the number of the so-called 2π-jumps in the phase signal by minimizing the refractive index difference between the specimen and its surrounding medium, suppressing ambiguity during the unwrapping procedure involved in the reconstruction.[12] Note that the chamber is waterproof enough to also work with less viscous immersion media such as water or physiological solution.

3. Holograms processing and tomographic reconstruction

Digital holographic microscopy (DHM) provides quantitative measurement of the OPL distribution that enable to describe semi-transparent samples, such as living cells with a diffraction-limited transverse resolution and a sub-wavelength axial accuracy.[22] The hologram processing, to reconstruct the complex diffracted wavefront, is described in details in Refs. 19 and 20. Briefly, it consists in multiplying the hologram by a digital reference wave simulating an illumination wave, then a propagation calculation within the Fresnel approximation allows to reconstruct a focused image of the specimen in a plane of coordinates, where a digital phase correction is applied to compensate for the wave front curvature induced by the objective lens and other aberrations of the optical imaging system.

In DHM, the reconstructed phase distribution depends on both specimen thickness and specimen RI distribution.[22] If in first approximation the case of a weekly diffracting object is assumed, the optical path length of the collimated illuminating photons across the specimen is parallel to the optical axis. This assumption was found to be in very good agreement with the DHM data in the case of cellular imaging.[23] The reconstructed phase distribution is therefore directly proportional to this optical path length:

$$\varphi(x,y) = \int 2\pi/\lambda \, \Delta n(x,y,z)\, dz \,, \tag{1}$$

where z shows the optical axis direction, λ is the wavelength of the light source and $\Delta n(x, y, z)$ is the difference between the 3D specimen RI spatial distribution and the RI of the surrounding medium. Consequently, $\varphi(x,y)$ is only proportional to the projection of $\Delta n(x, y, z)$ along the z-axis.

To achieve the tomographic reconstruction, the specimen is rotated step by step in the system, covering a total angle of π. 180 equally spaced holograms were acquired at a rate of 0.5 Hz and individually reconstructed. The representation of the reconstructed phase data as a function of the angle is known as a sinogram. The 3D signal $\Delta n(x, y, z)$ can be reconstructed from the sinograms by a filtered backprojection algorithm (see for ex. Ref. 24). Instead of backpropagation[25] algorithm usually recommended in ODT, a backprojection is used consistently with the assumption of a phase proportional to the optical path length across the specimen. For this purpose, the standard inverse Radon transform was used and implemented slice-by-slice along the rotation axis. For further details about the validity of the employed tomographic technique, one should refer to Ref. 26, where it is shown that the so-called hybrid filtered backprojection equivalent to the reconstruction algorithm used in the present work, i.e. consisting in first a backpropagation in the Fresnel approximation of the measured wavefronts to the object plane followed by a backprojection algorithm, gives nearly equivalent results to the standard recommended backpropagation algorithm.

#71852 - $15.00 USD Received 9 June 2006; revised 20 July 2006; accepted 24 July 2006

4. Results and discussion

Tomographic reconstructions were performed on 5 different *Hyalosphenia papilio* during this study. Central cuts in the reconstructed 3D refractive index volumes for 4 different amoebae are presented on Fig. 3 and Fig. 4. On these images, the cellular body of the amoebae themselves insides their testate can be easily discriminated thanks to the large difference (>0.2) between the cell RI and the RI inside the testate.

One can note on these images that the refractive index inside the testate is lower compared to the surrounding medium. This is due to the fact that glycerol (n=1.473) was used as immersion liquid: the mix of some remaining water inside the testate with the surrounding glycerol explains this decrease of the refractive index value. Note that if the measurement was performed immediately after the immersion of the amoeba in the glycerol, the refractive index inside the test corresponded directly to water (n=1.33), while in the presented measurements, higher values are obtained, indicating clearly the presence of glycerol inside the test. The presence of glycerol around the cellular body may slightly change its volume, but no dramatic changes were noticed during cells preparation and observation.

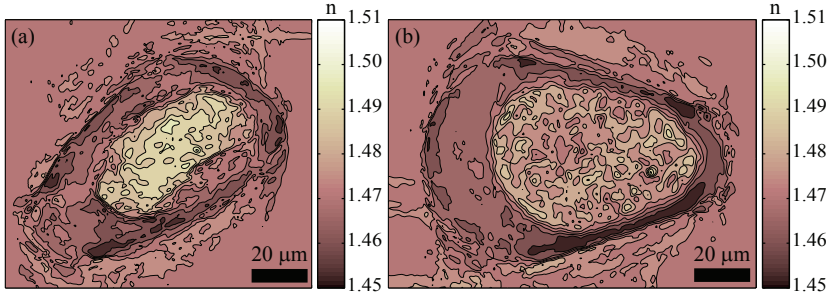

Fig. 3. Cuts in the tomographic reconstructions of 2 different *Hyalosphenia papilio*. Discrete values of the measured refractive index n are coded in false colors, the color-coding scales being displayed on the right part of each corresponding cut.

Morphometry measurements can be achieved on the tomographic reconstruction, to determine for example the biovolume of the amoebae. These volumes were evaluated by considering only the voxels with a refractive index value above an appropriate threshold. Note that the reconstructed volumes were first convoluted with a gaussian filter to minimize errors due to the reconstruction noise, and that the detected volumes distinct from the main cellular body were removed from counting.

The obtained results are presented in Table 1; the error ranges correspond to the optical resolution of the system. These volume measurements are compared in Table 1 with the estimation methods based on size measurements performed with light microscopy,[17-18] where such biovolumes estimations are calculated from the observed individuals using the formula for an ellipsoid:

$$V = \tfrac{4}{3}\pi \cdot w \cdot l \cdot d \cdot \tfrac{1}{8}, \qquad (2)$$

where w, l and d are respectively the width, the length and the depth of the amoeba, and 1/8 is a form factor.

The estimated errors on the volume estimation with Eq. (2) displayed in Table 1 correspond to an accuracy of 2 µm in the size measurements. DHM tomography clearly delivers the most precise estimations of the biovolumes, i.e. with the lowest standard error. This shows the advantage of taking into account the actual shape of the cellular body instead not an ellipsoid approximation, in which slightly errors in the dimension measurement lead to large variation in the volume estimation.

#71852 - $15.00 USD Received 9 June 2006; revised 20 July 2006; accepted 24 July 2006

Table 1. Estimated biovolumes for *Hyalosphenia papilio*.

	Biovolumes [μm^3]	
Testate amoeba	DHM tomography	Light microscopy
n°1: Fig. 3(a)	$6.54 \cdot 10^4 \pm 0.05 \cdot 10^4$	$2.8 \cdot 10^4 \pm 1.2 \cdot 10^4$
n°2: Fig. 3(b)	$7.36 \cdot 10^4 \pm 0.04 \cdot 10^4$	$3.7 \cdot 10^4 \pm 1.5 \cdot 10^4$
n°3: Fig. 4(a)	$6.54 \cdot 10^4 \pm 0.04 \cdot 10^4$	$4.9 \cdot 10^4 \pm 1.7 \cdot 10^4$
n°4: Fig. 4(b)	$8.09 \cdot 10^4 \pm 0.04 \cdot 10^4$	$3.2 \cdot 10^4 \pm 1.3 \cdot 10^4$
n°5: not presented	$3.94 \cdot 10^4 \pm 0.02 \cdot 10^4$	$2.5 \cdot 10^4 \pm 1.1 \cdot 10^4$
Means	$6.49 \cdot 10^4 \pm 0.04 \cdot 10^4$	$3.4 \cdot 10^4 \pm 1.3 \cdot 10^4$

The tomography also reveals that those volumes are under-estimated by nearly 50% with the actual standard method. This comparison illustrates the potential of DHM tomography for the precise and accurate estimation of biovolumes, which allows to determining biomasses. More generally, our results also show that in addition to the well-recognized problem of estimating the number of microorganisms in the environment,[27] more attention should be devoted to the estimation of the biovolume and biomass of individual species. A reliable estimate of biomass is crucial for understanding of the role of different microorganisms in the microbial food webs,[17,18,28] or the effect of environmental stress like organic pollutants or heavy metals on selected organisms in ecotoxicology.

At present, the whole reconstruction process involved in DHM tomography, including specimen manipulation, holograms acquisition/processing and tomographic reconstruction still requires too many operator interventions to calculate systematically the biovolumes of large amount of amoeba. However, as suggested above, this technique could help to derive allometric relationships that would greatly increase the precision of biovolumes and biomass estimates.

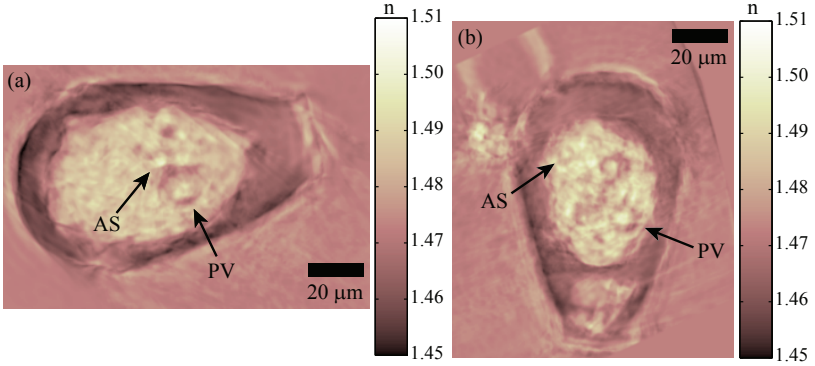

Fig. 4. Animations [1.3MB (a), 1.7MB (b)] through the tomographic reconstructions of two selected *Hyalosphenia papilio* presenting some clearly visible inner structures tentatively identified as algal symbionts (AS) and phagocytic vacuoles (PV). The gray-level scales of the measured refractive index n are displayed on the right part of each corresponding cut.

The actual resolution in the tomographic reconstruction is mainly limited because of mechanical instabilities. Theoretically, the optical resolution in all three dimensions for the tomographic reconstructions is about 1.5 µm, but an inaccurate centering of the MP on its rotation axis leads to a precession movement of the specimen during rotation that tends to derogate from the final tomography resolution. Therefore, during the reconstruction, a re-centering numerical procedure based on the MP edges detection in the phase images has been applied. Even if it is not currently possible to identify accurately all the symbiotic algae, with

#71852 - $15.00 USD Received 9 June 2006; revised 20 July 2006; accepted 24 July 2006

diameter around 3 µm,[29] and other organelles present in the amoeba cellular body, some of these organelles (principally the phagocytic vacuoles, but also some algal symbionts) are visible in the tomographic reconstructed volumes. Due to discrete color scale, it may be difficult to notice them in Fig. 3, but the continuous color scale make their spherical shape clearly visible, as shown in Fig. 4, especially in the linked movies presenting animations through the reconstructed volumes, in which they appear like spheres in the cellular body. This shows that potentially, the tomographic reconstructions could also be used to solve the problem of symbiotic algae counting and volume estimate inside the amoeba cellular body.

5. Conclusion

The present work illustrates that DHM tomography, with a resolution better than 3 µm, may successfully be applied to living specimen tomography. In comparison to a previous paper,[12] the presented technique, using a patch clamp micropipette to manipulate and rotate the specimen in a dedicated observation chamber, is much more flexible and opens wide perspectives in 3D cell imaging: the 3D quantitative refractive index distributions furnish invaluable data on the cell components optical properties, potentially leading to information about organelles intracellular distribution. Furthermore, it has been shown that morphometric measurements may be extracted from the tomographic data, by detecting for example the extension of the cellular body thanks to its specific refractive index contrast within the 3D reconstructions. The presented results shed new light on the biovolume estimation technique of testate amoeba, by stressing that the common biovolume measurement technique under-estimates systematically the actual values by 50%.

Acknowledgements

This work has been supported by the Swiss National Science Foundation (grant n° 205320-103885/1) and by EU project RECIPE (Reconciling Commercial Exploitation of Peat With Biodiversity in Peatlands Ecosystems). RECIPE is partly supported by the European Commission (n° EVK2-2002-00269) and partly, for the Swiss partners EPFL and WSL-AR, by the Swiss Federal Office for Education and Science (SER n° 01.0438-1).

The SEM image of Fig. 1(b) was kindly provided by Dr. Jerry Kudenov and Keiko Kishaba, University of Alaska, Anchorage.

The authors also would like to thank the people at Lyncée Tec SA (www.lynceetec.com), PSE-A, CH-1015 Lausanne, for their enthusiasm and their constructive comments during the paper preparation.

#71852 - $15.00 USD Received 9 June 2006; revised 20 July 2006; accepted 24 July 2006

5.3 Comments on DHM-based optical diffraction tomography

5.3.1 The origins

The idea of tomographic reconstructions based on quantitative phase measurements finds its origin in the early seventies: recording the complex wavefront diffracted by a transparent or semi-transparent object under varying illumination angles allowing to reconstruct its 3D scattering potential. The theoretical bases of the so-called optical diffraction tomography (ODT) have been developed by Wolf [Wol69] followed by Dändliker and Weiss [Dän70], and Carter and Ho were among the first to exploit those theory to reconstruct a 2D scattering potential from holograms [Car70b, Car74], followed by Fercher*et al.* for the 3D case [Fer79]. If the principle of ODT is quite simple, its experimental implementation remains a demanding task. To collect the waves diffracted by a specimen in different directions, one must basically rotate even the specimen or the imaging system. This movement must be accomplished accurately enough, to maximize the spatial resolution of the tomographic reconstruction. The technique used to measure the complex diffracted wavefronts must also guarantee an excellent accuracy, especially in phase, to ensure a precise evaluation of the scattering potential.

If nowadays computers and digital cameras deeply facilitate ODT implementation, from computer-controlled actuated mechanical systems to numerical reconstruction algorithms, pioneers works have been performed in the field much before the all-digital days. In the field of holographic interferometry, in which a double exposed hologram is recorded, firstly without any object, then in the presence of the object, Heflinger *et al.* mentioned in 1966 already, that if several parallel beams are used, each traversing the test region in a different direction, one would be able to select any of these directions and examine the resulting interferograms individually and compare them eventually [Hef66]. In the same paper illustrated with aerodynamic experiments (bullets shot in different gas), considerations about the system cylindrical geometry allow to deduce quantitative data in a way very similar to ODT, which inspired Rowley to formalize further the approach analytically [Row69]. A system comprising three holographic plates on each of which several holograms were sequentially reconstructed was used by Matulka and Collins in 1971 to rebuilt the three-dimensional density field of an aerodynamic phenomenon [Mat71]. In 1972 Junginger and Van Haeringen used a method considering line phase integral to measure the refractive index field in incandescent lamps from interferograms of the bulb taken under different angles [Jun72]. When computers became largely available, works were done to implement numerical reconstruction algorithms (see for example [Swe73, Ves84, Tie90]), to replace the traditional visual counting of fringes and analytic backprojection of phase values as achieved in the previously cited papers. There was also a transition period, till the mid 1990s and the apparition of the first digital cameras, during which the hologram were still recorded on photographic plates, while computers were in charge of the tomographic reconstruction [Tie90, Phi92].

5.3.2 Optical diffraction tomography in microscopy

In all the above-cited papers, only macroscopic specimens are investigated. Microscopic interferometry, necessary to aim to microscopic specimens ODT, also finds its origin in the mid last century [Gab48,

Bar52, Bar53, Dav52], and among its recent applications, we can mention following examples. Noda *et al.* used a oblique illumination and coherent light in a conventional phase-contrast microscope [Nod92]. Vishnyakov *et al.* combined phase shifting interferometry (PSI) with a Linnik interferometer also allowing multiple angles illumination [Vis98, Vis99, Vis03, Vis04]. Lauer used PSI to record the Fourier spectrum of the diffracted wavefront, varying the illumination direction by changing the direction of the beam itself [Lau02]. PSI was also used by Górski *et al.* to reconstruct the refractive index of optical phase elements [Gór02] and optical fibers [Gór04, Gór06, Gór07], or by Dewandel *et al.* for dendritic crystal growth monitoring [Dew05]. Józwicka and Kujawinska presented a DHM setup, with an optical arrangement allowing recording of simultaneously three projections [Józ05, Józ06]. In the field of optical fibers characterization, Bachim *et al.* employed a interferometer with a procedure identifying the fringes minima locations, allowing phase imaging with a single acquisition [Bac05b, Bac05a], while Barakat *et al.* used a Fizeau interferometer [Bar01].

Different works achieving ODT at the microscale must also be reported, mostly with a rotation of the specimen relatively to a fixed illumination beam when the object is not cylindrically symmetric, in which the complex diffracted wavefront was measured with non-intereferometric techniques. Maleki *et al.* compared ODT reconstructions of optical fibers profiles based on data obtained through a direct intensity-only algorithm [Mal92] and an iterative phase-retrieval algorithm [Mal93]. In all their works comparing backprojection with backpropagation, Wedberg *et al.* used also an iterative phase-retrieval algorithm to extract the complex optical field from intensity measurements [Wed95a, Wed95b, Wed96], as did Halse *et al.* in their study of combining 2D tomographic sections to build full 3D tomographic volume [Hal03]. Barty *et al.* or Roberts *et al.* preferred a direct phase-retrieval algorithm, based on 3 intensity measurements performed on different focus planes [Pag98], to evaluate the refractive index distribution in optical fibers [Bar00, Rob02].

There are really few successful applications of ODT techniques to biological specimen imaging: Lauer used his tomographic microscope to observe bacteria and yeasts [Lau02], Noda *et al.* investigated green mold (Aspergillus oryzae) [Nod92], and Vishnyakov and Levin observed human red blood cells and lymphocites [Vis98, Vis99], providing some of the few quantitative refractive index data on biological specimen besides the two paper presented in this chapter [Cha06a, Cha06b].

An extensive use of ODT in cellular imaging is restrained for several reasons, the principal certainly being the fact that cells are obviously non cylindrically symmetric, and that all the tomographic reconstructions based on a single complex wavefront evaluation [Ves85, Mal92, Wed95a, Rob02] are not applicable. Recording several images is then mandatory to reconstruct correctly the specimen in 3D, requiring to move either the specimen itself [Far89, Bar00, Wed95b, Wed95a, Gór04, Gór06, Gór07, Dew05, Cha06a, Cha06b] or some parts of the microscope [Nod92, Vis98, Vis99, Lau02]. Moving parts increase the experimental setup complexity and occasionally generates some micromovements of the specimen during the recording routine, such as precession in the case of rotated specimen, that should be compensated digitally before tomographic reconstruction [Bar00, Gór04, Gór06, Cha06a, Cha06b]. The presence of actuators in the system may also introduce vibrations, which can become really annoying when classical PSI is used: the precise phase steps between each required intensity recording may be disturbed, leading to an inaccurate reconstruction of the diffracted wavefront. Furthermore, in the presence of vibrations, only phase differences can be measured, as the phase relations between successive recorded waves can usually not be controlled. Because it requires only a single hologram for amplitude and phase extraction, DHM naturally overcomes the problem of phase relation during recording, and also reduces the recording procedure duration. The relative phase of the reference and object waves between two successive measurements being not controlled, a phase offset must be adjusted on a reference area for each reconstructed wavefront (see Colomb's thesis for details on the offset adjustment [Col06]). In the two articles of the present chapter about single cell tomography, the reference area is simply taken outside the cell, where the light only cross the perfusion medium. Note that the ODT formulation proposed by Lauer, despite its use of phase-shifting interferometry, allow a proper control of the phase relation between the illuminating, scattered and reference waves [Lau02].

5.3.3 The Radon transform approach

As in many of the mentioned papers [Row69, Mat71, Jun72, Vis98, Vis99, Bar00, Rob02, Gór04, Gór06], the two papers in the present chapter assume that light propagates along straights rays in the specimen, therefore this particular tomographic reconstruction process is summarized hereafter.

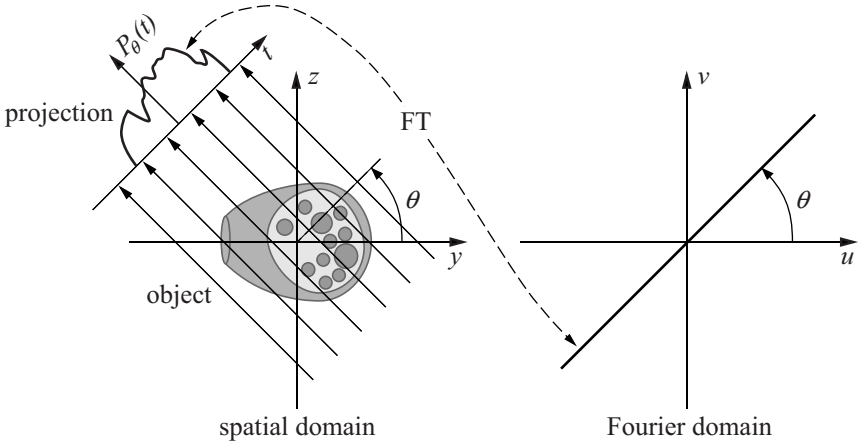

Figure 5.1: Scheme of the Fourier slice theorem: the projection of a 2D function $\Delta n(x, y, z)$ taken at an angle θ is related by a Fourier transform (FT) to a radial line in the 2D Fourier spectrum of the function.

When straight rays are considered, the measured phase $\varphi(x, y)$ for an illumination direction z is simply

$$\varphi(x, y) = \int \frac{2\pi}{\lambda} \Delta n(x, y, z) dz, \tag{5.1}$$

where $\Delta n(x, y, z)$ is the difference between the specimen refractive index 3D spatial distribution and the refractive index of the surrounding medium. In other words, $\varphi(x, y)$ is simply proportional to the projection of the $\Delta(x, y, z)$ in the direction z. Considering only a slice of the object parallel to the y axis (in the case of specimen rotated along the x axis), this projection can be viewed as the Radon transform $P_\theta(t)$ for the 2D function $\Delta n(y, z)$:

$$\begin{aligned} P_\theta(t) &= \int_{(\theta,t)line} \frac{2\pi}{\lambda} \Delta n(y, z) ds \\ &= \int_{-\infty}^{\infty} \int_{-\infty}^{\infty} \frac{2\pi}{\lambda} \Delta n(y, z) \delta(y \cos\theta + z \sin\theta - t) dy dz \end{aligned} \tag{5.2}$$

where δ is the usual delta function $\iint f(y, z)\delta(y - y_0, z - z_0)dydz = f(y_0, z_0)$.

Using the so-called Fourier slice theorem, the projection $P_\theta(t)$ can be related to a radial line in the 2D Fourier spectrum of the function $\Delta n(y, z)$ by a simple Fourier transform. A scheme illustrating this procedure is presented on Fig. 5.1. This way, by changing the angle of projection θ, the frequency domain is fully covered, and the initial function $\Delta n(y, z)$ is reconstructed by mean of an inverse Fourier transform. For 3D objects varying along the rotation axis x, this procedure can be applied successively to all the slices to finally achieve the complete 3D reconstruction of $n(x, y, z)$. A complete development of the Fourier slice theorem, properties of the Radon transform as well as discussions on inversions algorithms can be found in the book on computerized tomography by Kak and Slaney [Kak01]. Consideration about resolution in function of the number of views and sampling can additionally be found in papers by Matulka and Collins [Mat71], Sweeney and Vest [Swe73] or Tieng and Chen [Tie90].

Refractive index accuracy

In DHM-based tomography, the accuracy in the refractive index accuracy depends mostly on the phase accuracy, while the 3D spatial resolution Δx is determined by the numerical aperture (NA) of the microscope as in standard optical microscopy:

$$\Delta x = 1.22 \frac{\lambda}{NA}, \tag{5.3}$$

where λ is the considered wavelength. If the angular sampling is sufficient, the inverse Radon transform described above, preserves the resolution of the initial images taken at different orientation [Mat71, Swe73, Tie90].

In the two papers forming this chapter, an accuracy in the refractive index of 0.01 is evaluated. A small analysis presented hereafter illustrates that this accuracy is not limited by the DHM phase accuracy.

From Eq. 5.1, we can estimate the sensitivity of a DHM phase image to a refractive index change Δn as

$$\Delta n = \frac{\Delta\varphi}{2\pi} \cdot \frac{\lambda}{d}, \tag{5.4}$$

where $\Delta\varphi$ is in this case the phase accuracy, and d is the thickness of an homogeneous specimen. Substituting values in Eq. 5.4 for a standard DHM cellular imaging experiment, i.e. λ=635 nm, $d = 5\ \mu m$ and $\Delta\varphi = 2^{\circ}$, one obtain that DHM is sensitive to refractive index change as low as $7 \cdot 10^{-4}$ (or even lower if spatial and/or temporal averaging is applied to the phase images [Rap05]). Therefore, the accuracy of the 3D refractive index reconstruction is not limited by the DHM phase accuracy in the two presented papers, which is more than one order of magnitude better, but mainly by the mechanical micromovements during rotation, in spite of the numerical procedures applied to the individual images to compensate them. The micromovements tend to blur the reconstructed 3D image, resulting in an averaging in the refractive index distribution, i.e. a lost in accuracy. According to Russ, the amount of run-out should be less that one-tenth of the aimed resolution [Rus02]. In our case, the run-out during rotation is reduced to few tenths of micron, resulting in a final resolution in the micrometer range.

5.3.4 Validity of the inverse Radon transform approach

An important issue in ODT at the microscale concerns the validity and accuracy of the tomographic reconstruction. In the original formulation by Wolf [Wol69] and in its first usage by Carter [Car70a], diffraction of light by the specimen is considered in the Born approximation, while in some other early works mentioned above, light is assumed to propagate along straight rays within the specimen [Row69, Mat71, Jun72]. Diffraction occurs when the specimen is in the order of the wavelength of the illuminating beam, therefore when visible light is used to probe specimens above the millimeter range with weakly-varying refractive index, as in some of the pioneer works already mentioned, the approximation of straight rays is obviously non-abusive [Hef66, Mat71, Phi92]. In those cases, the refractive index reconstruction is simple to implement and calculation costs are low, when compared to reconstruction models including diffraction [Wol69, Car70b, Iwa75, Fer79, Kak01]. If the validity of this hypothesis may be dangerously compromised for specimens at the microscale, few works report the error in tomographic reconstructions when this hypothesis is improperly used. Cha and Vest discussed the case of strongly refracting objects and proposed a ray tracing approach to correct the results obtained with inverse Radon transform [Cha79], while Norton and Linzer or Lira and Charles proposed respectively in the same purpose a perturbation analysis of the refraction [Nor82] or an iterative correction [Lir87]. Górski analyzed quantitatively tomographic reconstructions of an optical fiber achieved under the straight rays hypothesis, compared his results with a simulation based on a Huyghens-Fresnel model taking diffraction into account, and confronted his results with experimental data [Gór04, Gór06]. Defining a step-index fiber (62 μm core diameter, 125 μm cladding diameter), he calculated the accuracy in the refractive index determination as a function of the step-index within the fiber. As his studies furnish some of the few quantitative results available in ODT at the microscale, they constitute an interesting discussion basis about the method accuracy when the inverse Radon transform is used. Therefore, some of his results are summarized in Table 5.1.

Table 5.1: Errors of $n(x, y, z)$ as a function of Δn calculated by Górski for a step-index fiber (62 μm core diameter, 125 μm cladding diameter) [Gór04]. The accuracy has been calculated as the standard deviation over the full reconstructed field, or on a narrowed field, in which the signal is evaluated only in constant areas but not at the refractive index change boundaries (i.e. core/cladding, cladding/surrounding medium).*

Δn	0.015	0.025	0.035	0.045	0.055	0.065
Accuracy	0.0010	0.0016	0.0020	0.0040	0.0045	0.0050
Accuracy*	0.0009	0.0031	0.0017	0.0028	0.0031	0.0034

Important studies have also been performed by Wedberg *et al.*, comparing reconstructions obtained with the so-called backprojection, backpropagation, hybrid backprojection or hybrid backpropagation techniques, in the case of circularly symmetric micro-objects ODT [Wed95a, Wed95b, Wed96]. In backprojection, straight rays are considered, being equivalent to the inverse Radon transform approach. In backpropagation, diffraction is taken into account, under even the Born or Rytov's approximation (a

clear presentation of the differences between those approximations applied to ODT has been written by Iwata and Nagata [Iwa75]. In the hybrid backpropagation or backprojection, the complex field is first backpropagated from the detector position to the centre of the specimen, taking diffraction into account, after what backprojection or backpropagation is used: this way, in the hybrid backprojection, light is considered to propagate straight only within the specimen. For a large range of objects (step-index objects with sizes 10λ, 50λ and 100λ, refractive index values Δn up to 0.05), it has been shown that no significant differences occurs between hybrid backprojection and hybrid backpropagation [Wed95a]. In the same framework, Halse *et al.* investigated the possibility of a slice-by-slice implementation to rebuilt 3D specimen from 2D ODT sections [Hal03]. In a recent paper, Górski and Osten compared backpropagation and backprojection to investigate a photonic crystal fiber, composed by 3.6 μm channels arranged at 8 μm interval [Gór07]. Both techniques allowed proper reconstruction of the internal fiber arrangement, even if less artifacts were present when diffraction was considered.

In their work on optical fibers ODT, Barty *et al.* and Roberts *et al.* have also used the hypothesis of straightly propagating light [Bar00, Rob02]. Their tomographic reconstruction featured even the smallest details (fiber core of few microns with refractive index variation of 0.005), and were in good agreement with the manufacturer's data and comparative measurements.

A last interesting consideration about the legitimization of the inverse Radon transform approach can be found in Marquet's thesis, where the wave transmitted through a cell is investigated, without any tomographic reconstruction [Mar03]. He simulated the wavefront diffracted by a cell with help of a Monte-Carlo simulation in the Born approximation: a semi-spherical shape with 15 μm diameter d was considered, with a refractive index difference of 0.04 compared to the perfusion medium. The diffraction order is iteratively increased, until convergence of the transmitted field, obtained in this case for the 6^{th} order. According to Iwata and Nagata, a rough criterion of validity for the first Born approximation is that $k\Delta nd \ll 1$, where k is the wave vector [Iwa75]. The case studied by Marquet is slightly out of the suggested reasonable limit, because for such a large refractive index variation, a specimen diameter $d \ll 10$ μm is prescribed. This certainly explains why the first iteration in the simulation fails to properly describe the diffracted wavefront, and why 6 iterations are necessary. But the most important result of this study is obtain when the 6^{th} iteration of the simulation is compared to the wavefront calculated with the brutal approximation of straightly propagating light: beside small oscillation at the cell boundaries, no significant difference is observed. This example shows that if the first Born approximation is misused, the result can be even more inaccurate that the non-diffractive approach. In ODT studies, Wedberg and Stamnes also observed improper reconstructions, when an algorithm developed in the first Born approximation was used and the required using conditions were not fully respected [Wed95a]. They also observed in the same paper, in agreement with observations made by Iwata and Nagata [Iwa75], that algorithms based on the Rytov approximation were less constraining regarding the specimen properties.

Results obtained with pollen grains and testate amoebas

In most of the studies discussing the ODT accuracy, some of which are used to confirm the results of the two ODT papers presented here, the test objects take the form of step-indices and are therefore strongly disadvantageous regarding diffraction [Wed95a, Wed95b, Wed96, Gór04, Gór06]. Wedberg *et al.* already showed that an object with a graded index is more favorable and lead to less imprecision during reconstruction, showing even perfect agreement between hybrid backprojection, hybrid backpropagation and theoretical prediction [Wed95a]. This fact is also to keep in mind when discussing ODT results obtained in cellular imaging, as most of the specimen contain slowly density variation, like the core of the pollen grain presented here, and not only highly localized diffracting elements.

For a step-index of 0.065, Górski obtained an accuracy in the reconstructed refractive index of 0.005 over the complete field of view, and of 0.0031 on a narrowed field excluding abrupt refractive index changing regions (see Table 5.1). This result confirm that using of the straight rays hypothesis is non-abusive if the aimed accuracy is not below 0.005, or when object areas are in the range of few tens of microns are considered. In the studies presented in the two paper forming this chapter, in which the invesetigated specimens present comparable sizes and refractive index variations with Górski's studies [Cha06a, Cha06b], the accuracy is announced to be 0.01. Mainly limited by the micromovements during rotation of the specimen, which cannot be completely suppressed digitally, the refractive index accuracy would in that case not be significantly improved if diffraction were taken into account in the reconstruction process. In his later paper studying photonic crystal fibers, Górski shows that some artefacts may appear if the diffraction is neglected during reconstruction [Gór07], he also shows that all the small features in the

reconstructed volume are correctly placed in spite of the artefacts, what is of primary importance regarding the possibility of describing the internal arrangement of some organelles in cellular imaging. In the amoebas study, even if the goal of the paper is to extract the cell morphometry with a rough threshold applied to the 3D refractive index values, the visible organelles of few microns inside the amoebas (i.e. the symbiotic algae or the phagocytic vacuoles) illustrate encouragingly this possibility.

Comments on DHM-based ODT bibliography

[Bac05a] B. L. Bachim and T. K. Gaylord. "Microinterferometric optical phase tomography for measuring small, asymmetric refractive-index differences in the profiles of optical fibers and fiber devices". Appl. Opt. **44**(3): 316–327 (2005).

[Bac05b] B. L. Bachim, T. K. Gaylord and S. C. Mettler. "Refractive-index profiling of azimuthally asymmetric optical fibers by microinterferometric optical phase tomography". Opt. Lett. **30**(10): 1126–1128 (2005).

[Bar52] R. Barer. "Interference Microscopy and Mass Determination". Nature (London) **169**(4296): 366–367 (1952).

[Bar53] R. Barer. "Determination of dry mass, thickness, solid and water concentration in living cells". Nature (London) **172**(4389): 1097–1098 (1953).

[Bar00] A. Barty, K. A. Nugent, A. Roberts and D. Paganin. "Quantitative phase tomography". Opt. Commun. **175**(4-6): 329–336 (2000).

[Bar01] N. Barakat, H. A. El-Hennawi, E. A. El-Ghafar, H. El-Ghandoor, R. Hassan and F. El-Diasty. "Three-dimensional refractive index profile of a GRIN optical waveguide using multiple beam interference fringes". Opt. Commun. **191**(1-2): 39–47 (2001).

[Car70a] W. H. Carter. "Computational Reconstruction of Scattering Objects from Holograms". J. Opt. Soc. Am. **60**(3): 306–314 (1970).

[Car70b] W. H. Carter. "Computational reconstructions of scattering objects from holograms". J Opt Soc Amer **60**(3): 306–314 (1970).

[Car74] W. H. Carter and P. C. Ho. "Reconstruction of inhomogeneous scattering objects from holograms". Appl. Opt. **13**(1): 162–172 (1974).

[Cha79] S. Cha and C. M. Vest. "Interferometry and Reconstruction of Strongly Refracting Objects". J. Opt. Soc. Am. **69**(10): 1474–1474 (1979).

[Cha06a] F. Charrière, A. Marian, F. Montfort, J. Kühn, T. Colomb, E. Cuche, P. Marquet and C. Depeursinge. "Cell refractive index tomography by digital holographic microscopy". Opt. Lett. **31**(2): 178–180 (2006).

[Cha06b] F. Charrière, N. Pavillon, T. Colomb, T. Heger, E. Mitchell, P. Marquet, B. Rappaz and C. Depeursinge. "Living specimen tomography by digital holographic microscopy: morphometry of testate amoeba". Opt. Express **14**(16): 7005–7013 (2006).

[Col06] T. Colomb. *Numerical aberrations compensation and polarization imaging in digital holographic microscopy*. Thesis 3455, Ecole Polytechnique Fédérale de Lausanne (2006).

[Dän70] R. Dändliker and D. Weiss. "Reconstruction of three-dimensional refractive index from scattered waves". Opt. Commun. **1**(7): 323–328 (1970).

[Dav52] H. G. Davies and M. H. F. Wilkins. "Interference microscopy and mass determination". Nature **169**(4300): 541 (1952).

[Dew05] J. L. Dewandel, M. Héraud, S. Rex, M. Mathes, T. Lanen and L. Joannes. "Interferometric optical tomography applied to dendritic crystal growth model scenes". In "Proc. SPIE-Int. Soc. Opt. Eng.", (2005), vol. 5856 PART II, pp. 808–810.

[Far89] G. W. Faris and H. M. Hertz. "Tunable Differential Interferometer for Optical Tomography". Appl. Opt. **28**(21): 4662–4667 (1989).

[Fer79] A. F. Fercher, H. Bartelt, H. Becker and E. Wiltschko. "Image formation by inversion of scattered field data: experiments and computational simulation". Appl. Opt. **18**(14): 2427–2439 (1979).

[Gór02] W. Górski and M. Kujawińska. "Three-dimensional reconstruction of refractive index inhomogeneities in optical phase elements". Optics and Lasers in Engineering **38**(6): 373–385 (2002).

[Gór04] W. Górski. "The influence of diffraction in microinterferometry and microtomography of optical fibers". Optics and Lasers in Engineering **41**(3): 565–583 (2004).

[Gór06] W. Górski. "Tomographic microinterferometry of optical fibers". Optical Engineering **45**(12): 125002 (2006).

[Gór07] W. Górski and W. Osten. "Tomographic imaging of photonic crystal fibers". Opt. Lett. **32**(14): 1977–1979 (2007).

[Gab48] D. Gabor. "A New Microscopic Principle". Nature **161**(4098): 777–778 (1948).

[Hal03] Ø. R. Halse, J. J. Stamnes and A. J. Devaney. "Three-dimensional diffraction tomography by two-dimensional sectioning". Opt. Commun. **224**(4-6): 185–195 (2003).

[Hef66] L. O. Heflinger, R. F. Wuerker and R. E. Brooks. "Holographic Interferometry". J. Appl. Phys. **37**(2): 642–649 (1966).

[Iwa75] K. Iwata and R. Nagata. "Calculation of Refractive-Index Distribution from Interferograms Using Born and Rytovs Approximation". Japanese Journal of Applied Physics **14**: 379–383 (1975).

[Józ05] A. Jóźwicka and M. Kujawińska. "Digital holographic tomograph for amplitude-phase microelements testing". In "Proc. SPIE-Int. Soc. Opt. Eng.", (2005), vol. 5958, pp. 1–9.

[Józ06] A. Jóźwicka and M. Kujawińska. "Experimental proof-of-principle 3D measurements of microobjects by digital holographic tomography". In "Proc. SPIE-Int. Soc. Opt. Eng.", (2006), vol. 6188.

[Jun72] H. G. Junginger and W. Van Haeringen. "Calculation of three-dimensional refractive-index field using phase integrals". Opt. Commun. **5**(1): 1–4 (1972).

[Kak01] A. C. Kak and M. Slaney. *Principles of Computerized Tomographic Imaging*. Soc. of Ind. and Appl. Math (SIAM, 2001).

[Lau02] V. Lauer. "New approach to optical diffraction tomography yielding a vector equation of diffraction tomography and a novel tomographic microscope". J. Microsc. **205**: 165–176 (2002).

[Lir87] I. H. Lira and C. M. Vest. "Refraction Correction in Holographic-Interferometry and Tomography of Transparent Objects". Appl. Opt. **26**(18): 3919–3928 (1987).

[Mal92] M. H. Maleki, A. J. Devaney and A. Schatzberg. "Tomographic Reconstruction from Optical Scattered Intensities". J. Opt. Soc. Am. A **9**(8): 1356–1363 (1992).

[Mal93] M. H. Maleki and A. J. Devaney. "Phase-Retrieval and Intensity-Only Reconstruction Algorithms for Optical Diffraction Tomography". J. Opt. Soc. Am. A **10**(5): 1086–1092 (1993).

[Mar03] P. Marquet. *Développement d'une nouvelle technique de microscopie optique tridimensionnelle, la microscopie holographique digitale. Perspectives pour l'étude de la plasticite neuronale*. Ph.D. thesis, Université de Lausanne (2003).

[Mat71] R. D. Matulka and D. J. Collins. "Determination of three-dimensional density fields from holgoraphic interferograms". J. Appl. Phys. **42**(3): 1109–1119 (1971).

[Nod92] T. Noda, S. Kawata and S. Minami. "Three-dimensional phase-contrast imaging by a computed tomography microscope". Appl. Opt. **31**: 670–674 (1992).

[Nor82] S. J. Norton and M. Linzer. "Correcting for ray refraction in velocity and attenuation tomography: A perturbation approach". Ultrason. Imaging **4**(3): 201–233 (1982).

[Pag98] D. Paganin and K. A. Nugent. "Noninterferometric phase imaging with partially coherent light". Phys. Rev. Lett. **80**(12): 2586–2589 (1998).

[Phi92] H. Philipp, T. Neger, H. Jager and J. Woisetschlager. "Optical tomography of phase objects by holographic interferometry". Measurement **10**(4): 170–181 (1992).

[Rap05] B. Rappaz, P. Marquet, E. Cuche, Y. Emery, C. Depeursinge and P. J. Magistretti. "Measurement of the integral refractive index and dynamic cell morphometry of living cells with digital holographic microscopy". Opt. Express **13**(23): 9361 – 9373 (2005).

[Rob02] A. Roberts, K. Thorn, M. L. Michna, N. Dragomir, P. Farrell and G. Baxter. "Determination of bending-induced strain in optical fibers by use of quantitative phase imaging". Opt. Lett. **27**(2): 86–88 (2002).

[Row69] P. D. Rowley. "Quantitative interpretation of three-dimensional weakly refractive phase objects using holographic interferometry". J Opt Soc Amer **59**(11): 1496–1498 (1969).

[Rus02] J. C. Russ. *The image processing handbook* (CRC Press, Boca Raton, FL, 2002).

[Swe73] D. W. Sweeney and C. M. Vest. "Reconstruction of three-dimensional refractive index fields from multidirectional interferometric data". Appl. Opt. **12**(11): 2649–2664 (1973).

[Tie90] S. M. Tieng and H. T. Chen. "Holographic tomography by SART and its application to reconstruction of 3D temperature distribution". Warme- und Stoffubertragung Zeitschrift **26**(1): 49–56 (1990).

[Ves84] C. M. Vest and I. Prikryl. "Tomography by iterative convolution: empirical study and application to interferometry". Appl. Opt. **23**(14): 2433–2440 (1984).

[Ves85] C. M. Vest. "Tomography for Properties of Materials That Bend Rays - a Tutorial". Appl. Opt. **24**(23): 4089–4094 (1985).

[Vis98] G. N. Vishnyakov and G. G. Levin. "Optical Microtomography of Phase Objects". Optics and Spectroscopy **85**(1): 73–77 (1998).

[Vis99] G. N. Vishnyakov, G. G. Levin, A. V. Likhachev and V. V. Pikalov. "Phase Tomography of 3D Biological Microobjects: Numerical Simulation and Experimental Results". Optics and Spectroscopy **87**(3): 413–419 (1999).

[Vis03] G. N. Vishnyakov, G. G. Levin and V. L. Minaev. "Tomographic Microscopy of Three-Dimensional Phase Objects in Spatially Incoherent Light". Optics and Spectroscopy **95**(1): 134–138 (2003).

[Vis04] G. N. Vishnyakov, G. G. Levin, V. L. Minaev, V. V. Pickalov and A. V. Likhachev. "Tomographic Interference Microscopy of Living Cells". Microscopy and Analysis **18**(1-6): 15–17 (2004).

[Wed95a] T. C. Wedberg, J. Stamnes and W. Singer. "Comparison of the filtered backpropagation and the filtered backprojection algorithms for quantitative tomography". Appl. Opt. **34**(28): 6575–6581 (1995).

[Wed95b] T. C. Wedberg and J. J. Stamnes. "Experimental examination of the quantitative imaging properties of optical diffraction tomography". J. Opt. Soc. Am. A. **12**(3): 493– (1995).

[Wed96] T. C. Wedberg and J. J. Stamnes. "Recent results in optical diffraction microtomography". Measurement Science and Technology **7**(3): 414–418 (1996).

[Wol69] E. Wolf. "Three-dimensional structure determination of semi-transparent object from holographic data". Opt. Commun. **1**(4): 153–156 (1969).

Chapter 6

Perfusion solution dispersion used for simultaneous cellular morphometry and refractive index measurement with Digital Holographic Microscopy

Paper to be submitted to Optics Letters, 2007.

Benjamin Rappaz[a*], Florian Charrière[b*], Christian Depeursinge[b], Pierre J. Magistretti[a] and Pierre Marquet[c]

[a] *Ecole Polytechnique Fédérale de Lausanne (EPFL), Brain Mind Institute, CH-1015 Lausanne, Switzerland*
[b] *Ecole Polytechnique Fédérale de Lausanne (EPFL), Imaging and Applied Optics Institute, CH-1015 Lausanne, Switzerland*
[c] *Centre de neurosciences psychiatriques, Département de psychiatrie DP-CHUV, Site de Cery, CH-1008 Prilly-Lausanne, Switzerland*
[*] *These authors contributed equally to the present work.*

Digital Holographic Microscopy (DHM) allows optical path length (OPL) measurements with nanometric accuracy. OPL variations induced by cells on a transmitted wave depend on both the refractive index (RI) of cells and their thickness. This Letter presents a dual-wavelength technique exploiting the dispersion of the perfusion medium to obtain a set of equations, allowing decoupling the contributions of the RI and the cellular thickness to the total phase signal. The two wavelengths are chosen in the vicinity of the absorption peak of a dye added to the perfusion medium, where the absorption is accompanied by a strong variation of the dye RI as a function of the wavelength.

OCIS codes: 090.1760, 120.3940, 120.5050, 170.1530

Recently, new emerging quantitative phase microscopy techniques (QPM) have demonstrated their capability to provide accurate 3D imaging of transparent living cells [Mar05, Kem06, Lue06, Cur05]. Practically, the wave front retardation induced on the transmitted wave arises from the difference in refractive index (RI) between the specimen and the surrounding medium and is proportional to the thickness of the observed transparent specimen. Consequently, quantitative phase signal provides information about both cell morphology and intracellular content related to the RI. However, such a quantitative phase signal remains also difficult to interpret, due to its dual dependency on cell morphology and RI. E.g. a

cellular swelling, induced by a hypotonic stress, produces a paradoxical phase decrease [Rap05]. Accordingly, some strategies have been developed to separately measure morphology and RI. In the papers by Kemper *et al.* or Lue *et al.*, the cell integral RI has been measured by trapping cells between two cover glasses, whose distance apart is experimentally determined [Kem06, Lue06]. On the other hand, in the paper by Curl *et al.*, a combined method involving confocal microscopy to determine cell thickness and QPM to calculate the intracellular refractive index has been proposed [Cur05]. In a previous work, we have developed a specific decoupling procedure based on digital holographic microscopy (DHM), allowing to directly calculate from the quantitative phase signal the corresponding cell morphology and integral RI. This procedure is particularly useful for measuring, in the same experimental conditions, both cell morphology changes and their associated integral RI variations related to the modification of intracellular content, particularly the protein concentration, occurring during biological processes [Rap05]. Practically, it consists in perfusing cells consecutively with two iso-osmolar perfusion solutions having different refractive indices and to record the two corresponding holograms. However, the solutions exchange time within the perfusion chamber precludes the possibility to monitor dynamic changes of cell morphometry and RI occurring during fast biological processes. To overcome these drawbacks, we present a DHM dual-wavelength technique, inspired by the first works of Barer [Bar69] or Chaubal *et al.* [Cha67, Cha68], which exploits the dispersion of the perfusion medium to obtain a set of equations, allowing decoupling the contributions of the RI and the cellular thickness to the total phase signal. Obtaining dispersion, which induces a phase variation significantly larger than the phase noise fluctuations, is a prerequisite condition to determine RI and the cell thickness. Thus, we present a DHM dual-wavelength technique combining with the utilization of an extracellular dye, which guaranties a significant variation of the perfusion solution RI within the vicinity of the absorption peak in accordance with the Kramers Kronig (KK) relations. The transmission DHM used for the present study has been described in details elsewhere [Mar05, Rap05]. Results presented here have been obtained with a 20x 0.35 NA microscope objective (MO) for the colorant RI calibration and with a 63x 0.85 NA MO for the yeasts measurements. The camera is an 8 bits, black and white CCD, with a pixel size of 6.45 μm, and a maximum frame rate of 25 Hz. For a 512 x 512 pixels hologram, the field of view, is 160 μm wide with the 20x MO and 60μm with the 63x MO. The CCD exposure time can be reduced down to 1 μs. With an INTEL Core 2 2.4 GHz, the rate of the phase image reconstruction, described extensively in a paper by Colomb *et al.* [Col06], reaches the value of 15 Hz. The light source is a tunable optical parametric amplifier (Coherent OPA 9400) supplied by a femtosecond kHz titanium:sapphire laser system (oscillator Coherent Mira 900 plus regenerative amplifier Coherent RegA 9000). The source, which wavelength can be adjusted in the range 490-700 nm, produces about 10 mW of laser light intensity with a coherence length of 60 μm. The model cells used for this study, Schizosaccharomyces pombe (fission yeast) were cultured in a classical YPD medium at 30°C before imaging. All experiments on yeasts were conducted at room temperature with YPD medium containing 30 mM SRB1. Dye selection has been achieved from rate of diffusion through cell membrane and from dispersion properties assessed thanks to the knowledge of absorption spectra related to refractive indices through the KK relations. For convenience, we use a subtractive KK analysis defined by

$$n(\omega) = n(\omega_0) + \frac{c}{\pi}(\omega^2 - \omega_0^2) P \int_0^{\omega} \frac{\mu_a(\omega')}{(\omega^2 - \omega'^2)(\omega_0^2 - \omega'^2)}\, d\omega', \tag{6.1}$$

where P is the Cauchy principal value of the integral, μ_a is the absorption coefficient and $n(\omega_0)$ is the refractive index measured at a reference frequency to provide scaling of the calculated curves [Ahr71]. Accordingly, the fluorescent dye Sulforhodamine B1 (SRB1), widely used in cell biology, has been selected. In addition to the prediction of the KK relations, the RI dispersion of 30 mM SRB1 solution was also experimentally measured. Clear fused quartz round capillaries, with 50 μm internal diameter and 80 μm outer diameter were used to achieve differential measurements, by comparing the DHM phase images obtained for a capillary filled with a test solution containing 30 mM SRB1 and one with a test solution without colorant. The test solution contained water with 10% w/v Nycodenz, a nonionic density gradient medium which strongly shift the RI (Sigma-Aldrich), and the capillary was surrounded by an index matching liquid. Both the Nycodenz and the index matching liquid are used to obtain a weak diffracting capillary inducing few phase jumps. Therefore a phase unwrapping procedure allows to efficiently determining the actual phase shift induced by the filled capillary with respect to its surrounding medium. Knowing the geometry of the capillary, comparison of the phase shift obtained with and without colorant gives directly the RI shift due to SRB1, independently of the test solution. The RI of the solution

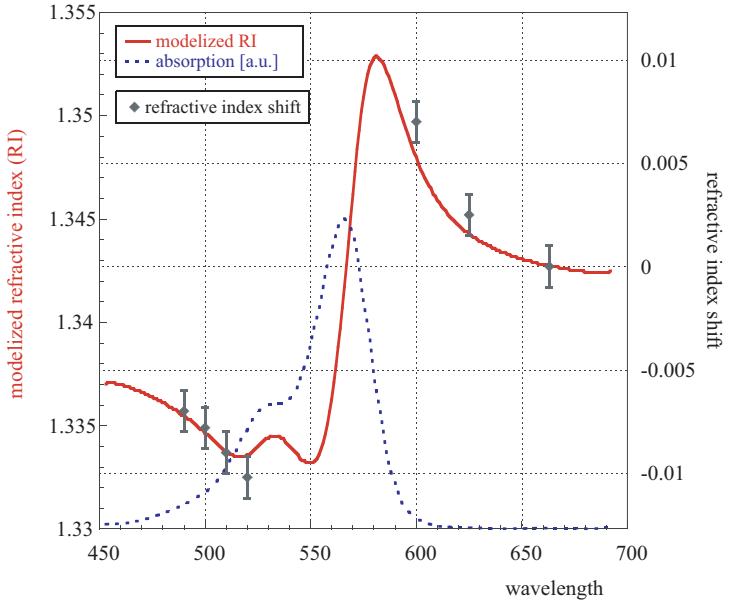

Figure 6.1: Comparison of the Kramers-Kronig prediction with experimental results. Dashed curve: measured absorption curve of SRB1. Continuous curve: modelized variation of the real part of the refractive index in the vicinity of the absorption peak. Dots: measured experimental shift.

measured at a reference value, is required to obtain absolute RI values from the KK relation as well as from the phase shift measurements. Practically, this reference value (1.3427 ± 0.0002) was measured at 663 nm with an Abbe 2WAJ refractometer. RI values obtained from phase shift measurements yield a good agreement with the dispersion curve as a function of the wavelength calculated from the subtractive KK analysis taking into account the SRB1 absorption spectrum within the 450-700 nm range (see Fig. 6.1).

Measurement of the optical path length (OPL) for each cell was measured at 5 points around the absorption maximum of SRB1 (565 nm), two at lower wavelengths (490 nm and 500 nm) and 3 at higher wavelengths (600 nm, 625 nm and 663 nm). Those points were chosen close to the absorption peak in order to obtain a significant refractive index shift, but not to close to still allow an exploitable light transmission and avoiding any significant fluorescent emission. A gradient based edge detection algorithm was used to determine the cell contour. At each wavelength, the mean OPL estimated over the entire body of each cell was measured for 15 successive images acquired at 1 Hz:

$$OPL = (n_c - m_m)\, d, \tag{6.2}$$

where n_c is the mean RI of the cell, n_m the RI of the perfusion medium at the specific wavelength and d the mean thickness of the cell.

The two monitored cells and the measured values are displayed in Fig. 6.2. As expected, the OPL increases or decreases as the wavelength approaches the absorption peak from the left or the right respectively. The RI of the cell was calculated by taking a system of two OPL measurements achieved at two different wavelengths:

$$n_c = OPL_1 \left(\frac{n_{m1} - n_{m2}}{OPL_1 - OPL2} \right) + n_{m1}, \tag{6.3}$$

where the indices $i = 1, 2$ in n_{mi} and OPL_i refer to the two different wavelengths considered. A standard error calculus shows that the precision on n_c strongly decreases as the two wavelengths get closer. Therefore, to guarantee a high accuracy in the calculus of n_c only measured OPL pairs for wavelengths separated by 50 nm or more were considered. This criterion gives 7 couples for each cell. Considering the precision of the measurement of the mean OPL_i (about 1.2 nm) and the RI of the solutions n_{mi} (0.001), the precision of the measurement was found to be 0.002. We measured a RI of 1.388 ± 0.002 for the upper cell in Fig. 6.2 and 1.393 ± 0.002 for the lower cell. This value is in the normal range of RI for biological

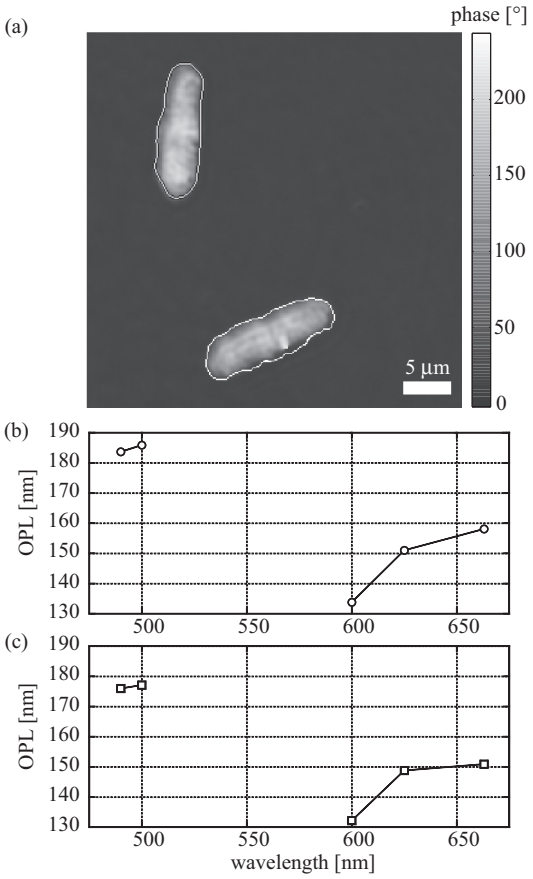

Figure 6.2: (a) Phase image of two yeasts (S. Pombe) at 490 nm with measured ROI highlighted in white; (b) and (c) variation of the optical path length for the two monitored cells (resp. upper and lower cell) as a function of the wavelength.

cells [Rap05]. In a parallel experiment during which the OPL of yeast cells has been measured without colorant in the perfusion medium, the dispersion of the mean cell RI for the 480-700 nm range has been found to be negligible, i.e. below the decoupling procedure sensitivity. Therefore, the RI measured with Eq. 6.3 can be considered as constant in the investigated wavelengths range. Additional observations with DHM have concluded that during the observation time (15 min), the colorant had not significantly penetrated inside the cells, thus the modulation of the RI related to wavelength changes occurs only in the perfusion medium nm and not in the cells themselves. In its present implementation, the dual wavelength recording is performed sequentially (about 10 seconds are required for switching). The concept of recording simultaneously two holograms at different wavelengths has recently been demonstrated in reflection DHM by Kühn *et al.* and could be applied without adaptation to the proposed decoupling technique, thus making real-time imaging possible [KÖ7]. Simultaneous morphometric and refractive index measurement is a tremendous advantage of the present technique for dynamic cellular studies compared to the existing techniques [Kem06, Lue06, Cur05, Rap05]. In addition to the presented decoupling procedure, the modulation of the extracellular RI allowed by the technique presents a promising feature: by matching the extracellular RI and the cytoplasmic RI the contrast of intracellular organelles and structures will be greatly increased allowing their investigation.

This work has been supported by the Swiss National Science Foundation (grant n° 205320-112195/1). The authors also would like to thank the people at Lyncée Tec SA (www.lynceetec.com), PSE-A, CH-1015 Lausanne, for their dynamism and the fructuous discussions during the paper preparation. Benjamin Rappaz's and Florian Charrière's emails are respectively benjamin.rappaz@epfl.ch and florian.charriere@a3.epfl.ch

References

[Ahr71] R. K. Ahrenkiel. "Modified Kramers- Kronig analysis of optical spectra". J. Opt. Soc. Am. **61**(12): 1651–1655 (1971).

[Bar69] R. Barer. "Variation of refractive index of solutions with wavelength". J. Histochem. Cytochem. **17**(6): 423–424 (1969).

[Cha67] K. A. Chaubal, Z. Lodin and J. Pilny. "A New Approach to Determination of Thickness of Biological Specimens by 2 Wavelength Method Using Interference Microscopy". Acta Histochem. **26**(1): 131–143 (1967).

[Cha68] K. A. Chaubal, Z. Lodin and K. Korgaonkar. "Determination of difference in refractive index of cellular fluid at wavelengths of 436 and 546 mmu". J. Histochem. Cytochem. **16**(4): 271–272 (1968).

[Col06] T. Colomb, F. Montfort, J. Kühn, N. Aspert, E. Cuche, A. Marian, F. Charrière, S. Bourquin, P. Marquet and C. Depeursinge. "Numerical parametric lens for shifting, magnification and complete aberration compensation in digital holographic microscopy". J. Opt. Soc. Am. A **23**(12): 3177–3190 (2006).

[Cur05] C. L. Curl, C. J. Bellair, T. Harris, B. E. Allman, P. J. Harris, A. G. Stewart, A. Roberts, K. A. Nugent and L. M. D. Delbridge. "Refractive index measurement in viable cells using quantitative phase-amplitude microscopy and confocal microscopy". Cytometry **65A**(1): 88–92 (2005).

[KÖ7] J. Kühn, T. Colomb, F. Montfort, F. Charrière, Y. Emery, E. Cuche, P. Marquet and C. Depeursinge. "Real-time dual-wavelength digital holographic microscopy with a single hologram acquisition". Opt. Express **15**(12): 7231–7242 (2007).

[Kem06] B. Kemper, D. Carl, J. Schnekenburger, I. Bredebusch, M. Schafer, W. Domschke and G. von Bally. "Investigation of living pancreas tumor cells by digital holographic microscopy". Journal of Biomedical Optics **11**(3): 034005 (2006).

[Lue06] N. Lue, G. Popescu, T. Ikeda, R. R. Dasari, K. Badizadegan and M. S. Feld. "Live cell refractometry using microfluidic devices". Opt. Lett. **31**(18): 2759–2761 (2006).

[Mar05] P. Marquet, B. Rappaz, P. J. Magistretti, E. Cuche, Y. Emery, T. Colomb and C. Depeursinge. "Digital holographic microscopy: a noninvasive contrast imaging technique allowing quantitative visualization of living cells with subwavelength axial accuracy". Opt. Lett. **30**(5): 468–470 (2005).

[Rap05] B. Rappaz, P. Marquet, E. Cuche, Y. Emery, C. Depeursinge and P. J. Magistretti. "Measurement of the integral refractive index and dynamic cell morphometry of living cells with digital holographic microscopy". Opt. Express **13**(23): 9361 – 9373 (2005).

Chapter 7

Aberrations characterization of microscope objectives with digital holography

7.1 On the complex three-dimensional amplitude point spread function of lenses and microscope objectives: theoretical aspects, simulations and measurements by digital holography

Paper published in Journal of Microscopy **225**, 156-169 (2007).

Journal of Microscopy, Vol. 225, Pt 2 February 2007, pp. 156–169
Received 9 May 2006; accepted 21 September 2006

On the complex three-dimensional amplitude point spread function of lenses and microscope objectives: theoretical aspects, simulations and measurements by digital holography

A. MARIAN*[1], F. CHARRIÈRE*[1], T. COLOMB*, F. MONTFORT*, J. KÜHN*, P. MARQUET† & C. DEPEURSINGE*
**Ecole Polytechnique Fédérale de Lausanne (EPFL), Imaging and Applied Optics Institute, Station 17, CH-1015 Lausanne, Switzerland*
†Centre de neurosciences psychiatriques, Département de psychiatrie DP-CHUV, Site de Cery, CH-1008 Prilly-Lausanne, Switzerland

Key words. Aberrations identification, aberrations quantification, amplitude point spread function, diffraction models, digital holography, phase measurement, phase point spread function.

Summary

The point spread function is widely used to characterize the three-dimensional imaging capabilities of an optical system. Usually, attention is paid only to the intensity point spread function, whereas the phase point spread function is most often neglected because the phase information is not retrieved in noninterferometric imaging systems. However, phase point spread functions are needed to evaluate phase-sensitive imaging systems and we believe that phase data can play an essential role in the full aberrations' characterization. In this paper, standard diffraction models have been used for the computation of the complex amplitude point spread function. In particular, the Debye vectorial model has been used to compute the amplitude point spread function of $\times 63/0.85$ and $\times 100/1.3$ microscope objectives, exemplifying the phase point spread function specific for each polarization component of the electromagnetic field. The effect of aberrations on the phase point spread function is then analyzed for a microscope objective used under nondesigned conditions, by developing the Gibson model (Gibson & Lanni, 1991), modified to compute the three-dimensional amplitude point spread function in amplitude and phase. The results have revealed a novel anomalous phase behaviour in the presence of spherical aberration, providing access to the quantification of the aberrations.

Correspondence to: Florian Charrière. Ing. phys. dipl. EPFL, Imaging and Applied Optics Institute, BM 4.142, Station 17, CH-1015 Lausanne, Switzerland. Tel: +41 21 693 51 82; fax: +41 21 693 37 01; e-mail: florian.charriere@a3.epfl.ch

[1] These authors have contributed equally to this work.

This work mainly proposes a method to measure the complex three-dimensional amplitude point spread function of an optical imaging system. The approach consists in measuring and interpreting the amplitude point spread function by evaluating in amplitude and phase the image of a single emitting point, a 60-nm-diameter tip of a Near Field Scanning Optical Microscopy fibre, with an original digital holographic experimental setup. A single hologram gives access to the transverse amplitude point spread function. The three-dimensional amplitude point spread function is obtained by performing an axial scan of the Near Field Scanning Optical Microscopy fibre. The phase measurements accuracy is equivalent to $\lambda/60$ when the measurement is performed in air. The method capability is demonstrated on an Achroplan $\times 20$ microscope objective with 0.4 numerical aperture. A more complete study on a $\times 100$ microscope objective with 1.3 numerical aperture is also presented, in which measurements performed with our setup are compared with the prediction of an analytical aberrations model.

1. Introduction

1.1. Theory

Among the techniques available nowadays to characterize an optical imaging system, the point spread function (PSF) takes an important place. In the PSF approach, the object is decomposed into infinitesimal point sources and the image is determined as the superposition of the field distribution corresponding to each point-source object. The complex field distribution, corresponding to such a point-source object, is

defined as the amplitude point spread function (APSF) of the system, whose modulus squared gives the intensity or irradiance point spread function (IPSF) and whose phase gives the phase point spread function (PPSF). Usually, attention has been paid mainly on the IPSF, but the relevance of the PPSF has grown with the development of coherent or partially coherent microscopy techniques that allow phase measurements, including standard interferometric techniques (Mach-Zehnder, white-light, Linnick, etc.). In particular, the development of digital holographic microscopy (DHM) necessitates a thorough determination of APSF. Numerous studies have been performed to compensate for the phase aberrations inherent to coherent optical systems, mainly without *a priori* knowledge of either them or further theoretical analysis (see, e.g. Colomb *et al.*, 2006 which present a new aberrations compensation procedure, conjointly with a review of existing techniques). An appropriate understanding of phase aberrations, based on systematic theoretical analysis of the PPSF, may provide innovative aberrations compensation methods, from which the coherent imaging techniques like DMH will take advantage. Hanser *et al.*, and Braat *et al.*, have recently demonstrated the interest of theoretical PPSF, respectively, by characterizing a wide-field fluorescence microscope through its phase-retrieved pupil functions based on intensity measurement (Hanser *et al.*, 2004), and by retrieving the aberration function of high-NA optical systems with the so-called extended Nijboer–Zernike approach (Braat *et al.*, 2003). In their respective measurement of a lens APSF, Walford *et al.* (2002) and Dändliker *et al.* (2004), have shown how phase singularities, characterized by a phase jump of $\pm\pi$ on a closed path around the singularity ($\oint d\varphi = \pm 2\pi$) play a role in aberrations identification. The study of their 3D conformation has been shown to be closely correlated to the presence and type of aberrations.

The theoretical models used in calculation of the PSF of a lens are based on the diffraction theory. Integral expressions have been developed to compute the 3D diffraction pattern resulting from the diffraction of a circular aperture. A comprehensive review has been given by Gibson (Gibson & Lanni, 1989). They include scalar wave models for both on- and off-axis point sources, based on paraxial approximation. Similarly, vectorial models based on the electromagnetic field theory have been developed (Richards & Wolf, 1959), but for all models attention was paid essentially to the intensity distribution and the phase was generally not considered. Linfoot & Wolf (1956) gave a first detailed description of the 3D phase distribution near the focus of an aberration-free lens, by using the Lommel's functions to evaluate the diffraction integral. Based on the scalar diffraction theory, Farnell (1957) calculated the phase in the image region of a microwave lens and verified also his predictions by experimental measurements (Farnell, 1958). A more efficient way to calculate the intensity and phase distributions near the focus was obtained later by the recourse to fast Fourier transform. This may be applied in the Fraunhofer approximation where the diffraction integral can be viewed as a Fourier transform of the pupil function (Born & Wolf, 1980; Selligson, 1981; Mills & Thompson, 1986).

An optical system can hardly be totally aberration free. Even if primary optical aberrations are well corrected, as in a high quality and expensive microscope objectives (MOs), aberrations can still result from residual misalignment and slight imperfections of the optics. But more often, they are caused by their inappropriate use in nondesigned conditions such as inadequate cover slip thickness, cover slip refractive index or immersion oil refractive index. They can even arise from the specimen under investigation, generally because of focusing media refractive index mismatch. The aberrations theory has been addressed by many authors (see, e.g. Born & Wolf, 1980). The occurrence of aberrations when a MO is used under inappropriate conditions has been analyzed in detail by Gibson (Gibson & Lanni, 1991), who proposed a simple model, based on the scalar diffraction theory and geometrical optics calculations, in order to quantify these aberrations. The same problem, that is, the focusing through dielectric interfaces with different thicknesses and refractive indices, has been treated in a general context by Török (Török & Varga, 1997; Török, 1998), who developed a rigorous model based on the vectorial theory. Recently, Haeberlé combined the Gibson and the Török models and formulated a very accurate and easy-to-use expression for conventional microscopy (Haeberlé, 2003). All these papers predict only the aberrated IPSF and only few works present the PPSF in the presence of primary aberrations (Selligson, 1981; Mills & Thompson, 1986), for low and moderate NA systems.

In coherent microscopy, DHM in particular, a variety of irradiation schemes may be considered: collimated beam (plane wave), as well as focussed beam (spherical wave). We, therefore focus, in the present paper, on the main component of the microscope which is the MO, lead by the idea of obtaining valuable information in amplitude and phase for a later use in aberrations compensation in DHM. Calculation results of both the IPSF and the PPSF are given in the presence of aberrations for high NA MO in some selected cases. A more complete and systematic review of the phase behaviour for each type of aberration has been carried out by Marian (2005).

1.2. APSF measurement techniques

Usually the PSF is measured by acquiring images of small fluorescent beads with diameter under the instrument resolution limit (Gibson & Lanni, 1991). This method was successfully applied, for the measurement of the axial PSF intended to be used in deconvolution and optical sectioning microscopy (Gibson & Lanni, 1991). The main drawback of this experimentally measured PSF is the low signal-to-noise ratio resulting mainly from the shot noise due to the low-intensity signal provided by such small objects. On the other hand, the PSF is measured on a separate setup, under

nondesigned optical conditions of the microscope, which can be quite different from the experimental imaging conditions. In addition to the required presence of small and isolated structure in the sample, the accuracy of the method decreases under deep specimen imaging conditions.

Anyway, all these measurements only take into account the IPSF, neglecting the phase which can play an essential role, for example, in quantifying the aberrations present in the system to completely characterize a lens or a MO. Selligson (1981) proposed already, a method based on a Mach-Zender interferometer, allowing measuring the IPSF and PPSF of lenses subjected to classical aberrations. However, his method requires a point-to-point scan of the focal region and was quite slow at that time, taking up to 20 min for a grid of 32×32 points and, therefore, needing a carefully stabilized measuring system. Schrader (Schrader & Hell, 1996), Juskaitis (Juskaitis & Wilson, 1998) and Walford (Walford *et al.*, 2002) also proposed to record an interference image of a point object, but several images are necessary to reach this goal and a 3D scan of the focal region is also required. Another approach consists of evaluating the complex wavefront at the exit pupil of the MO: Beverage used a Shack-Hartmann wavefront sensor to directly measure the pupil function combined with a Fourier transform calculus to recover its PSF (Beverage *et al.*, 2002) and Török used a Twyman-Green interferometer for measurement and the Debye–Wolf diffraction theory to predict the complex APSF (Török & Fu-Jen, 2002). It is also possible to retrieve the phase from intensity measurements only: Hanser (Hanser *et al.*, 2004) obtained the complex pupil function from defocused IPSF images of subresolution beads with a phase-retrieval algorithm, whereas Braat *et al.* (2003) retrieved the aberration function of high-NA optical systems with the so-called extended Nijboer–Zernike approach. Dändliker *et al.* (2004) measured the APSF of a microlens with a Mach-Zehnder interferometer modified to obtain high spatial accuracy. The microlens is illuminated by a plane wave and moved three-dimensionally is the system to record the 3D APSF, requiring, therefore, no subresolution object.

We propose here an experimental setup, capable to measure the 3D complex APSF of a first-degree optical system, like a simple lens or a complex MO. The method is derived from digital holography, specifically from DHM, where a MO is inserted in the object arm of an off-axis holographic setup (Cuche *et al.*, 1999). The DHM allows to measure the transverse IPSF and PPSF from a single recorded hologram, whereas at least three images are required with a common phase-shifting techniques used, for example, by Selligson (1981) or Dändliker *et al.* (2004). The axial IPSF and PPSF are obtained by performing a fast nanometre step z-scan within a range of tenths of micrometres and acquiring the corresponding stack of holograms at video rate. The originality of the method lies in its capacity to record the full 3D APSF from a rapid 1D z-scan, minimizing, therefore, the noise contribution from external perturbations during the measurements. The scanning rate is currently limited by the charge coupled device (CCD) frame rate (25 Hz), and could be drastically improved with a faster CCD. The integration time for a single hologram is in the millisecond range with the current 100 mW laser source. To assess accurate estimation of the axial PPSF, the temporal stability of the system during the holograms stack acquisition is monitored thanks to a second holographic setup inserted in the system.

2. Theoretical models for the calculation of the ideal 3D APSF

Different methods can be used to evaluate the diffraction integral and, therefore, to calculate the 3D APSF of a first-order optical system, where the optical system could be a simple lens as well as a MO represented by its equivalent lens. For example, in the scalar Debye theory, based on the Debye approximation (see Gu, 2000), the field in the focal plane $U(P_2)$ is expressed as a superposition of plane waves of different propagation directions $\vec{s}$ within the solid angle Ω subtended by the lens (see Fig. 1):

$$U(P_2) = \frac{i}{\lambda} \int\int_{\Omega} P(P_1) \exp[i\varphi(P_1)] \exp(-ik\vec{s} \cdot \vec{r}_2)\, d\Omega, \tag{1}$$

where $P(P_1)$ represents the apodization function in the lens plane (Innes & Bloom, 1966; Gu, 2000), $\vec{r}_2$ gives the position of the observation point in the focal plane, λ is the wavelength and k is the wavenumber defined as $k = 2\pi/\lambda$ $\exp[i\varphi(P_1)]$, corresponding to the phase aberration function in the pupil plane, may be developed in terms of standard polynomials or Zernike polynomials to distinguish the contribution of each aberration type (spherical, coma, astigmatism, etc.). In this equation, as well as in the rest of the paper, the time dependence of the field $\exp(-i\omega t)$ has been implicitly assumed.

The Debye theory combines in this way the geometrical and the wave optics, because all the individual plane waves

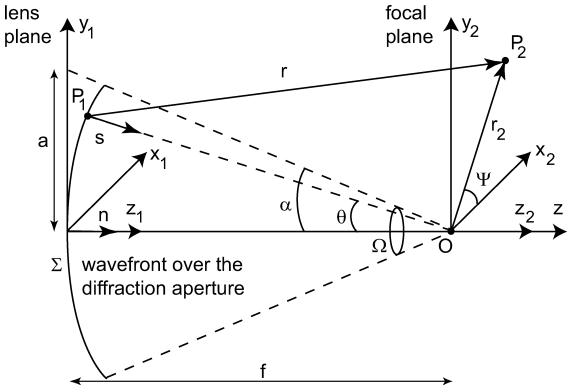

Fig. 1. Scalar Debye theory: focusing of a spherical wave through a lens of focal f, half-aperture a, maximum subtended half angle α.

can be seen as corresponding to the optical rays from the geometrical optics. The Debye integral generally is valid for Fresnel numbers much larger than unity (Wolf & Li, 1981) and in addition, the observation point must be close to the optical axis, especially when aberrations are present in the system (Sheppard, 2000). Within the paraxial limit $\sin\ \theta \approx \theta$ (Fig. 1), the scalar Debye theory can be consequently simplified, leading to an expression similar to that obtained in the Fresnel approximation (Gu, 2000). A comparison between these two theories (Marian, 2005) shows that significant discrepancies appear if a higher NA is considered (above 0.65). The two models yield comparable results for lower NA, with an easier implementation and a reduced calculation time if the paraxial model is used.

The Debye theory can be generalized in a vectorial form, by taking into account the vectorial nature of the electromagnetic field and the polarization state of the incident field (Ignatowsky, 1919; Richards & Wolf, 1959; Luneburg, 1966). The simulations presented here are based on this theory. The advantage of using the vectorial theory as a first choice is the accuracy in predicting specific features of high NA systems such as apodization and depolarization effects (Gu, 2000), or symmetry break in the focal point (Dorn *et al.*, 2003).

We have considered here the case of an incident field linearly polarized in the x direction, but the expressions could be generalized for any arbitrary polarization state (Mansuripur, 2002). Even if the incident field had a component only along the x direction, the field at the focal plane will have components along all the three directions x (unit vector $\vec{i}$), y (unit vector $\vec{j}$) and z (unit vector $\vec{k}$) (Fig. 2) and for a specific position can be calculated as follows (Gu, 2000):

$$\vec{E}(r_2, z_2, \psi) = \frac{\pi i}{\lambda}\{[i_0 + i_2\cos(2\psi)]\vec{i} + i_2\sin(2\psi)\vec{j} + 2ii_1\cos\psi\vec{k}\}, \tag{2}$$

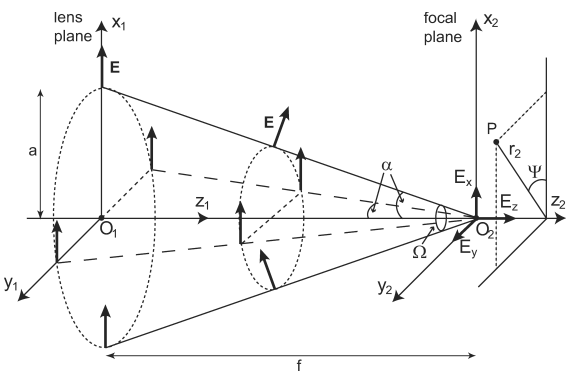

Fig. 2. Vectorial model: focusing of a linearly polarized (x direction) beam through a lens of focal length f, half-aperture a, maximum subtended half angle α.

where (r_2, z_2) are the radial and axial coordinates of the observation point at the focal plane relative to the focus point and ψ is the azimuth angle defining the radial direction r_2. When $\psi = 0$, the direction is along the vertical x axis, whereas for $\psi = \pi/2$ the direction is along the horizontal y axis. The definition of this angle is important in the vectorial theory where the symmetry about the optical axis in the focal plane is broken due to the depolarization effect, unlike in the scalar model.

i_0, i_1, i_2 are three integrals expressed as follows:

$$\begin{aligned} i_0 &= \int_0^\alpha P(\theta)\sin\theta(1+\cos\theta)J_0(kr_2\sin\theta) \\ &\quad \times \exp(-ikz_2\cos\theta)\,d\theta, \\ i_1 &= \int_0^\alpha P(\theta)(\sin\theta)^2 J_1(kr_2\sin\theta) \\ &\quad \times \exp(-ikz_2\cos\theta)\,d\theta, \\ i_2 &= \int_0^\alpha P(\theta)\sin\theta(1-\cos\theta)J_2(kr_2\sin\theta) \\ &\quad \times \exp(-ikz_2\cos\theta)\,d\theta, \end{aligned} \tag{3}$$

where J_0, J_1, J_2 are the Bessel function of the first kind and of the zero, first and, respectively, second order and the function $P(\theta) = \sqrt{\cos\theta}\exp[i\varphi(\theta)]$ represents the pupil aberration function in which $\sqrt{\cos\theta}$ is the apodization function for a system obeying the Abbe sine condition (Innes & Bloom, 1966; Gu, 2000), like a MO. The Abbe sine condition that is satisfied for all MOs, permits considering, within this vectorial theory, large angles that are not compatible with a paraxial approximation.

The presence of the three components in the image plane:

$$\begin{aligned} E_x &= \frac{\pi i}{\lambda}\left[i_0 + i_2\cos(2\psi)\right], \\ E_y &= \frac{\pi i}{\lambda} i_2\sin(2\psi), \\ E_z &= \frac{\pi i}{\lambda} 2ii_1\cos\psi, \end{aligned} \tag{4}$$

leads consequently to three intensity components I_x, I_y, I_z and three phases P_x, P_y, P_z that must be considered as independent.

To illustrate the result of vectorial theory, Fig. 3 presents the intensity and the phase distributions for each component in the focal plane of a ×63 MO with 0.85 NA. The wavelength for the calculations was $\lambda = 532$ nm, and calculations were performed on a $4 \times 4\ \mu m^2$ surface in the xy plane. The structure of each component can be explained by simple geometrical considerations. In our particular case the incident electric vector oscillates along the x direction and, after the refraction by the lens, it is bent in accordance to the refraction law. Consequently, the field at the focus contains not only components with the same polarization as the incident one

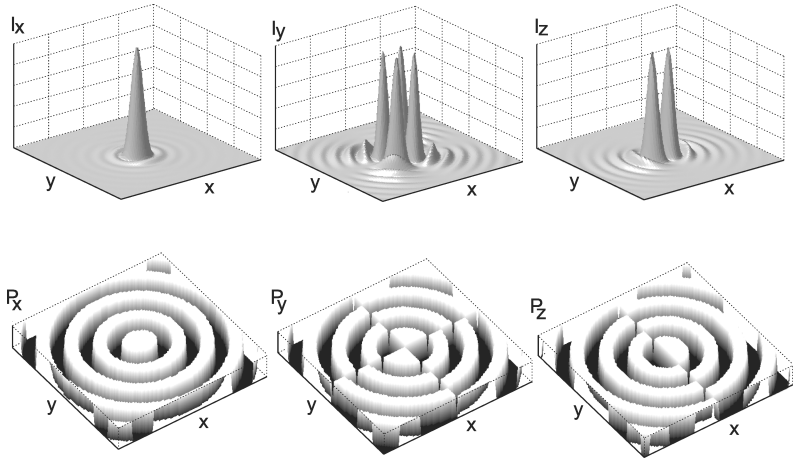

Fig. 3. The *x*-, *y*- and *z*-components of the vectorial transverse APSF (*xy*) for a ×63/0.85 MO. I_x: I_y: I_z, are in proportion of, respectively, 1: 0.0032: 0.1290. Calculations were performed on a 4×4 mm^2 surface in the *xy* plane for all the component. The intensity distributions are normalized, the phase distributions are coded between $-\pi$ = black and $+\pi$ = white.

(*x* direction), but also orthogonal (*y* direction) and longitudinal (*z* direction) components. This effect is called depolarization, as the electric vector looses its initial polarization state. In Fig. 2, one can observe that the rays in the *yz* plane will contribute only to I_x component, the rays in the *xz* plane will contribute to both the I_x and I_z components, whereas the intermediate rays situated between these planes bring contributions to all the three components I_x, I_y and I_z. The I_x distribution in the *xy* plane is obtained by superposition of all the *x* components from each ray and the same reasoning holds for the I_y and I_z distribution. In Fig. 3, the absence of the I_y and I_z in the *yz* plane is illustrated with the apparition of a zero intensity line along the *y* direction in the I_y and I_z distributions. Similarly, the absence of the I_y component in the *xz* plane explains the dark line along the *x* direction in the I_y distribution.

The total intensity *I* in the focal plane (the transverse IPSF) can be calculated as the sum of the intensity components

$$\begin{aligned} I &= \vec{E}\,\vec{E}^{*} \\ &= (E_x\vec{i} + E_y\vec{j} + E_z\vec{k})(E_x\vec{i} + E_y\vec{j} + E_z\vec{k})^{*} \\ &= |E_x|^2 + \left|E_y\right|^2 + |E_z|^2 \\ &= I_x + I_y + I_z, \end{aligned} \tag{5}$$

but it is undoubtedly improper to define a 'total phase', as the phase of the resulting vectorial field $\vec{E}$, because its orientation is continuously changing. Consequently, the phase of each component P_x, P_y and P_z must be considered apart and calculated as such. Because of the uneven contributions coming from each component, the resulting total intensity in the focal plane does not present a radial symmetry any more but exhibits a radial elliptical distribution. The weights of each component of the total intensity are not equally distributed and for the case of the ×63/0.85 MO considered as typical example, the maximum intensity components ratio I_x: I_y: I_z, taken at the focus, are in proportion of, respectively, 1: 0.0032: 0.1290. These ratios depend on the NA, with increasing weights of I_y and I_z increasing for increasing NA, and observing that the radial elliptical deformation becomes more pronounced as NA increases.

Note that for small NA, the depolarization effect is very small and even disappears, resulting from the fact that for small angles, $J_1(kr_2 \sin\theta)$ and $J_2(kr_2 \sin\theta)$ become negligible compared to $J_0(kr_2 \sin\theta)$. Therefore, the field at the focus (see Eq. 3) can be reasonably approximated by the scalar expression $E(r_2, z_2, \psi) \cong \frac{\pi i}{\lambda} I_0$.

In the case of high NA, I_y is negligible compared to I_x and I_z, and one can observe that the main lobe of the total intensity distribution is essentially broadened because of the depolarization effect observable in the *x* direction, that is, the direction of polarization, whereas the *yz* distribution is nearly similar to the *yz* distribution obtained with the scalar model (Marian, 2005). Therefore, an ellipse can be defined with two orthogonal axes measured by the FWHM (full width at half maximum) of the central lobe of the radial IPSF, along the *x* direction profile (for $y = 0$) and, respectively, along the *y* direction profile (for $x = 0$). Then an ellipticity factor can be calculated as the difference in length between the two axes of the ellipse, expressed in percent relatively to the axis length not affected by the depolarization effect (*y* axis in the case of a *x*-polarized light). A quantitative comparison shows that for low numerical apertures, this factor is in order of 2.8% for a 0.35 NA (≈20° subtended half angle) and, respectively, 6.2% for a 0.5 NA (≈30° subtended half angle). The deviation increases significantly with the NA. For an immersion oil ×100 with 1.3 NA MO (≈70° subtended half angle), it reaches 30%. We can objectivize the physical limit to the scalar model if

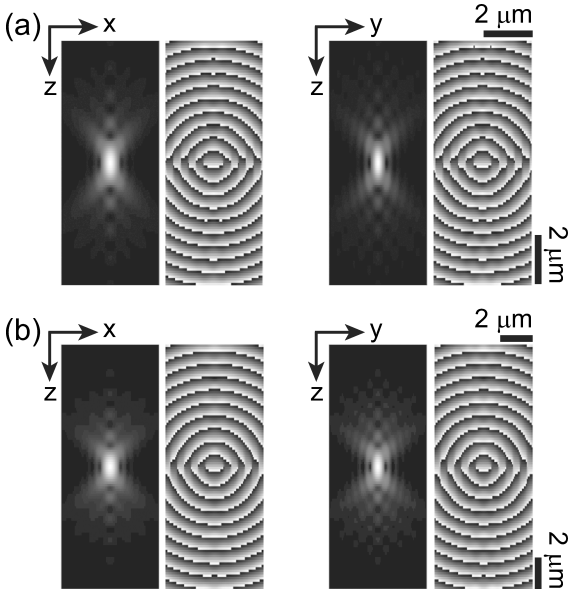

Fig. 4. APSF computed in the axial direction with the vectorial model for a ×63/0.85 MO (a) and a ×100/1.3 MO (b). The intensity distributions are enhanced by a nonlinear distribution of the grey levels, the phase distributions are coded in 8 bits between $-\pi$ = black and $+\pi$ = white.

we consider as tolerable a maximal error corresponding to an ellipticity factor of 10%. This deviation corresponds to a 0.65 NA (≈40° subtended half angle), above which the use of the vectorial model is imposed for an accurate APSF description. However, the above considerations are valid for a linear incident polarization only, whereas in the case of an unpolarized beam, an average among all the polarization states occurs and the scalar model can be still used.

Figure 4 presents the axial APSF (total intensity I and phase x component P_x) calculated for a an ×63/0.85 MO (Fig. 4a) and, respectively, a ×100/1.3 MO used with a 1.518 immersion oil (Fig. 4b). The simulations were performed using the vectorial theory. We have named axial APSF an axial section along the optical axis through the 3D APSF, whereas the transverse APSF is the xy section at the focal point through the 3D APSF. We present here both the xz and the yz sections. Concerning the phase images, only the P_x component is represented. In the yz plane ($\psi = \pi/2$), because there is only an x-component contribution as already discussed before, only P_x is defined, whereas in the xz plane ($\psi = 0$), both P_x and P_z appear due to the x and z contributions. No y component appears in these plans and, therefore, P_y is not defined. If we consider an intermediate section between xz and yz, for example, for $\psi = \pi/4$, all three phases P_x, P_y, P_z are defined separately. It is in principle possible to measure individually each polarization component in amplitude and phase, for instance by using a dedicated holographic setup (see further) with the appropriate polarization state in the reference beam interfering with the field emerging from the lens.

3. The 3D APSF in the presence of aberrations

Aberrations are present in most optical imaging systems: lenses, lenses assembly and MO. They are generally a consequence of the fabrication process; spherical aberrations in particular are due to grinding and polishing process of the lens which naturally tends to produce spherical surfaces. These aberrations are usually compensated by the recourse to the assembly of several lenses having complementary geometrical and dielectric characteristics. Other types of aberrations appear when the focused beam crosses one or several dielectric layers, for which the MO has not been designed. To analyze the aberrations appearing when a MO is used under inappropriate conditions, Gibson (Gibson & Lanni, 1991) proposed a simple approach, based on the scalar diffraction theory and geometrical optics calculations. The aberration function is obtained through a calculation involving the ideal design parameters of the MO (cover slip refractive index, cover slip thickness, immersion oil refractive index) and their effective value. The simulations presented here were obtained by implementing the approach suggested by Haeberlé (2003), who combined the Gibson and the vectorial Török models. Figure 5 summarizes the results of the simulations of the APSF of a ×100 MO with 1.3 NA, with nonpolarized light, used under different conditions. If nonpolarized light is diffracted by the MO, the birefringence caused by the high NA MO would mix the cross-polarized components of the beam, while keeping a nonzero correlation among the cross-polarized components of the beam. Therefore, the cross-polarized components of the outgoing beam would cancel out for statistical reason, because the cross-polarized component of the emitted field would be uncorrelated. Therefore, the use of nonpolarized light ensures

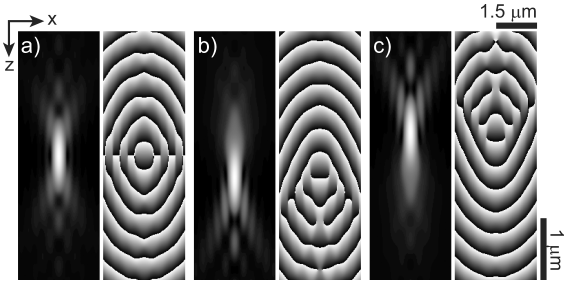

Fig. 5. Axial APSF (xz) examples when the cover slip and the immersion oil refractive index are varied according to Gibson model: ideal case ng = 1.525, ni = 1.518 (a), cover slip refractive index is varied ng = 1.530 (b), immersion oil refractive index is varied ni = 1.514 (c). The MO considered here was ×100/1.30. The intensity distributions are enhanced by a nonlinear distribution of the grey levels, the phase distributions are coded in eight bits between $-\pi$ = black and $+\pi$ = white.

the phase map to be identical for all the possible polarization orientations of the reference wave; hence, only one is presented in Fig. 5. The design conditions of the MO are defined by an immersion oil of refractive index equal to 1.518 and a cover slip of 0.17-mm thickness and 1.525 refractive index (standard value for some manufacturers). In this case, the APSF is perfectly symmetric, both transversally and axially (Fig. 5a), as predicted in the case of nonaberrated APSF. Any small deviation from the ideal conditions leads to significant aberrations (Fig. 5b and c). The main lobe of the APSF is shifted from the central position (Fig. 5b and c), which indicates the presence of spherical aberration. It was proved (Gibson, 1991) that high-order spherical aberrations are necessary to describe properly this kind of aberrations. For example, the aberrations induced by the immersion oil refractive index variation can be properly described by using third- and fifth-order spherical aberration, whereas the use of a nondesigned cover slip requires third-, fifth-, seventh- and even more higher-order spherical aberration. It was also observed that the cover slip thickness variation has only a small influence, whereas the cover slip refractive index variation affects drastically the APSF, even for very small variation about 0.001. Figure 5 shows these aberration effects, when the refractive index of the immersion oil was changed from the ideal 1.518 value to 1.514 (Fig. 5b) and when the refractive index of the cover slip was changed from 1.525 to 1.530 (Fig. 5c). For Fig. 5b and c, the corresponding aberration function expressed in term of Zernike coefficients contains mainly the so-called power [$Z_3 = 3^{1/2}(2x^2 + 2y^2 - 1)$] and primary spherical [$Z_{10} = 5^{1/2}(6(x^4 + 2x^2y^2 + y^4 - x^2 - y^2) + 1)$] aberrations, the other coefficients being in those cases negligible. The coefficients values are $Z_3 = 2.36$ and $Z_{10} = -0.56$ for Fig. 5b, respectively, and $Z_3 = -1.96$ and $Z_{10} = -0.48$ for Fig. 5c. The high sensitivity related to the immersion oil refractive index suggests that high attention must be paid at the rapid change of the immersion oil refractive index with the wavelength (about 0.01 throughout the visible spectrum) or due to the temperature variations (about −0.0004 per additional degree). Concerning the cover slip, we must mention also that MOs can be found which include a correction collar to compensate for the cover slip thickness variation. This is done by a slight displacement of some lenses that compose the objective. However, because of the large number of orders of spherical aberration appearing (Gibson, 1991), it is unlikely that the movement of a small number of lenses would be sufficient to compensate for all of the significant orders of the spherical aberration introduced.

As an example of the interest and use of the phase (PPSF) modifications induced by optical aberrations, the following situation has been treated: theoretical calculations of the phase variations along the optical axis have been performed in the presence of aberrations and compared to the absence of aberrations, for the same 100× 1.3 NA MO as above. The results are presented in Fig. 6. Indeed, it is usually expected that the phase increases linearly along the optical

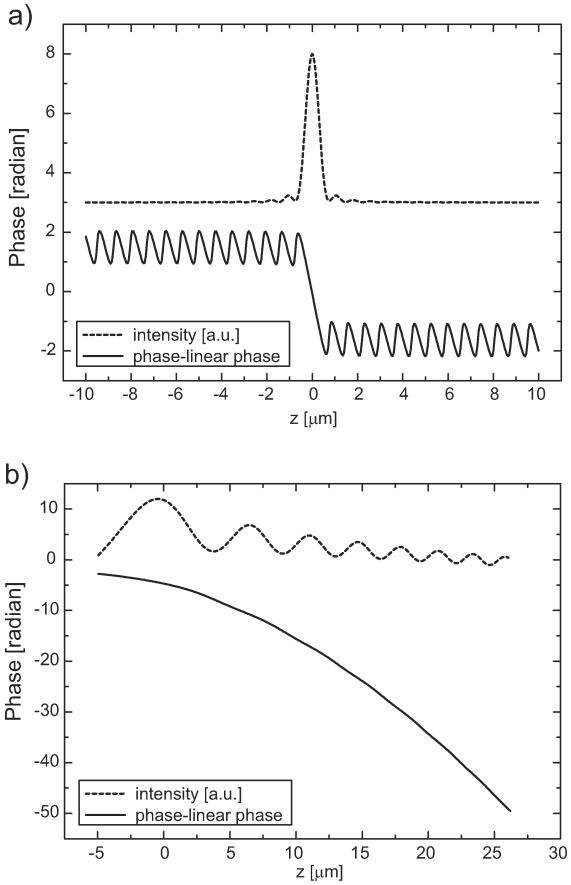

Fig. 6. Axial profiles through the *xz* section of the IPSF and PPSF for the ×100/1.30 MO, without (a) and with (b) spherical aberrations induced by the use of nondesigned parameters (cover slip, immersion oil). A linear phase corresponding to the displacement along the optical axis has been subtracted in both (a) and (b) to enhance the anomalous phase behaviour in presence of aberration.

axis, proportionally to the displacement, but modulated by the so-called phase anomaly at each passage through an intensity minimum on the optical axis (see, e.g. Farnell, 1958; Born & Wolf, 1980). In the designed conditions, the subtraction of a linear phase from the axial phase leads as expected (Fig. 6a) to the observation of a 2π rapid phase shift for the main axial intensity lobe, and phase jumps smaller than π for all the others secondary lobes. But the phase, except for the modulations described above, remains proportional to the displacement along the optical axis. This is no more the case in the presence of aberrations, where the proportionality is not preserved, as can be seen from Fig. 6b, where is presented a simulation of the axial APSF in the presence of the high-order spherical aberrations induced by the absence of appropriate cover slip and immersion oil. The axial phase, from which the same

linear phase has been subtracted, diverges rapidly from the linear phase when going away from the main intensity lobe. Furthermore, the phase anomalies associated with the passage through the axial intensity minima are weakened and the intensity minima being less deep compared to the designed case, and cannot be distinguished anymore. An experimental verification for this case will be presented further in the paper. These first results suggest that these anomalies in the phase axial phase profile could be exploited to identify the aberrations and possibly to quantify their presence. A more complete and systematic study of the phase nonlinearity, comparable to the ones conducted by Farnell (1958) in the case of microwaves lenses, could be developed and lead to the identification of the aberrations, possibly to quantify their presence from their axial phase profile.

4. APSF measurement

4.1. Experimental setup

Our setup is based on a Mach-Zehnder interferometer configuration. In the object arm, a point-source object is imaged through the MO or through the lens to characterize. (Fig. 7). As a point source we use a near field scanning optical microscopy (NSOM) fibre, with a 60-nm-diameter emitting tip. The light source is a $\lambda = 532$ nm laser (frequency-doubled Nd: YAG) with adjustable power up to 100 mW and the laser is coupled in the optical fibre by a lens. The MO is mounted on micrometric *xyz* platforms combined with tilt facilities, allowing for proper alignment of the MO to avoid aberrations coming from the setup misalignment. Fine fibre movements, are achieved by a piezoelectric *xyz* stage, which permits nanometric displacements (1 step = 1.22 nm, within a range of 80 μm). A CCD camera (CCD1) is positioned at a large distance of about 1500 mm to create a sufficiently high magnification (about 1000× for a 100× MO) image of the point object,

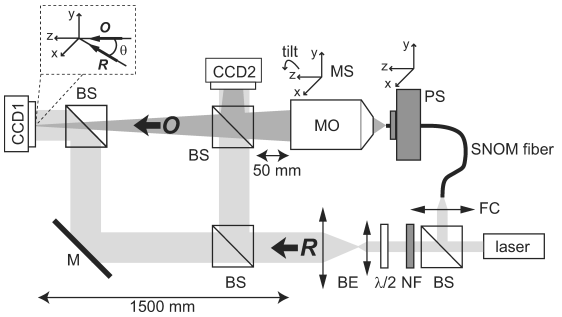

Fig. 7. Experimental setup for the APSF measurement: BS beam-splitter, BE beam expander, NF neutral density filter, λ/2 half-wave plate, M mirror, FC fibre coupling lens, PS piezo system, MS micrometric stage, MO microscope objective, *O* object wave, *R* reference wave. Inset: a detail showing the off-axis geometry at the incidence on the CCD.

in order to obtain an optimal sampling by the CCD sensitive area (512 × 512 pixels, pixel size 6.7 μm) of the diffraction pattern spatial distribution. As the MOs are now commonly infinity corrected, this large distance also ensures a correct use of the MO, that is, a correct working distance. The setup includes also a second CCD camera (CCD2), which is used for alignments purposes: the MO needs to be carefully aligned on the optical axis defined by the *z*-scanning direction of the fibre and the position the CCD1 to assure a correct characterization of the MO without external influences coming from the setup misalignments imperfections (tilt, coma, astigmatism). This alignment procedure is revealed to be significantly facilitated when the pupil of the MO is monitored on CCD2. Indeed, due to the large image distance of 1500 mm, a small tilt change of the MO moves the image out of the CCD1. CCD2 is also used to estimate the setup stability during the *z*-scan, as it will be pointed out further.

The reference wave **R** is first enlarged by using a beam-expander, and then combined, by means of a beam-splitter, with the object wave **O** emerging directly from the MO. An off-axis geometry was considered on both CCDs, which means that **O** and **R** impinge the hologram plane with different angles (see inset Fig. 7). The angle between **O** and **R** must be chosen in order to obtain fringes correctly sampled by the CCD camera. Neutral density filters were used to adjust the light intensity in the reference arm. The adjustment of the intensity ratio between **R** and **O** is essential in order to obtain high contrasts images (Charrière *et al.*, 2006). A half-wave plate was also inserted in the setup to control the polarization state in the reference arm, aiming at maximizing the fringes contrast on the hologram. Experimentally, no important change on the hologram fringes contrast is observed when rotating the half-wave plate, attesting for nearly circularly polarized light outgoing of the NSOM tip in the object arm. A remark on the exactness of the method needs to be done: to measure what corresponds to the exact definition of the APSF of the MO, one should in principle scan the image field, that is, moving CCD2, with the NSOM tip remaining fixed in the focus of the MO. Measuring the APSF for a fix image plan and a moving NSOM tip adds little aberration, as the MO is aberration free for only the focus position, but the added aberration remains somehow negligible with regard to the short excursion of the *z*-scan. Furthermore, moving with an interferometric precision the NSOM tip is easily achieved with the piezoelectric *xyz* stage; by scanning the image field, the scanning range would be increased by the square of the optical system magnification, reaching centimetres or even metres with a magnification of 1000, making the interferometric measurement extremely difficult if not impossible.

4.2. Holograms reconstruction

In digital holography a CCD camera is used to record the hologram, instead of a photographic plate or photorefractive

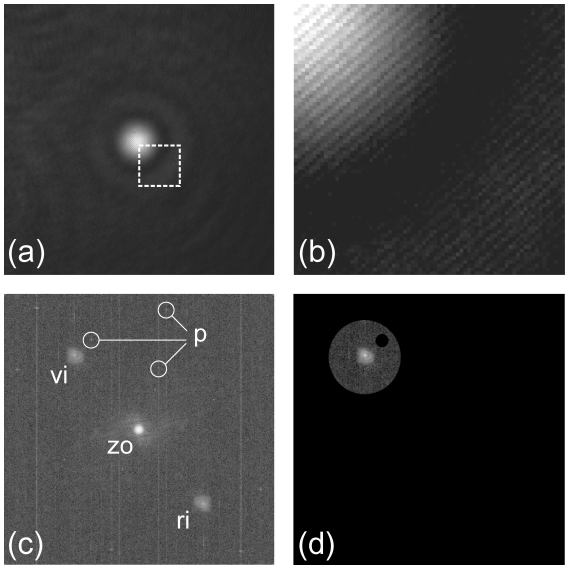

Fig. 8. (a) Example of an experimental 512 × 512 8-bits hologram; (b) a zoom, corresponding to the dashed square of (a), where the interference fringes appear more visible; (c) the Fourier spectrum of (a) containing the zero order (zo), the real image (ri), the virtual image (vi) and also parasitic interferences spatial frequencies (p); (d) Fourier spectrum after application of the bandpass filter.

crystal traditionally used in classical optical holography. The hologram (Fig. 8a and b) is formed by the interference between the wave field diffracted from the object to be analyzed, that is, the object wave **O** and a reference wave **R** provided from the same source, in order to keep the coherence properties. The hologram intensity is given by:

$$I_H(x, y) = |\mathbf{R}|^2 + |\mathbf{O}|^2 + \mathbf{R}^*\mathbf{O} + \mathbf{R}\mathbf{O}^*, \qquad (6)$$

where $\mathbf{R}^*$ and $\mathbf{O}^*$ denote the complex conjugates of the reference wave and, respectively, the object wave. The digital hologram, resulting from the 2D sampling of $I_H(x,y)$ by the CCD camera, is transmitted to a computer where the hologram reconstruction is numerically performed.

Our reconstruction process consists in evaluating the interferogram using a Fourier-transform method (Malacara & De Vore, 1992) with the following steps. In a first step, we compute the Fourier transform (Fig. 8c) of the hologram. In a second step, only the $\mathbf{R}^*\mathbf{O}$ or the $\mathbf{R}\mathbf{O}^*$ spatial frequencies are selected in the amplitude spectrum, by applying a simple filter (Fig. 8d). Due to the off-axis geometry, these spatial frequencies are separated in the Fourier plane, symmetrically located with respect to the zero-order spatial frequencies. The larger the angle θ between R and O is, the better the separation between these spatial frequencies terms will be. In this filter process, we use a filter with a bandwidth as close as possible to the $\mathbf{R}^*\mathbf{O}$ or $\mathbf{R}\mathbf{O}^*$ bandwidth, in order to keep a maximum of high frequencies and consequently a maximum of details in the reconstructed image. Moreover this filter allows eliminating the influence of parasitic reflections (Fig. 8c) that are not detectable in the hologram due to their low intensity but are clearly visible in the spectrum. The third step simulates the re-illumination of the hologram with the reference wave, considering that in the Fourier space this multiplication by **R** corresponds to a translation of the selected frequencies to the centre of the Fourier plane. This procedure must be carefully achieved in order to avoid the introduction of any phase error during the reconstruction. It is performed by an automatic algorithm described in (Colomb *et al.*, 2006). Briefly, this algorithm is based on a calibration on a constant phase surface, which is, in our case, obtained by an important defocus of the NSOM point source: the NSOM point is moved away from the focal point till the object wave recorded on CCD1 corresponds to a cut-off portion of a slowly converging or diverging spherical wave (Wang *et al.*, 1995), where the phase can be assumed to be constant on a transversal plane. Once this calibration of the system is done, the entire stack of holograms is processed in the same way. In a last step, the complex amplitude (i.e. the APSF) is obtained by an inverse Fourier transform and the IPSF and PPSF are afterwards extracted as the modulus squared and the argument of the APSF. The intensity and phase information can be separated in two different images (see, e.g.Fig. 11b), even though only a single hologram is required to restore them. The accuracy in a phase transverse distribution was assessed at about $\lambda/60$ for transmission measurement conducted in air or $\lambda/40$ for oil immersion with a refractive index of 1.518 consistently with the results presented further. We also mention that the values extracted for the PPSF are quantitative values modulus 2π, whereas the IPSF values are extracted up to a multiplicative constant that depends on the intensity of the reference wave.

4.3. Setup stability

The measurement of the axial APSF may require a *z*-scan of the point object. During this scan, a stack of holograms is obtained by scanning the NSOM tip along the optical axis within a range of tenths of micrometres and with a well-controlled step accuracy of a few nanometres. Each hologram is afterwards reconstructed, following the aforementioned reconstruction process. Consequently, the axial intensity and phase can be estimated. The acquisition of a hologram stack, performed at 25 Hz, takes from seconds to a few minutes, depending on the considered step and range. Therefore, stability must be ensured during the hologram stack acquisition, to provide accurate estimation of the axial PPSF.

As in all interferometric techniques, many factors can affect the phase measurement, principally mechanical vibrations and air turbulences. To overcome these drawbacks, the system was isolated on an antivibratory bench, and the whole stage

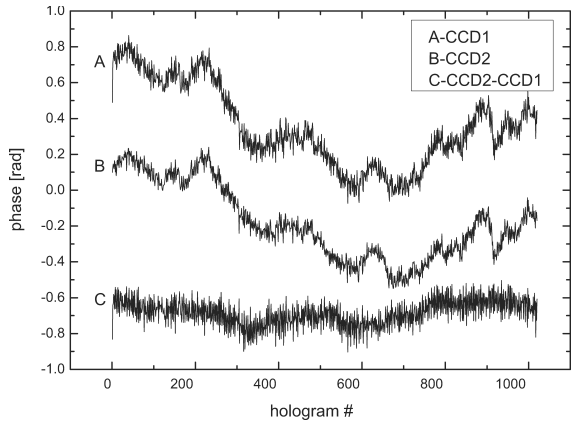

Fig. 9. Temporal phase fluctuations at CCD1, CCD2, and the phase difference between the to phases (1000 holograms recorded in 40 s).

was also protected from air turbulences by curtains. Moreover, the object and the reference arms were also surrounded by plexiglas tubes to minimize the perturbations coming from air turbulences. The particular choice of positioning CCD2 very close to the MO output pupil and the fact of synchronizing it with CCD1 by an external trigger, permit the precise determination and monitoring of the phase fluctuations, which appear along the **O** and **R** paths, and along the fibre of the NSOM tip in particular.

A static measure was performed, that is, the NSOM fibre was kept at the same position and a holograms stack was acquired during a time laps equal with the one estimated for an axial *z*-scan (40 s for 1000 holograms). The holograms recorded by both CCD1 and CCD2 were reconstructed, according to the previously described reconstruction process, and the time fluctuations of the phase were measured and averaged over a small region of about 30×30 pixels. The results are presented in Fig. 9 where it can be noticed that the CCD1 and CCD2 signals are well correlated, with a temporal standard deviation of 0.071 radians (4.11°) calculated onto the difference between the two phase signals. This means that the temporal phase fluctuations observed on the two CCDs are similar, and that no additional noise disturbs the waves along the lengthy path to CCD1.

CCD2, positioned very close to the MO, intercepts the object wave sufficiently far from the focal point (around 1500 mm), so that the wave can be considered as behaving as a cut-off portion of a uniform spherical wave (Wang *et al.*, 1995). Therefore, any displacement of the NSOM fibre along the optical axis is followed by a global and uniform phase change on the wavefront recorded on CCD2, proportional to the displacement of the fibre. When a *z*-scan is performed, this *a priori* knowledge of the global phase signal to be recorded on CCD2, allows us to evaluate the stability of the setup during the scan.

5. Results and discussions

In order to illustrate the performance of the disclosed method and apparatus, 3D APSF measurements are presented. The example of a special MO will be taken. Some MO types permit the correction of aberration introduced by cover slips of different thickness, by means of an adjustable collar placed on the objective body. By turning the collar to a specific position, corresponding to some particular cover slip thickness, a slight displacement of some built-in lenses inside the MO, introduces variety of aberrations ranging from positive to negative sphericity aberrations, covering therefore, the different possibilities encountered in using cover slips of various thickness. We have used such an objective in order to observe the spherical aberration, which appears when the correction collar is turned from one extremity to the other. The measured MO was a long-distance Achroplan $\times 20$ with a numerical aperture 0.4 and a correction corresponding to a cover slip thickness varying from 0 to 1.5 mm. The MO was mounted in the optical setup without cover slip and the axial APSF has been measured for three particular positions of the correction collar: 0, 0.5 and 1. For each of the three correction collar positions, a stack of 740 holograms was recorded, corresponding to a total axial scan of 44.4 μm with 60-nm steps. The holograms were reconstructed and new stacks containing the intensity and respectively the phase images were created, providing the 3D IPSF and respectively the 3D PPSF. The axial APSF is obtained by sectioning the new stacks longitudinally, whereas the transverse APSF is obtained by performing a transversal section at a specific axial position. The results are summarized in Fig. 10.

We can observe that in the 0.5 collar position (Fig. 10b) the APSF is almost aberration free, except maybe a small amount of spherical aberration which can be identified from the slight asymmetry. When the collar is turned symmetrically with respect to the central 0.5 position (Fig. 10a and c), we can observe a symmetrical shift and conjointly, the intensity of the central spot of the IPSF is distributed in the secondary lateral lobes, what is typical for the spherical aberration. Note that for the position 1 of the correction collar (Fig. 10c) the fringes on the holograms were slightly saturated at the maximal intensity position, due to a nonperfect adjustment of the CCD1 dynamic range, what explains the dark spot appearing in the centre of the reconstructed intensity image. The axial shift during the collar turns is clearly observed and the shift distance may be used to quantify the amount of spherical aberration. This example also shows how the proposed method can be used to determine the best correction for given experimental conditions. The insets of Fig. 10b enhance the phase singularities, also called phase vortices or phase dislocations, appearing at the zero intensity points. These singularities are characterized, in a 2D representation, by a phase change of $\pm\pi$ on a closed path around the singularity: $\oint d\varphi = \pm 2\pi$. Great attention has recently been paid

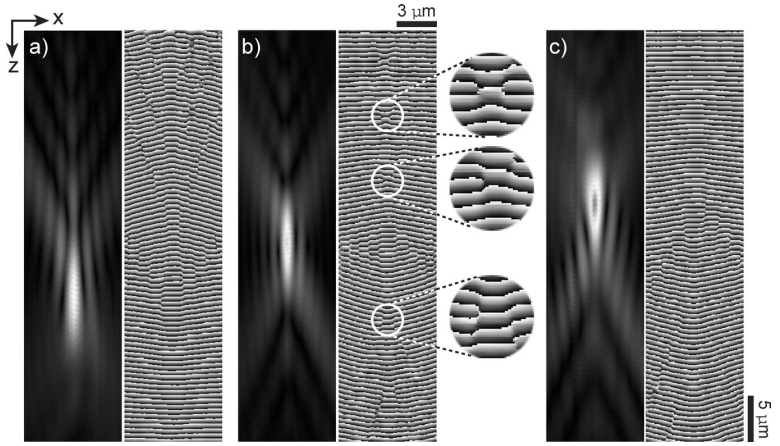

Fig. 10. Axial APSF (amplitude and phase) for different cover slip thickness compensation in an adjustable collar ×20 0.4 NA microscope objective: collar at position 0 (a), 0.5 (b) and 1 (c). The insets enhance the phase singularities appearing at the zero intensity points. The intensity distributions are enhanced by a nonlinear distribution of the grey levels, the phase distributions are coded in eight bits between $-\pi$ = black and π = white.

to the structure of these zero intensity points both theoretically and experimentally. Totzeck and Tiziani extensively and clearly described this phenomena and its possible use in super-resolution imaging in their study of the 2D complex field diffracted by subwavelength structures (Totzeck & Tiziani, 1997). Walford *et al.* (2002) and Dändliker *et al.* (2004) also discussed these singularities in their measurement of a lens APSF and showed that the study of their 3D conformation can play a role in aberrations identification. Thanks to the shorter acquisition time required for a complete 3D APSF measurement with our system (1D scan vs. 3D scan), the external noise sources including vibrations, air fluctuation or relative movements of the setup components, are minimized, the phase singularities more clearly identifiable in the 2D phase distributions. Furthermore the presented measuring technique is applicable without restriction to high NA MO, as pointed out in the next paragraph.

A more specific study has been conducted on a ×100 MO with 1.3 numerical aperture. The ideal conditions of use for this MO, predicted by the manufacturer, are an immersion oil of 1.518 refractive index and a cover slip of 0.17-mm thickness with 1.525 refractive index. Ideally, the specimen is supposed to be placed immediately behind the cover slip. If the ideal conditions are satisfied, the measured APSF is perfectly axially symmetric, assuming no misalignment in the setup. As it was shown before in the present paper, any small deviation from the ideal parameters induces spherical aberrations and causes significant modifications in the APSF shape. In our measurements, we have chosen to perform the axial scan by moving the object (the NSOM point) instead of the MO. The measurements presented in Fig. 11 (top) were achieved without cover slip but using the ideal immersion oil. The hologram stack was acquired with an axial step of 30.5 nm

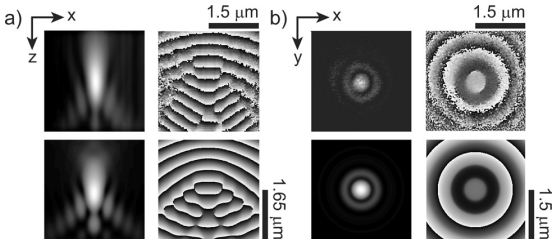

Fig. 11. Axial (a) and radial (b) comparisons in amplitude and phase between experimental APSF measurement (up) and calculated APSF with the Gibson and Lanni model [10] for a ×100 1.3 NA microscope objective. Measurements performed in oil (n = 1.518) without cover slip. The intensity distributions are enhanced by a nonlinear distribution of the grey levels, the phase distributions are coded in 8 bits between $-\pi$ = black and π = white.

and reconstructed by using the process described in subsection 4.2 (4.2 Holograms reconstruction).

Figure 11a compares the measured axial APSF (top) with the theoretically computed axial APSF (bottom). The theoretical simulation was obtained by using the scalar Gibson model (Gibson & Lanni, 1991), adapted for the case when the axial scan is performed by moving the object instead of the MO. Normally the use of a vectorial model, taking into account the polarization of light, is more suitable to calculate the APSF of such a high numerical aperture MO, notably to reproduce the circular asymmetry of the radial APSF. But, in the present work, the scalar model reveals itself sufficient as the light outgoing the NSOM fibre tip is nearly circularly polarized and the measurement is performed on the image side with a small NA. Therefore, the scalar model can be used in first approximation (the *xy*-distribution prediction will be

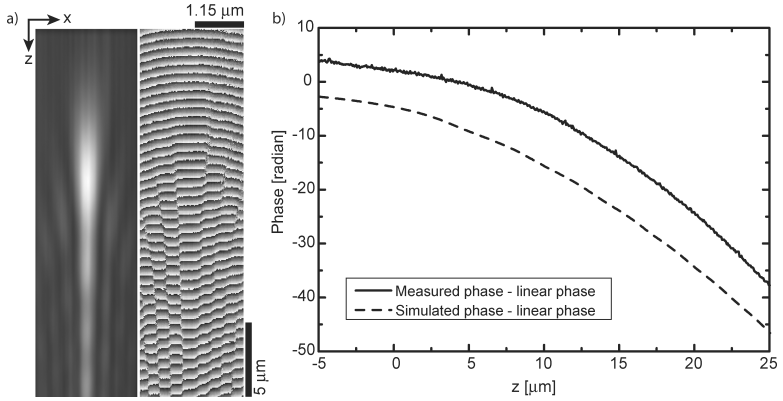

Fig. 12. (a) Measured *xz* sections of the IPSF and PPSF for the ×100/1.30 MO used under nondesigned conditions (no cover slip, no immersion oil); (b) simulated and measured phase profile behaviour — from which a linear phase corresponding to the displacement along the optical axis has been subtracted — along the optical axis.

somehow too narrow), and one can benefit from its speed advantages for calculations. The *z*-step in the simulation was 10 nm, which allows explaining the theoretical smoother phase image. The intensity was normalized and the grey levels were distributed nonlinearly to enhance low-intensity details. The phase was wrapped, taking values between 0 and 2π radians. As expected, the axial APSF is asymmetric, due to spherical aberrations caused by the absence of cover slip.

The transverse APSF, obtained by transverse sectioning of the 3D APSF in the plane corresponding to the axial IPSF maximum value, is shown in Fig. 11b: measurement (top) and theoretical simulation (bottom). The airy pattern is clearly visible both in the amplitude and phase images, with its central disk and the surrounding rings. As expected, phase π-jumps are observed at each passage through the amplitude minima. Due to the presence of spherical aberration, the phase is not constant but decreases smoothly toward the centre inside the regions delimited by the airy rings. As one can see from Fig. 11, the analytical model and the measured data are in excellent agreement, assessing the prediction of the Gibson and Lanni approach for calculating the aberrations due to a nondesigned use of the MO.

The last result presented concerns the experimental verification of the novel phase behaviour in the presence of optical aberrations induced by nondesigned conditions of use presented in subsection 3 (3. The 3D APSF in the presence of aberrations). Theoretical calculations and experimental results are presented in Fig. 12, for the same 100× 1.3 NA MO as above, used without immersion oil and without cover slip. The broadening of the APSF along the optical axis may be observed in Fig. 12a. As expected, the axial phase, from which a linear phase has been subtracted, diverges rapidly when going away from the main intensity lobe. In can be seen in Fig. 12b that simulation and experiment are in good agreement.

6. Conclusion

We have reviewed in the present paper different models, corresponding to various simplifying assumptions: scalar, paraxial and vectorial. Depending on the NA of MO and polarization of the beam, they can be applied to compute the 3D APSF of a lens or MO. It is obvious that the more adequate model is the vectorial one, including considerations about the polarization state and separate calculus of each field component. The differences between the vectorial and the scalar model are not very significant when low and moderate NA systems are considered, but may become important for high NA systems typically above 0.65 NA. The advantage brought by the scalar model is its simple implementation and reduced computation time, which, for low and moderate NA system can be further reduced by considering the paraxial approximation. For the first time, the complex APSFs are calculated in amplitude and phase according to the vectorial formulation applied to the Gibson model. First calculations reveal the 3D phase distribution within the PSF as a function of polarization, whereas the second ones illustrate the changes accompanying high NA MO under nondesigned conditions. The simulations, performed with the Gibson model, enlighten the phase variation on the optical axis, in the presence of aberrations caused by nondesigned conditions (refractive index, cover slip type): the axial phase is no more simply proportional to the displacement along the axis. This observation, experimentally verified, suggests that the study of the phase variations on the axis could provide a very sensitive indicator of the presence of aberrations, and also as a quantitative measure of the aberrations weight.

Theoretical analyses of imaging systems PSF have been widely and systematically conducted. Nowadays each microscope user can benefit from a better skill in the design of

MOs. Most recent deconvolution algorithms have contributed to the enhancement of the image quality. In this context, the PPSF role, obvious in all phase-sensitive imaging techniques, can also play an essential role in aberrations identifications and quantifications in microscopy as it already has been discussed. The results presented in this paper provide a new contribution to the problem of aberrations identification and removal by introducing the concept of PPSF as a sensitive index to lenses or MO imperfections.

To fulfil experimental requirements we have developed a fast, reliable and quantitative method for measuring the APSF of an optical system, and MOs in particular. A 1D scan, performed by moving a NSOM fibre tip along the optical axis in the focal region of the MO, leads to the full complex 3D description of the APSF after numerically processing the holographic digitally recorded data. The accuracy of the phase determination reaches up to $\lambda/60$ when performed in air. The setup can easily be adapted to the working parameters of a given MO (immersion oil thickness and refractive index, cover slip thickness and refractive index, specimen position, etc.) allowing a precise and reliable characterization of the MO in its using conditions. This effective measurement can be used as a simple and efficient technique to assess the predictions of an analytical model, like the Gibson & Lanni approach used in this paper (Gibson & Lanni, 1991). Furthermore, the knowledge of the exact APSF, giving a direct access to the optical aberrations present in the system, allows, within the frame work of phase-sensitive imaging techniques, including DHM, a precise interpretation of the measured phase on a given specimen by numerically compensating for all these aberrations.

Acknowledgements

This research has been supported by the Swiss National Science Foundation (SNSF) grant 205320-103885/1. The authors gratefully acknowledge Prof. C. J. R. Sheppard for the valuable discussions on theoretical aspects about the PSF. The authors also warmly thank Etienne Cuche, from the start-up company Lyncée Tec SA (www.lynceetec.com), for his enthusiasm and his precious comments on digital holography.

References

Beverage, J.L., Shack, R.V. & Descour, M.R. (2002) Measurement of the three-dimensional microscope point spread function using a Shack-Hartmann wavefront sensor. *J. Microsc.* **205**, 61–75.

Born, M. & Wolf, E. (1980) *Principles of Optics*. Pergamon, Oxford.

Braat, J.M. (2003) Extended Nijboer-Zernike representation of the vector field in the focal region of an aberrated high-aperture optical system. *J. Op. Soc. Am. A* **22**, 2281–2292.

Charrière, F., Colomb, T., Montfort, F., Cuche, E., Marquet, P. & Depeursinge, C. (2006) Shot noise influence in reconstructed phase image SNR in digital holographic microscopy. *Appl. Opt.* 45, 7667–7673.

Colomb, T., Cuche, E., Charrière, F., Kühn, K., Aspert, N., Montfort, F., Marquet, P. & Depeursinge, C. (2006) Automatic procedure for aberration compensation in digital holographic microscopy and applications to specimen shape compensation. *Appl. Opt.* **45**, 851–863.

Cuche, E., Bevilacqua, F. & Depeursinge, C. (1999) Digital holography for quantitative and phase-contrast imaging. *Opt. Lett.* **24**, 291–293.

Dändliker, R., Tortora, P., Vaccaro, L. & Nesci, A. (2004) Measuring optical phase singularities at subwavelength resolution. *J. Opt. A* **6**, 189–196.

Dorn, R., Quabis, S. & Leuchs, G. (2003) The focus of light — linear polarization breaks the rotational symmetry of the focal spot. *J. Mod. Opt.* **12**, 1917–1926.

Farnell, G.F. (1957) Calculated intensity and phase distribution in the image space of a microwave lens. *Can. J. Phys.* **35**, 777–783.

Farnell, G.F. (1958) On the axial phase anomaly for microwave lenses. *J. Opt. Soc. Am. A.* **48**, 643–647.

Gibson, S.F. & Lanni, F. (1989) Diffraction by a circular aperture as a model for three-dimensional optical microscopy. *J. Opt. Soc. Am. A* **6**, 1357–1367.

Gibson, S.F. & Lanni, F. (1991) Experimental test of an analytical model of aberration in an oil-immersion objective lens used in three-dimensional light microscopy. *J. Opt. Soc. Am. A* **8**, 1601–1613.

Gu, M. (2000) *Advanced Optical Imaging Theory*. Springer Verlag, Berlin Heidelberg.

Haeberlé, O. (2003) Focusing of light through a stratified medium: a practical approach for computing microscope point spread functions. Part I: Conventional microscopy. *Opt. Commun.* **216**, 55–63.

Hanser, B.M., Gustafsson, M.G.L., Agard, D.A. & Sedat, J.W. (2004) Phase-retrieved pupil functions in wide-field fluorescence microscopy. *J. Microsc.* **216**, 32–48.

Ignatowsky, V.S. (1919) Diffraction by a lens of arbitrary aperture. *Trans. Opt. Inst. Petr.* **4**, 1–36.

Innes, D.J. & Bloom, A.L. (1966) Design of optical systems for use with laser beams. *Spectra-Phys. Laser Tech. Bull.* **5**, 1–10.

Juskaitis, R. & Wilson, T. (1998) The measurement of the amplitude point spread function of microscope objective lenses. *J. Microsc.* **189**, 8–11.

Linfoot, B.E. & Wolf, E. (1956) Phase distribution near focus in an aberration-free diffraction image. *Proc. Phys. Royal Soc. B*, **LXIX**, 823–832.

Luneburg, R.K. (1966) *Mathematical Theory of Optics*. University of California Press, Berkeley and Los Angeles.

Malacara, D. & De Vore, S.L. (1992) Interferogram evaluation and wavefront techniques. *Optical Shop Testing* (ed. by D. Malacara). Wiley, New York.

Mansuripur, M. (2002) *Classical Optics and its Applications*. Cambridge University Press, Cambridge.

Marian, A. (2005, first published in 2006) *Measurement and interpretation of the 3D amplitude point spread function of lenses and microscope objectives*. PhD thesis, EPFL, Lausanne.

Mills, J.P. & Thompson, B.J. (1986) Effect of aberrations and apodization on the performance of coherent optical systems. I. The amplitude impulse response. *J. Opt. Soc. Am. A* **3**, 694–703.

Richards, B. & Wolf, E. (1959) Electromagnetic diffraction in optical systems II. Structure of the image field in an aplanatic system. *Proc. Royal Soc. A* **253**, 358–379.

Schrader, M. & Hell, S.W. (1996) Wavefronts in the focus of a light microscope. *J. Microsc.* **184**, 143–148.

Selligson, J.L. (1981) *Phase measurement in the focal region of an aberrated lens*. PhD thesis, University of Rochester, New York.

Sheppard, C.J.R. (2000) Validity of the Debye approximation. *Opt. Lett.* **25**, 1660–1662.

Török, P. & Fu-Jen, K. (2002) Point-spread function reconstruction in high aperture lenses focusing ultra-short laser pulses. *Opt. Comm.* **213**, 97–102.

Török, P. & Varga, P. (1997) Electromagnetic diffraction of light focused through a stratified medium. *Appl. Opt.* **36**, 2305–2312.

Török, P. (1998) Focusing of electromagnetic waves through a dielectric interface by lenses of finite Fresnel number. *J. Opt. Soc. Am. A*, **15**, 3009–3015.

Totzeck, M. & Tiziani, H.J. (1997) Phase-singularities in 2D diffraction fields and interference microscopy. *Opt. Comm.* **138**, 365–382.

Walford, J.N., Nugent, K.A., Roberts, A. & Scholten, R.E. (2002) High-resolution phase imaging of phase singularities in the focal region of a lens. *Opt. Lett.* **27**, 345–347.

Wang, W., Friberg, A.T. & Wolf, E. (1995) Structure of focused fields in systems with large Fresnel numbers. *J. Opt. Soc. Am. A* **12**, 1947–1953.

Wolf, E. & Li, Y. (1981) Conditions for the validity of the Debye integral representations of focused fields. *Opt. Commun.* **39**, 205–210.

7.2 Amplitude point spread function measurement of high NA microscope objectives by digital holographic microscopy

Paper published in Optics Letters **32**, 2456-2458 (2007).

2456 OPTICS LETTERS / Vol. 32, No. 16 / August 15, 2007

Amplitude point-spread function measurement of high-NA microscope objectives by digital holographic microscopy

Florian Charrière,[1,*] Anca Marian,[1] Tristan Colomb,[2] Pierre Marquet,[2] and Christian Depeursinge[1]

[1]*Ecole Polytechnique Fédérale de Lausanne (EPFL), Imaging and Applied Optics Institute, CH-1015 Lausanne, Switzerland*

[2]*Centre de Neurosciences Psychiatriques, Département de Psychiatrie DP-CHUV, Site de Cery, CH-1008 Prilly-Lausanne, Switzerland*

[*]*Corresponding author: florian.charriere@a3.epfl.ch*

Received June 13, 2007; accepted July 11, 2007;
posted July 24, 2007 (Doc. ID 84133); published August 10, 2007

We present here a three-dimensional evaluation of the amplitude point-spread function (APSF) of a microscope objective (MO), based on a single holographic acquisition of its pupil wavefront. The aberration function is extracted from this pupil measurements and then inserted in a scalar model of diffraction, allowing one to calculate the distribution of the complex wavefront propagated around the focal point. The accuracy of the results is compared with a direct measurement of the APSF with a second holographic system located in the image plane of the MO. Measurements on a 100× 1.3 NA MO are presented. © 2007 Optical Society of America

OCIS codes: 090.1760, 090.1000, 110.1220, 110.4850.

The point-spread function (PSF), the image of a single source point through the optical system, remains today the usual way to characterize an optical imaging system, specifically a microscope objective (MO). Commonly, only the intensity point-spread function (IPSF) is considered, neglecting the phase point-spread function (PPSF). In phase-sensitive microscopy techniques, including digital holographic microscopy (DHM) [1], an exact knowledge of the PPSF becomes of major importance to properly interpret the measured phase signal, and eventually compensate for the aberrations in the system. Therefore, measuring both the IPSF and the PPSF, defining the complex amplitude point-spread function (APSF), is mandatory to fully characterize a MO. Interferometric techniques, requiring a three-dimensional (3D) scan of the focal region with several signal acquisitions at each position, were proposed by Selligson [2] and Juskaitis and Wilson [3]. Another idea consists in measuring the complex wavefront at the exit pupil of the MO and recovering the 3D APSF with a diffraction calculation based on these pupil-function (PF) measurements. Beverage *et al.* used a Shack–Hartmann wavefront sensor combined with a Fourier transform calculus to recover its PSF [4]; the PF sampling is relatively low compared with the sampling of a CCD camera, as used in the present Letter, which can limit an accurate extraction of all the PF aberrations. Török and Fu-Jen used a Twyman–Green interferometer for PF measurement and the Debye–Wolf diffraction theory to predict the complex APSF [5]; a well-calibrated spherical mirror is required as reference, and a double passage of the light through the MO may cause certain aberrations to cancel and others to double. Hanser *et al.* obtained the complex PF from defocused IPSF images of subresolution beads with a phase-retrieval algorithm [6]; a comparison between the recovered 3D PSF and direct measurement is presented only for the IPSF, neglecting the PPSF. Digital holography has finally already been used in a live star test procedure by Heil *et al.* [7], but only IPSF was again considered. In the present Letter, a pupil-based evaluation of the 3D APSF is, for the first time to our knowledge, compared in amplitude and phase with a direct measurement of the APSF in the image plane of the MO, thanks to an original digital holographic setup involving two cameras.

The setup (Fig. 1), is based on a Mach–Zehnder interferometer. The light source is a $\lambda = 532$ nm laser (frequency-doubled Nd:YAG) with adjustable power up to 100 mW. In the object arm, the laser is coupled in a scanning near-field optical microscopy (SNOM) fiber with a 60 nm diameter emitting tip used as a pointlike object. The MO is mounted on micrometric *xyz* stages with tilt facilities for a proper alignment of the MO on the optical axis. The fiber is installed on a piezoelectric *xyz* stage, permitting nanometric displacements within a range of 80 μm. The first CCD camera, CCD1, is positioned at a distance of 1500 mm to create a sufficiently high magnification (about 1000× for a 100× MO) to obtain an optimal

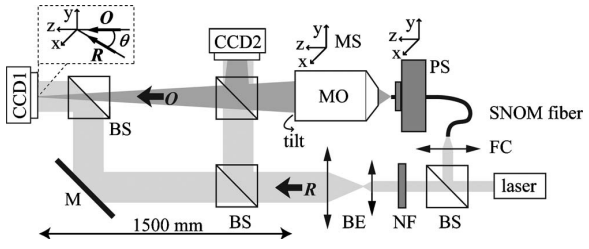

Fig. 1. Setup for APSF measurement: BS, beam splitter; BE, beam expander, NF, neutral density filter; $\lambda/2$ half-wave plate; M, mirror; FC, fiber-coupling lens; PS, piezo system, MS, micrometric stage; MO, microscope objective; *O*, object wave; *R*, reference wave. Inset, detail of the off-axis geometry at the incidence on the CCD.

0146-9592/07/162456-3/$15.00

August 15, 2007 / Vol. 32, No. 16 / OPTICS LETTERS 2457

sampling by the CCD of the SNOM tip diffraction; here the CCD is used with sensitive area around 3.4 mm in size (512×512 pixels with size 6.7 μm). A beam splitter, placed as close as possible from the MO, enables a second CCD camera, CCD2, to capture an image of the PF of the MO. The reference wave R is first enlarged with a beam expander, after which it is superimposed, by means of beam splitters at two different locations on the object beam O to produce a hologram on each CCD. An off-axis geometry was considered on both CCDs (see inset Fig. 1). The light intensity of the reference beam is adjusted with neutral density filters. Measurements presented here have been achieved on a vibrations-insulating table protected by curtains. The object and the reference arms were surrounded by plexiglass tubes to minimize the perturbations coming from the air turbulences. Recorded holograms are processed as follows. First, a filtering in the Fourier space is achieved to preserve only the interesting interference term while removing the DC term and the twin image term [8], after which the reillumination of the filtered hologram with the reference wave is simulated. An automatic algorithm (15 Hz with a P4 2.8 Ghz), extensively described in [9], performs this procedure, which must carefully be carried out to avoid any phase-error generation during the reconstruction process.

For a given position of the SNOM tip, the processing of a single digital hologram recorded on CCD1 allows for a quantitative measurement of the transverse APSF in amplitude and phase. Thus, a single scan of the SNOM tip along the optical axis is sufficient to acquire a stack of holograms describing the complete 3D APSF of the MO. This method, described completely in [10], presents several advantages, as far as speed and ease of use are concerned (the scan is performed at 25 Hz), when compared with other techniques [2–7].

On the CCD2-hologram, the recorded object wavefront corresponds in first approximation to the MO PF. This approximation results from the very slow convergence of the beam emerging from the MO [11], which indeed forms an in-focus image on CCD1 placed at a distance of 1500 mm, much larger than the short propagation distance between the real MO pupil and the CCD2 chip (~50 mm). In [9] Colomb *et al.* explains how to compensate for the phase aberrations induced by the optical component of the setup, including the MO, in the reconstructed phase images. This compensation is based on the evaluation of the phase distribution along profiles traced in the phase image at locations where the phase is known to be constant. This automatic procedure is able to provide quantitative values of the aberrations in terms of coefficients calculated according to a mathematical model. In [9], a polynomial model was used to describe the phase function, while in the present study a Zernike polynomials (ZP) description is used. The ZP Z_i are specifically well adapted to accurately describe the phase aberrations in the pupil aberration function $P(x,y)$, which can be developed in a series $P(x,y)=\Sigma_i \alpha_i Z_i$, where the α_i are coefficients and the Z_i are defined on a circular pupil with unitary radius. A summary of the used Z_i is presented in Table 1. To properly evaluate the aberration coefficients, the fitting procedure of [9] is applied three times sequentially. First, a simple 2D linear mathematical model is used in the reconstruction process to compensate for the tilt aberration due to the off-axis geometry. The corresponding intensity and phase distribution is presented in Figs. 2(a) and 2(b). Second, a 2D parabolic function is applied on the obtained phase distribution to compensate for the field curvature due to the focusing of the wavefront to CCD2. The remaining phase function distribution, representing the aberrations of the PF, is presented in Fig. 2(c). Third, the Zernike polynomials model is applied to the aberration function, providing its direct decomposition in terms of aberration coefficients. Figure 2(d) shows the phase distribution after subtraction of its evaluation with the Zernike polynomial, and as expected appears nearly constant, except the remaining circular patterns due to the light diffraction on MO aperture present on all the phase images of Fig. 2, proving that the used model is able to correctly describe the aberration function. The measurements presented in this Letter have been achieved with a 100 ×, 1.3 NA MO, in immersion oil (1.518 refractive index), but without coverslip to intentionally introduce aberrations. In Table 1, the extracted coefficients for each aberration type are presented, showing a pre-

Table 1. Zernike Polynomials and Measured Coefficients in the Pupil of the MO

Polynomial	Cartesian Form	Description	Coefficient
Z_0	1	Piston	−4.930
Z_1	2x	Tilt y	0.051
Z_2	2y	Tilt y	−0.008
Z_3	$3^{1/2}(2x^2+2y^2-1)$	Power	−0.338
Z_4	$6^{1/2}(2xy)$	Astig. y	0.038
Z_5	$6^{1/2}(x^2-y^2)$	Astig. x	0.069
Z_6	$8^{1/2}(3x^2y+3y^2-2y)$	Coma y	0.034
Z_7	$8^{1/2}(3x^3+3xy^2-2x)$	Coma x	−0.051
Z_8	$8^{1/2}(3x^2y-y^3)$	Trefoil y	0.031
Z_9	$8^{1/2}(x^3-3xy^2)$	Trefoil x	0.018
Z_{10}	$5^{1/2}(6(x^4+2x^2y^2+y^4-x^2-y^2)+1)$	1^{ary} spherical	−0.573

2458 OPTICS LETTERS / Vol. 32, No. 16 / August 15, 2007

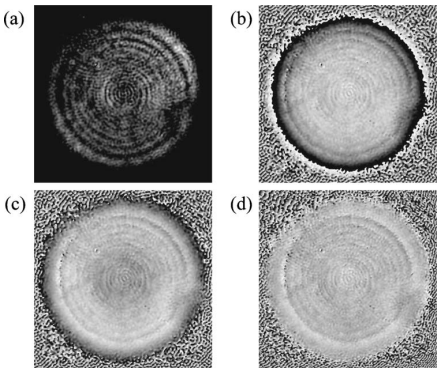

Fig. 2. Reconstructed images of the pupil hologram: (a) intensity, (b) direct measured phase, (c) aberration function, (d) residual phase after aberration function subtraction. Phase images gray-scale range is between $-\pi$ and π.

dominant primary spherical aberration. The extracted coefficients and the corresponding aberrations were introduced in a scalar model of diffraction [12] to calculate the 3D APSF of our MO in the situation described in Fig. 3:

$$U(r_2,\psi,z_2) = \frac{i}{\lambda}\int_0^{2\pi}\int_0^{\alpha} P(\theta,\varphi)\exp[ikr_2 \sin\theta\cos(\varphi-\psi) - ikz_2\cos\theta]\sin\theta d\theta d\varphi, \quad (1)$$

where $U(r_2,\psi,z_2)$ is the APSF in polar coordinates, k is the wavevector, α is the maximum angle of convergence of rays in image space, and (θ,φ) is the pupil aberration function in term of θ and φ (see Fig. 3).

Therefore, with our setup, we are able to compare the APSF calculated from a single evaluation of aberrations coefficients of the MO PF with a direct measurement of the 3D APSF in the MO image plane performed by scanning the SNOM tip along the optical axis. The results are summarized in Fig. 4, presenting x–z and x–y image comparisons in amplitude and phase between experimental APSF (top) and calculated with the scalar model of diffraction with aberration description extracted in the pupil (bottom). In the middle of Fig. 4, a completely calculated APSF obtained with the Gibson and Lanni model was added, which predicts the APSF for a use of the MO under nonstandard conditions [13]. As it can be seen on Fig. 4, the two measured APSFs and the theoretical one are in good agreement. This work illustrates

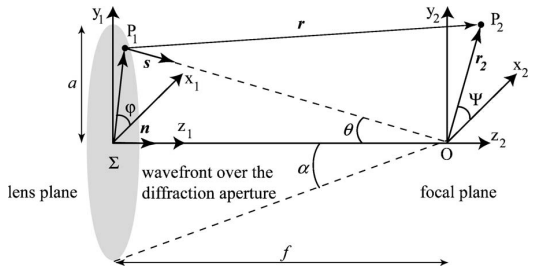

Fig. 3. Focusing through a lens of aperture a, focal f, and maximum subtended half-angle α.

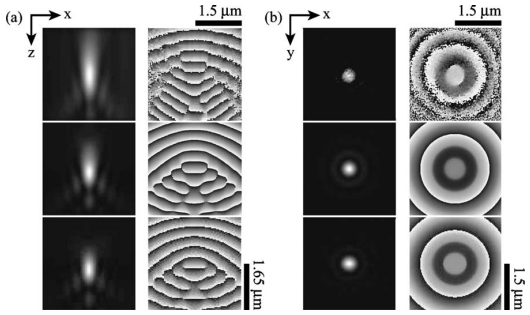

Fig. 4. (a) x–z and (b) x–y image comparisons in amplitude and phase between APSF measurement (top) calculated APSF with the Gibson and Lanni model (middle) and calculated with the scalar model of diffraction with aberration description extracted in the pupil (bottom). Measurements performed in oil ($n=1.518$) without coverslip for a $\times 100$ 1.3 NA microscope objective. (Intensity images are enhanced by a nonlinear distribution of the gray levels; phase images gray-scale range is between $-\pi$ and π.)

that a reliable estimation of the complete 3D APSF can be extracted from a single holographic acquisition of a MO PF. The validity of the method is for the first time to our knowledge not only attested through the comparison with a well-known theoretical aberrations model but also with a direct and quantitative measurement of the 3D APSF. The single-hologram recording, allowing one to drastically reduce the acquisition time and consequently the stability requirement, remains the main advantage of the pupil evaluation method compared with the direct measurement method.

This research has been supported by the Swiss National Science Foundation grant 205320-112195/1.

References

1. P. Marquet, B. Rappaz, P. J. Magistretti, E. Cuche, Y. Emery, T. Colomb, and C. Depeursinge, Opt. Lett. **30**, 468 (2005).
2. J. L. Selligson, "Phase measurement in the focal region of an abberated lens," Ph.D. dissertation (University of Rochester, 1981).
3. R. Juskaitis and T. Wilson, J. Microsc. **189**, 8 (1998).
4. J. L. Beverage, R. V. Shack, and M. R. Descour, J. Microsc. **205**, 61 (2002).
5. P. Török and K. Fu-Jen, Opt. Commun. **213**, 97 (2002).
6. B. M. Hanser, M. G. L. Gustafsson, D. A. Agard, and J. W. Sedat, J. Microsc. **216**, 32 (2004).
7. J. Heil, J. Wesner, W. Müller, and T. Sure, Appl. Opt. **42**, 5073 (2003).
8. E. Cuche, P. Marquet, and C. Depeursinge, Appl. Opt. **39**, 4070 (2000).
9. T. Colomb, E. Cuche, F. Charrière, J. Kühn, N. Aspert, F. Montfort, P. Marquet, and C. Depeursinge, Appl. Opt. **45**, 851 (2006).
10. A. Marian, F. Charrière, T. Colomb, F. Montfort, J. Kühn, P. Marquet, and C. Depeursinge, J. Microsc. **225**, 156 (2007).
11. W. Wang, A. T. Friberg, and E. Wolf, J. Opt. Soc. Am. A **12**, 1947 (1995).
12. M. Gu, *Advanced Optical Imaging Theory* (Springer-Verlag, 2000).
13. S. F. Gibson and F. Lanni, J. Opt. Soc. Am. A **8**, 1601 (1991).

Chapter 8

Conclusion

At the first glance the present thesis address many research topics, dealing conjointly with metrology (chapter 3), noise behavior (chapter 4), optical tomography (chapter 5), refractive index measurement (chapter 6) or optical aberrations characterization (chapter 7). In its diversity, this thesis aims humbly to address some of the multiple aspects of DHM as those facets require some consideration when setting up a DHM experiment.

The studies on the influence of shot noise in DHM phase images accuracy constitute a very valuable results pragmatically speaking. For the first time in the framework of DHM, the best achievable phase accuracy is expressed as a function of the quantity of light available [Cha06a, Cha07a]: this results can from now on be used daily in the lab, like a simple lookup table, to precisely quantify the noise contribution caused by the shot noise only. This is of primary importance, as the phase accuracy determines directly the precision of the technique, being in metrology [Keb99, Keb00, Keb01b, Keb01a, Mül05, Sin05, Cha06b], in DHM-based tomographic imaging [Vis98, Vis99, Lau02, Józ05, Józ06, Cha06c, Cha06d, Gór04, Gór06, Gór07] or in refractive index measurements [Beu96, Zha03, Lue06, Rap05, Kem06, Mar07b, Hos06, Son06, Tyc01].

In the tomographic experiments, it has been proved that quantitative refractive index (RI) 3-dimensional imaging based on DHM measurement is possible in the context of cell microscopy [Cha06c], and that morphometric data can be extracted from the reconstructions [Cha06d]. The knowledge of the 3D RI spatial distribution of a cell leads to invaluable information concerning the distribution and the optical properties of the intracellular organelles. Until today and in spite of this major issue, optical diffraction tomography applied successfully to cell imaging has provided few quantitative results [Vis98, Vis99]. Reliable RI values are difficult to obtain from the literature, as different measuring techniques were applied to different type of cells. A good review of the available techniques and RIs in the literature can be found in the first chapter of Dunn's thesis [Dun97]. Most of the presented techniques are designed to evaluate the RI of a specific cell component (membrane, nucleus, cytoplasm, etc.), and in this sense the method we propose is more general, as it furnishes a complete 3D distribution of the RI inside the cell.

Following an original idea proposed by Barer in the 1950s already in the framework of classical cellular interferometry [Bar52, Bar53, Bar57], it has been shown that DHM can be used to determine the RI and morphology of cells [Kem06, Lue06, Rap05]. As the RI is a function of the cell dry mass, depending on the intra-cellular concentration and the organelles arrangement, the optical phase shift induced by the specimen on the transmitted wave front can be regarded as a powerful endogenous contrast agent. Inspired by the first work of Barer [Bar69] or Chaubal *et al.* [Cha67, Cha68], the dual-wavelengths technique demonstrated in this thesis exploits the dispersion of the perfusion medium to obtain a set of equations, allowing decoupling the contributions of the RI and the cellular thickness to the total phase signal [Rapon]. The dispersion must be large enough to guaranty a good accuracy in the refractive index determination: following an idea of Marquet, the two wavelengths are chosen in the vicinity of the absorption peak of a dye added to the perfusion medium, where the absorption is accompanied by a strong variation of the dye RI as a function of the wavelength [Mar03a, Mar03b]. This DHM dual-wavelengths technique being adaptable for real-time imaging [Küh07], it presents a strong advantage compared to the other recently proposed phase imaging techniques for cellular RI determination [Lue06, Rap05, Kem06, Cur05].

In DHM, aberrations are usually compensated even by realizing a calibration of the system before measurement [Ind01, Ped01, Fer03], or by correcting the images taking advantage of some known information about the specimen properties [Cuc99, DN02, dN05, Col06b, Col06c, Mon06, Mic07]. In the

framework of numerical optics proposed by Colomb [Col06a, Col06d] the knowledge of the exact Amplitude Point Spread Function (APSF), giving a direct access to the optical aberrations present in the system, should allow a precise interpretation of the measured phase on a given specimen by numerically compensating for all these aberrations. The first difficulty with this approach applied to DHM concerns the acquisition of the APSF not only in intensity but also in phase. Interferometric techniques have been proposed, but they require a 3D-scan of the focal region with several signal acquisitions at each position [Sel81, Juš98]. Another idea consists in measuring the complex wavefront at the exit pupil of the MO and recovering the 3D APSF with a diffraction calculation [Bev02, Tör02, Han04, Hei03]. Two approaches proposing an original setup for complex amplitude point spread function (APSF) measurement of microscope objectives with DHM are presented at the end of the current thesis. In the first approach, a 1D scan, performed by moving a SNOM (Scanning Near field Optical Microscope) fiber tip along the optical axis in the focal region of the MO, leads to the full complex 3D description of the APSF after numerically processing the holographic digitally recorded data. The setup can easily be adapted to the working parameters of a given MO (immersion oil thickness and refractive index, cover slip thickness and refractive index, specimen position, etc.) allowing a precise and reliable characterization of the MO in its using conditions [Mar07a]. The second approach propose an estimation of the complete 3D APSF, derived from a single holographic acquisition of a MO pupil function. The validity of the method is attested through the comparison with a well-known theoretical aberrations model, but also with the first approach for APSF measurement [Cha07b]. The single-hologram recording, allowing to drastically reduce the acquisition time and consequently the stability requirement, are the main advantage of the pupil evaluation method compared to the direct measurement method.

This thesis is in some way representative of the current position of the relatively young DMH among older quantitative phase imaging techniques: well-established results are presented conjointly with ongoing works and prospective research. DHM has now certainly won its place in metrology, as illustrated by the paper on the microlenses characterization (chapter 3), and the studies about the influence of the shot noise on the phase accuracy will certainly be helpful in that field also (chapter 4). The capacity of DHM in quantitative cell tomography has been proved (chapter 5), but its use for extensive and systematic studies still necessitates work to fully automatize the reconstruction process. As it has been seen, the rotation of the specimen in the microscope is currently a limiting factor for both the resolution and the refractive index accuracy; therefore, other experimental configurations, proposing noticeably an xyz-scan instead of the rotation [Vis04], should be thoroughly investigated. Concerning the proposed decoupling procedure (chapter 6), allowing distinction between the refractive index and the height of cells, real time imaging will be possible as it has already been implemented successfully in dual-wavelenghts DHM [Küh07], and the main remaining work concerns the choice of the ideal dye to be placed in the perfusion medium: beside its dispersion properties, the dye must prove non-toxicity and should not penetrate inside the cell. The numerical parametric lenses and the digital optics formalism introduced by Cuche [Cuc00] and generalized by Colomb [Col06a] is certainly a key feature of DHM, greatly facilitating the phase reconstruction and even capable of aberrations compensation. It is to expect that the APSF evaluation techniques proposed in the present work (chapter 7), will open new ways within this framework, based on effective measurements of aberrations, instead of using *a priori* information about the specimen under investigation.

Conclusion bibliography

[Bar52] R. Barer. "Interference Microscopy and Mass Determination". Nature (London) **169**(4296): 366–367 (1952).

[Bar53] R. Barer. "Determination of dry mass, thickness, solid and water concentration in living cells". Nature (London) **172**(4389): 1097–1098 (1953).

[Bar57] R. Barer. "Refractometry and interferometry of living cells". J. Opt. Soc. Am. **47**(6): 545–556 (1957).

[Bar69] R. Barer. "Variation of refractive index of solutions with wavelength". J. Histochem. Cytochem. **17**(6): 423–424 (1969).

[Beu96] J. Beuthan, O. Minet, J. Helfmann, M. Herrig and G. Müller. "The spatial variation of the refractive index in biological cells". Phys. Med. Biol. **41**(3): 369–382 (1996).

[Bev02] J. L. Beverage, R. V. Shack and M. R. Descour. "Measurement of the three-dimensional microscope point spread function using a Shack-Hartmann wavefront sensor". J. Microsc. **205**(1): 61–75 (2002).

[Cha67] K. A. Chaubal, Z. Lodin and J. Pilny. "A New Approach to Determination of Thickness of Biological Specimens by 2 Wavelength Method Using Interference Microscopy". Acta Histochem. **26**(1): 131–143 (1967).

[Cha68] K. A. Chaubal, Z. Lodin and K. Korgaonkar. "Determination of difference in refractive index of cellular fluid at wavelengths of 436 and 546 mmu". J. Histochem. Cytochem. **16**(4): 271–272 (1968).

[Cha06a] F. Charrière, T. Colomb, F. Montfort, E. Cuche, P. Marquet and C. Depeursinge. "Shot noise influence in reconstructed phase image SNR in digital holographic microscopy". Appl. Opt. **45**(29): 7667–7673 (2006).

[Cha06b] F. Charrière, J. Kühn, T. Colomb, F. Montfort, E. Cuche, Y. Emery, K. Weible, P. Marquet and C. Depeursinge. "Characterization of microlenses by digital holographic microscopy". Appl. Opt. **45**(5): 829–835 (2006).

[Cha06c] F. Charrière, A. Marian, F. Montfort, J. Kühn, T. Colomb, E. Cuche, P. Marquet and C. Depeursinge. "Cell refractive index tomography by digital holographic microscopy". Opt. Lett. **31**(2): 178–180 (2006).

[Cha06d] F. Charrière, N. Pavillon, T. Colomb, T. Heger, E. Mitchell, P. Marquet, B. Rappaz and C. Depeursinge. "Living specimen tomography by digital holographic microscopy: morphometry of testate amoeba". Opt. Express **14**(16): 7005–7013 (2006).

[Cha07a] F. Charrière, B. Rappaz, J. Kühn, T. Colomb, P. Marquet and C. Depeursinge. "Influence of shot noise on phase measurement accuracy in digital holographic microscopy". Opt. Express **15**(14): 8818–8831 (2007).

[Cha07b] F. Charrière, A. Marian, T. Colomb, P. Marquet and C. Depeursinge. "Amplitude point spread function measurement of high NA microscope objectives by digital holographic microscopy". Opt. Lett. **32**(17): 2456–2458 (2007).

[Col06a] T. Colomb. *Numerical aberrations compensation and polarization imaging in digital holographic microscopy*. Thesis 3455, Ecole Polytechnique Fédérale de Lausanne (2006).

[Col06b] T. Colomb, E. Cuche, F. Charrière, J. Kühn, N. Aspert, F. Montfort, P. Marquet and C. Depeursinge. "Automatic procedure for aberration compensation in digital holographic microscopy and applications to specimen shape compensation". Appl. Opt. **45**(5): 851–863 (2006).

[Col06c] T. Colomb, J. Kühn, F. Charrière, C. Depeursinge, P. Marquet and N. Aspert. "Total aberrations compensation in digital holographic microscopy with a reference conjugated hologram". Opt. Express **14**(10): 4300–4306 (2006).

[Col06d] T. Colomb, F. Montfort, J. Kühn, N. Aspert, E. Cuche, A. Marian, F. Charrière, S. Bourquin, P. Marquet and C. Depeursinge. "Numerical parametric lens for shifting, magnification and complete aberration compensation in digital holographic microscopy". J. Opt. Soc. Am. A **23**(12): 3177–3190 (2006).

[Cuc99] E. Cuche, P. Marquet and C. Depeursinge. "Simultaneous amplitude-contrast and quantitative phase-contrast microscopy by numerical reconstruction of Fresnel off-axis holograms". Appl. Opt. **38**(34): 6994–7001 (1999).

[Cuc00] E. Cuche. *Numerical reconstruction of digital holograms: application to phase-contrast imaging and microscopy*. Thesis 2182, Ecole Polytechnique Fédérale de Lausanne (2000).

[Cur05] C. L. Curl, C. J. Bellair, T. Harris, B. E. Allman, P. J. Harris, A. G. Stewart, A. Roberts, K. A. Nugent and L. M. D. Delbridge. "Refractive index measurement in viable cells using quantitative phase-amplitude microscopy and confocal microscopy". Cytometry **65A**(1): 88–92 (2005).

[DN02] S. De Nicola, P. Ferraro, A. Finizio and G. Pierattini. "Wave front reconstruction of Fresnel off-axis holograms with compensation of aberrations by means of phase-shifting digital holography". Optics and Lasers in Engineering **37**(4): 331–340 (2002).

[dN05] S. de Nicola, A. Finizio, G. Pierattini, P. Ferraro and D. Alfieri. "Angular spectrum method with correction of anamorphism for numerical reconstruction of digital holograms on tilted planes". Opt. Express **13**(24): 9935–9940 (2005).

[Dun97] A. Dunn. *Light scattering properties of cells*. Ph.D. thesis, University of Texas (1997).

[Fer03] P. Ferraro, S. De Nicola, A. Finizio, G. Coppola, S. Grilli, C. Magro and G. Pierattini. "Compensation of the inherent wave front curvature in digital holographic coherent microscopy for quantitative phase-contrast imaging". Appl. Opt. **42**(11): 1938–1946 (2003).

[Gór04] W. Górski. "The influence of diffraction in microinterferometry and microtomography of optical fibers". Optics and Lasers in Engineering **41**(3): 565–583 (2004).

[Gór06] W. Górski. "Tomographic microinterferometry of optical fibers". Optical Engineering **45**(12): 125002 (2006).

[Gór07] W. Górski and W. Osten. "Tomographic imaging of photonic crystal fibers". Opt. Lett. **32**(14): 1977–1979 (2007).

[Han04] B. M. Hanser, M. G. L. Gustafsson, D. A. Agard and J. W. Sedat. "Phase-retrieved pupil functions in wide-field fluorescence microscopy". J. Microsc. **216**(1): 32–48 (2004).

[Hei03] J. Heil, J. Wesner, W. Muller and T. Sure. "Artificial star test by real-time video holography for the adjustment of high-numerical-aperture micro-objectives". Appl. Opt. **42**(25): 5073–5085 (2003).

[Hos06] M. M. Hossain, D. S. Mehta and C. Shakher. "Refractive index determination: an application of lensless Fourier digital holography". Optical Engineering **45**(10): 106203–7 (2006).

[Ind01] G. Indebetouw and P. Klysubun. "Spatiotemporal digital microholography". J. Opt. Soc. Am. A **18**(2): 319–325 (2001).

[Józ05] A. Jóźwicka and M. Kujawińska. "Digital holographic tomograph for amplitude-phase microelements testing". In "Proc. SPIE-Int. Soc. Opt. Eng.", (2005), vol. 5958, pp. 1–9.

[Józ06] A. Jóźwicka and M. Kujawińska. "Experimental proof-of-principle 3D measurements of microobjects by digital holographic tomography". In "Proc. SPIE-Int. Soc. Opt. Eng.", (2006), vol. 6188.

[Juš98] R. Juškaitis and T. Wilson. "The measurement of the amplitude point spread function of microscope objective lenses". J. Microsc. **189**(1): 8–11 (1998).

[Küh07] J. Kühn, T. Colomb, F. Montfort, F. Charrière, Y. Emery, E. Cuche, P. Marquet and C. Depeursinge. "Real-time dual-wavelength digital holographic microscopy with a single hologram acquisition". Opt. Express **15**(12): 7231–7242 (2007).

[Keb99] V. Kebbel, M. Adams, H. J. Hartmann and W. Juptner. "Digital holography as a versatile optical diagnostic method for microgravity experiments". Measurement Science and Technology **10**(10): 893–899 (1999).

[Keb00] V. Kebbel, H.-J. Hartmann and W. P. O. Jüptner. "Characterization of micro-optics using digital holography". In "Proc. SPIE-Int. Soc. Opt. Eng.", (2000), vol. 4101, p. B/.

[Keb01a] V. Kebbel, H. J. Hartmann and W. P. O. Jüptner. "Application of digital holographic microscopy for inspection of micro-optical components". In "Proc. SPIE-Int. Soc. Opt. Eng.", (2001), vol. 4398, pp. 189–198.

[Keb01b] V. Kebbel, H. J. Hartmann and W. P. O. Jüptner. "A new approach for testing of aspherical micro-optics with high numerical aperture". In "Proc. SPIE-Int. Soc. Opt. Eng.", (2001), vol. 4451, pp. 345–355.

[Kem06] B. Kemper, D. Carl, J. Schnekenburger, I. Bredebusch, M. Schafer, W. Domschke and G. von Bally. "Investigation of living pancreas tumor cells by digital holographic microscopy". Journal of Biomedical Optics **11**(3): 034005 (2006).

[Lau02] V. Lauer. "New approach to optical diffraction tomography yielding a vector equation of diffraction tomography and a novel tomographic microscope". J. Microsc. **205**: 165–176 (2002).

[Lue06] N. Lue, G. Popescu, T. Ikeda, R. R. Dasari, K. Badizadegan and M. S. Feld. "Live cell refractometry using microfluidic devices". Opt. Lett. **31**(18): 2759–2761 (2006).

[Mül05] J. Müller, V. Kebbel and W. Jüptner. "Digital holography as a tool for testing high-aperture micro-optics". Optics and Lasers in Engineering **43**(7): 739–751 (2005).

[Mar03a] P. Marquet. *Développement d'une nouvelle technique de microscopie optique tridimensionnelle, la microscopie holographique digitale. Perspectives pour l'étude de la plasticite neuronale*. Ph.D. thesis, Université de Lausanne (2003).

[Mar03b] P. Marquet, E. Cuche, C. Depeursinge and P. Magistretti. "Digital holographic imaging apparatus has container that contains medium in which sample is located" (2003).

[Mar07a] A. Marian, F. Charrière, T. Colomb, F. Montfort, J. Kühn, P. Marquet and C. Depeursinge. "On the complex three-dimensional amplitude point spread function of lenses and microscope objectives: theoretical aspects, simulations and measurements by digital holography". J. Microsc. **225**(2): 156–169 (2007).

[Mar07b] P. Marquet, Y. Emery, T. Colomb, F. Charrière, J. Kühn, C. Depeursinge, B. Rappaz, P. Jourdain and P. Magistretti. "Digital holographic microscopy for the study of cellular structure and dynamics". In "Focus on Microscopy FOM07", (Valencia, 2007).

[Mic07] L. Miccio, D. Alfieri, S. Grilli, P. Ferraro, A. Finizio, L. De Petrocellis and S. D. Nicola. "Direct full compensation of the aberrations in quantitative phase microscopy of thin objects by a single digital hologram". Appl. Phys. Lett. **90**: 041104 (3 pages) (2007).

[Mon06] F. Montfort, F. Charrière, T. Colomb, E. Cuche, P. Marquet and C. Depeursinge. "Purely numerical compensation for microscope objective phase curvature in digital holographic microscopy: influence of digital phase mask position". J. Opt. Soc. Am. A **23**(11): 2944–2953 (2006).

[Ped01] G. Pedrini, S. Schedin and H. J. Tiziani. "Aberration compensation in digital holographic reconstruction of microscopic objects". J. Mod. Opt. **48**(6): 1035–1041 (2001).

[Rap05] B. Rappaz, P. Marquet, E. Cuche, Y. Emery, C. Depeursinge and P. J. Magistretti. "Measurement of the integral refractive index and dynamic cell morphometry of living cells with digital holographic microscopy". Opt. Express **13**(23): 9361 – 9373 (2005).

[Rapon] B. Rappaz, F. Charrière, C. Depeursinge, P. J. Magistretti and P. Marquet. "Perfusion solution dispersion used for simultaneous cellular morphometry and refractive index measurement with Digital Holographic Microscopy" (*In preparation*).

[Sel81] J. L. Seligson. *Phase measurement in the focal region of an aberrated lens.* Ph.D. thesis, University of Rochester, New York (1981).

[Sin05] P. Singh, M. S. Faridi, C. Shakher and R. S. Sirohi. "Measurement of focal length with phase-shifting Talbot interferometry". Appl. Opt. **44**(9): 1572–1576 (2005).

[Son06] W. Z. Song, X. M. Zhang, A. Q. Liu, C. S. Lim, P. H. Yap and H. M. M. Hosseini. "Refractive index measurement of single living cells using on-chip Fabry-Pérot cavity". Appl. Phys. Lett. **89**: 203901 (3 pages) (2006).

[Tör02] P. Török and F. J. Kao. "Point-spread function reconstruction in high aperture lenses focusing ultra-short laser pulses". Opt. Commun. **213**(1-3): 97–102 (2002).

[Tyc01] V. P. Tychinski. "Coherent phase microscopy of intracellular processes". Physics-Uspekhi **44**(6): 617–629 (2001).

[Vis98] G. N. Vishnyakov and G. G. Levin. "Optical Microtomography of Phase Objects". Optics and Spectroscopy **85**(1): 73–77 (1998).

[Vis99] G. N. Vishnyakov, G. G. Levin, A. V. Likhachev and V. V. Pikalov. "Phase Tomography of 3D Biological Microobjects: Numerical Simulation and Experimental Results". Optics and Spectroscopy **87**(3): 413–419 (1999).

[Vis04] G. N. Vishnyakov, G. G. Levin, V. L. Minaev, V. V. Pickalov and A. V. Likhachev. "Tomographic Interference Microscopy of Living Cells". Microscopy and Analysis **18**(1-6): 15–17 (2004).

[Zha03] J. L. Zhao, P. Zhang, J. B. Zhou, D. X. Yang, D. S. Yang and E. P. Li. "Visualizations of light-induced refractive index changes in photorefractive crystals employing digital holography". Chin. Phys. Lett. **20**(10): 1748–1751 (2003).

florian charrière

passage perdonnet 1
ch-1005 lausanne
florian.charriere@a3.epfl.ch

29 years old
single
swiss

education

2003–2007	PhD in Digital Holographic Microscopy, Institute of Applied Optics, Ecole Polytechnique Fédérale de Lausanne (EPFL); thesis director: Prof. Ch. Depeursinge
	postgraduate formation in optics, EPFL doctoral school
	SPIE Best Student Paper Award finalist, BiOS 2006, San Jose CA, USA
1998–2003	MSc in Physics, EPFL, diploma thesis at the Institute of Applied Optics; exchange during the 3rd year at the Eidgenössische Technische Hochschule Zürich (ETHZ)
1994–1998	maturité scientifique, collège du Sud, Bulle

experiences

2003–2007	research assistant at the Institute of Applied Optics, EPFL supervision of practical work, semester projects and diploma thesis in digital holography
2001	2 months bilingual training period at the Federal Office of Metrology (METAS), Bern: tests and calibration of a soot generator
1999-2002	call-operator (French and German) 8h/week at Swisscom's information, Fribourg

languages

French	mother tongue
English	fluent in speaking and writing
German	good in speaking and understanding, basic skill in writing

computer skills

programming	Matlab, Labview
publishing	LaTeX, Photoshop, Illustrator, Acrobat, Office

hobbies and interest

gastronomy	tea enthusiast, wines and cheeses amateur, new flavors discoverer
music	active listener, odd producer

publications

peer-reviewed papers: first author

[1] F. Charrière, J. Kühn, T. Colomb, F. Montfort, E. Cuche, Y. Emery, K. Weible, P. Marquet and C. Depeursinge. "Characterization of microlenses by digital holographic microscopy". Appl. Opt. **45**(5): 829–835 (2006).

[2] F. Charrière, T. Colomb, F. Montfort, E. Cuche, P. Marquet and C. Depeursinge. "Shot noise influence in reconstructed phase image SNR in digital holographic microscopy". Appl. Opt. **45**(29): 7667–7673 (2006).

[3] F. Charrière, A. Marian, F. Montfort, J. Kühn, T. Colomb, E. Cuche, P. Marquet and C. Depeursinge. "Cell refractive index tomography by digital holographic microscopy". Opt. Lett. **31**(2): 178–180 (2006).

[4] F. Charrière, N. Pavillon, T. Colomb, T. Heger, E. Mitchell, P. Marquet, B. Rappaz and C. Depeursinge. "Living specimen tomography by digital holographic microscopy: morphometry of testate amoeba". Opt. Express **14**(16): 7005–7013 (2006).

[5] F. Charrière, B. Rappaz, J. Kühn, T. Colomb, P. Marquet and C. Depeursinge. "Influence of shot noise on phase measurement accuracy in digital holographic microscopy". Opt. Express **15**(14): 8818–8831 (2007).

[6] A. Marian*, F. Charrière*, T. Colomb, F. Montfort, J. Kühn, P. Marquet and C. Depeursinge. "On the complex three-dimensional amplitude point spread function of lenses and microscope objectives: theoretical aspects, simulations and measurements by digital holography". J. Microsc. **225**(2): 156–169 (2007). *Those authors contributed equally to this work.

[7] F. Charrière, A. Marian, T. Colomb and C. Depeursinge. "Amplitude point spread function measurement of high NA microscope objectives by digital holographic microscopy" Opt. Lett. **32**(17): 2456–2458 (2007).

[8] B. Rappaz*, F. Charrière*, C. Depeursinge, P. J. Magistretti and P. Marquet. "Simultaneous cell morphometry and refractive index measurement with dual-wavelength Digital Holographic Microscopy and dye enhanced dispersion of perfusion medium" (*Submitted to Opt. Lett., 2007*). *Those authors contributed equally to this work.

peer-reviewed papers: co-author

[1] P. Massatsch, F. Charrière, E. Cuche, P. Marquet and C. Depeursinge. "Time-domain optical coherence tomography with digital holographic microscopy". Appl. Opt. **44**(10): 1806–1812 (2005).

[2] T. Colomb, E. Cuche, F. Charrière, J. Kühn, N. Aspert, F. Montfort, P. Marquet and C. Depeursinge. "Automatic procedure for aberration compensation in digital holographic microscopy and applications to specimen shape compensation". Appl. Opt. **45**(5): 851–863 (2006).

[3] T. Colomb, J. Kühn, F. Charrière, C. Depeursinge, P. Marquet and N. Aspert. "Total aberrations compensation in digital holographic microscopy with a reference conjugated hologram". Opt. Express **14**(10): 4300–4306 (2006).

[4] T. Colomb, F. Montfort, J. Kühn, N. Aspert, E. Cuche, A. Marian, F. Charrière, S. Bourquin, P. Marquet and C. Depeursinge. "Numerical parametric lens for shifting, magnification and complete aberration compensation in digital holographic microscopy". J. Opt. Soc. Am. A **23**(12): 3177–3190 (2006).

[5] F. Montfort, F. Charrière, T. Colomb, E. Cuche, P. Marquet and C. Depeursinge. "Purely numerical compensation for microscope objective phase curvature in digital holographic microscopy: influence of digital phase mask position". J. Opt. Soc. Am. A **23**(11): 2944–2953 (2006).

[6] F. Montfort, T. Colomb, F. Charrière, J. Kühn, P. Marquet, E. Cuche, S. Herminjard and C. Depeursinge. "Submicrometer optical tomography by multiple-wavelength digital holographic microscopy". Appl. Opt. **45**(32): 8209–8217 (2006).

[7] J. Kühn, T. Colomb, F. Montfort, F. Charrière, Y. Emery, E. Cuche, P. Marquet and C. Depeursinge. "Real-time dual-wavelength digital holographic microscopy with a single hologram acquisition". Opt. Express **15**(12): 7231–7242 (2007).

patents

[1] C. Depeursinge, F. Charrière, T. Colomb, A. Marian and P. Marquet. "Method and apparatus to measure and compute the amplitude point spread function and associated parameters of a coherent optical imaging system" (2006).

[2] T. Colomb, E. Cuche, N. Aspert, J. Kühn, P. Marquet, C. Depeursinge, F. Montfort, F. Charrière, A. Marian, S. Bourquin, Y. Emery and S. Herminjard. "Wave front sensing method and apparatus" (2006).

conference proceedings: first author

[1] F. Charrière, J. Kühn, T. Colomb, F. Montfort, E. Cuche, Y. Emery, K. Weible and C. D. Depeursinge. "Microlenses metrology with digital holographic microscopy". In "Optical Measurement Systems for Industrial Inspection Iv, Pts 1 and 2", (2005), vol. 5856, pp. 447–453.

[2] F. Charrière, P. Marquet, E. Cuche and C. D. Depeursinge. "Shot noise influence in reconstructed phase images SNR in digital holographic microscopy". In "Progress in Biomedical Optics and Imaging - Proceedings of SPIE", (2005), vol. 5864, pp. 1–4.

[3] F. Charrière, P. Marquet, M. Von Ehr, E. Cuche and C. Depeursinge. "Digital holographic microscopy applied to pollen cells analysis and recognition". In "Progress in Biomedical Optics and Imaging - Proceedings of SPIE", (2005), vol. 5864, pp. 1–4.

[4] F. Charrière, T. Colomb, E. Cuche, P. Marquet and C. Depeursinge. "Digital Holographic Microscopy Applied to Diffraction Tomography of a Cell Refractive Index". In O. S. o. America, ed., "Biomedical Optics", (Fort Lauderdale, Florida, 2006), p. paper TuH6.

[5] F. Charrière, T. Colomb, P. Marquet and C. Depeursinge. "Digital holographic microscopy for complex pupil function evaluation of high NA microscope objectives". In FOM06, ed., "Focus On Microscopy", (Perth, Western Australia, 2006).

[6] F. Charrière, E. Cuche, P. Marquet and C. Depeursinge. "Biological cell (pollen grain) refractive index tomography with digital holographic microscopy". In J. A. Conchello, C. J. Cogswell and T. Wilson, eds., "Three-Dimensional and Multidimensional Microscopy: Image Acquisition and Processing Xiii", (Spie-Int Society Optical Engineering, Bellingham, 2006), *Proceedings of the Society of Photo-Optical Instrumentation Engineers (Spie)*, vol. 6090, pp. 9008–9008.

[7] F. Charrière, F. Montfort, E. Cuche and C. D. Depeursinge. "Shot noise perturbations in digital holographic microscopy phase images". In "Proc. SPIE-Int. Soc. Opt. Eng.", (Varna, 2006), *Holography 2005: International Conference on Holography, Optical Recording, and Processing of Information*, vol. 6252.

[8] F. Charrière, F. Montfort, J. Kühn, T. Colomb, A. Marian, E. Cuche, P. Marquet and C. Depeursinge. "Use of digital holographic microscopy in tomography". In R. Grzymala and O. Haeberle, eds., "Biophotonics and New Therapy Frontiers", (Spie-Int Society Optical Engineering, Bellingham, 2006), *Proceedings of the Society of Photo-Optical Instrumentation Engineers (Spie)*, vol. 6191, pp. O1910–O1910.

[9] F. Charrière, N. Pavillon, T. Colomb, E. Cuche, Y. Emery, P. Marquet, B. Rappaz and C. Depeursinge. "Quantitative refractive index micro-tomography with Digital Holographic Microscopy: an efficient tool for metrology in nanotechnology and life sciences". In "The 10th Annual European Conference On Micro and Nanoscale Technologies for the Biosciences", (Montreux, 2006).

[10] F. Charrière, N. Pavillon, T. Colomb, T. Heger, E. Mitchel, P. Marquet, B. Rappaz and C. Depeursinge. "Digital Holographic Microscopy for quantitative micro-tomography of living specimen: volume estimation of Hyalosphenia papilio". In "EOS European Optical Society Annual Meeting", (Paris, 2006).

[11] F. Charrière, J. Kühn, T. Colomb, E. Cuche, P. Marquet and C. Depeursinge. "Sub-cellular quantitative optical diffraction tomography with digital holographic microscopy". In "Progress in Biomedical Optics and Imaging - Proceedings of SPIE", (San Jose, CA, 2007), *Imaging, Manipulation, and Analysis of Biomolecules, Cells, and Tissues V*, vol. 6441.

[12] F. Charrière, A. Marian, T. Colomb and C. Depeursinge. "Amplitude point spread function measurement of high NA microscope objectives by digital holographic microscopy" (in preparation).

[13] F. Charrière, B. Rappaz, T. Colomb, J. Kühn, P. Marquet, Y. Emery, E. Cuche and C. Depeursinge. "Effect of shot noise in the phase accuracy in digital holographic microscopy". In "Focus on Microscopy FOM07", (Valencia, 2007).

conference proceedings: co-author

[1] T. Colomb, F. Charrière, P. Marquet and C. Depeursinge. "Full aberration compensation in digital holographic microscopy". In FOM06, ed., "Focus On Microscopy", (Perth, Western Australia, 2006).

[2] T. Colomb, J. Kühn, F. Charrière, P. Marquet, N. Aspert and C. Depeursinge. "Real-Time Phase Recovery of Biologicall Cell in Digital Holographic Microscopy by Use of a Self-Calibration Hologram". In "Biomedical Optics", (Optical Society of America, Fort Lauderdale, 2006), *Technical Digest (CD)*, vol. in press, p. paper TuI47.

[3] T. Colomb, J. Kuhn, E. Cuche, F. Charrière, F. Montfort, A. Marian, N. Aspert, P. Marquet and C. Depeursinge. "Automatic procedure for aberrations compensation in digital holographic microscopy - art. no. 618805". In C. Gorecki, A. K. Asundi and W. Osten, eds., "Optical Micro- and Nanometrology in Microsystems Technology", (Spie-Int Society Optical Engineering, Bellingham, 2006), *Proceedings of the Society of Photo-Optical Instrumentation Engineers (Spie)*, vol. 6188, pp. 18805–18805.

[4] C. D. Depeursinge, F. Charrière, A. M. Marian, F. Montfort, T. B. Colomb, J. Kühn, E. Cuche, Y. Emery, P. Marquet and P. J. Magistretti. "Digital Holographic Microscopy applied to Metrology". In W. Osten and M. Takeda, eds., "Optical Metrology in Production Engineering", (Spie-Int Society Optical Engineering, Bellingham, 2004), *Proceedings of the Society of Photo-Optical Instrumentation Engineers (Spie)*, vol. 5457, pp. 504–512.

[5] C. Depeursinge, F. Charrière, A. M. Marian, T. Colomb, F. Montfort, J. Kühn, N. Aspert, M. Botkine, F. Marquet, S. Bourquin, E. Cuche, Y. Emery, P. Marquet and P. J. Magistretti. "Digital Holographic Microscopy, a new imaging technology applied to nanotechnology and life". In H. Bjelkhagen, ed., "Application of holographic and optical coherence methods", (Proc. SPIE, Holo 05, Bulgaria, 2005).

[6] C. D. Depeursinge, A. M. Marian, F. Montfort, T. Colomb, F. Charrière, J. Kühn, N. Aspert, M. Botkine, M. S. Ghislain, F. Marquet, E. Cuche, Y. Emery, P. Marquet and P. J. Magistretti. "Digital Holographic Microscopy, a new imaging technology applied to biological cells and tissues". In "Conference on Lasers and Electro-Optics Europe - Technical Digest", (Munich, 2005), 2005 Conference on Lasers and Elctro-Optics Europe.

[7] C. Depeursinge, F. Charrière, T. Colomb, J. Kühn, Y. Emery, E. Cuche, P. Marquet and B. Rappaz. "Digital holographic microscopy: a new 3D imaging technique". In FOM06, ed., "Focus On Microscopy", (Perth, Western Australia, 2006).

[8] C. D. Depeursinge, A. M. Marian, F. Montfort, T. Colomb, F. Charriere and J. Kuhn. "Digital Holographic Microscopy (DHM) applied to optical metrology: A resolution enhanced imaging technology applied to inspection of microscopic devices with subwavelength resolution". In W. Osten, ed., "Fringe 2005", (Springer-Verlag Berlin, Berlin, 2006), pp. 308–314.

[9] Y. Emery, E. Cuche, F. Marquet, N. Aspert, P. Marquet, J. Kühn, M. Botkine, T. Colomb, F. Montfort, F. Charrière and C. Depeursinge. "Digital Holography Microscopy (DHM): Fast and robust systems for industrial inspection with interferometer resolution". In W. Osten, C. Gorecki and E. Novak, eds., "Optical Measurement Systems for Industrial Inspection Iv, Pts 1 and 2", (Spie-Int Society Optical Engineering, Bellingham, 2005), *Proceedings of the Society of Photo-Optical Instrumentation Engineers (Spie)*, vol. 5856, pp. 930–937.

[10] Y. Emery, E. Cuche, F. Marquet, N. Aspert, P. Marquet, J. Kühn, M. Botkine, T. Colomb, F. Montfort, F. Charrière, C. Depeursinge, P. Debergh and R. Conde. "Digital Holographic Microscopy (DHM) for metrology and dynamic characterization of MEMS and MOEMS - art. no. 61860N". In H. Urey and A. ElFatatry, eds., "Mems, Moems, and Micromachining Ii", (Spie-Int Society Optical Engineering, Bellingham, 2006), *Proceedings of the Society of Photo-Optical Instrumentation Engineers (Spie)*, vol. 6186, pp. N1860–N1860.

[11] J. Kühn, E. Cuche, Y. Emery, T. Colomb, F. Charrière, F. Montfort, M. Botkine, N. Aspert and C. Depeursinge. "Measurements of corner cubes microstructures by high-magnification Digital Holographic Microscopy - art. no. 618804". In C. Gorecki, A. K. Asundi and W. Osten, eds., "Optical Micro- and Nanometrology in Microsystems Technology", (Spie-Int Society Optical Engineering, Bellingham, 2006), *Proceedings of the Society of Photo-Optical Instrumentation Engineers (Spie)*, vol. 6188, pp. 18804–18804.

[12] J. Kühn, F. Charrière, T. Colomb, E. Cuche, Y. Emery and C. Depeursinge. "Digital holographic microscopy for nanometric quality control of micro-optical components". In "Proc. SPIE-Int. Soc. Opt. Eng.", (San Jose, CA, 2007), *Integrated Optics: Devices, Materials, and Technologies XI*, vol. 6475.

[13] P. Marquet, B. Rappaz, T. Colomb, F. Charrière, J. Kühn, Y. Emery, E. Cuche, C. Depeursinge and P. Magistretti. "Digital holographic microscopy, a new optical imaging technique to investigate cellular dynamics - art. no. 61910U". In R. Grzymala and O. Haeberle, eds., "Biophotonics and New Therapy Frontiers", (Spie-Int Society Optical Engineering, Bellingham, 2006), *Proceedings of the Society of Photo-Optical Instrumentation Engineers (Spie)*, vol. 6191, pp. U1910–U1910.

[14] F. Montfort, F. Charrière, T. Colomb, J. Kühn, E. Cuche and C. Depeursinge. "Tomography using multiple wavelengths in digital holography: Method, simulations and experiments - art. no. 618802". In C. Gorecki, A. K. Asundi and W. Osten, eds., "Optical Micro- and Nanometrology in Microsystems Technology", (Spie-Int Society Optical Engineering, Bellingham, 2006), *Proceedings of the Society of Photo-Optical Instrumentation Engineers (Spie)*, vol. 6188, pp. 18802–18802.

[15] F. Montfort, F. Charrière, J. Kühn, T. Colomb, E. Cuche, Y. Emery, P. Marquet and C. Depeursinge. "Multi-wavelength digital holographic microscopy for sub-micron topography of reflecting specimens". In "Progress in Biomedical Optics and Imaging - Proceedings of SPIE", (San Jose, CA, 2007), *Three-Dimensional and Multidimensional Microscopy: Image Acquisition and Processing XIV*, vol. 6443.

[16] B. Rappaz, F. Charrière, J. Kühn, P. Marquet, C. Depeursinge and P. Magistretti. "Measurement of the integral refractive index of erythrocytes with a Digital Holographic Microscope". In "EOS European Optical Society Annual Meeting", (Paris, 2006).

[17] B. Rappaz, A. Barbul, F. Charrière, J. Kühn, P. Marquet, R. Korenstein, C. Depeursinge and P. Magistretti. "Erythrocytes volume and refractive index measurement with a digital holographic microscope". In "Progress in Biomedical Optics and Imaging - Proceedings of SPIE", (San Jose, CA, 2007), *Optical Diagnostics and Sensing VII*, vol. 6445.

[18] P. Marquet, Y. Emery, T. Colomb, F. Charrière, J. Kühn, C. Depeursinge, B. Rappaz, P. Jourdain and P. Magistretti. "Digital holographic microscopy for the study of cellular structure and dynamics". In "Focus on Microscopy FOM07", (Valencia, 2007).